Stability and Dynamics of Anti-Surfactant Solutions

Justin J. A. Conn

Department of Mathematics and Statistics

University of Strathclyde

A thesis presented in partial fulfilment of the requirements for the degree of Doctor of Philosophy

January 2017

Declaration of Authenticity and Author's Rights

This thesis is the result of the author's original research. It has been composed by the author and has not been previously submitted for examination which has led to the award of a degree.

Signed:

Date:

Contents

Acknowledgements

First and foremost, I would like to thank my supervisors Prof. Stephen K. Wilson, Dr Brian R. Duffy, and Dr David Pritchard for the opportunity to continue my studies, and for their absolutely invaluable aid over the past three and a half years. I would also like to thank Prof Khellil Sefiane for his expert advice on the direction and impact of the research contained in this thesis.

I would like to thank my family for their support over the course of writing this thesis, especially my mother Libby and my brother Jonathan, who have always been willing to listen to my rambles about the glory of mathematics, and my rants of frustration and stress while in the death throes of writing up, and who always managed to drag me back to neutral when I started thinking too highly, or too lowly, of myself. Jonathan also drew some pictures of some chemicals that appear in Chapter 1 and demanded recognition of that fact, so a special thanks goes to him.

I would also like to thank Dr Ben Snow, my office mate since starting my postgraduate studies until early last year, and a good friend throughout and since. Without Ben to bounce ideas off of, much of the work in this thesis would have taken rather longer to complete.

Finally, I would like to thank the University of Strathclyde for funding my postgraduate studies.

Abstract

We formulate a fluid-dynamical model describing the behaviour of solutions consisting of a fluid solvent and a dissolved solute, and whose surface tension depends on the concentration of the solute. By considering the surface excess of the dissolved solute, this model can describe the Marangoni-driven flow both of fluids in which there is a surfactant present (which decreases surface tension) and of fluids in which there is an anti-surfactant present (which increases surface tension). By investigating the linear stability of an initially quiescent fluid layer, we predict a novel instability that is possible for anti-surfactant solutions, but not for surfactant solutions, and analyse the conditions for the onset of this instability. We formulate the equations governing the flow of a thin film of surfactant or anti-surfactant solution, and demonstrate the wide range of dynamical behaviour that may be displayed by such solutions. In particular, we perform fully non-linear, unsteady numerical computations, and compare the results obtained with the linear approximation for an initially quiescent thin film subject to both small and large perturbations. We analyse the difference in behaviour between surfactants and anti-surfactants when the thin film is subject to large, local disturbances to either the surface concentration or the bulk concentration. We also obtain analytical solutions to reduced versions of the equations governing the flow of a thin film when the Marangoni effect is dominant. We focus on so-called "perfectly soluble" anti-surfactants for which the surface concentration is identically zero. For problems in which the initial condition is discontinuous, the method of characteristics is employed to obtain simple-wave solutions. Finally, we derive a general, doubly-infinite family of similarity solutions of the reduced (i.e., Marangoni-only) equations, and investigate two of the most interesting cases in detail.

Chapter 1

Introduction

1.1 Surface Tension and the Marangoni Effect

In this thesis we investigate the behaviour of solutions consisting of a fluid solvent and a dissolved solute and whose surface tension depends on the concentration of the solute. In particular, we focus on solutes that increase the surface tension of the solution, and on scenarios in which the **Marangoni effect** (i.e., flow induced by gradients in surface tension) plays a crucial role.

The surface tension of a fluid can depend on the temperature of the fluid, or on the concentration of a dissolved solute or colloidal dispersion. Where the temperature or concentration at the free surface of such a fluid is spatially non-uniform, the resulting gradients of temperature or concentration cause gradients of the surface tension of the fluid. These gradients of surface tension induce an interfacial flow, and by viscous action this flow is transmitted into the bulk of the fluid; this is the well-known Marangoni effect. Surface tension can also depend on, for example, the orientation of the fluid molecules (say, in a liquid crystal), or on an external electromagnetic field, but we do not consider these effects in this thesis.

The first published discovery of flow induced by gradients of surface tension was in 1855 by James Thomson (the elder brother of William Thompson, who would later be known as Lord Kelvin), who noticed that when a drop of alcohol is placed into water, a flow radiating outwards from the drop occurs [106]. Thomson

also documented the phenomenon of the "tears", or "legs", of wine seen most easily in wine with high alcohol content in a container such as a wine glass. Where the wine meets the sides of the glass its free surface curves upwards (it could, of course, curve downwards on some materials, but then the "tears" do not form). The resulting curvature of the free surface increases the vapour pressure of both the water and the alcohol that comprise the wine [110]. Both components therefore evaporate at a faster rate than in the rest of the wine, and, moreover, the alcohol, being more volatile than the water, evaporates at the fastest rate. The wine near the sides of the glass therefore has a lower alcohol content than the rest of the wine. A gradient in concentration, and thus a gradient in the surface tension of the wine, results. This gradient causes more wine to be drawn up the sides of the glass where it climbs to a maximum height, forms droplets, and falls back into the bulk of the wine under its own weight: the so-called "tears", or "legs", of wine.

In 1878, more than twenty years after Thomson, and unaware of his earlier work, Carlo Marangoni [53] published his work on the same problem of alcohol spreading on the surface of water and, perhaps unfairly to Thomson, the phenomenon of flow induced by gradients in surface tension is now known as the Marangoni effect. This thesis will principally be concerned with the Marangoni effect due to concentration gradients (so-called solutocapillarity), but we will begin with a brief discussion of the more widely studied thermal Marangoni effect (so-called thermocapillarity) to provide important historical, physical, and mathematical context for this work.

1.2 Thermocapillarity

In 1900, Henri Bénard [7] performed his famous experiments in which a thin layer of spermaceti oil was heated uniformly from below. Bénard noticed that when the layer was heated sufficiently strongly, a pattern of roughly hexagonal convection cells formed and, incorrectly (as shown almost 60 years later), attributed this phenomenon solely to buoyancy effects, i.e., to variations in the density of the

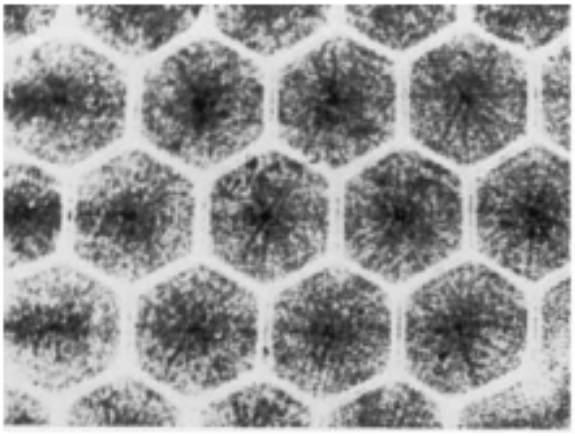

Figure 1.1: Example of the stable hexagonal convective patterning of the type seen in Bénard's experiments, reprinted from [80], with permission from Cambridge University Press.

fluid due to the thermal gradients. Bénard did, however, also theorise that surface tension played some role because he saw a slight depression in the free surface occurring in the centres of the convective cells. Figure 1.1 shows an example of the stable hexagonal convective patterning of the type seen in Bénard's experiments, reprinted from [80].

In 1916, Lord Rayleigh [79] demonstrated theoretically, through a linear stability analysis of a flat layer of fluid using the Boussinesq approximation, that buoyancy effects could cause the type of instability seen by Bénard. Lord Rayleigh predicted that the layer is unstable when a critical value of what would later be called the *Rayleigh number* (a ratio of destabilising buoyancy effects to stabilising diffusive effects) is exceeded. In 1940, this analysis was extended by Pellew and Southwell [71], who performed a much more comprehensive analysis, including the effects of different boundary conditions on the critical Rayleigh number.

In 1958, Pearson [70] revisited the question of what caused the instability seen in Bénard's experiments. While Lord Rayleigh showed that an instability can be caused by buoyancy effects alone, Pearson noted that instability can occur even when the layer of fluid is on the underside of a solid substrate, and so buoyancy cannot be the sole cause. In addition, given the values of the parameters of Bénard's experiments, the critical Rayleigh number calculated by Lord Rayleigh

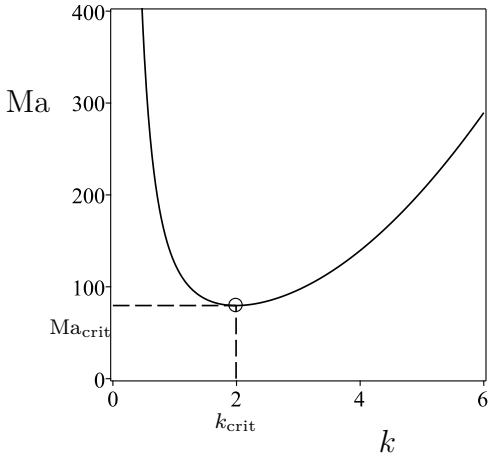

Figure 1.2: Marginal stability curve for the Marangoni number Ma as a function of the wavenumber of the perturbation k in the limit of zero Biot number (a ratio of heat transfer to thermal conductivity, denoted L by Pearson), given by equation (27) in Pearson [70], with $L = 0$. $\mathrm{Ma}_{\mathrm{crit}} \simeq 80$ and $k_{\mathrm{crit}} \simeq 2$ denote the critical Marangoni number and the critical wavenumber, respectively.

was *not*, in fact, exceeded. Pearson believed that the Marangoni effect alone was sufficient to explain the instability, and demonstrated using a linear stability analysis of a flat layer that there is a critical *Marangoni number* (a ratio of surface tension gradients to viscosity), above which the layer could be unstable, and even with conservative estimates of the values of the physical parameters, this critical value *was* exceeded in Bénard's experiments. Figure 1.2 shows the marginal stability curve for the Marangoni number Ma as a function of the wavenumber of the perturbation k in the limit of zero Biot number (a ratio of heat transfer at the free surface to thermal conductivity, denoted L by Pearson), given by equation (27) in Pearson [70], with $L = 0$. $\mathrm{Ma}_{\mathrm{crit}} \simeq 80$ and $k_{\mathrm{crit}} \simeq 2$ denote the critical Marangoni number and the critical wavenumber, respectively.

Following the analysis by Pearson, a slew of publications emerged extending the analysis in various ways.

Scriven and Sternling [88] extended the model used by Pearson to allow for deformation of the free surface. While Pearson found that there is a non-zero critical Marangoni number (namely $\mathrm{Ma}_{\mathrm{crit}} \simeq 80$) above which the layer is unstable, Scriven and Sternling found that when the free surface is allowed to deform

this critical Marangoni number is zero (i.e., $\mathrm{Ma}_{\mathrm{crit}} = 0$ at $k_{\mathrm{crit}} = 0$) and for any positive Marangoni number the layer is always unstable for sufficiently small wavenumbers.

Nield [62] extended the model used by Pearson to include the effects of buoyancy. Nield demonstrated that both the Marangoni effect and buoyancy effects can cause instability, and that the two effects reinforce each other. Nield [62] also identified the important role of the depth of the fluid: for thin layers, surface tension is the dominant cause of instability, whereas for thicker layers, buoyancy dominates.

Disturbed by the result of Scriven and Sternling that a layer heated from below is always unstable for sufficiently small wavenumbers, Smith [92] improved upon their model by considering a two-layer model in which two layers of fluid (say, water and air) are separated by a single free surface and each layer is bounded above or below by a solid substrate. Smith found that, as predicted by Pearson, a non-zero critical Marangoni number exists above which the system is unstable, and recovered the value originally obtained by Pearson in the appropriate limit, namely $\mathrm{Ma}_{\mathrm{crit}} \simeq 80$ and $k_{\mathrm{crit}} \simeq 2$.

Vidal and Acrivos [109] showed numerically using the Pearson model that the onset of convection is always steady when the layer is heated from below, i.e., that the assumption of *exchange of stabilities* is valid (i.e., that the growth rate of perturbation is a purely real quantity). Subsequently, Takashima [99, 100] performed a similar analysis to that of Vidal and Acrivos, but for the Nield model rather than the Pearson model. Like Vidal and Acrivos, Takashima found that the principle of exchange of stabilities holds.

Zeren and Reynolds [121] extended the Smith model to include the effects of buoyancy, and found that when the layer is heated from below, the critical Marangoni number is increased relative to the value obtained by Smith, and when the layer is heated from above, the critical Marangoni number is decreased. Zeren and Reynolds also found that when the layer is heated from above, only the Marangoni effect causes instability, but when the layer is heated from below, both the Marangoni effect and buoyancy effects can cause instability, and the

dominant effect depends on the wavenumber of the perturbation.

Takashima [101,102] published a two-part paper analysing the Pearson model but allowing for surface deformation, and for the fluid layer to be suspended on the underside of a horizontal substrate. In the first part [101], the principle of exchange of stabilities was assumed to hold, and a critical Marangoni number was derived which recovered the result obtained by Pearson when surface deformation is neglected. In the second part [102], the principle of exchange of stabilities was *not* assumed hold. Takashima showed that the onset of instability can be oscillatory in nature, i.e., the layer can be *overstable*. Crucially, this overstability occurs only when the layer is heated sufficiently strongly from above.

Cloot and Lebon [12] performed a comprehensive non-linear stability analysis of the thermocapillary stability problem and obtained many results about the stability, instability, or overstability of a fluid layer when heated from above or below, and about the preferred convective patterns. In particular, Cloot and Lebon determined that convective rolls and rectangular cells are unstable, but that hexagonal cells are stable, and are therefore the preferred convective pattern.

In 1987, a comprehensive review of the large body of early work on this thermocapillary stability problem was published by Davis [18], who included much more than has been included in this brief overview of the problem. Since then there has, of course, been much more work done on thermocapillary problems, both in terms of linear and non-linear stability, and on dynamics (see, for example, [30, 31]). Much of the more recent work is described in the more recent review by Craster and Matar [15], or in the book by Kalliadasis et al. [44]. In addition, the International Marangoni Association (IMA)[1], an association dedicated to interfacial fluid dynamics, organise biennial conferences at which many presentations concern problems in which the Marangoni effect is a prominent feature, including both the thermo- and soluto-capillary problems.

[1] `http://marangoniassociation.com`

1.3 Solutocapillarity

The surface tension of a fluid may depend not only on the temperature of the free surface, but also on the concentration of one or more dissolved species: the solutocapillary effect. The variation of surface tension due to impurities in a fluid was first described by Agnes Pockels (see [19] for a short biography of this pioneering amateur surface chemist), who published fifteen papers between the years of 1891 and 1933 documenting her measurements of the surface tension of water in the presence of various solutes and dissolved species. Among these findings was the fact that soaps and detergents tend to decrease the surface tension of water when in solution, and that many salts tend to increase the surface tension of water when in solution.

1.3.1 Surfactants

In the late 1920s the Swiss biologist Kurt von Neergaard identified the role of so-called "surfactants" in the respiratory process, where they reduce the surface tension of the thin films of mucus that line the pulmonary tracts, increasing the pulmonary compliance of the lungs [111]. Some time later, these pulmonary surfactants were identified as consisting of the same general type of molecule as many soaps and detergents. All of these molecules consist of two parts: a hydrophobic "tail" which is typically a long carbon chain, and a hydrophilic "head" which can be either ionic or non-ionic. These types of molecules, which decrease the surface tension of a fluid by being positively adsorbed at the free surface (i.e., the molecules preferentially accumulate on the free surface; see section 1.4 for more information), were subsequently named **surf**ace **act**ive ag**ents**, or **surfactants** for short [58].

The first mathematical treatment of the solutocapillary problem where the solute is a surfactant was an investigation of the spreading of a localized monolayer of insoluble surfactant (i.e., a surfactant whose molecules are present solely on the free surface of the fluid) placed on top of a thin film of otherwise clean fluid. The surface tension of the fluid was taken to be a decreasing function of the

concentration of surfactant on the free surface. This problem was considered first by Borgas and Grotberg [8], who found steady state solutions in which diffusion of the monolayer along the free surface is important, and a travelling wave solution in which a shock (i.e., a discontinuity) exists in the film thickness when the monolayer is scraped (rather than diffusing) along the surface by a blade.

The work of Borgas and Grotberg [8] was extended in various ways. Numerical integration of the equations introduced by Borgas and Grotberg [8] was performed by Gaver and Grotberg [24], who predicted that a localised initial distribution of insoluble surfactant induces a Marangoni flow which enhances the spreading of the monolayer over the spreading that would be caused by diffusion alone. As the surfactant spreads, a front forms at the leading edge of the spreading monolayer, the film thins behind this leading edge, and surface diffusion is found to have little effect on spreading. This spreading behaviour was confirmed experimentally by Gaver and Grotberg [25]. However, as Swanson *et al.* [98] subsequently demonstrated, the experiments performed by Gaver and Grotberg [25] were performed for surfactant quantities much greater than is sufficient to form a monolayer. This fact prompted Swanson *et al.* [98] to suggest that the equations originally formulated by Borgas and Grotberg do not, in fact, apply in the monolayer regime in which they were intended to apply, and to suggest that the model formulated by Thiele *et al.* [105] in terms of gradient dynamics may be more appropriate. In this thesis, we do not use the Thiele *et al.* [105] model since we will primarily be interested in situations in which the free surface is sparsely populated of particles relative to the bulk of the fluid, and instead build upon the model introduced by Borgas and Grotberg [8].

The spreading behaviour seen numerically and experimentally by Gaver and Grotberg [24, 25] was shown by Jensen and Grotberg [39] to be self-similar when surface diffusion and capillarity (i.e., the effects of mean surface tension) are neglected. Jenesen and Grotberg [39] derived an analytical similarity solution for the spreading of the monolayer, and found that the front seen numerically and experimentally may be mathematically idealised as a shock, which is locally smoothed by weak diffusion and capillarity. Spreading laws were also derived,

which show that the monolayer spreads as $t^{\frac{1}{3}}$ (where t denotes time) in a two-dimensional geometry, and as $t^{\frac{1}{4}}$ in an axisymmetric geometry. When surfactant is being supplied to the system as t^m, these spreading laws become $t^{\frac{1+m}{3}}$ in a two-dimensional geometry, and $t^{\frac{1+m}{4}}$ in an axisymmetric geometry. These self-similar solutions correspond to special cases of a wider range of self-similar behaviour [38]. A closely related type of behaviour can be seen when a localized amount of surfactant is *removed* from the system [97], where the system acts to fill in the "hole" in the surfactant distribution [38].

The Borgas and Grotberg model [8] was extended by Jensen and Grotberg [40], Espinosa *et al.* [23], and Jensen *et al.* [41] to include the effects of solubility, i.e., when the surfactant molecules are also present in the bulk of the fluid rather than solely on the free surface. Crucially, the assumption was still made that the surface tension is a function of the surface concentration only: we will argue in Chapter 2 that this is an appropriate assumption only when the surface concentration is high relative to the bulk concentration. The bulk and surface concentrations of surfactant are related by an adsorption law (i.e., a flux of solute between the bulk and surface) at the free surface. When this adsorption process is assumed to be rapid, the analysis is drastically simplified since only the bulk concentration needs to be tracked; Howell *et al.* [34] and Morgan *et al.* [60] considered this regime. In comparison with the insoluble surfactant case, the rate of spreading for a soluble surfactant is reduced, but the deformations of the free surface are more pronounced at later times. Further information on the spreading of insoluble and soluble surfactants in thin films is provided in the reviews by Afsar-Siddiqui *et al.* [3], and Craster and Matar [15].

Surfactants are relevant not just biologically, but also in many industrial processes such as coating flows [49, 51, 86, 87], printing [27], oil recovery [28, 29], and processes that involve drops or bubbles [6, 45, 54, 113], since they can have a strong effect on the dynamical behaviour. The presence of surfactants is required in some industrial coating processes, but can sometimes cause significant problems. For example, the presence of a surfactant can cause wetting failure during coating flows on rotating cylinders [49] or moving plates [51]. Surfactants can also cause

delays in the levelling of inkjet-printed patterns [27], leading to problems in the production of microfluidic devices, for example.

The stability of a two-dimensional horizontal layer of soluble surfactant solution was first analysed theoretically by Schwartz *et al.* [86, 87], who showed that the levelling of the free surface is retarded when a surfactant is present [87], but that the layer will always remain stable. In three dimensions, the layer may be unstable to transverse perturbations, leading to the phenomenon of fingering patterns [56, 57, 114]. Note that these fingering patterns are not the same phenomenon as the well-known Saffman-Taylor fingering instability [82], which is driven by differences in viscosity between two fluids, rather than by gradients in surface tension.

The dynamics of spreading or evaporating droplets, or of bubbles travelling along pipes for example, can also be profoundly changed by the addition of a soluble surfactant. Spreading droplets without surfactant can spread as slowly as $t^{\frac{1}{10}}$ [103], but the presence of a high-concentration surfactant can drastically increase the rate at which the drop spreads, with spreading laws as fast as t^1 or even faster [6, 45]. The mechanism of this "superspreading" is not fully understood, but the roles of micelles [93, 94] and solubility of the surfactant were investigated in the comprehensive work of Karapetsas *et al.* [45]. The role of surfactants in the breakup and coalescence of droplets and bubbles is also of industrial interest [113], as are the flow transitions that can be seen in droplets when the surfactant concentration is much higher than the critical micelle concentration (CMC) [54, 94] (which will be discussed briefly in section 1.4).

1.3.2 Anti-surfactants

While surfactants *decrease* the surface tension of a fluid (by being positively adsorbed), there are other solutes that *increase* the surface tension of a fluid, by being *negatively adsorbed* (i.e., the molecules of these solutes are preferentially *expelled* from the free surface). Most notably, this includes many salts when added to water [52, 69, 89, 123], water added to short-chain alcohols such as ethanol [33, 108], and certain resins that are included in solvent-based paints [35, 68,

115, 118]. Such behaviour may be conveniently referred to as '**anti-surfactant**' behaviour, and the solute as an '**anti-surfactant**'. We discuss the differences between surfactants and anti-surfactants in section 1.4.

At first glance it may appear that a mathematical model describing the behaviour of surfactant solutions may also be used to describe the behaviour of anti-surfactant solutions, except the we interchange the solute and solvent so that the surfactant is now treated as the solvent, and the medium in which the surfactant is dissolved is treated as the solute. However, this does not hold since for surfactants (or anti-surfactants), the bulk (or surface) is sparsely populated, and thus one cannot in general think of them as the solvent. Instead a two phase model would be required. This would be the approach if we wished to model, say, a water/alcohol system, where the line between solute and solvent is somewhat more blurred.

In comparison with the large body of work on the effect of surfactants on the stability and dynamics of fluids, there has been relatively little work done on anti-surfactants from a mathematical point of view. The fact that salts, such as sodium chloride, increase the surface tension of water was first published by Pockels with the aid of translation by Lord Rayleigh [75]. Since then, many authors have performed experiments measuring the surface tension of solutions of many different salts, by a variety of methods [20, 52, 89, 108]. Similarly, the Marangoni effect induced by alcohols in water has been studied since the time of Thomson [106] and Marangoni [53], and the Marangoni effect induced by water in alcohol is simply the reverse, with the water playing the role of the *solute* rather than the *solvent*. The surface tension of certain binary mixtures of alcohol and water, such as water and hexanol, can also be a non-monotonic function of the temperature, with a well-defined minimum in surface tension at a critical temperature [1, 84, 85]. Such binary mixtures are called *self-rewetting fluids*, and have the potential to increase greatly the efficiency of heat transfer devices [83].

Aside from the experimental measurements of surface tension, there have been relatively few investigations into the behaviour of anti-surfactant solutions. Analytical and numerical work has been carried out in the context of drying paint

films, where the resin in certain solvent-based paints has anti-surfactant properties [35, 68, 115, 118]. Overdiep [68] developed a model to describe these solvent-based paints, under the assumption that the resin molecules are completely excluded from the paint-air interface (i.e., the free surface). Overdiep determined that, in the absence of evaporation, the surface of the paint levels as though there was no resin present, and the resin itself becomes spatially uniform due to diffusion. However, when the paint layer is evaporating, *overstability* can occur — an unwanted phenomenon in the context of drying paint films. The Overdiep model [68] was extended to include the effects of concentration-dependent viscosity [118], and diffusivity [35]. Howison *et al.* [35] also showed that, in regimes in which the flow is dominated entirely by the Marangoni effect, shocks can develop in the film thickness, and these regimes should typically be avoided when an aesthetically pleasing flat coat of paint is desired. Weidner *et al.* [115] demonstrated that the levelling of a paint film attached to the underside of a horizontal substrate can be carefully controlled through specific choices of the resin.

One of the main tools used to analyse the behaviour of anti-surfactant solutions has been molecular dynamics (MD), which is a very useful computational method for analysing the behaviour of physical systems at very small (i.e., nano) scales. The effect of salt concentration on the wetting and evaporation of nanodroplets has been investigated using MD by Daub *et al.* [17], Caleman and van der Spoel [10], Wang *et al.* [112], and Zhang *et al.* [122]. In particular, these MD simulations correctly capture the increase in surface tension seen experimentally, and also confirm that the molecules of these anti-surfactants tend to be expelled from the free surface.

1.4 Comparison Between Surfactants and Anti-surfactants

Surfactant molecules behave differently from anti-surfactant molecules in the vicinity of a free surface. Specifically, as mentioned above, surfactant molecules tend to be positively adsorbed (i.e., tend to accumulate at a free surface), whereas

anti-surfactant molecules tend to be negatively adsorbed (i.e., tend to be expelled from the free surface). In general terms, this difference in behaviour is due to the way in which the free energy in the solvent–solute system is minimised: surfactant molecules accumulate at the free surface because it is energetically favourable to do so, and anti-surfactant molecules tend to be expelled from the free surface for the same reason. It is less clear *why* these respective behaviours are energetically favourable, and also *why* they affect surface tension in the specific way that they do. In order to elucidate this, we must consider the structures of the constituent molecules of surfactants and anti-surfactants.

1.4.1 Surfactants

In general, surfactant molecules comprise two parts: a hydrophilic "head", and a hydrophobic "tail" [78, 81]. The hydrophilic head is much more variable that the tail, and depends on the specific surfactant that is being considered, but is generally small and inorganic (i.e., does not primarily consist of carbon and hydrogen). The hydrophobic tail is typically a medium- to long-chain hydrocarbon (i.e., a chain of about 6 or more carbon atoms). Figure 1.3 shows the chemical structure of four examples of industrially and biologically important surfactants[2]. Figure 1.4, reprinted from [21], shows a plot of the surface tension of the surfactant di(hexyl)glucoside, and the positive adsorption of the surfactant molecules at the free surface, and demonstrates the decreasing surface tension that is the defining characteristic of surfactants.

Surfactant molecules preferentially adsorb at the free surface, with the hydrophobic hydrocarbon tail pointing out of the fluid, and the hydrophilic head pointing into the fluid and remaining completely submerged. Figure 1.5 shows a schematic diagram of the preferred behaviour of surfactant molecules at a free surface.

The relationship between surface tension and (positive or negative) adsorption is given by the **Gibbs isotherm**, which is obtained by considering the surface

[2]The properties and uses of these chemicals can be found on, for example, the PubChem website `https://pubchem.ncbi.nlm.nih.gov/`

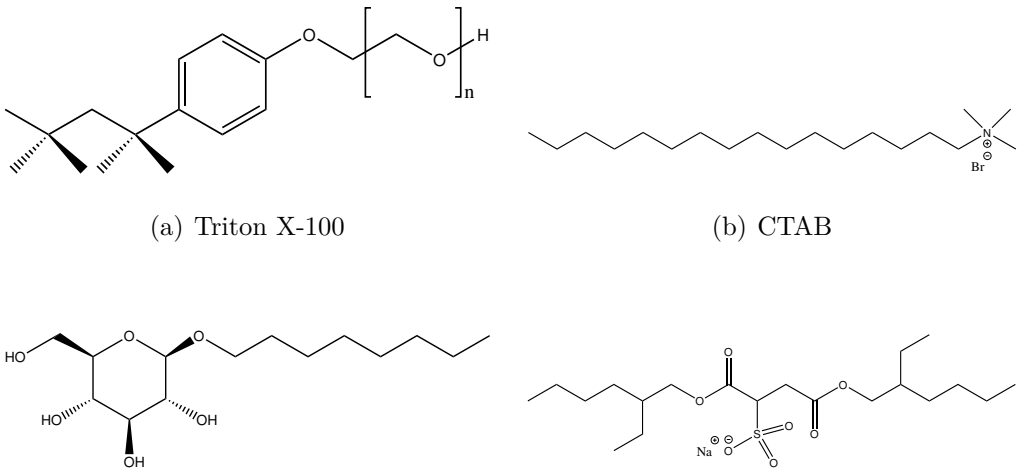

(a) Triton X-100

(b) CTAB

(c) Octyl glucoside

(d) Docusate

Figure 1.3: The chemical structure of four examples of industrially and biologically important surfactants.

energy of a free surface on which solute molecules may adsorb (see, e.g., [89] for a derivation of this equation), namely

$$c^*_{\mathrm{eq}} \frac{\mathrm{d}\sigma^*_{\mathrm{eq}}}{\mathrm{d}c^*_{\mathrm{eq}}} = -R^* T^* \Gamma^*_{\mathrm{eq}} \tag{1.4.1}$$

where the star denotes dimensional quantities, the subscript "eq" denotes that the quantity is measured in equilibrium, c^*_{eq} is the bulk concentration of the dissolved solute directly beneath the free surface, R is the ideal gas constant, T is the (constant) temperature, and Γ is the **surface excess**, defined to be the excess surface concentration over that which would be present if the bulk concentration prevailed as far as the free surface itself [47, 59]. This key quantity is essentially the difference between the surface concentration s and the bulk concentration c, and will be defined explicitly later. Since the molecules of a surfactant tend to accumulate at the free surface, surfactants are characterised by a *positive* surface excess. Thus, from equation (1.4.1), surfactants must decrease the surface tension of the fluid. For present purposes we may treat both the positive surface excess and the decrease in surface tension as equivalent characterisations of a surfactant, since they are simply different ways of describing the same phenomenon.

The Gibbs isotherm (1.4.1) applies only for dilute solutions. For surfactants this restriction is especially important. Since surfactant molecules tend to ac-

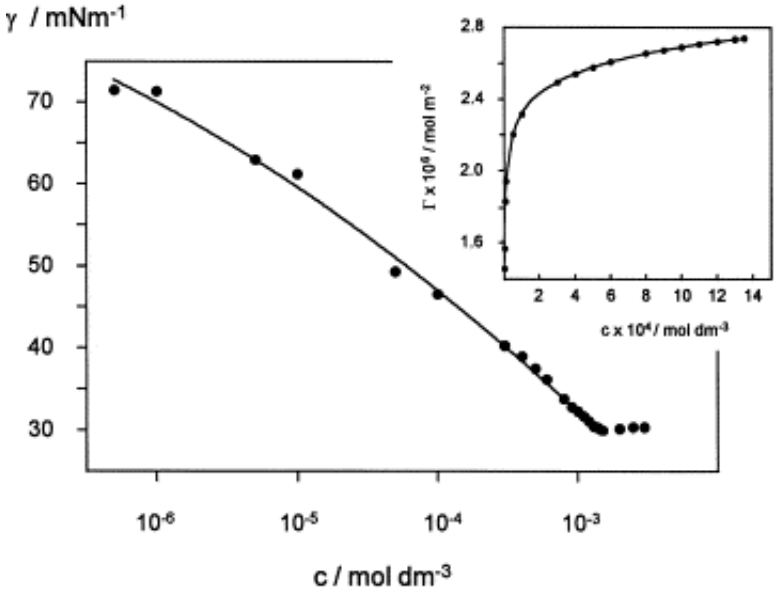

Figure 1.4: The surface tension of the surfactant di(hexyl)glucoside, and the positive adsorption of the surfactant molecules at the free surface, reprinted from [21], with permission from Elsevier.

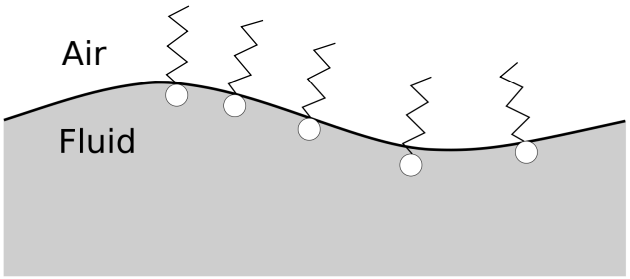

Figure 1.5: Schematic diagram of the preferred behaviour of surfactant molecules at a free surface.

cumulate at the free surface, and there is a limit to the amount of free space on the free surface, there is a maximum packing surface concentration $s = s_\infty$, beyond which any additional surfactant molecules must move into the bulk of the fluid. Increasing the concentration further causes the surfactant molecules in the bulk to start forming aggregate structures called micelles [93]. The critical concentration beyond which micelles will form is referred to as the critical micelle concentration (CMC), and is generally greater than the concentration required for $s = s_\infty$. In this thesis we will assume that the concentration of surfactant or anti-surfactant is far enough from the maximum packing concentration that we

need not consider packing effects or the formation of micelles, i.e., we make the assumption $s \ll s_\infty$.

1.4.2 Anti-Surfactants

In contrast to surfactant molecules, anti-surfactant molecules tend to be small, relatively simple, and typically either charged or highly polar. Figure 1.6 shows the chemical structure of three examples of industrially and biologically important anti-surfactants[3], but other types of anti-surfactants exist; as has already been mentioned, the resin in certain high-gloss paints has anti-surfactant properties [35]. The most common examples of anti-surfactants, however, are sodium chloride (common table salt) when added to water, and water when added to short-chain alcohols such as ethanol. Figure 1.7, reprinted from [69], shows the surface tension of several salts in water, and the (negative) adsorption of the salt ions to the free surface. Figure 1.8 shows the variation in the surface tension of water in ethanol, where χ is the mole fraction of water in the mixture, using data taken from [108]. Both of these figures demonstrate the increasing surface tension that is the defining characteristic of anti-surfactants. In extremely dilute salt-water solutions, the phenomenon known as the *Jones–Ray* effect [42, 43, 73] also occurs, where the surface tension *decreases* over the range of micromolar concentrations. However, we do not consider the Jones–Ray effect further here, as the concentrations at which it occurs are very small, and the departure of surface tension from the value of the pure solvent is typically no more than 0.0002%.

Anti-surfactant molecules, in contrast with surfactants, are preferentially *expelled* from the free surface, leaving the surface relatively sparsely populated, as shown in the right-hand plot in Figure 1.7. The exact mechanism through which this expulsion occurs is not completely understood, but present theory suggests that the ions are repelled from any interface across which there is a change in dielectric constant, through the interactions with image charges in the atmosphere layer [16, 55, 65, 74]. Since the molecules are preferentially expelled from the free

[3]The properties and uses of these chemicals can be found on, for example, the PubChem website `https://pubchem.ncbi.nlm.nih.gov/`

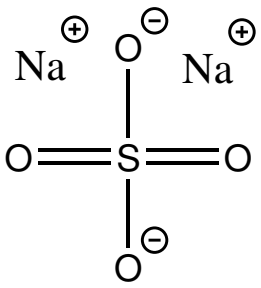

(a) Sodium sulfate

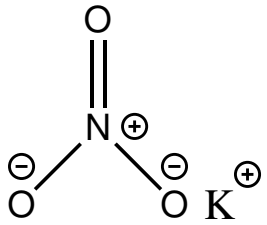

(b) Potassium nitrate

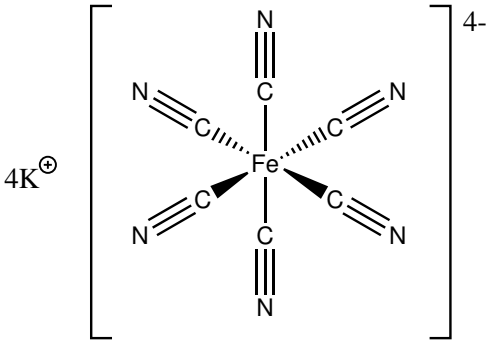

(c) Potassium ferrocyanide

Figure 1.6: The chemical structure of three examples of industrially and biologically important anti-surfactants.

surface, anti-surfactants have a *negative* surface excess.

Regardless of the precise mechanism through which a non-zero surface excess is produced, the effect on surface tension remains the same. If, by any process, the surface excess of a dissolved solute is negative, then by the Gibbs adsorption isotherm (1.4.1), the surface tension of the solution will necessarily be increased relative to that of the pure solvent. This is the situation for anti-surfactants.

1.5 Outline of Thesis

In this thesis we construct a fluid dynamical model describing the free surface flow of a solution in which a surfactant or anti-surfactant is dissolved. By considering the surface excess of the dissolved solute, the model we formulate can describe not only classical surfactants, whether soluble or insoluble, but also anti-surfactants

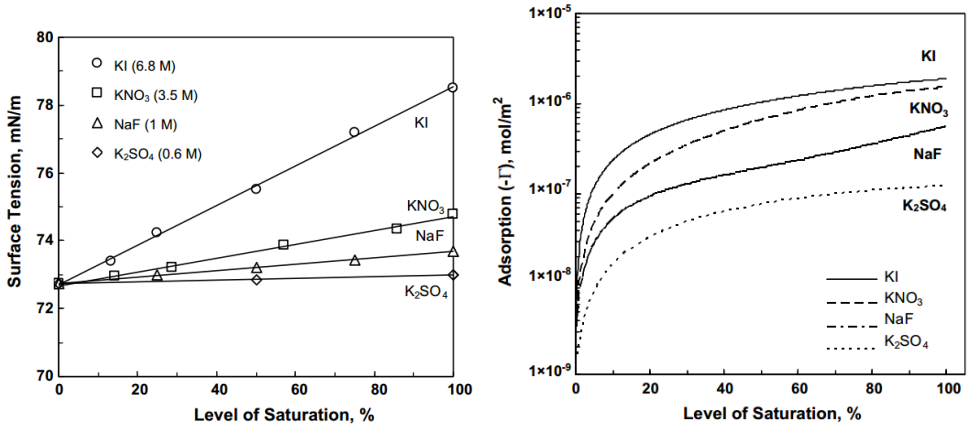

Figure 1.7: Surface tension of several salts in water, and the (negative) adsorption of the salt ions to the free surface, reprinted from [69], with permission from Elsevier.

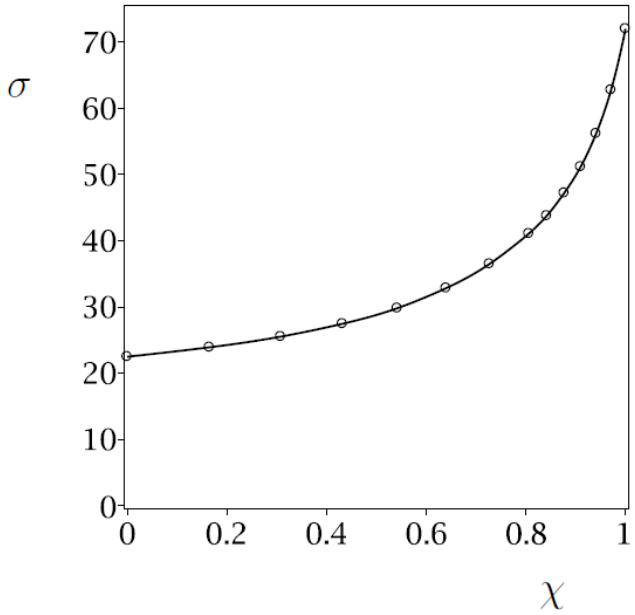

Figure 1.8: Surface tension of water in ethanol, where χ is the mole fraction of water in the mixture, with data taken from [108].

in a thermodynamically consistent way. Using this model we investigate the behaviour of anti-surfactant solutions and, where possible, compare it to the behaviour seen in classical surfactant solutions. In particular, we perform a linear stability analysis of a layer of arbitrary depth, and investigate the asymptotic limits of an infinitely deep layer and a thin film. We also investigate the dynamical behaviour of thin films of anti-surfactant solutions, and focussing particularly on the case in which the solute is completely excluded from the free surface, such as the resin in solvent-based paints [35].

In Chapter 2 we give a detailed derivation of the equations used to describe a general surfactant or anti-surfactant. We discuss the hydrodynamics, which is standard, briefly, and focus on the kinetics and transport of the solute. An account of the derivation of this model was recently published in *Physical Review E* [14].

In Chapter 3 we perform a comprehensive linear stability analysis of a surfactant or anti-surfactant solution for a horizontal layer of arbitrary depth lying on top of an impermeable substrate. We consider several special cases: a clean fluid, an insoluble surfactant, and a "perfectly soluble" anti-surfactant, for all of which a stationary layer is shown to be unconditionally stable. We then consider the asymptotic limit of an infinitely deep layer, which we find can be unstable in certain cases; a mechanism for this instability is hypothesised. Through a marginal stability analysis, and through considering several asymptotic limits such as the long-wave limit, we derive conditions on parameters for which the layer will be unstable, and comment on the nature of the instability; an account of this analysis also appears in [14]. We then consider the effect of finite depth on the stability of the layer; we find that the infinite-depth limit is singular, and that for any finite layer depth, oscillatory behaviour is possible, but is an inherently long-wave phenomenon.

In Chapter 4 we derive the equations describing a thin film of surfactant or anti-surfactant solution and perform a linear stability analysis. The stability characteristics for a layer of arbitrary depth are much easier to determine in this limit, and we derive several conditions on parameters for which the thin film will

be unstable.

In Chapter 5 we numerically integrate the thin-film equations derived in Chapter 4, both within and outwith the linear regime. We compare the results from the linear stability analysis obtained in Chapter 4 with the numerical solutions for the evolution of a sinusoidally perturbed layer, for perturbations with both small and large amplitudes. The linear approximation is good for small-amplitude perturbations, as expected, but also turns out to be accurate even for perturbations with $O(1)$ amplitudes. We also consider the evolution of a layer in which a localized amount of surfactant or anti-surfactant is initially added to the surface or bulk of the fluid, and find that there is a separation of timescales. Specifically, there is a short timescale over which the flux acts to bring the surface and bulk concentrations into equilibrium, and a long timescale over which capillarity, diffusion, and the Marangoni effect dominate.

In Chapter 6 we obtain analytical solutions in the special cases of an insoluble surfactant and a "perfectly soluble" anti-surfactant when the Marangoni effect is dominant, and both capillarity and solute diffusion are assumed to be negligible. We find that the equations describing this surface-tension-driven flow of a "perfectly soluble" anti-surfactant can be written in characteristic form, and the method of characteristics is used to solve a family of Riemann problems. Similarity solutions are also obtained for both an insoluble surfactant and a "perfectly soluble" anti-surfactant.

In Chapter 7 we summarise the analysis and results contained in the thesis, present conclusions, and suggest possible directions for extensions to the model and for future work.

1.6 Publications and Presentations

The work presented in Chapter 2 and in Section 3.5 was recently published in *Physical Review E* [14]. In addition, much of the work described in this thesis has been communicated through oral presentations at several local, national, and international conferences. In particular, I have presented various aspects of this

thesis at the following conferences and events: the British Applied Mathematics Colloquium 2014, Cardiff; the 7th Conference of the International Marangoni Association 2014, Vienna; the annual Society for Industrial and Applied Mathematics (SIAM) Ph.D. Student Conference 2014, Reading; the 4th Joint British Applied Mathematics Colloquium and British Mathematics Colloquium 2015, Cambridge; the 28th Scottish Fluid Mechanics Meeting 2015, Glasgow; the British Applied Mathematics Colloquium 2016, Oxford; the 29th Scottish Fluid Mechanics Meeting 2016, Edinburgh; the 8th Conference of the International Marangoni Association 2016, Bad Honnef; and a Continuum Mechanics and Industrial Mathematics (CMIM) group research seminar in the Department of Mathematics and Statistics in the University of Strathclyde in November 2016.

In addition, aspects of this thesis has been presented by my supervisors Prof. Stephen K. Wilson (SKW) and Dr David Pritchard (DP) at the following conferences and events: a research seminar in the BP Institute for Multiphase Flows 2014, Cambridge (DP); the 6th International Symposium on Bifurcations and Instabilities in Fluid Dynamics 2015, Paris (SKW); the 68th Annual Meeting of the American Physical Society Division of Fluid Dynamics 2015, Boston (SKW); the 24th International Congress of Theoretical and Applied Mathematics 2016, Montréal (SKW); and a research seminar in the Oxford Centre for Industrial and Applied Mathematics 2016, Oxford (SKW).

Chapter 2

Model Formulation

2.1 Introduction

In this Chapter, we formulate the model that will be used throughout this thesis to describe the behaviour of surfactant or anti-surfactant solutions.

In section 2.2, we formulate the general problem that we will consider throughout the rest of this thesis, define notation, and introduce the key concept of the surface excess of a dissolved solute.

In section 2.3, we briefly discuss the hydrodynamics of the problem, and state the appropriate hydrodynamical equations and boundary conditions, all of which is standard for problems involving the Marangoni effect.

In section 2.4, we discuss the transport and adsorption of the dissolved solute, and state the appropriate equations and boundary conditions governing these. We also prescribe the key constitutive relation governing the flux of solute at the free surface, and the surface tension of the solution as a function of the surface and bulk concentrations.

Finally, in section 2.5, we discuss the dimensional parameters that appear in the model formulated in the previous section, and give the values that these parameters will take throughout the rest of this thesis.

2.2 Problem Formulation

We begin by outlining the general model that will be used to describe the behaviour of anti-surfactants [14, 35, 123]. In the following, dimensional quantities will be denoted with a superscript star, with dimensionless quantities shown without. We initially formulate this model for the following problem: consider a layer of surfactant or anti-surfactant solution of constant density, ρ^*, and viscosity, μ^*, placed on top of a solid, impermeable, smooth substrate. We allow the particles of surfactant or anti-surfactant to be present both on the free surface and within the bulk of the fluid. We neglect any deposition onto the substrate, and also the formation of micelle/vesicle structures within the bulk of the fluid, the latter of which is only applicable to very high-concentration surfactants, above a critical micelle concentration (CMC) [93], as mentioned in section 1.4.

We use Cartesian coordinates (x^*, y^*, z^*), with reference to which the fluid velocity is denoted by

$$\mathbf{u}^* = (u^*(x^*, y^*, z^*, t^*), v^*(x^*, y^*, z^*, t^*), w^*(x^*, y^*, z^*, t^*)), \tag{2.2.1}$$

where time is denoted by t^*. The fluid–air interface (free surface) is denoted by $z^* = h^*(x^*, y^*, t^*)$, and the substrate lies at $z^* = -d^*$. The pressure in the fluid is denoted $p^*(x^*, y^*, z^*, t^*)$, with the constant atmospheric pressure denoted p_{a}^*. Gravitational forces are ignored, which is reasonable since the gravitational Bond number is small for length scales small than $10^{-5/2}\,\mathrm{m}$ and we consider length scales that are at largest $10^{-3}\,\mathrm{m}$. Figure 2.1 shows a schematic diagram of the geometry considered.

Within the fluid there are two separate regions in which surfactant or anti-surfactant particles may be present, namely the bulk region and the surface region, in which we denote their concentrations as follows: the volumetric bulk concentration, $c^*(x^*, y^*, z^*, t^*)$, measured in $\mathrm{mol\,m^{-3}}$; and the areal surface concentration, $s^*(x^*, y^*, t^*)$, measured in $\mathrm{mol\,m^{-2}}$. Physically, there is, in addition, a bulk region directly below the free surface called the subsurface region which mediates solute transfer between the bulk of the fluid and the free surface [11];

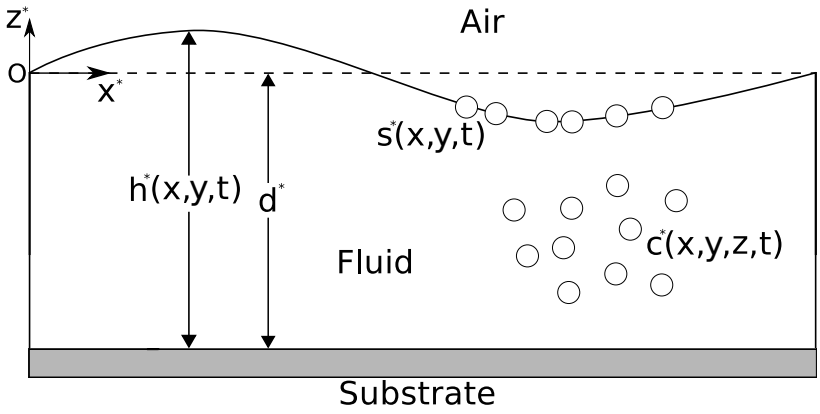

Figure 2.1: Schematic diagram of the geometry considered.

within this subsurface region there may be high gradients of bulk concentration, but we assume that it may be described by the same equations as the rest of the bulk.

We define the *surface excess*, $\Gamma^*(x^*, y^*, t^*)$, to be the excess surface concentration over that which would be present if the bulk concentration prevailed to the surface itself [59]. As stated in the introduction, this key quantity is essentially the difference between the surface concentration and the bulk concentration directly beneath the free surface, and is written [47, 59] as

$$\Gamma^* = s^* - \eta^* \, c^*|_{z^*=h^*} \, , \tag{2.2.2}$$

where η^* is the notional thickness of the free surface and is taken to be of the order of a few ångströms [11].

Recall from the introduction that surfactant molecules are preferentially positively adsorbed at a free surface and, consequently, $\Gamma^* > 0$ for surfactants, while anti-surfactant molecules are preferentially negatively adsorbed and, consequently, $\Gamma^* < 0$ for anti-surfactants.

Note that when the surface concentration is very high relative to the bulk concentration (specifically when $s^* \gg \eta^* c^*$), the surface excess is well approximated by s^*, which justifies the usual approach for surfactants. However, as we describe soon, in general, and in particular for anti-surfactants, it is necessary to distinguish between s^* and Γ^*.

2.3 Hydrodynamics

We begin the model formulation with the hydrodynamics, all of which is standard (see, for example, Acheson [2]). We start with the balance of mass and balance of linear momentum — the continuity and Navier–Stokes equations:

$$\nabla^* \cdot \mathbf{u}^* = 0, \tag{2.3.1}$$

$$\rho^* \left(\frac{\partial \mathbf{u}^*}{\partial t^*} + \mathbf{u}^* \cdot \nabla^* \mathbf{u}^* \right) + \nabla^* p^* - \mu^* \nabla^{*2} \mathbf{u}^* = \mathbf{0}. \tag{2.3.2}$$

These two equations are subject to the following standard no-slip and no-penetration boundary conditions at the substrate:

$$\mathbf{u}^* = \mathbf{0} \qquad \text{on} \quad z^* = -d^*. \tag{2.3.3}$$

At the free surface we have the balance of normal and tangential stresses, namely,

$$\mathbf{n} \cdot \mathbf{T}^* \cdot \mathbf{n} = -\left(\nabla_{\mathrm{s}}^* \cdot \mathbf{n}\right) \sigma^* \qquad \text{on} \quad z^* = 0, \tag{2.3.4}$$

$$\mathbf{t}_i \cdot \mathbf{T}^* \cdot \mathbf{n} = \mathbf{t}_i \cdot \nabla_{\mathrm{s}}^* \sigma^* \qquad \text{on} \quad z^* = 0, \tag{2.3.5}$$

where $\mathbf{n}$ and $\mathbf{t}_i$, for $i = 1, 2$, are the unit normal and tangent vectors to the free surface, respectively, $\mathbf{T}^*$ is the total stress tensor, given by

$$\mathbf{T}^* = -p^* \mathbf{I} + \mu^* \left(\nabla^* \mathbf{u}^* + (\nabla^* \mathbf{u}^*)^T \right), \tag{2.3.6}$$

$\sigma^*(x^*, y^*, z^*, t^*)$ is the surface tension of the fluid, and ∇_s^* is the surface gradient operator [96, 119] defined as

$$\nabla_s^* = \nabla^* - \mathbf{n} \left(\mathbf{n} \cdot \nabla^* \right). \tag{2.3.7}$$

Along with these we have the kinematic boundary condition,

$$\frac{\partial h^*}{\partial t^*} + u^* \frac{\partial h^*}{\partial x^*} + v^* \frac{\partial h^*}{\partial y^*} = w^*. \tag{2.3.8}$$

By integrating the continuity equation (2.3.1) with respect to the vertical coordinate z^*, and by making use of the no-penetration condition (2.3.3), we may replace (2.3.8) by

$$\frac{\partial h^*}{\partial t^*} + \nabla^* \cdot \mathbf{Q}^* = 0, \tag{2.3.9}$$

where $\mathbf{Q}^*(x^*, y^*, t^*)$ is the horizontal volume flux, defined as

$$\mathbf{Q}^* = \int_{-d^*}^{h^*} \mathbf{u}^* \, \mathrm{d}z^*. \tag{2.3.10}$$

Equation (2.3.9) can often be more useful than (2.3.8), especially when considering flows of thin films of fluid.

2.4 Solute Kinetics and Transport

We have formulated all of the relevant hydrodynamical equations, along with the appropriate boundary conditions, but we must still consider the kinetics and transport of solute within the fluid. Questions to address include: how does the concentration of surfactant or anti-surfactant within the bulk of the fluid evolve? And in the free surface? What kind of adsorption/desorption occurs between the bulk of the fluid and free surface? How does the surface tension depend upon these concentrations?

In order to model how the solute behaves, we require transport equations for the evolution of the bulk and the surface concentrations; we assume that the only transport phenomena at work are advection, diffusion, and bulk–surface flux between the bulk of the fluid and the free surface, the latter of which we denote by $J^*(x^*, y^*, t^*)$.

Thus, we have an advection–diffusion equation for the evolution of the bulk concentration, namely

$$\frac{\partial c^*}{\partial t^*} + \mathbf{u}^* \cdot \nabla^* c^* = \mathrm{D}_\mathrm{b}^* \nabla^{*2} c^*, \tag{2.4.1}$$

where D_b^* is a bulk diffusion coefficient. Along with this equation we have two boundary conditions. First, there is no flux of solute through the substrate, and so on $z^* = -d^*$ we have

$$\frac{\partial c^*}{\partial z^*} = 0. \tag{2.4.2}$$

Second, there is a flux of particles between the bulk of the fluid and the free surface, with some bulk solute becoming surface solute, and vice versa, and so at $z^* = h^*$ we have

$$-\mathrm{D}_\mathrm{b}^* \nabla^* c^* \cdot \mathbf{n} = J^*. \tag{2.4.3}$$

Note that J^* is defined to be the flux of solute moving *from* the bulk of the fluid *to* the free surface, and has yet to be prescribed.

It is slightly more difficult to formulate the equivalent advection–diffusion equation for the surface concentration, as the advective and diffusive transport is restricted to the free surface. Nonetheless, as Pereira and Kalliadasis [72] show, the evolution of the surface concentration is governed by

$$\frac{\partial s^*}{\partial t^*} + \mathbf{u}^* \cdot \nabla^*_{xy} s^* + s^* \nabla^*_{\mathrm{s}} \cdot \mathbf{u}^* = \mathrm{D}^*_{\mathrm{s}} \nabla^{*2}_{\mathrm{s}} s^* + J^*, \tag{2.4.4}$$

where $\mathrm{D}^*_{\mathrm{s}}$ is a surface diffusion coefficient, ∇^*_{s} is, again, the surface gradient operator, and $\nabla^*_{xy} = (\partial_{x^*}, \partial_{y^*})$. It should be noted that a slightly different equation governing the transport of surface concentration derived by, for example, Stone [96] has been used extensively throughout the literature. However, there are some ambiguities in the definition of the time derivative in the equation arrived at by Stone, which were clarified by Wong *et al.* [119], who obtained (2.4.4) using a differential geometrical argument. Periera and Kalliadasis [72] have, more recently, given a much more straightforward derivation of (2.4.4), which highlights the difference between it and the widely used equation. However, the two equations coincide in a linear regime, and at leading order in the thin-film limit, and so for most cases studied in the literature the differences between the two equations are inconsequential.

The question remains as to the exact form of the bulk–surface flux J^*. In the present work we wish to capture the qualitative behaviour of the system, but without, as mentioned earlier, the distracting complications of, for example, a maximum surface concentration due to packing effects, or micelle formation in the bulk of the fluid. Similarly, we do not attempt to represent the underlying ionic interactions that control the surface excess and its effects [55], but in the spirit of established surfactant models [8, 40, 45, 46, 57] we subsume these effects into a simple flux between the bulk of the fluid and the free surface. Thus, we consider the linear bulk–surface flux

$$J^* = k_1^* \eta^* c^* - k_2^* s^*, \tag{2.4.5}$$

where k_1^* and k_2^*, both measured in s^{-1}, are rate constants determining the rate

of particle adsorption to, and desorption from, the free surface, respectively. It is also possible to arrive at equation (2.4.5) from a purely chemical standpoint: if nothing but the adsorption and desorption of solute is considered, then the sorptive process may be regarded as a "chemical reaction", namely

$$c^* \underset{k_2^*}{\overset{\eta^* k_1^*}{\rightleftharpoons}} s^*. \tag{2.4.6}$$

Applying the law of mass action, we may then write

$$\frac{\mathrm{d}s^*}{\mathrm{d}t^*} = k_1^* \eta^* c^* - k_2^* s^*, \tag{2.4.7}$$

and we can then identify that $\mathrm{d}s^*/\mathrm{d}t^* = J^*$.

When $J^* = 0$ the surface concentration is in equilibrium with the bulk concentration in the subsurface region, and this is a good approximation when flow and transport processes are slow compared to the kinetics of bulk–surface solute transfer. This state will be referred to as "surface–bulk equilibrium", and it should be noted that a system in surface–bulk equilibrium may still be evolving through slow diffusion-controlled adsorption [9, 11, 60]. In surface–bulk equilibrium, $J^* = 0$, and equation (2.4.5) recovers the Henry isotherm [11],

$$s_{\mathrm{eq}}^* = \frac{k_1^* \eta^*}{k_2^*} c_{\mathrm{eq}}^* = K \eta^* c_{\mathrm{eq}}^*, \tag{2.4.8}$$

where we have defined

$$K = \frac{k_1^*}{k_2^*}, \tag{2.4.9}$$

which is an equilibrium rate constant determining whether the rate of adsorption to, or the rate of desorption from, the free surface is faster. The quantity $K\eta^*$ is sometimes known as Henry's adsorption constant. If the solute is a surfactant then particles accumulate at the free surface and $k_1^* > k_2^*$, giving $K > 1$; alternatively, if the solute is an anti-surfactant then particles accumulate in the bulk and $k_2^* > k_1^*$, giving $K < 1$. Thus K is a single parameter that mathematically determines whether the solute is a surfactant or an anti-surfactant. In the more general situation in which $J^* \neq 0$ both kinetics and diffusion play a part in bulk-surface solute transfer, a regime sometimes referred to as "mixed-kinetic adsorption" [11].

Finally, we require a constitutive relationship for surface tension as a function of concentration, i.e., an equation of state. There are many different equations of state in the literature, such as the popular Sheludko equation of state [45,90], but all of them make the crucial assumption that surface tension is a monotonically decreasing function of surface concentration only [15,39,40,45]. A naïve approach is to make the same assumption for anti-surfactants, but this is not consistent with the underlying physical chemistry [89].

Instead, we must consider the *Gibbs adsorption isotherm* [11,89], as mentioned in section 1.4, namely

$$c^*_{\mathrm{eq}} \frac{\mathrm{d}\sigma^*_{\mathrm{eq}}}{\mathrm{d}c^*_{\mathrm{eq}}} = -R^*T^*\Gamma^*_{\mathrm{eq}}, \tag{2.4.10}$$

where R^* is the ideal gas constant, T^* is the (constant) temperature, and the subscript "eq" denotes that the quantity is measured in equilibrium. Equation (2.4.10) is an equilibrium equation of state giving surface tension as a function of the equilibrium surface excess Γ^*_{eq} and *not* simply of the surface concentration s^*_{eq}. In equilibrium, the Henry isotherm (2.4.8) applies and we write $s^*_{\mathrm{eq}} = K\eta^* c^*_{\mathrm{eq}}$; solving (2.4.10) for σ^*_{eq} we obtain

$$\sigma^*_{\mathrm{eq}} = \sigma^*_{\mathrm{solv}} - R^*T^*\Gamma^*_{\mathrm{eq}} = \sigma^*_{\mathrm{solv}} - R^*T^*\eta^*(K-1)c^*_{\mathrm{eq}}, \tag{2.4.11}$$

where σ^*_{solv} is the surface tension of pure solvent. Note that if $K > 1$ then surface tension will *decrease* with equilibrium bulk concentration, i.e., surfactant behaviour, and similarly if $K < 1$ then surface tension will *increase* with equilibrium bulk concentration, i.e., anti-surfactant behaviour.

The equilibrium equation of state (2.4.11) can be extended to non-equilibrium conditions in various ways. In general, we expect σ^* to depend instantaneously on both bulk and surface concentration; any function that reduces to (2.4.11) when in surface-bulk equilibrium could, in principle, be considered. For simplicity and definiteness, we therefore choose the following linear equation of state:

$$\sigma^* = \sigma^*_{\mathrm{solv}} + R^*T^*(1-K)\left(\frac{1-\theta}{K}s^* + \eta^*\theta c^*\right), \tag{2.4.12}$$

where θ is an artificial tuning parameter that could, in principle, take any value and (2.4.12) will still reduce to the Gibbs isotherm (2.4.10) in equilibrium. Choosing $\theta = 0$ will make σ^* depend only on the surface concentration s^*, regardless

of whether the solute is a surfactant or an anti-surfactant; choosing $\theta = 1$ will make σ^* depend only on the bulk concentration c^*, again regardless of whether the solute is a surfactant or an anti-surfactant. Perhaps more interesting is the choice $\theta = 1/(1-K)$ which makes σ^* a function only of the surface excess Γ^*. As part of the present analysis, we will explore the differences that choosing these different values of θ causes.

Equation (2.4.12) may also be written in the form

$$\sigma^* = \sigma^*_{\text{solv}} - R^*T^*\left(\Gamma^* + aJ^*\right), \tag{2.4.13}$$

where

$$a = \frac{1-\theta}{k_1} + \frac{\theta}{k_2} \tag{2.4.14}$$

is simply a rescaled version of θ. Equation (2.4.13) makes it much clearer that our chosen equation of state reduces to the Gibbs adsorption isotherm (2.4.11) in surface-bulk equilibrium, i.e., when $J^* = 0$. Choosing $a = 1/k_1^*$ will make σ^* a function of s^* only; choosing $a = 1/k_2^*$ will make σ^* a function of c^* only; choosing $a = 0$ will make σ^* a function of Γ^* only.

2.5 Parameter Values

Within the model formulated in the previous sections, there appear a number of dimensional parameters, whose values we now discuss.

Table 2.1 shows the values for the important physical parameters appearing in the model, for four different solutions comprising salts dissolved in water that exhibit the anti-surfactant effect.

Columns two and three give two different measures of concentration, with column two giving percentage mass of solute in solution, and column three giving molar concentration.

Columns four and five give the density and viscosity of the solution for each concentration. Notice that, at a moderate concentration, say, of $1\,\text{mol}\,\text{m}^{-3}$, the density and viscosity of the salt solution is not significantly different from that of pure water, and it then seems reasonable, simply for convenience, to estimate

these two quantities as being equal to their values for pure water, and so we take the density to be $\rho^* = 1000\,\mathrm{kg\,m^{-3}}$ and the viscosity to be $\mu^* = 10^{-3}\,\mathrm{Pa\,s}$.

Column six gives the bulk diffusivity of each salt when in dilute solution (i.e. in the limit as concentration goes to zero) with water, calculated using the formula [32]

$$\mathrm{D}_\mathrm{b}^* = \frac{(z_+ + |z_-|)\,\mathrm{D}_+^*\,\mathrm{D}_-^*}{z_+\,\mathrm{D}_+^* + |z_-|\,\mathrm{D}_-^*}, \tag{2.5.1}$$

where z_+, z_- are the charges of the component cation and anion, respectively, and D_+^*, D_-^* are the diffusion coefficients of the component cation and anion, respectively. These diffusion coefficients range from about $1.5\text{–}3 \times 10^{-9}\,\mathrm{m^2\,s^{-1}}$, so we estimate D_b^* for all salts to be $\mathrm{D}_\mathrm{b}^* = 2 \times 10^{-9}\,\mathrm{m^2\,s^{-1}}$. Surface diffusivity, D_s^*, is very difficult to measure experimentally, but the assumption that $\mathrm{D}_\mathrm{s}^* = \mathrm{D}_\mathrm{b}^*$ is justified when the diffusing particles are large [4, 26, 104]. We therefore assume that surface diffusivity is equal to bulk diffusivity, i.e., $\mathrm{D}_\mathrm{s}^* = \mathrm{D}_\mathrm{b}^* = 2\times10^{-9}\,\mathrm{m^2\,s^{-1}}$.

Column seven gives experimentally obtained values for the surface tension of the solution, with the concentration at which the measurement was taken. Note that all of these surface-tension values are increasing with concentration and are greater than $\sigma_\mathrm{solv}^* = 7.28 \times 10^{-2}\,\mathrm{N\,m^{-1}}$, the surface tension of pure solvent (water in this case), illustrating the anti-surfactant effect.

The surface thickness, η^*, is taken to be $\eta^* = 10^{-9}\,\mathrm{m}$, as we expect the free surface to be a mono-layer of water/solute particles. The kinetic rate constants k_1^* and k_2^* are much more difficult to determine with certainty: a review by Noskov [63] emphasises how difficult it is to measure these constants. For example, if the kinetics are fast enough, then the dynamic surface tension will be completely controlled by diffusion (often called the diffusion-limited regime [11]), and this makes it very difficult to measure the values of the kinetic constants. In the review by Chang and Franses [11], the Langmuir reaction rate constant for octanol is found to be $O(10^{-5})\,\mathrm{m\,s^{-1}}$. The relevant length scale in order to compare with our reaction rates (which are measured in $\mathrm{s^{-1}}$) is η^*; thus we obtain rate constants that are $O(10^4)\,\mathrm{s^{-1}}$. As an upper bound on the values of k_1^* and k_2^*, Long and Nutting [52] state that surface–bulk equilibrium should theoretically be established in $O(10^{-10})\,\mathrm{s}$, and Noskov [63] offers the following explanation: if

there are no energy barriers associated with the adsorption or desorption, then these processes correspond simply to the diffusion of particles across the thickness of the surface layer, and the timescale associated with this diffusion is $\eta^{*2}/\mathrm{D}_\mathrm{s}^*$. Taking D_s^* and η^* as above, this corresponds to rates that are $O(10^{10})\,\mathrm{s}^{-1}$. We may therefore consider k_1^* and k_2^* to lie anywhere in the very wide range between $O(10^4)\,\mathrm{s}^{-1}$ and $O(10^{10})\,\mathrm{s}^{-1}$.

Table 2.2 is the analogue of Table 2.1, but gives values of the physical parameters for a water/alcohol system, in which a low concentration of water acts as a solute in small-chain alcohols, such as methanol or ethanol, which acts as the solvent. The surface tension of this water/alcohol system behaves as a salt/water system does, i.e., as an increasing amount of solute (water in this case) is added to the solvent (alcohol in this case), the surface tension of the solution increases. As Table 2.2 shows, the values of the physical parameters for a water/alcohol system are of the same order of magnitude as for a salt/water system, and the mathematical treatment of the two types of system will be identical. Thus, the term "anti-surfactant" can be taken to apply to either of the above examples, i.e., salts in water, or water in small chain alcohols.

To summarise, representative values for the physical parameters are given in Table 2.3, and these are applicable to both salt/water, and water/alcohol systems.

2.6 Summary

In this Chapter, we have formulated the model that will be used throughout the thesis to describe the evolution of a layer of surfactant or anti-surfactant solution with a single free surface, sitting on top of a horizontal, impermeable substrate. In this model, the hydrodynamics is coupled to the transport of the surface and bulk concentrations of the dissolved solute through the balance of normal and tangential stresses at the free surface, i.e., through the Marangoni effect. By considering the surface excess of the dissolved solute, and by choosing a specific bulk–surface flux, we derived an equation of state relating the surface

tension of the fluid to the concentrations of the dissolved solute from the Gibbs isotherm. This equation of state can describe not only classical surfactants, but also anti-surfactants.

The hydrodynamics and solute transport are governed by the continuity equation, the Navier–Stokes equation and advection–diffusion equations for the transport of bulk and surface concentration,

$$\nabla^* \cdot \mathbf{u}^* = 0, \tag{2.6.1}$$

$$\rho^* \left(\frac{\partial \mathbf{u}^*}{\partial t^*} + \mathbf{u}^* \cdot \nabla^* \mathbf{u}^* \right) + \nabla^* p^* - \mu^* \nabla^{*2} \mathbf{u}^* = \mathbf{0}, \tag{2.6.2}$$

$$\frac{\partial c^*}{\partial t^*} + \mathbf{u}^* \cdot \nabla^* c^* = \mathrm{D}_\mathrm{b}^* \nabla^{*2} c^*, \tag{2.6.3}$$

$$\frac{\partial s^*}{\partial t^*} + \mathbf{u}^* \cdot \nabla_{xy}^* s^* + s^* \nabla_s^* \cdot \mathbf{u}^* = \mathrm{D}_\mathrm{s}^* \nabla_s^{*2} s^* + J^*. \tag{2.6.4}$$

These equations are subject to the boundary conditions

$$\mathbf{u}^* = \mathbf{0} \quad \text{on} \quad z^* = -d^*, \tag{2.6.5}$$

$$\mathbf{n} \cdot \mathbf{T}^* \cdot \mathbf{n} = -\left(\nabla_\mathrm{s}^* \cdot \mathbf{n} \right) \sigma^* \quad \text{on} \quad z^* = h^*, \tag{2.6.6}$$

$$\mathbf{t} \cdot \mathbf{T}^* \cdot \mathbf{n} = \mathbf{t} \cdot \nabla_\mathrm{s}^* \sigma^* \quad \text{on} \quad z^* = h^*, \tag{2.6.7}$$

$$\frac{\partial h^*}{\partial t^*} + \nabla^* \cdot \mathbf{Q}^* = 0 \quad \text{on} \quad z^* = h^*, \tag{2.6.8}$$

$$\frac{\partial c^*}{\partial z^*} = 0 \quad \text{on} \quad z^* = -d^*, \tag{2.6.9}$$

$$-\mathrm{D}_\mathrm{b}^* \nabla^* c^* \cdot \mathbf{n} = J^* \quad \text{on} \quad z^* = h^*, \tag{2.6.10}$$

which are the no-slip and no-penetration conditions, the balance of normal stresses at the free surface, the balance of tangential stresses at the free surface, the kinematic condition, no flux of solute through the substrate, and the flux of solute at the free surface, respectively. The bulk-surface flux J^* is given by

$$J^* = k_1^* \eta^* c^* - k_2^* s^*, \tag{2.6.11}$$

and the surface tension σ^* is given by

$$\sigma^* = \sigma_\mathrm{solv}^* + R^* T^* (1 - K) \left(\frac{1 - \theta}{K} s^* + \eta^* \theta^* c^* \right). \tag{2.6.12}$$

Table 2.1: Physical parameter values for a variety of salts dissolved in water, in SI units. All values are taken from the CRC Handbook of Chemistry and Physics [32], with the exception of the values for surface tension (references for which are included in the table).

Salt	**Concentration** (mass %)	**Concentration** ($\mathrm{mol\,m^{-3}}$)	**Density** ($\mathrm{kg\,m^{-3}}$)	**Dynamic Viscosity** (Pa s)	**Bulk Diffusivity** ($\mathrm{m^2\,s^{-1}}$)	**Surface Tension** ($\mathrm{N\,m^{-1}}$)
Sodium	1	7.12×10^2	1.01×10^3	1.020×10^{-3}		7.2305×10^{-2} [32]
Chloride	5	8.85×10^2	1.03×10^3	1.085×10^{-3}	1.611×10^{-9}	7.3519×10^{-2} [32]
	10	1.83×10^3	1.07×10^3	1.193×10^{-3}	for all	7.5148×10^{-2} [32]
	25	5.09×10^3	1.19×10^3	1.906×10^{-3}	concentrations	8.0766×10^{-2} [32]
Potassium	1	1.79×10^2	1.01×10^3	1.019×10^{-3}		
Hydroxide	5	9.29×10^2	1.04×10^3	1.102×10^{-3}	2.855×10^{-9}	$7.2 - 7.8 \times 10^{-2}$ [91]
	10	1.94×10^3	1.09×10^3	1.233×10^{-3}	for all	at ≈ 0 to ≈ 3 $\mathrm{mol\,m^{-3}}$
	20	4.21×10^3	1.18×10^3	1.619×10^{-3}	concentrations	
Potassium	1	1.35×10^2	1.00×10^3	0.999×10^{-3}		
Chloride	5	6.91×10^2	1.03×10^3	0.996×10^{-3}	1.994×10^{-9}	$7.2 - 8.2 \times 10^{-2}$ [52, 91, 120]
	10	1.46×10^3	1.06×10^3	0.988×10^{-3}	for all	at ≈ 0 to ≈ 5 $\mathrm{mol\,m^{-3}}$
	20	3.04×10^3	1.13×10^3	1.012×10^{-3}	concentrations	
Sodium	1	1.18×10^2	1.01×10^3	1.007×10^{-3}		
Nitrate	5	6.07×10^2	1.03×10^3	1.032×10^{-3}	1.568×10^{-9}	$7.2 - 7.7 \times 10^{-2}$ [48, 91]
	10	1.26×10^3	1.07×10^3	1.081×10^{-3}	for all	at ≈ 0 to ≈ 5 $\mathrm{mol\,m^{-3}}$
	20	2.69×10^3	1.14×10^3	1.263×10^{-3}	concentrations	

Table 2.2: Values of the physical parameters for a low concentration of water dissolved in small chain alcohols, in SI units, taken from Vazquez [108]. Missing values are a due to insufficient accuracy of the reported experimental values.

Salt	**Concentration** (mass %)	**Concentration** ($\mathrm{mol\,m^{-3}}$)	**Density** ($\mathrm{kg\,m^{-3}}$)	**Dynamic Viscosity** (Pa s)	**Bulk Diffusivity** ($\mathrm{m^2\,s^{-1}}$)	**Surface Tension** ($\mathrm{N\,m^{-1}}$)
Water in	1	7.12×10^2	1.01×10^3	1.020×10^{-3}		7.2305×10^{-2} [108]
methanol	5	8.85×10^2	1.03×10^3	1.085×10^{-3}	1.611×10^{-9}	7.3519×10^{-2} [108]
	10	1.83×10^3	1.07×10^3	1.193×10^{-3}	for all	7.5148×10^{-2} [108]
	25	5.09×10^3	1.19×10^3	1.906×10^{-3}	concentrations	8.0766×10^{-2} [108]
Water in	1	7.1×10^1	1.01×10^3	1.026×10^{-3}		—
ethanol	5	3.67×10^2	1.04×10^3	1.163×10^{-3}	1.524×10^{-9}	7.490×10^{-2} [108]
	10	7.68×10^2	1.09×10^3	1.390×10^{-3}	for all	7.554×10^{-2} [108]
	25	1.68×10^3	1.19×10^3	2.227×10^{-3}	concentrations	—

Parameter	**Value (SI units)**
Surface tension of solvent	$\sigma^*_{\text{solv}} = 7 \times 10^{-2}\,\text{N}\,\text{m}^{-1}$
Density	$\rho^* = 10^3\,\text{kg}\,\text{m}^{-3}$
Viscosity	$\mu^* = 10^{-3}\,\text{Pa}\,\text{s}$
Bulk diffusivity	$\text{D}^*_{\text{b}} = 2 \times 10^{-9}\,\text{m}^2\,\text{s}^{-1}$
Surface diffusivity	$\text{D}^*_{\text{s}} = 2 \times 10^{-9}\,\text{m}^2\,\text{s}^{-1}$
Surface layer thickness	$\eta^* = 10^{-9}\,\text{m}$
Kinetic rate constants	$k^*_1 = k^*_2 = 10^4 - 10^{10}\,\text{s}^{-1}$
Gas constant	$R^* \simeq 8\,\text{J}\,\text{mol}^{-1}\,\text{K}^{-1}$
Temperature	$300\,\text{K}$

Table 2.3: Representative values of the physical parameters applicable to both sodium chloride dissolved in water and water dissolved in methanol.

Chapter 3

Linear Stability of a Quiescent Layer

3.1 Introduction

In this Chapter, we investigate the linear stability of a quiescent layer of surfactant- or anti-surfactant-laden fluid with uniform bulk and surface concentrations at their equilibrium values, c_{i}^* and $\eta^* c_{\mathrm{i}}^*$, respectively, throughout the fluid. We restrict the problem to two dimensions, and assume that the fluid layer is uniform in the y-direction. The layer of fluid occupies the region $-d^* \leq z^* \leq 0$ in the base state, with the substrate at $z^* = -d^*$ and the unperturbed free surface at $z^* = 0$. Since gravity is neglected, the pressure is equal to p_{a} throughout the fluid layer. In the perturbed state, the free surface is at $z^* = h^*(x^*, t^*)$.

In section 3.2, we non-dimensionalise the system of equations and boundary conditions (2.6.1)–(2.6.10), and give estimates of the values of the resulting dimensionless parameters.

In section 3.3, we linearise about the static base state and seek normal-mode solutions to the linearised system, in the usual manner. This gives a linear, algebraic system in terms of the amplitudes of the normal-mode perturbations and, for non-trivial solutions, the determinant of the resulting coefficient matrix must vanish. From this we obtain the dispersion relation of the system, relating the growth rates of perturbations to their wavenumbers, and the physical parameters

in the system.

In section 3.4, we consider four special cases: a pure solvent, an insoluble surfactant, a "perfectly soluble" anti-surfactant, and an infinitely deep layer of surfactant or anti-surfactant solution. In the former three cases the layer is unconditionally stable, but in the latter case it can be linearly *unstable* to perturbations certain wavenumbers; a mechanism for this instability is hypothesised. Through asymptotic analysis of the dispersion relation corresponding to the infinite-depth case, we derive several conditions on when such a layer can be unstable.

Finally, in section 3.6, we consider the effects of finite depth on the instability found in section 3.5. We find that the region of parameter space that leads to instability is largest when the layer is infinitely deep; decreasing the depth of the layer has the effect of stabilising the system. We note that oscillatory behaviour is possible for a layer of finite depth (and discuss this in Appendix A), but that it is an inherently long-wave phenomenon.

3.2 Non-Dimensionalisation

We begin by putting the model (2.6.1)–(2.6.10) into dimensionless form using the following scalings, recalling that stars denote dimensional quantities:

$$\begin{cases} (x^*, z^*, h^*, d^*) = L^*(x, z, h, d), \quad t^* = \dfrac{L^*}{U^*}t, \\ (u^*, w^*) = U^*(u, w), \quad p^* = \dfrac{\mu^* U^*}{L^*}p, \quad T^* = \dfrac{\mu^* U^*}{L^*}T \\ c^* = c_{\mathrm{i}}^* c, \quad s^* = \eta^* c_{\mathrm{i}}^* s, \quad \sigma^* = \sigma_{\mathrm{solv}}^* \sigma. \end{cases} \tag{3.2.1}$$

Pressure is scaled in the expectation that viscous forces will dominate over inertial forces. Surface tension is scaled by the surface tension of pure solvent, σ_{solv}^*, and the concentrations are scaled by the bulk concentration in the base state, c_{i}^*. Note that we scale the surface concentration by $\eta^* c_{\mathrm{i}}^*$ since the dimensions of s^* and c^* differ by a factor of a length scale. We leave the velocity scale U^*, and length scale L^*, arbitrary for the time being, and choose them later depending on the relevant physical balances by, for example, setting a capillary number or a Marangoni number equal to unity to choose U^*, and by setting the layer depth

or a Péclet number equal to unity to choose L^*.

In the following we use subscript notation to denote differentiation. With the scalings (3.2.1), the continuity equation (2.6.1) becomes

$$u_x + w_z = 0. \tag{3.2.2}$$

The x- and z-components of the Navier–Stokes equation (2.6.2) become

$$\mathrm{Re}\,(u_t + uu_x + wu_z) + p_x - u_{xx} - u_{zz} = 0, \tag{3.2.3}$$

$$\mathrm{Re}\,(w_t + uw_x + ww_z) + p_z - w_{xx} - w_{zz} = 0, \tag{3.2.4}$$

where we have defined the Reynolds number, which is a measure of the ratio of inertia to viscosity, as

$$\mathrm{Re} = \frac{\rho^* U^* L^*}{\mu^*}. \tag{3.2.5}$$

The bulk concentration evolution equation (2.6.3) becomes

$$c_t + uc_x + wc_z - \frac{1}{\mathrm{P_b}}\,(c_{xx} + c_{zz}) = 0, \tag{3.2.6}$$

where we have defined the bulk Péclet number, which is a measure of the ratio of advection to diffusion of bulk solute, as

$$\mathrm{P_b} = \frac{U^* L^*}{\mathrm{D_b^*}}. \tag{3.2.7}$$

Similarly, the surface concentration evolution equation (2.6.4) becomes

$$s_t + (us)_x - \frac{1}{\mathrm{P_s}} s_{xx} - \mathrm{Da_a}(Kc - s) = 0, \tag{3.2.8}$$

where we have defined the surface Péclet number, which is a measure of the ratio of advection to diffusion of surface solute, as

$$\mathrm{P_s} = \frac{U^* L^*}{\mathrm{D_s^*}}, \tag{3.2.9}$$

and the advective Damköhler number, which is a measure of the ratio of the rate of bulk–surface solute transfer to advection of surface solute, as

$$\mathrm{Da_a} = \frac{k_2^* L^*}{U^*}, \tag{3.2.10}$$

and $K = k_1^*/k_2^*$ is the equilibrium rate constant discussed in Chapter 2. The above equations are subject to the no-slip and no-penetration conditions (2.6.5), along with the no-flux condition (2.6.9), on the substrate $z = -d$:

$$u = w = 0 \qquad \text{on} \qquad z = -d, \tag{3.2.11}$$

$$c_z = 0 \qquad \text{on} \qquad z = -d. \tag{3.2.12}$$

At the free surface $z = h$ equations (3.2.3), (3.2.4), and (2.6.3) are also subject to the balance of normal stresses (2.6.6) which, with (2.6.12), becomes

$$\mathbf{n}\cdot\mathbf{T}\cdot\mathbf{n} + (\nabla_\mathrm{s}\cdot\mathbf{n})\left[\frac{1}{\mathrm{Ca}} + \mathrm{Ma}(1-K)\left(\frac{1-\theta}{K}s + \theta c\right)\right] = 0 \quad \text{on} \quad z = h, \tag{3.2.13}$$

where we have defined the capillary number, which is a measure of the ratio of viscosity to surface tension, as

$$\mathrm{Ca} = \frac{\mu^* U^*}{\sigma^*_{\mathrm{solv}}}, \tag{3.2.14}$$

and the Marangoni number, which is a measure of the ratio of surface tension variation to viscosity, as

$$\mathrm{Ma} = \frac{R^* T^* \eta^* c_\mathrm{i}^*}{\mu^* U^*}. \tag{3.2.15}$$

At the free surface we also have the balance of tangential stresses (2.6.7) which, with (2.6.12), becomes

$$\mathbf{t}\cdot\mathbf{T}\cdot\mathbf{n} - \mathrm{Ma}(1-K)\mathbf{t}\cdot\nabla_\mathrm{s}\left(\frac{1-\theta}{K}s + \theta c\right) = 0 \quad \text{on} \quad z = h, \tag{3.2.16}$$

where the definition of ∇_s in unchanged from the three-dimensional case, but we redefine $\nabla = (\partial/\partial x, \partial/\partial z)$ to be the two-dimensional gradient operator.

The kinematic condition (2.6.8) scales straightforwardly to give

$$h_t + u h_x = w \qquad \text{on} \qquad z = h. \tag{3.2.17}$$

Finally, we have the flux of solute between bulk and surface regions at the free surface (2.6.10) which, with (2.6.11), becomes

$$\nabla c\cdot\mathbf{n} + \mathrm{Da_d}\,(Kc - s) = 0 \qquad \text{on} \qquad z = h, \tag{3.2.18}$$

where we have defined the diffusive Damköhler number, which is the ratio of the rate of bulk–surface solute transfer to bulk diffusion, as

$$\mathrm{Da_d} = \frac{k_2^* \eta^* L^*}{\mathrm{D_b^*}}. \tag{3.2.19}$$

Throughout this scaling process we have left the horizontal length scale L^* and the horizontal velocity scale U^* arbitrary, but in order to determine the size of each of the dimensionless parameters that have been introduced, and which are summarised in Table 3.1 (with arbitrary U^* and L^*), we now must choose specific values of U^* and L^*.

We consider two choices for U^*. We may choose U^* to reflect the choice that we consider flow driven by gradients of surface tension, i.e., by Marangoni effects, and thus set $\mathrm{Ma} = 1$ to obtain

$$U^* = U^*_{\mathrm{Ma}} = \frac{R^* T^* \eta^* c_{\mathrm{i}}^*}{\mu^*}. \tag{3.2.20}$$

Alternatively, we may choose U^* to reflect the choice that we consider flow driven by mean surface tension, i.e., by capillarity, and thus set $\mathrm{Ca} = 1$ to obtain

$$U^* = U^*_{\mathrm{Ca}} = \frac{\sigma^*_{\mathrm{solv}}}{\mu^*}; \tag{3.2.21}$$

this is the scale that will be used in, for example, the special case of a clean solvent in which there are no Marangoni effects.

We also consider two choices for the length scale L^*. In general, we choose L^* to reflect the choice that we consider situations in which there is a balance between advective and diffusive transport of solute by setting $\mathrm{P_b} = \mathrm{P_s} = 1$, i.e.,

$$L^* = L^*_{\mathrm{P_s}} = \frac{\mathrm{D_s^*}}{U^*} = \frac{\mathrm{D_b^*}}{U^*} = L^*_{\mathrm{P_b}}, \tag{3.2.22}$$

for either $U^* = U^*_{\mathrm{Ma}}$ or $U^* = U^*_{\mathrm{Ca}}$. In the special case in which there is no solute present, i.e., for pure solvent, this length scale is not appropriate. Instead L^* is chosen so that the scaled depth of the undisturbed layer is $d = 1$, i.e., we choose $L^* = d^*$. In addition, we also make this choice in the special cases of an insoluble surfactant, and of a "perfectly soluble" anti-surfactant.

Tables 3.2 and 3.3 show the values that will henceforth be used for each of the dimensionless parameters in the system for different choices of U^* and L^*, using

Parameter	**Expression**
Re	$\dfrac{\rho^* U^* L^*}{\mu^*}$
$\mathrm{P_b}$	$\dfrac{U^* L^*}{\mathrm{D_b^*}}$
$\mathrm{P_s}$	$\dfrac{U^* L^*}{\mathrm{D_s^*}}$
$\mathrm{Da_a}$	$\dfrac{k_2^* L^*}{U^*}$
$\mathrm{Da_d}$	$\dfrac{k_2^* \eta^* L^*}{\mathrm{D_b^*}}$
Ca	$\dfrac{\mu^* U^*}{\sigma_{\mathrm{solv}}^*}$
Ma	$\dfrac{R^* T^* \eta^* c_{\mathrm{i}}^*}{\mu^* U^*}$

Table 3.1: Dimensionless parameters with arbitrary horizontal velocity scale U^* and horizontal length scale L^*.

Parameter	**Expression**	**Value Taken**
U^*_{Ma}	$\dfrac{R^*T^*\eta^*c_{\mathrm{i}}^*}{\mu^*}$	$O(1)\,\mathrm{m\,s^{-1}}$
$L^*_{\mathrm{P_s}}$	$\dfrac{\mu^*\mathrm{D}_{\mathrm{b}}^*}{R^*T^*\eta^*c_{\mathrm{i}}^*}$	$O(10^{-9})\,\mathrm{m}$
Re	$\dfrac{\rho^*\mathrm{D}_{\mathrm{b}}^*}{\mu^*}$	$O(10^{-3})$
$\mathrm{P_b}$	1	1
$\mathrm{P_s}$	1	1
$\mathrm{Da_a}$	$\dfrac{k_2^*\mu^{*2}\mathrm{D}_{\mathrm{b}}^*}{\left(R^*T^*\eta^*c_{\mathrm{i}}^*\right)^2}$	0.05
$\mathrm{Da_d}$	$\dfrac{k_2^*\mu^*}{R^*T^*c_{\mathrm{i}}^*}$	0.5
Ca	$\dfrac{R^*T^*\eta^*c_{\mathrm{i}}^*}{\sigma^*_{\mathrm{solv}}}$	1
Ma	1	1

Table 3.2: Dimensionless parameters and the values that will be taken for each based on the characteristic velocity scale $U^* = U^*_{\mathrm{Ma}}$ and the characteristic length scale $L^* = L^*_{\mathrm{P_s}}$.

Parameter	**Expression**	**Value Taken**
U^*_{Ca}	$\dfrac{\sigma^*_{\mathrm{solv}}}{\mu}$	$O(10^1)\,\mathrm{m\,s^{-1}}$
$L^*_{\mathrm{P_s}}$	$\dfrac{\mu^*\mathrm{D}^*_{\mathrm{b}}}{\sigma^*_{\mathrm{solv}}}$	$O(10^{-8})\,\mathrm{m}$
Re	$\dfrac{\rho^*\mathrm{D}^*_{\mathrm{b}}}{\mu^*}$	$O(10^{-3})$
$\mathrm{P_b}$	1	1
$\mathrm{P_s}$	1	1
$\mathrm{Da_a}$	$\dfrac{k^*_2\mathrm{D}^*_{\mathrm{b}}\mu^{*2}}{\sigma^{*2}_{\mathrm{solv}}}$	0.05
$\mathrm{Da_d}$	$\dfrac{k^*_2\eta^*\mu^*}{\sigma^*_{\mathrm{solv}}}$	0.5
Ca	1	1
Ma	$\dfrac{R^*T^*\eta^*c^*_{\mathrm{i}}}{\sigma^*_{\mathrm{solv}}}$	1

Table 3.3: Dimensionless parameters and the values that will be taken for each based on the characteristic velocity scale $U^* = U^*_{\mathrm{Ca}}$ and the characteristic length scale $L^* = L^*_{\mathrm{P_s}}$.

the values in Table 2.3. In Table 3.2 we have chosen $U^* = U^*_{\mathrm{Ma}}$ and $L^* = L^*_{\mathrm{P_s}}$, and in Table 3.3 we have chosen $U^* = U^*_{\mathrm{Ca}}$ and $L^* = L^*_{\mathrm{P_s}}$. Note that since $\mathrm{Re} \ll 1$ in both of these tables, we henceforth make the assumption that $\mathrm{Re} = 0$ and neglect inertial effects. It is also worth noting that the same parameter group that serves as the capillary number Ca in Table 3.2 also serves as the Marangoni number Ma in Table 3.3. In the three special cases in which we make the choice $L^* = d^*$, the values of the appropriate dimensionless parameters will be discussed in the corresponding sections.

We proceed with both U^* and L^* kept arbitrary for the time being, and make particular choices only when we consider specific cases. With U^* and L^* kept arbitrary, both Ca and Ma will appear in the system of equations and boundary conditions, but one or the other will be set to unity as appropriate depending on the choice of U^* and L^* made.

3.3 Linear Stability Analysis

We now linearise and seek normal-mode solutions to the system of dimensionless equations derived in section 3.2. To do so, we make the ansatz

$$\begin{cases} u(x,z,t) = \varepsilon\phi U(z), \quad w(x,z,t) = \varepsilon\phi W(z), \quad p(x,z,t) = \varepsilon\phi P(z), \\ h(x,t) = \varepsilon\phi H, \quad c(x,z,t) = 1 + \varepsilon\phi C(z), \quad s(x,t) = K + \varepsilon\phi S, \end{cases} \tag{3.3.1}$$

where $\phi = \mathrm{e}^{\omega t + ikx}$, $k \geq 0$ is the wavenumber of the perturbations to the base state, ω is the (in general, complex valued) growth rate of these perturbations, the capital letters are the amplitudes of the perturbations, and ε is a small parameter.

Using the ansatz (3.3.1) the governing equations (3.2.2)–(3.2.4) and (3.2.6) become, to $O(\varepsilon)$ in the limit $\varepsilon \to 0$,

$$ikU(z) + W'(z) = 0, \tag{3.3.2}$$

$$ikP(z) + k^2 U(z) - U''(z) = 0, \tag{3.3.3}$$

$$P'(z) + k^2 W(z) - W''(z) = 0, \tag{3.3.4}$$

$$\left(\omega \mathrm{P_b} + k^2\right) C(z) - C''(z) = 0, \tag{3.3.5}$$

while the surface concentration evolution equation (3.2.8) reduces to the boundary condition

$$\left(\omega + \frac{k^2}{\mathrm{P_s}}\right) S + ikKU(0) - \mathrm{Da_a}(KC(0) - S) = 0. \tag{3.3.6}$$

The boundary conditions at the substrate (3.2.11)–(3.2.12) become

$$U(-d) = 0, \tag{3.3.7}$$

$$W(-d) = 0, \tag{3.3.8}$$

$$C'(-d) = 0. \tag{3.3.9}$$

The boundary conditions at the free surface (3.2.13)–(3.2.18) become

$$\omega H - W(0) = 0, \tag{3.3.10}$$

$$2W'(0) - P(0) + k^2 \left[\frac{1}{\mathrm{Ca}} + \mathrm{Ma}\,(1 - K)\right] H = 0, \tag{3.3.11}$$

$$U'(0) + ikW(0) - \mathrm{Ma}(1 - K)ik \left[\frac{1 - \theta}{K} S + \theta C(0)\right] = 0, \tag{3.3.12}$$

$$C'(0) + \mathrm{Da_d}(KC(0) - S) = 0. \tag{3.3.13}$$

We may simplify the system (3.3.2)–(3.3.13) by solving for P and U in the Navier–Stokes equations (3.3.3) and (3.3.4), and using the continuity equation (3.3.2), to obtain

$$P(z) = \frac{1}{ik}(U''(z) - k^2 U(z)), \tag{3.3.14}$$

$$U(z) = -\frac{1}{ik} W'(z), \tag{3.3.15}$$

and an equation for $W(z)$,

$$W^{(4)}(z) - 2k^2 W''(z) + k^4 W(z) = 0. \tag{3.3.16}$$

The most general solution to (3.3.16) consistent with the substrate boundary conditions (3.3.7)–(3.3.8) is

$$W(z) = \left(A_1 + A_2 \frac{z}{d}\right) \sinh\left(k\,(z + d)\right) - kd\,(A_1 - A_2) \left(1 + \frac{z}{d}\right) \cosh\left(k\,(z + d)\right) \tag{3.3.17}$$

where A_1 and A_2 are constants of integration, and, similarly, the most general solution to (3.3.5) consistent with the substrate boundary condition (3.3.9) is

$$C(z) = A_3 \cosh\left(\sqrt{\omega \mathrm{P_b} + k^2}\,(z+d)\right), \tag{3.3.18}$$

where A_3 is a constant of integration. The free surface boundary conditions (3.3.10)–(3.3.13) become

$$\omega H - W(0) = 0, \tag{3.3.19}$$

$$W'''(0) - 3k^2 W'(0) - k^4\left[\frac{1}{\mathrm{Ca}} + \mathrm{Ma}\,(1-K)\right] H = 0, \tag{3.3.20}$$

$$W''(0) + k^2 W(0) - \mathrm{Ma}(1-K)k^2\left[\frac{1-\theta}{K} S + \theta C(0)\right] = 0, \tag{3.3.21}$$

$$C'(0) + \mathrm{Da_d}(KC(0) - S) = 0, \tag{3.3.22}$$

and the surface concentration boundary condition (3.3.6) becomes

$$\left(\omega + \frac{k^2}{\mathrm{P_s}}\right) S - KW'(0) - \mathrm{Da_a}(KC(0) - S) = 0. \tag{3.3.23}$$

Substituting the solution for $W(z)$, given by (3.3.17), and the solution for $C(z)$, given by (3.3.18), into the free surface boundary conditions (3.3.19)–(3.3.23) yields a linear algebraic system for the integration constants A_1–A_3, and the amplitudes of the initial perturbations to the film thickness, H, and the surface concentration, S. In order for this linear system to have a non-trivial solution, the determinant of the 5×5 coefficient matrix M must vanish, leading to a dispersion relation which relates the growth rates of perturbations, ω, to the wavenumber of perturbations, k. The entries of M are as follows:

$$M_{11} = kd\cosh(kd) - \sinh(kd), \quad M_{12} = -kd\cosh(kd),$$
$$M_{13} = 0, \quad M_{14} = 0, \quad M_{15} = \omega, \tag{3.3.24}$$

$$M_{21} = 2\left(kd\sinh(kd) - \cosh(kd)\right), \quad M_{22} = -2kd\sinh(kd),$$
$$M_{23} = 0, \quad M_{24} = 0, \quad M_{25} = -\left[\frac{1}{\mathrm{Ca}} + \mathrm{Ma}\,(1-K)\right] k, \tag{3.3.25}$$

$$M_{31} = 2k^2 d\cosh(kd), \quad M_{32} = -\frac{2(1+k^2d^2)}{d}\cosh(kd) - 2k\sinh(kd),$$
$$M_{33} = \mathrm{Ma}k\theta(1-K)\cosh(\xi d),$$
$$M_{34} = \mathrm{Ma}\frac{k(\theta-1)(K-1)}{K}, \quad M_{35} = 0, \tag{3.3.26}$$

$$M_{41} = 0, \quad M_{42} = 0, M_{43} = \xi \sinh(\xi d) + \mathrm{Da_d} K \cosh(\sqrt{\omega \mathrm{P_b} + k^2} d),$$
$$M_{44} = -\mathrm{Da_d}, \quad M_{45} = 0, \tag{3.3.27}$$

$$M_{51} = K k^2 d \sinh(kd), \quad M_{52} = -\frac{K(1+k^2d^2)}{d} \sinh(kd) - Kk \cosh(kd),$$
$$M_{53} = -\mathrm{Da_a} K \cosh(\sqrt{\omega \mathrm{P_b} + k^2} d), \quad M_{54} = \omega + \frac{k^2}{\mathrm{P_s}} + \mathrm{Da_a}, \quad M_{55} = 0, \tag{3.3.28}$$

where we have defined $\xi = \sqrt{\omega \mathrm{P_b} + k^2}$. The dispersion relation is then

$$\begin{aligned}
&\mathrm{MaP_s} k(1-K) \Big\{ k \left[\left(\frac{1}{\mathrm{Ca}} + \mathrm{Ma}\,(1-K) \right) \left(1 + 2k^2 d^2 \right) - 4d\omega \right] \\
&\quad - k \left(\frac{1}{\mathrm{Ca}} + \mathrm{Ma}\,(1-K) \right) \cosh(2kd) - 2\omega \sinh(2kd) \Big\} \\
&\quad \times \left[\mathrm{Da_d} K \cosh(\xi d) + (1-\theta) \xi \sinh(\xi d) \right] \\
&\quad + 2 \Big\{ 2\omega \left(1 + 2k^2 d^2 \right) - 2 \left(\frac{1}{\mathrm{Ca}} + \mathrm{Ma}\,(1-K) \right) k^2 d \\
&\quad + 2\omega \cosh(2kd) + k \left(\frac{1}{\mathrm{Ca}} + \mathrm{Ma}\,(1-K) \right) \sinh(2kd) \Big\} \\
&\times \left[\mathrm{Da_d} K \left(k^2 + \omega \mathrm{P_s} \right) \cosh(\xi d) + \xi \left(k^2 + \mathrm{P_s}\,(\mathrm{Da_a} + \omega) \right) \sinh(\xi d) \right] = 0.
\end{aligned} \tag{3.3.29}$$

The dispersion relation given by (3.3.29) is, in general, a transcendental equation for ω as a function of k, but in certain special cases analytical solutions can be found.

3.4 Special Cases

Before considering the general stability problem, we first consider some special cases.

First, in section 3.4.1, we reduce our problem to that of the levelling of a layer of pure solvent, i.e., of a fluid in which there is no solute present, so that the force due to surface tension depends only on the local curvature of the free surface: the only physical effect present is that of capillarity. Levelling of a clean solvent is a classical problem, and we demonstrate that in this case our results reduce to the classical results of Orchard [66].

Secondly, in section 3.4.2, we consider a layer of fluid with an insoluble surfactant present, i.e., a solute all of whose particles are on the surface, and consider

the effects of variable surface tension, without the added complication of solute transfer to and from the bulk of the fluid. The stability of thin films of solvent laden with insoluble surfactant has been studied previously by, for example, Schwartz et al. [87], who found that the insoluble surfactant system is linearly stable. A similar analysis has recently been carried out for a colloidal suspension by Tsai et al. [107], where the colloidal particles are described by their surface and bulk concentrations, and the problem in which all of the colloidal particles are situated on the free surface is treated as a special case, as it is here. The results obtained by Tsai et al. [107] for their "insoluble surface-active particles" problem are identical to the results that have been obtained previously for the insoluble surfactant problem.

Thirdly, in section 3.4.3, we consider, as a complement to the insoluble surfactant case, a layer of fluid in which there is dissolved a "perfectly soluble" anti-surfactant, i.e., a solute that does not adsorb onto the free surface at all. In this regime the system is always stable and, in fact, the evolution of the film thickness decouples from that of the bulk concentration. Even though the bulk concentration affects the surface tension of the fluid, it cannot by itself cause flow in the surface layer, and so the concentration field and the film thickness evolve independently. The stability of thin films of "perfectly soluble" anti-surfactant solution with evaporation of the solvent was first considered by Overdiep [68], and was subsequently extended by, for example, Wilson [118], and Howison *et al.* [35]. We demonstrate that our model recovers the results of these studies when evaporation is neglected.

Finally, in section 3.5, we consider the novel case of an infinitely deep layer of surfactant- or anti-surfactant-laden fluid in which the solute is present in both the surface and the bulk regions. In the limit $d \to \infty$, the boundary conditions at the substrate become far-field conditions, simplifying the analysis somewhat. In this infinite-depth regime a novel instability is predicted only for anti-surfactants, and asymptotic analysis of the dispersion relation (3.3.29) leads to certain conditions on when this instability can occur. In particular, we shall show that the value of the ratio of the Damköhler numbers is crucial to the stability of the system.

3.4.1 Pure Solvent (No Solute)

In order to reduce the system described by the dispersion relation (3.3.29) to the case in which there is no solute (henceforth called the Orchard problem [66]) we set $\mathrm{Ma} = \mathrm{Da_a} = \mathrm{Da_d} = K \equiv 0$, and take the limits $\mathrm{P_s} \to \infty$ and $\mathrm{P_b} \to \infty$. We choose the horizontal velocity scale to be $U^* = U^*_{\mathrm{Ca}}$ so that $\mathrm{Ca} = 1$, and choose the horizontal length scale to be $L^* = d^*$ so that $d = 1$. In this special case the dispersion relation (3.3.29) becomes

$$2\left(\cosh(2k) + 2k^2 + 1\right)\omega + k\left(\sinh(2k) - 2k\right) = 0. \tag{3.4.1}$$

Solving for ω we obtain the levelling rate of the free surface in the Orchard problem (henceforth called the Orchard mode), $\omega = \omega_{\mathrm{Orch}}$, where

$$\omega_{\mathrm{Orch}} = -\frac{k}{2}\frac{\sinh(2k) - 2k}{\cosh(2k) + 2k^2 + 1}. \tag{3.4.2}$$

It is straightforward to show that ω_{Orch} is real and negative for all $k > 0$, and therefore that the system is unconditionally stable, and that the free surface levels monotonically, i.e., that the amplitude of the free surface perturbation is a monotonically decreasing function of time. Physically, this represents levelling of the fluid layer due to mean surface tension, that is, due to the normal stresses produced by the curvature of the free surface. Figure 3.1 shows the (negative) growth rate $\omega = \omega_{\mathrm{Orch}}$ of perturbations in the Orchard problem, given by (3.4.2). Figure 3.2 shows a typical streamline pattern for the mode $\omega = \omega_{\mathrm{Orch}}$ given by (3.4.2) in the Orchard problem. Curvature of the perturbed free surface induces normal stresses which drive a flow. Fluid leaves the peaks of the free surface and flows into the troughs, thus re-distributing the fluid and flattening the free surface. It should be noted that, along with the flow in the normal direction away from the free surface, there is also a tangential flow along the free surface produced by the normal stresses, which has the same effect of re-distributing fluid from the peaks to the troughs of the free surface.

Asymptotically, ω_{Orch} obeys

$$\omega_{\mathrm{Orch}} = \frac{1}{3}k^4 + O(k^6) \quad \text{as} \quad k \to 0, \tag{3.4.3}$$

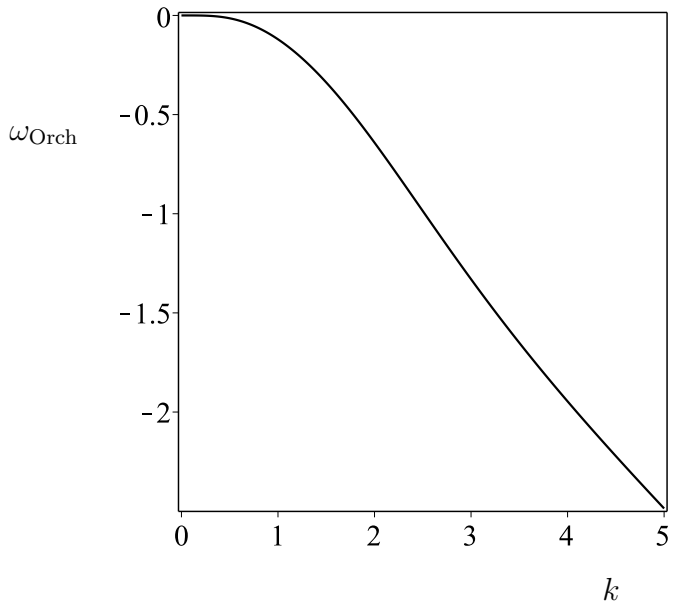

Figure 3.1: The (negative) growth rate $\omega = \omega_{\mathrm{Orch}}$ of perturbations in the Orchard problem, given by (3.4.2).

$$\omega_{\mathrm{Orch}} = -\frac{1}{2}k + O(k^3) \quad \text{as} \quad k \to \infty. \tag{3.4.4}$$

The long-wave limit $k \to 0$ of ω_{Orch}, given by (3.4.3), is simply the result that one would obtain in the thin-film (i.e., small aspect ratio) limit of the Orchard problem. Similarly, the short-wave limit $k \to \infty$ of ω_{Orch}, given by (3.4.4), is simply the result that one would obtain in the infinite-depth (i.e., $d \to \infty$) limit of the Orchard problem. To see why these equivalences hold, consider the quantity kd, i.e., the product of the wavenumber with the undisturbed depth of the layer: kd acts as an aspect ratio of the problem, with d the vertical length scale and k the reciprocal of the horizontal length scale. Since the thin-film problem corresponds to a small aspect ratio, this corresponds to the limit $kd \to 0$ but, since d has been scaled to unity, this is equivalent to taking the limit $k \to 0$. A similar argument applies for the infinite-depth problem and the limit $k \to \infty$, although, in all but this simple Orchard case, the particular distinguished limit that is taken to arrive at the appropriate infinite-depth case is more subtle, as we discuss later in section 3.5.5. Figure 3.3 shows a comparison of the growth rate $\omega = \omega_{\mathrm{Orch}}$, given by (3.4.2), in the Orchard problem, with its long- and short-wave asymptotic approximations given by (3.4.3) and (3.4.4), respectively, and demonstrates the

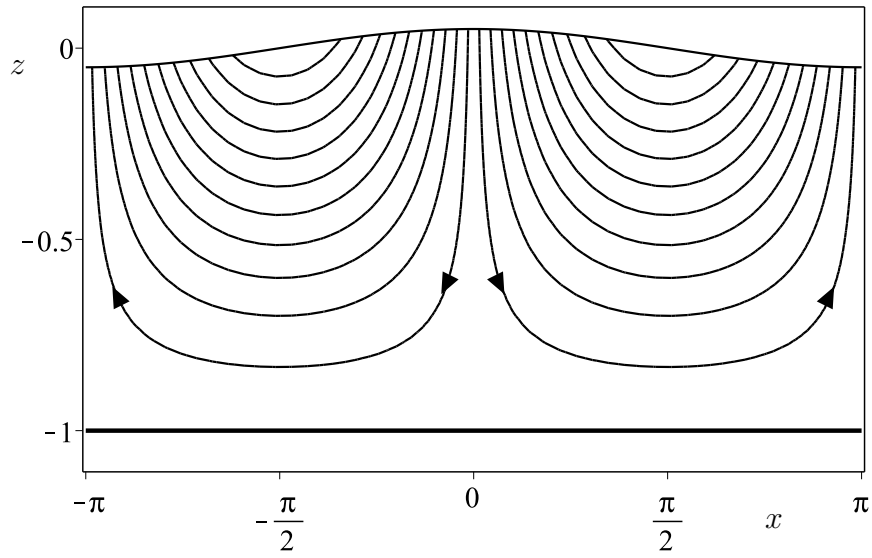

Figure 3.2: Typical streamline pattern for the mode $\omega = \omega_{\mathrm{Orch}}$ given by (3.4.2) in the Orchard problem with $k = 1$, where the flow is from the peaks to the troughs of the perturbed free surface as shown by the arrows, and the thick solid line represents the solid substrate.

good agreement that might be expected in these limits.

While the Orchard mode will feature heavily in the other problems we consider, there are certain regimes, such as the general infinite-depth and the "perfectly soluble" anti-surfactant regimes, in which the evolution of the free surface decouples from the evolution of the bulk and surface concentrations. In such cases there is/are one or more modes with $H = 0$ (recall that H is the amplitude of the perturbation to the film thickness), and a single mode with $H \neq 0$; the latter of these is simply the Orchard mode ω_{Orch}, and is therefore fully understood. In the limit of strong mean surface tension, $\mathrm{Ca} \to 0$, the Orchard mode is lost without affecting any of the other modes. In this limit, the leading order system is unchanged, with the exception that the normal stress boundary condition (3.3.11) becomes simply

$$H = 0, \tag{3.4.5}$$

which means that any perturbation to the free surface must have zero amplitude, i.e., the free surface remains flat.

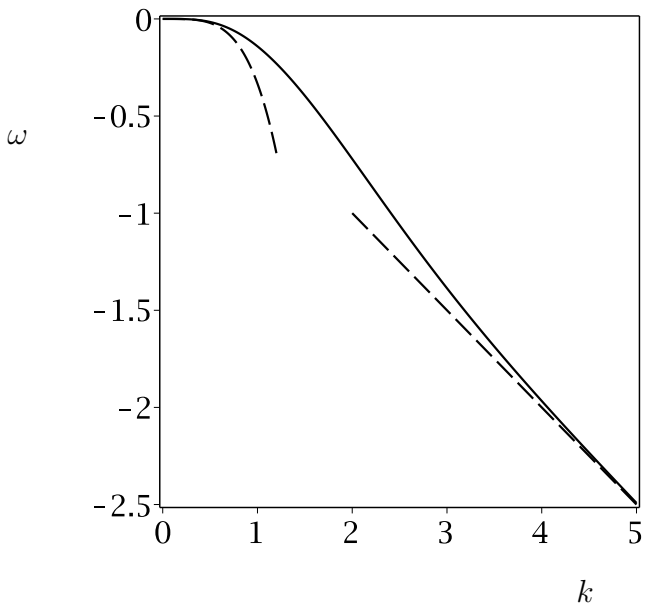

Figure 3.3: Comparison of the growth rate $\omega = \omega_{\text{Orch}}$, given by (3.4.2), in the Orchard problem, with its long- and short-wave asymptotic approximations given by (3.4.3) and (3.4.4), respectively.

3.4.2 Insoluble Surfactant

To reduce the system described by the dispersion relation (3.3.29) to the case in which the solute is an insoluble surfactant we set $\text{Da}_\text{a} = \text{Da}_\text{d} \equiv 0$, $K = 1$ (which is required due to the particular choice of scalings we have used), and take the limit $\text{P}_\text{b} \to \infty$. We also choose $\theta = 0$ so that the surface tension depends solely on the surface concentration. We choose the horizontal velocity scale to be $U^* = U^*_{\text{Ca}}$ so that $\text{Ca} = 1$, and choose the horizontal length scale to be $L^* = d^*$ so that $d = 1$. With these choices for U^* and d^*, the order-of-magnitude values of the two remaining parameters in the system are $\text{Ma} = O(1)$ and $\text{P}_\text{s} = O(10^6)$. In this case the dispersion relation (3.3.29) becomes

$$\begin{aligned}
&4\text{P}_\text{s}\left[2k^2 + 1 + \cosh(2k)\right]\omega^2 \\
&+ 2k\left\{\text{P}_\text{s}\left(\text{Ma}+1\right)\sinh(2k) + 2k\left[\cosh(2k) + \text{P}_\text{s}\left(\text{Ma}-1\right) + 1 + 2k^2\right]\right\}\omega \\
&+ k^2\left[2k\sinh(2k) + \text{MaP}_\text{s}\left(\cosh(2k)-1\right) - \left(2\text{MaP}_\text{s}+4\right)k^2\right] = 0. \qquad (3.4.6)
\end{aligned}$$

Solving (3.4.6) for ω we obtain two solutions for the growth rates, ω_1 and ω_2, both of which are purely real and negative, where we take $\omega_2 > \omega_1$ without loss of gen-

erality, and the system is always monotonically stable. The two levelling modes ω_1 and ω_2 are coupled (i.e., do not change independently when any parameter is varied) when $\mathrm{Ma} \neq 0$, but when $\mathrm{Ma} = 0$ they de-couple to give the Orchard levelling mode (3.4.2), and a pure-diffusive mode given by $\omega = \omega_{\mathrm{PD}}$, where

$$\omega_{\mathrm{PD}} = -\frac{1}{\mathrm{P_s}} k^2, \tag{3.4.7}$$

respectively.

Insoluble Surfactant: $\mathrm{P_s} \to \infty$**,** $\mathrm{Ma} = O(1)$**,** $k = O(1)$

Since $\mathrm{P_s} = O(10^6)$ we are motivated to take the limit $\mathrm{P_s} \to \infty$. In this limit, the dispersion relation (3.4.6) becomes

$$\begin{aligned} &4\left[2k^2 + 1 + \cosh(2k)\right]\omega^2 \\ &+ 2k\left[(\mathrm{Ma}+1)\sinh(2k) + 2\left(\mathrm{Ma}-1\right)k\right]\omega \\ &+ \mathrm{Ma}k^2\left(\cosh(2k) - 1 - 2k^2\right) = 0. \end{aligned} \tag{3.4.8}$$

Figure 3.4 shows the growth rates (a) ω_1, and (b) ω_2, of perturbations in the case of an insoluble surfactant in the limit $\mathrm{P_s} \to \infty$, as solutions to the dispersion relation (3.4.8) for three different values of Ma. The thick solid lines in Figure 3.4 correspond to the case in which $\mathrm{Ma} = 0$, with $\omega_1 = \omega_{\mathrm{Orch}}$ given by (3.4.2) in Figure 3.4(a), and $\omega_2 = \omega_{\mathrm{PD}}$ given by (3.4.7) in Figure 3.4(b). Note that since we have taken the limit $\mathrm{P_s} \to \infty$, $\omega_{\mathrm{PD}} \equiv 0$.

Numerical evidence suggests that, for any positive value of Ma, the rate of levelling given by ω_1 is faster than that given by the Orchard mode ω_{Orch}, given by (3.4.2), while the rate of levelling given by ω_2 is slower than that given by the Orchard mode. Both modes, however, are faster than the pure-diffusive mode ω_{PD} ($\equiv 0$ since $\mathrm{P_s} \to \infty$) given by (3.4.7). The dominant mode (i.e., the least negative ω) is always ω_2, regardless of the value of Ma, and so this is the mode that would be seen at large time in the physical system.

Insoluble Surfactant: $\mathrm{P_s} \to \infty$**,** $\mathrm{Ma} \to \infty$**,** $k = O(1)$

As Ma is increased, ω_1 moves closer to the ω-axis (i.e., the vertical axis), while ω_2 moves towards a non-trivial $O(1)$ limit. Specifically, in the limit as $\mathrm{Ma} \to \infty$,

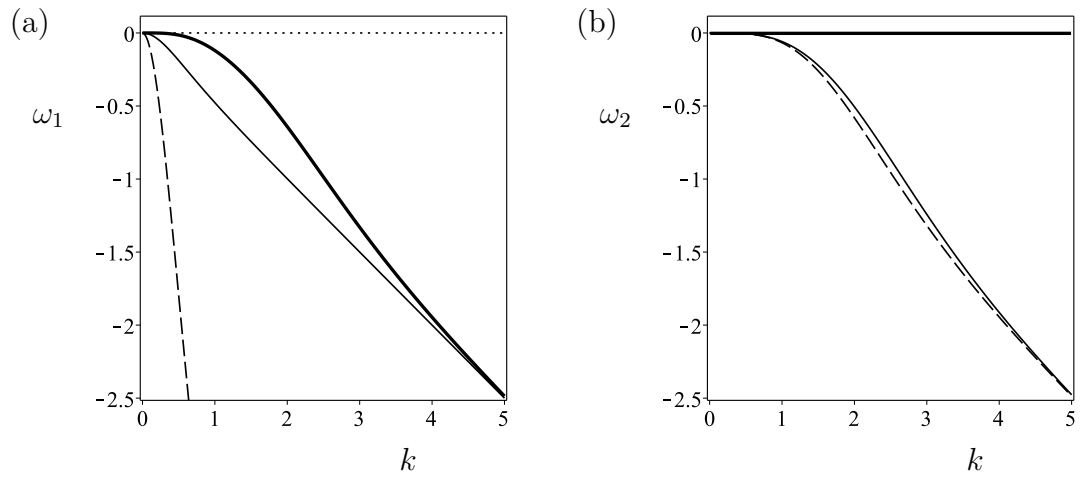

Figure 3.4: Growth rates (a) ω_1, and (b) ω_2, of perturbations in the case of an insoluble surfactant in the limit $\mathrm{P_s} \to \infty$, as solutions to the dispersion relation (3.4.8), for $\mathrm{Ma} = 0$ (thick solid line), $\mathrm{Ma} = 1$ (thin solid line), $\mathrm{Ma} = 10$ (dashed line).

ω_1 and ω_2 satisfy

$$\omega_1 \sim -\frac{k}{2}\frac{\sinh(2k)+2k}{\cosh(2k)+2k^2+1}\mathrm{Ma} \to -\infty \quad \text{as} \quad \mathrm{Ma} \to \infty, \tag{3.4.9}$$

$$\omega_2 \sim -\frac{k}{2}\frac{(\cosh(2k)-2k^2-1)}{\sinh(2k)+2k} = O(1) \quad \text{as} \quad \mathrm{Ma} \to \infty. \tag{3.4.10}$$

From (3.4.9) it is clear that $\omega_1 \to -\infty$ in the limit $\mathrm{Ma} \to \infty$, and is therefore lost. Figure 3.5 shows a comparison of the growth rate ω_2, given by (3.4.10), for an insoluble surfactant in the limit $\mathrm{P_s} \to \infty$ and $\mathrm{Ma} \to \infty$ (dashed), with the growth rate ω_{Orch} given by (3.4.2) in the Orchard problem (solid). This figure shows that the addition of an insoluble surfactant has the effect of slowing the levelling compared to that of pure solvent; this corroborates the results obtained by Schwartz et al. [87], though their work was done in the thin-film regime. Even when the concentration of solute is very high (neglecting complicated packing or electrostatic effects), or alternatively when the solute is strongly surface-active, both of which are captured in the limit $\mathrm{Ma} \to \infty$, the levelling rate is still slower than that given by the Orchard mode. This can be proved directly since, from (3.4.10) and (3.4.2), we have $\omega_2 > \omega_{\mathrm{Orch}}$. In the long-wave $k \to 0$ (strictly, in the distinguished limit $\mathrm{Ma} \to \infty$, $k \to 0$, with the product $\mathrm{Ma}k = O(1)$), ω_1 and ω_2

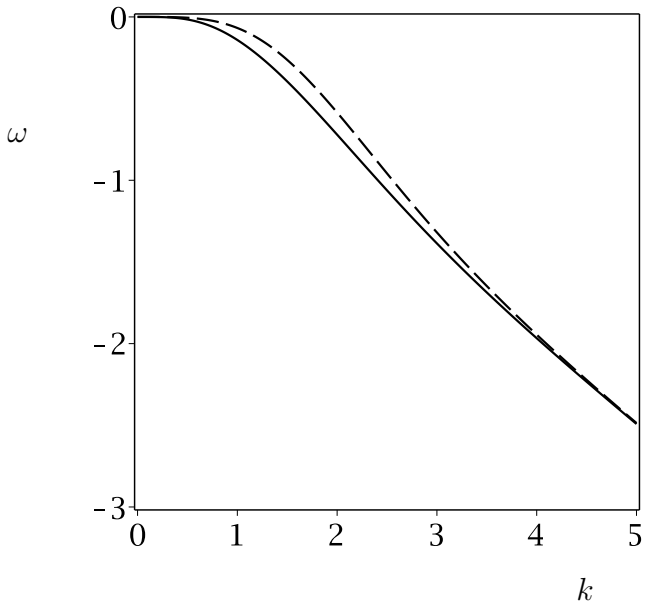

Figure 3.5: Comparison of the growth rate ω_2, given by (3.4.10), for an insoluble surfactant in the limit $\mathrm{P_s} \to \infty$ and $\mathrm{Ma} \to \infty$ (dashed), to the growth rate ω_{Orch} given by (3.4.2) in the Orchard problem (solid).

satisfy

$$\omega_1 \sim -\mathrm{Ma}k^2 \to 0 \quad \text{as} \quad \mathrm{Ma} \to \infty,\ k \to 0, \tag{3.4.11}$$

$$\omega_2 \sim -\frac{1}{12}k^4 \to 0 \quad \text{as} \quad \mathrm{Ma} \to \infty,\ k \to 0. \tag{3.4.12}$$

In fact, equations (3.4.11) and (3.4.12) correspond to the leading order long-wave $k \to 0$ behaviour of ω_1 and ω_2 regardless of the value of Ma.

Comparing (3.4.12) with (3.4.3) shows that, in the limit of large Ma, ω_2 is slower than the Orchard mode by a factor of four in the long-wave limit $k \to 0$, while Figure 3.5 shows that ω_2 is slower than ω_{Orch} for any wavenumber k. This increased hindrance to levelling in the limit $\mathrm{Ma} \to \infty$ is due to the free surface becoming a no-slip surface (rather than a no-shear surface, as in the Orchard case). This can be confirmed analytically by a linear stability analysis of the Orchard problem where the no-shear condition on the free surface is replaced by a no-slip condition on the free surface, and the resulting growth rate is identically $\omega = \omega_2$ given by (3.4.10).

Insoluble Surfactant: $\mathrm{P_s} \to \infty$**,** $\mathrm{Ma} = O(1)$**,** $k \to \infty$

In the short-wave limit $k \to \infty$, the two modes ω_1 and ω_2 satisfy

$$\omega_1 \sim -\frac{1}{2}\mathrm{Ma}k \to \infty \quad \text{as} \quad k \to \infty, \tag{3.4.13}$$

$$\omega_2 \sim -\frac{1}{2}k \quad \to \infty \quad \text{as} \quad k \to \infty, \tag{3.4.14}$$

which are a short-wave Marangoni mode, and the short-wave limit of the Orchard mode $\omega = \omega_{\mathrm{Orch}}$ given by (3.4.4), respectively.

Figure 3.6 shows a typical streamline pattern for the mode $\omega = \omega_2$ in the limit $\mathrm{P_s} \to \infty$ (and for $\mathrm{Ma} = O(1)$) for the dominant mode in the insoluble surfactant problem. Figure 3.7 shows a typical streamline pattern for the mode $\omega = \omega_1$ in the limit $\mathrm{P_s} \to \infty$ for the *sub*-dominant mode in the insoluble surfactant problem. As in the Orchard case, the curvature of the perturbed free surface induces normal stresses which drive flow from the peaks of the free surface to the troughs. However, concentration gradients now induce tangential stresses which drive flow tangentially to the free surface, in addition to the flow induced by the normal stresses. Initially, at peaks of the free surface there are peaks of the surface concentration, and hence there is initially low surface tension at the peaks, and fluid flows away from the peaks and towards the troughs. As fluid enters the troughs of the free surface, it leads to accumulation of surface concentration there, decreasing the surface tension. This causes a tangential flow which opposes the levelling of the free surface and explains why this insoluble-surfactant system levels more slowly than the pure-solvent (i.e., the Orchard) system. Crucially, even in the limit as $\mathrm{Ma} \to \infty$, the flow induced by tangential stress that opposes the levelling can never dominate the normal-stress-driven levelling, and so the system is always stable, as evidenced by the (negative) growth rate obtained in this limit, given by (3.4.10).

3.4.3 "Perfectly Soluble" Anti-Surfactant

To serve as the complement of the insoluble surfactant case in which solute is present only on the surface, we consider the "perfectly soluble" anti-surfactant

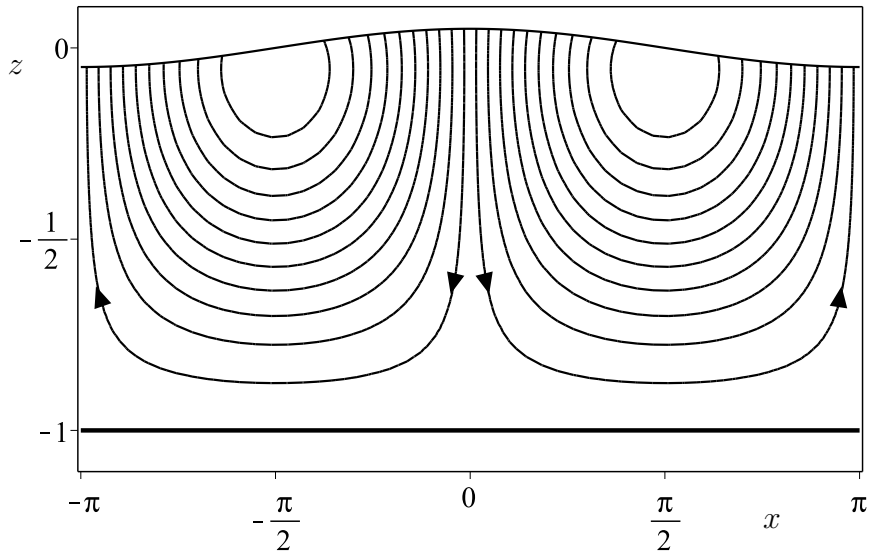

Figure 3.6: Typical streamline pattern for the mode $\omega = \omega_2$ in the limit $\mathrm{P_s} \to \infty$ (and for $\mathrm{Ma} = O(1)$) for the dominant mode in the insoluble surfactant problem, with $k = 1$ and $\mathrm{Ma} = 1$, where the flow is from the peaks to the troughs of the perturbed free surface as shown by the arrows, and the thick solid line represents the solid substrate.

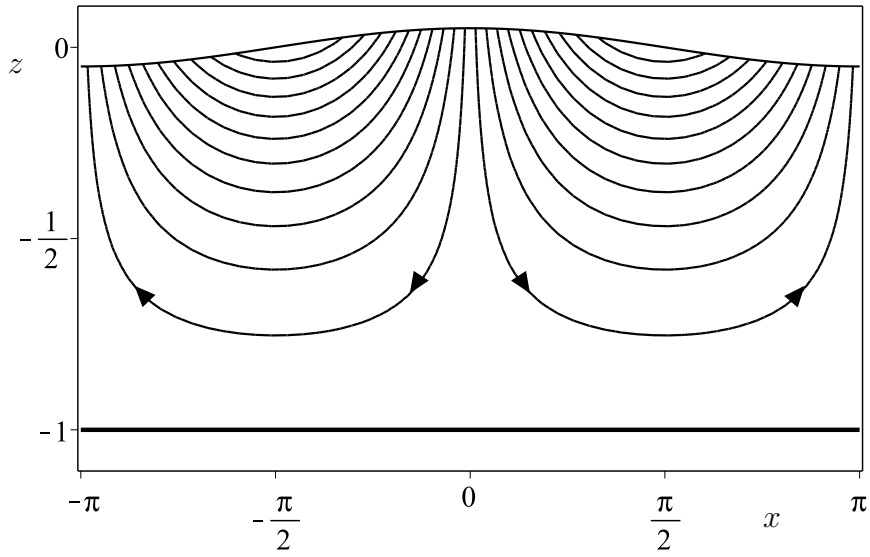

Figure 3.7: Typical streamline pattern for the mode $\omega = \omega_1$ in the limit $\mathrm{P_s} \to \infty$ (and for $\mathrm{Ma} = O(1)$) for the sub-dominant mode in the insoluble surfactant problem, with $k = 1$ and $\mathrm{Ma} = 1$, where the flow is from the peaks to the troughs of the perturbed free surface as shown by the arrows, and the thick solid line represents the solid substrate.

case in which the solute is *completely excluded* from the surface. This problem was first considered by Overdiep [68], in the context of drying paint films, where the resin in the paint is a "perfectly soluble" anti-surfactant. Overdiep's analysis was later extended by, for example, Wilson [118], and Howison *et al.* [35] to include the effects of variable diffusivity and viscosity. When evaporation is neglected in each of these papers, it is found that the thin paint film is stable, and in this section, we recover the results reported in these papers exactly.

To reduce our model to that describing a "perfectly soluble" anti-surfactant we must take the limit $k_2 \to \infty$ so that the rate transfer of solute *from* the surface *to* the bulk is infinitely fast, i.e., as soon as any solute particle enters the surface, it is instantly expelled to the bulk region. In this limit, $\mathrm{Da_a}$, $\mathrm{Da_d} \to \infty$ and $K \to 0$, so that the system is always in surface-bulk equilibrium, and the equilibrium state is such that $S \equiv 0$. We also choose $\theta = 1$ so that the surface tension depends solely on the bulk concentration. We choose the horizontal velocity scale to be $U^* = U^*_{\mathrm{Ca}}$ so that $\mathrm{Ca} = 1$, and choose the horizontal length scale to be $L^* = d^*$ so that $d = 1$. With these choices for U^* and d^*, the order-of-magnitude values of the two remaining parameters in the system are $\mathrm{Ma} = O(1)$ and $\mathrm{P_b} = O(10^6)$.

In this regime the dispersion relation (3.3.29) becomes

$$\sinh\left(\sqrt{\omega \mathrm{P_b} + k^2}\right)\sqrt{\omega \mathrm{P_b} + k^2} \times \left[2\left(\cosh(2k) + k^2 + 1\right)\omega + (\mathrm{Ma}+1)\,k\,(\sinh(2k) - 2k)\right] = 0. \tag{3.4.15}$$

The root $\sinh\left(\sqrt{\omega \mathrm{P_b} + k^2}\right)\sqrt{\omega \mathrm{P_b} + k^2} = 0$ leads to a series of bulk-diffusive modes

$$\omega = -\frac{k^2}{\mathrm{P_b}} - n^2\pi^2, \tag{3.4.16}$$

where n is any integer. When $n = 0$, equation (3.4.16) reduces to the pure diffusive mode given by (3.4.7) (with $\mathrm{P_b}$ instead of $\mathrm{P_s}$). These infinitely many bulk-diffusive modes represent the vertical structure of the bulk concentration throughout the layer.

The other root leads to a "modified" Orchard mode, namely

$$\omega = -(\mathrm{Ma}+1)\frac{k}{2}\frac{\sinh(2k) - 2k}{\cosh(2k) + 2k^2 + 1}, \tag{3.4.17}$$

which is faster than the standard Orchard mode $\omega = \omega_{\text{Orch}}$ given by (3.4.2) for any positive value of Ma. This is sensible since the bulk concentration increases the surface tension of the fluid, and so it might be reasonably expected that the layer would level at a faster rate that if there was no solute present.

It is interesting to note that the levelling rate of the free surface is independent of how the bulk concentration evolves and vice versa. Since the bulk concentration is perturbed there are bulk concentration gradients, and therefore surface-tension gradients which induce flow tangential to the free surface, but these do not affect the rate at which the free surface levels. The flow induced by concentration gradients is simply superposed on to the Orchard levelling, but since no solute accumulation can occur in the bulk, there is no feedback into the Orchard mode that would change the rate at which the free surface levels, except for the increase in mean surface tension (the factor $(\text{Ma} + 1)$ acts as a capillary number in this situation). The fact that no solute accumulation can occur in the bulk region can be explained by a continuity argument: if solute is advected horizontally to a particular position, the solute already present at that position would then advect vertically, and vice versa. Since the bulk solute has the freedom to be transported both vertically and horizontally, there can be no accumulation.

The mechanism through which the free surface of the "perfectly soluble" anti-surfactant solution levels is identical to that of the Orchard problem, and so the streamline pattern that is seen as the free surface levels is identical to that shown in Figure 3.2. Ultimately, the concentration gradients decay simply through diffusion.

3.5 Infinite-Depth Case

We now investigate the case of an infinitely deep layer of fluid in which the substrate lies infinitely far away from the free surface. In this infinite-depth regime, the substrate boundary conditions (3.3.7)–(3.3.9) become far-field conditions, applying as $z \to -\infty$. Since the depth of the layer is now infinite, we cannot use d^* as a length scale; instead, we choose $L^* = L^*_{\text{P}_\text{s}}$ so that $\text{P}_\text{s} = \text{P}_\text{b} = 1$. We also make

the choice $U^* = U^*_{\mathrm{Ma}}$ so that $\mathrm{Ma} = 1$, and so all of the dimensionless parameters are as given in Table 3.2.

The non-dimensionalisation and linearisation of the infinite-depth problem is very similar to that of the general finite-depth problem considered earlier in this chapter with only one difference. The most general solution to (3.3.16) for the amplitude of the vertical velocity component, and of (3.3.5) for the bulk concentration, consistent with the new far-field conditions, are now

$$W(z) = (A_1 + A_2 z)\,\mathrm{e}^{kz}, \tag{3.5.1}$$

$$C(z) = A_3 \mathrm{e}^{\xi z}, \tag{3.5.2}$$

respectively, and where we have defined $\xi = \sqrt{\omega + k^2}$. Substituting the solutions (3.5.1) and (3.5.2) into the free surface boundary conditions (3.3.19)–(3.3.23) yields a simplified linear system, and requiring non-trivial solutions yields the dispersion relations

$$2\omega + \left(\frac{1}{\mathrm{Ca}} + 1 - K\right) k = 0, \tag{3.5.3}$$

and

$$2\xi^3 + 2\mathrm{Da_d} K \xi^2 + \left[2\mathrm{Da_a} - (1-\theta)\,(1-K)\,k\right]\xi - \mathrm{Da_d} K\,(1-K)\,k = 0. \tag{3.5.4}$$

The former of these conditions corresponds to a modified version of the short-wave limit $k \to \infty$ of the Orchard mode given by (3.4.4), and governs the levelling of the free surface with no variation in either the bulk or the surface concentrations, as discussed in section 3.4.1. The latter condition corresponds to the evolution of the system with a flat free surface $H = 0$, with flow driven entirely by surface-tension gradients.

We now focus solely on the second condition (3.5.4), corresponding to the case in which the free surface remains flat. It is straightforward to obtain numerical solutions to equation (3.5.4), and thus plot the perturbation growth rate ω.

Figure 3.8 shows plots of typical growth rates for an anti-surfactant with $K = 0.5$, for various values of the ratio

$$\delta = \frac{\mathrm{Da_d}}{\mathrm{Da_a}}, \tag{3.5.5}$$

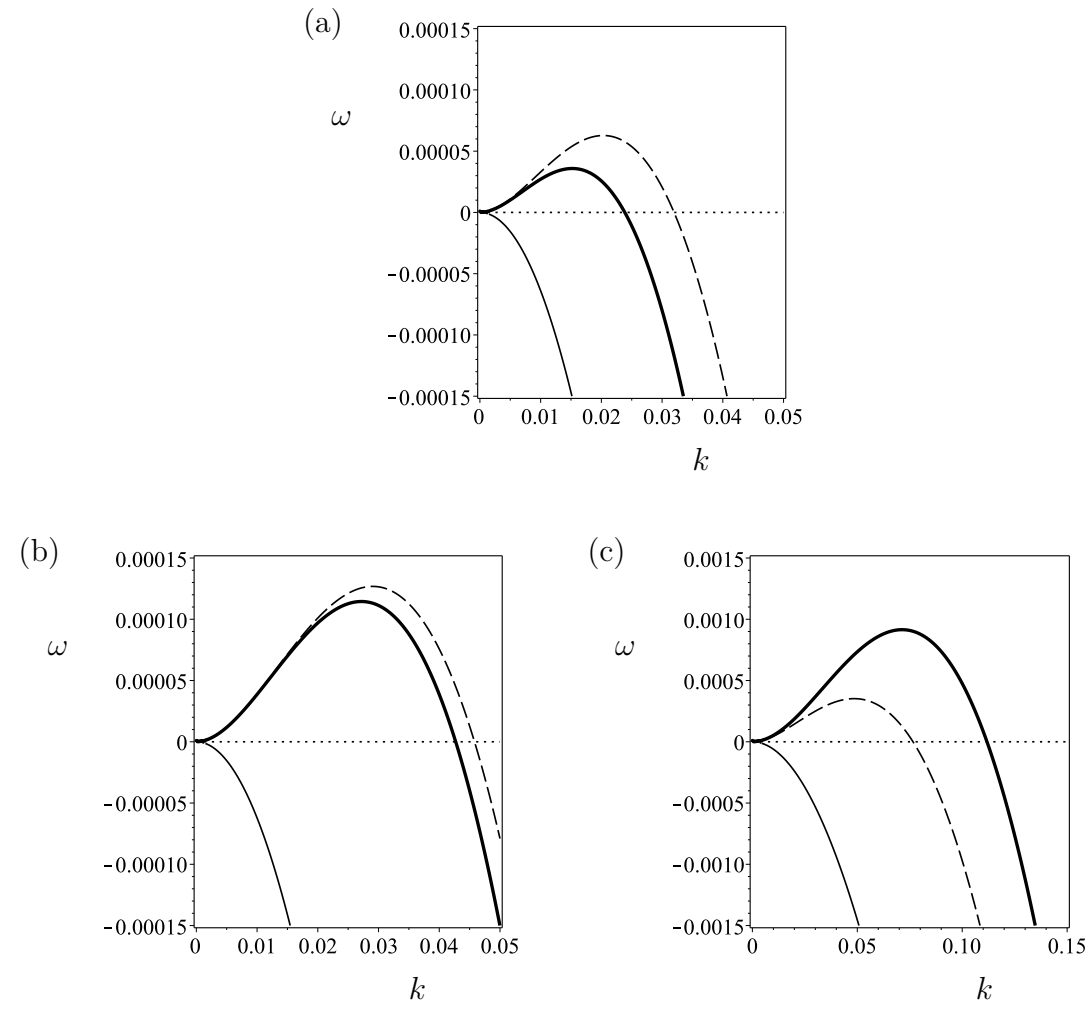

Figure 3.8: The growth rate of perturbations ω, i.e., the positive root of equation (3.5.4), as a function of the wavenumber k in the infinite-depth regime, for $\mathrm{Da_a} = 0.05$, $\mathrm{Da_d} = 0.5$ (thick solid), $\mathrm{Da_a} = 0.1$, $\mathrm{Da_d} = 0.5$ (thin solid), $\mathrm{Da_a} = 0.1$, $\mathrm{Da_d} = 1$ (dashed), $K = 0.5$, and (a) $\theta = 1/(1-K) = 2$, (b) $\theta = 1$, (c) $\theta = 0$, and all other parameters given by Table 3.2.

which will turn out to be important to the stability of the layer, and the parameter θ. In all three plots the thick solid line corresponds to growth rates where $\mathrm{Da_a} = 0.05$ and $\mathrm{Da_d} = 0.5$ (i.e., $\delta = 10$), the thin solid line corresponds to growth rates where $\mathrm{Da_a} = 0.1$ and $\mathrm{Da_d} = 0.5$ (i.e., $\delta = 5$), and the dashed line corresponds to growth rates where $\mathrm{Da_a} = 0.1$ and $\mathrm{Da_d} = 1$ (i.e., $\delta = 10$). Figure 3.8(a) shows a plot of growth rates for $\theta = 1/(1-K)$ ($= 2$ since $K = 0.5$), i.e., when the surface tension depends on the surface excess Γ. Figure 3.8(b) shows a plot of growth rates for $\theta = 1$, i.e., when the surface tension depends on the bulk concentration only. Figure 3.8(c) shows a plot of growth rates for $\theta = 0$, i.e., when the surface tension depends on the surface concentration only.

Figure 3.8 shows that growth rates ω may, in fact, be *positive*, signifying that the system may be linearly *unstable*. In particular, the system is unstable for large enough values of $\delta = \mathrm{Da_d}/\mathrm{Da_a}$, as shown by the fact that the thin solid lines, corresponding to $\delta = 5$, in each figure are negative for all k, and so the system is stable, while the thick solid lines and dashed lines, both corresponding to $\delta = 10$, are positive, and thus unstable, for a range of wavenumbers k. This instability occurs for all three values of the parameter θ, suggesting that the specific value of θ is not crucial in triggering the instability. The effects of changing the Damköhler numbers $\mathrm{Da_d}$ and $\mathrm{Da_a}$, along with θ, will be investigated further below.

In all cases in which instability occurs, it does so only at sufficiently small dimensionless wavenumbers, typically for $k = O(10^{-1})$, while typical maximum growth rates are of the order of $\omega = 10^{-4}$ to 10^{-3} and the corresponding dimensional timescales $L^*/(\omega U^*_{\mathrm{Ma}})$ for the instability to develop are therefore of the order of 10^{-8} to 10^{-7} s. Figure 3.8 is plotted for $K = 0.5$, i.e., for an anti-surfactant, showing this novel instability occurs for anti-surfactant solutions. Numerical evidence suggests that no instability is possible when $K > 1$, and thus that surfactant solutions are unconditionally *stable*.

3.5.1 Marginal Stability Analysis

Numerical evidence suggests that the solutions for ω to (3.5.4) are always purely real, and so we assume that the principle of exchange of stabilities holds, i.e., we

assume that $\omega \in \mathbb{R}$. This allows us to obtain marginal stability curves for various parameters by setting $\omega = 0$ (or, equivalently, $\xi = k$) in equation (3.5.4), and solving for the appropriate parameter.

Figure 3.9 shows typical marginal stability curves (solid) and curves of maximum growth rate (dash) for reference parameter values given by Table 3.2, with $K = 0.5$ and $\theta = 1/(1-K) = 2$ (where appropriate) so that the surface tension depends only on the surface excess.

A key feature of Figure 3.9 is that in each case the unstable region is largest when $k = 0$, and the transition to instability first occurs for long-wave perturbations, i.e., for $k = 0$, although within the unstable region the maximum growth rate generally occurs for a non-zero wavenumber, as shown by the numerically calculated dashed curves.

Figure 3.9(a) shows the marginal stability curve for $\mathrm{Da_a}$, which is given by

$$\mathrm{Da_a} = k^2 + \frac{1}{2}\left[\theta\left(1-K\right) + K\left(2\mathrm{Da_d}+1\right) - 1\right]k + \frac{1}{2}\mathrm{Da_d}K(1-K). \qquad (3.5.6)$$

In particular, it shows that larger values of $\mathrm{Da_a}$ stabilise the system. There is a critical value of $\mathrm{Da_a}$ below which the system is unstable for a range of wavenumbers, which we denote by $\mathrm{Da_{a,crit}}$. This critical value occurs at $k = 0$ and is therefore given by

$$\mathrm{Da_{a,crit}} = \frac{1}{2}\mathrm{Da_d}K\left(1-K\right) \qquad (3.5.7)$$

and is the *maximum* value of $\mathrm{Da_a}$ for which instability is possible. Equation (3.5.7) shows that instability becomes harder to trigger as $K \to 1$, since $\mathrm{Da_{a,crit}} \to 0$ in this limit, in which the anti-surfactant properties of the solute are lost. Similarly, instability becomes harder to trigger as $K \to 0$, since $\mathrm{Da_{a,crit}} \to 0$ in this limit, in which the solute becomes completely excluded from the free surface and, as we have seen in section 3.4.3, the "perfectly soluble" anti-surfactant system is unconditionally stable. Figure 3.9(a) also shows that there is a maximum wavenumber, which we denote by $k_{\max}$, which is the largest wavenumber that can be unstable; for $k > k_{\max}$ the system is stable for all values of $\mathrm{Da_a}$. This $k_{\max}$

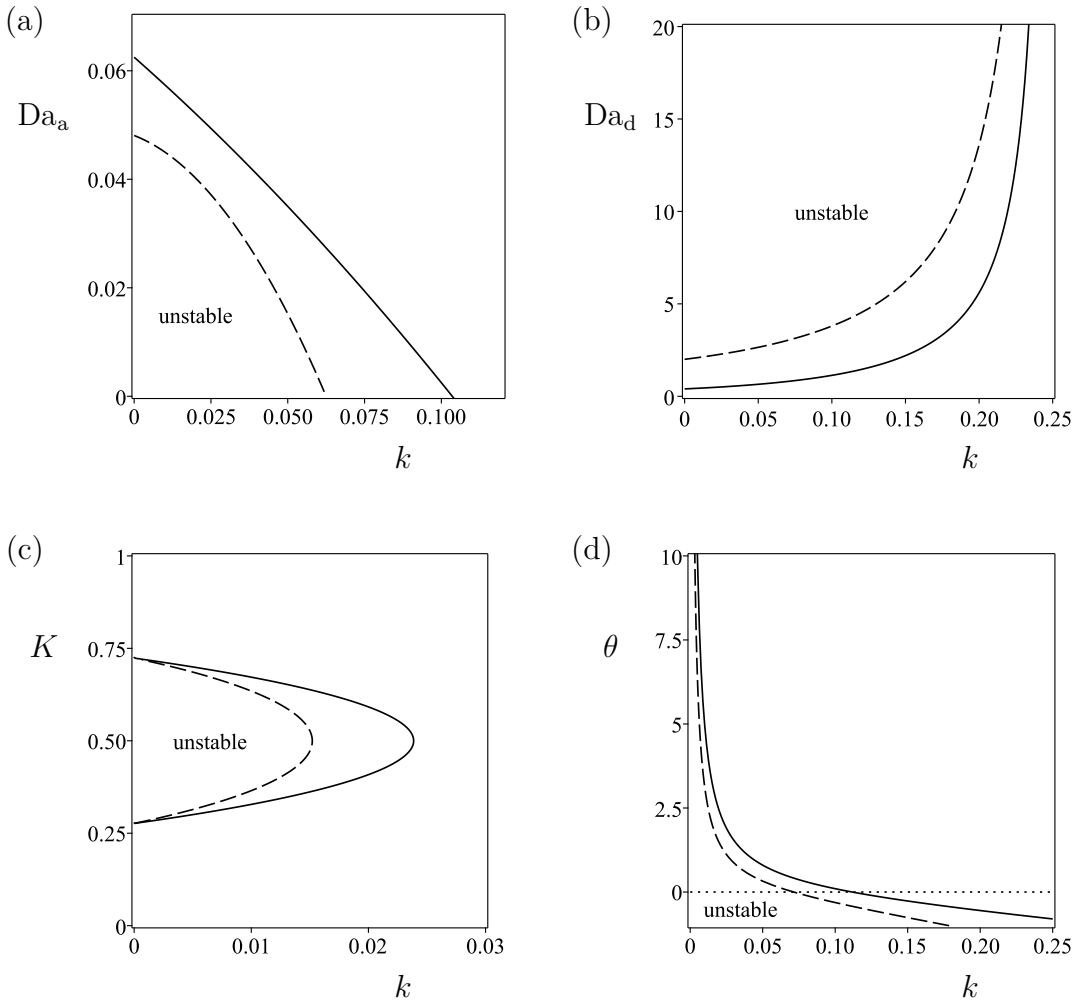

Figure 3.9: Marginal stability curves (solid) and curves of maximum growth rate (dash) for (a) the advective Damköhler number $\mathrm{Da_a}$, given by (3.5.6), (b) the diffusive Damköhler number $\mathrm{Da_d}$, given by (3.5.9), (c) the equilibrium rate constant K, given as the solutions to (3.5.4) with $\omega = 0$, (d) the parameter θ, given by (3.5.13), as a function of the wavenumber k in the infinite-depth limit $d \to \infty$, where $K = 0.5$, $\theta = 1/(1-K) = 2$, and all other parameters values are given by Table 3.2.

satisfies $\mathrm{Da_a} = 0$ in equation (3.5.6), and solving for k we find

$$k_{\max} = \frac{1}{4}\sqrt{(1-K)\left[(\theta-1)^2(1-K) + 4\mathrm{Da_d}(\theta+1)K\right] + 4{\mathrm{Da_d}}^2K^2} + \frac{1}{4}\left[K(\theta-1) - \theta + 1\right] - \frac{1}{2}\mathrm{Da_d}K. \tag{3.5.8}$$

Figure 3.9(b) shows the marginal stability curve for $\mathrm{Da_d}$, which is given by

$$\mathrm{Da_d} = -\frac{2k^2 + (\theta-1)(1-K)k + 2\mathrm{Da_a}}{K\left[2k - (1-K)\right]}. \tag{3.5.9}$$

In particular, it shows that larger values of $\mathrm{Da_d}$ destabilise the system. There is again a critical value of $\mathrm{Da_d}$ above which the system will be unstable for a range of wavenumbers. This critical value again occurs at $k = 0$ and is therefore given by

$$\mathrm{Da_{d,crit}} = \frac{2\mathrm{Da_a}}{K(1-K)}, \tag{3.5.10}$$

and is the *minimum* value of $\mathrm{Da_d}$ for which instability is possible. As in the $\mathrm{Da_a}$ case, there is also a maximum wavenumber $k_{\max}$, but in this case it is the value of k for which the $\mathrm{Da_d}$ marginal curve has a vertical asymptote, and is given by

$$k_{\max} = \frac{1}{2}(1-K). \tag{3.5.11}$$

Figure 3.9(c) shows the marginal stability curve for K, which is the solution for K of the dispersion relation (3.5.4) with $\omega = 0$ when solved for K. In particular, it shows that only a range of values of K will lead to instability. This is consistent with the explanation given for the variation of $\mathrm{Da_{a,crit}}$ with K, where in the limit $K \to 1$ the anti-surfactant properties of the solute are lost, and in the limit $K \to 0$ the problem reduces to the "perfectly soluble" anti-surfactant case. The critical values of K between which the system will be unstable for a range of wavenumbers may be determined by considering the long-wave limit of the dispersion relation, and are given by

$$K^{\pm}_{\mathrm{crit}} = \frac{1}{2} \pm \frac{1}{2}\sqrt{1 - \frac{8\mathrm{Da_a}}{\mathrm{Da_d}}}. \tag{3.5.12}$$

As in the previous cases, there is also a maximum wavenumber $k_{\max}$ (which is $k_{\max} \simeq 0.044$ in the reference case shown in Figure 3.9); while it is possible to find an analytical expression for $k_{\max}$, it has been omitted for brevity.

Figure 3.9(d) shows the marginal stability curve for θ, which is given by

$$\theta = -\frac{2k^2 + [2K\mathrm{Da_d} - (1-K)]\,k - \mathrm{Da_d}K\,(1-K)}{(1-K)\,k} \tag{3.5.13}$$

In particular, it shows that larger values of θ tend to stabilise the system, but for sufficiently small values of k, no choice of θ is sufficient to cause the system to become stable. There is no critical values of θ for which the system is stable for all wavenumbers (i.e., there is always a θ for which perturbations of any wavenumber are unstable), nor is there a maximum wavenumber that might be unstable. Since the typical unstable dimensionless wavenumbers are small, varying θ does not alter the stability of the system, as long as it remains of order unity. The particular value of θ chosen, be it $\theta = 0$, 1, or 2 (for an anti-surfactant with $K = 0.5$), therefore does not qualitatively matter.

Figure 3.10 shows how the $\mathrm{Da_a}$ marginal curve changes as the parameters $\mathrm{Da_d}$ and K are varied, where the thick solid curves correspond to the reference case as shown in Figure 3.9(a), and the arrows denote the direction of increasing value of the parameter.

Figure 3.10(a) shows how the $\mathrm{Da_a}$ marginal curve changes as $\mathrm{Da_d}$ is varied both above and below the reference value of $\mathrm{Da_d} = 0.5$. Increasing $\mathrm{Da_d}$ destabilises the system since the maximum value of $\mathrm{Da_a}$ required to trigger instability decreases as $\mathrm{Da_d}$ increases. Varying $\mathrm{Da_d}$ does not qualitatively change the $\mathrm{Da_a}$ marginal curve, but simply increases the width of the unstable region and the range of unstable wavenumbers. Both $\mathrm{Da_{a,crit}}$ given by (3.5.7) and $k_{\max}$ given by (3.5.8) increase as $\mathrm{Da_d}$ increases.

Figure 3.10(b) shows how the $\mathrm{Da_a}$ marginal curve changes as K is varied for $K \leq 0.5$. As K is increased up to $K = 0.5$, the width of the unstable region increases, reaching its maximum width at $K = 0.5$. The range of unstable wavenumbers behaves in the same way. For $0 < K \leq 0.5$, both $\mathrm{Da_{a,crit}}$ given by equation (3.5.7), and $k_{\max}$ given by (3.5.8) increase monotonically with K and are maximised at $K = 0.5$.

Figure 3.10(c) shows how the $\mathrm{Da_a}$ marginal curve changes as K is varied for $K \geq 0.5$. As K is increased from $K = 0.5$, both the width of the unstable region

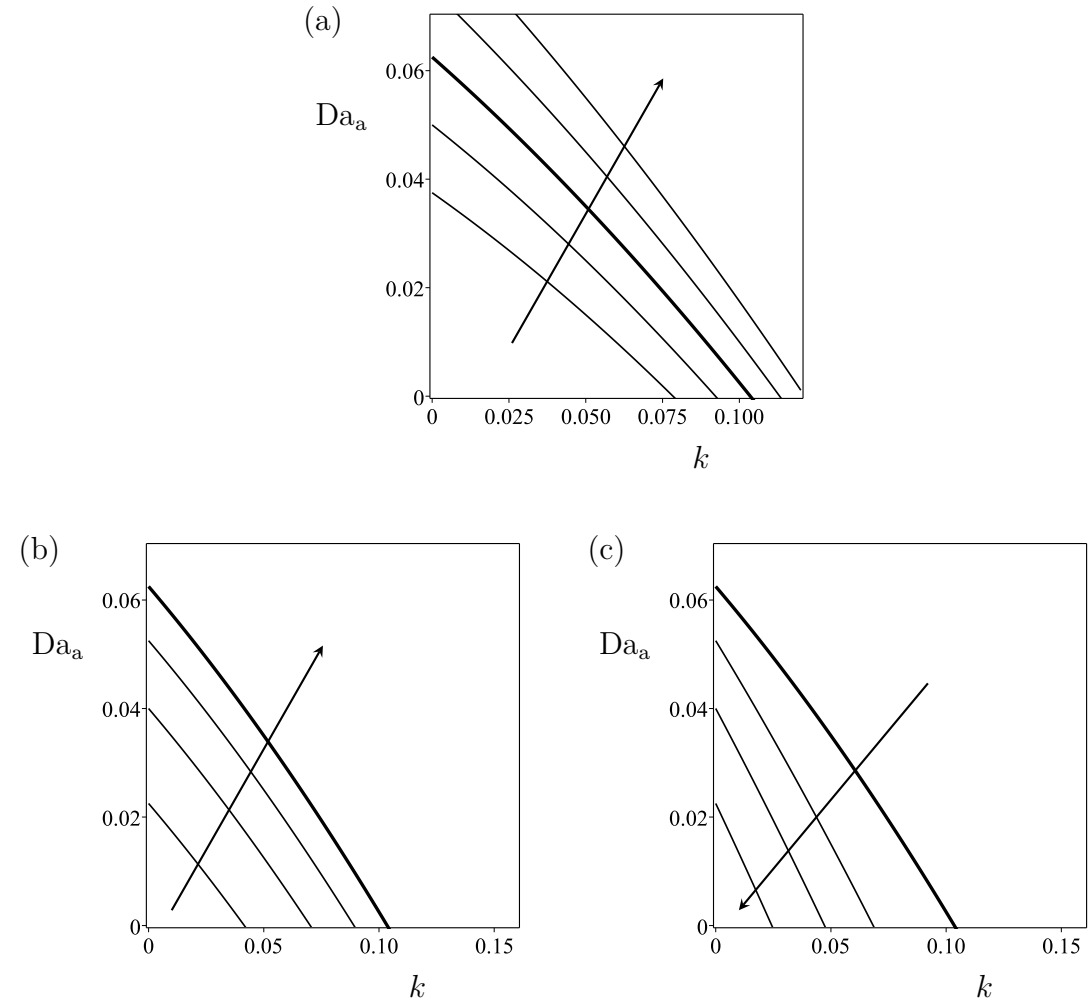

Figure 3.10: Marginal stability curves for the advective Damköhler number $\mathrm{Da_a}$ as a function of the wavenumber k in the infinite-depth limit $d \to \infty$, given by (3.5.6), for (a) $\mathrm{Da_d} = 0.3$, 0.4, 0.5, 0.6, 0.7, (b) $K = 0.1$, 0.2, 0.3, 0.5, (c) $K = 0.5$, 0.7, 0.8, 0.9. All other parameter values are given by Table 3.2 with $\theta = 1/(1-K)$, and where appropriate $\mathrm{Da_d} = 0.5$, $K = 0.5$. The thick solid curve corresponds to the reference case shown in Figure 3.9(a). In each plot, the arrow denotes the direction of increasing value of the variable.

and the range of unstable wavenumbers decrease monotonically, and the unstable region disappears completely in the limit $K \to 1$. For $0.5 \leq K < 1$, both $\mathrm{Da}_{\mathrm{a,crit}}$ given by equation (3.5.7), and $k_{\max}$ given by (3.5.8) decrease monotonically with K.

Figure 3.11 shows how the Da_{d} marginal curve changes as the parameters Da_{d} and K are varied.

Figure 3.11(a) shows how the Da_{d} marginal curve changes as Da_{a} is varied both above and below the reference value of $\mathrm{Da}_{\mathrm{a}} = 0.05$. Increasing Da_{a} stabilises the system since the minimum value of Da_{d} required to trigger instability increases as Da_{d} increases. Varying Da_{a} does not qualitatively change the Da_{d} marginal curve. In particular, only $\mathrm{Da}_{\mathrm{d,crit}}$ given by (3.5.10) varies with Da_{a}; from (3.5.11), $k_{\max}$ given by (3.5.11) is independent of the value of Da_{a}.

Figure 3.11(b) shows how the Da_{d} marginal curve changes as K is varied for $K \leq 0.5$. As K is increased up to $K = 0.5$, both $\mathrm{Da}_{\mathrm{d,crit}}$ and $k_{\max}$ decrease. From equation (3.5.10), $\mathrm{Da}_{\mathrm{d,crit}}$ is minimised at $K = 0.5$, and takes the minimum value $\mathrm{Da}_{\mathrm{d,crit}}^{\min} = \mathrm{Da}_{\mathrm{a}}$ whereas $k_{\max}$ given by (3.5.11) is a monotonically decreasing function of K for $0 < K < 1$, and so as K increases, the range of unstable wavenumbers decreases.

Figure 3.11(c) shows how the Da_{d} marginal curve changes as K is varied for $K \geq 0.5$. As stated for the $K \leq 0.5$ case, $\mathrm{Da}_{\mathrm{d,crit}}$ is minimised at $K = 0.5$, and so increasing K above this value causes $\mathrm{Da}_{\mathrm{d,crit}}$ to increase, and causes $k_{\max}$ to decrease monotonically. In the limit $K \to 1$, we have $\mathrm{Da}_{\mathrm{d,crit}} \to \infty$ and $k_{\max} \to 0$, illustrating that the system is stable for $K > 1$, i.e., that surfactant solutions are always stable.

Figure 3.12 shows how the K marginal curve changes as the ratio $\delta = \mathrm{Da}_{\mathrm{d}}/\mathrm{Da}_{\mathrm{a}}$ is varied, namely as δ is increased, both the range of K that lead to instability and the range of unstable wavenumbers increase, i.e., both the separation between the values of $K_{\mathrm{crit}}^{\pm}$ and the value of $k_{\max}$ increases. As $\delta \to \infty$, $K_{\mathrm{crit}}^{\pm} \to 1/2 \pm 1/2$, signifying that all values of $0 \leq K \leq 1$ will lead to instability, and the range of unstable wavenumber tends to a finite and non-zero limit, namely $k_{\max} \to 0.5$.

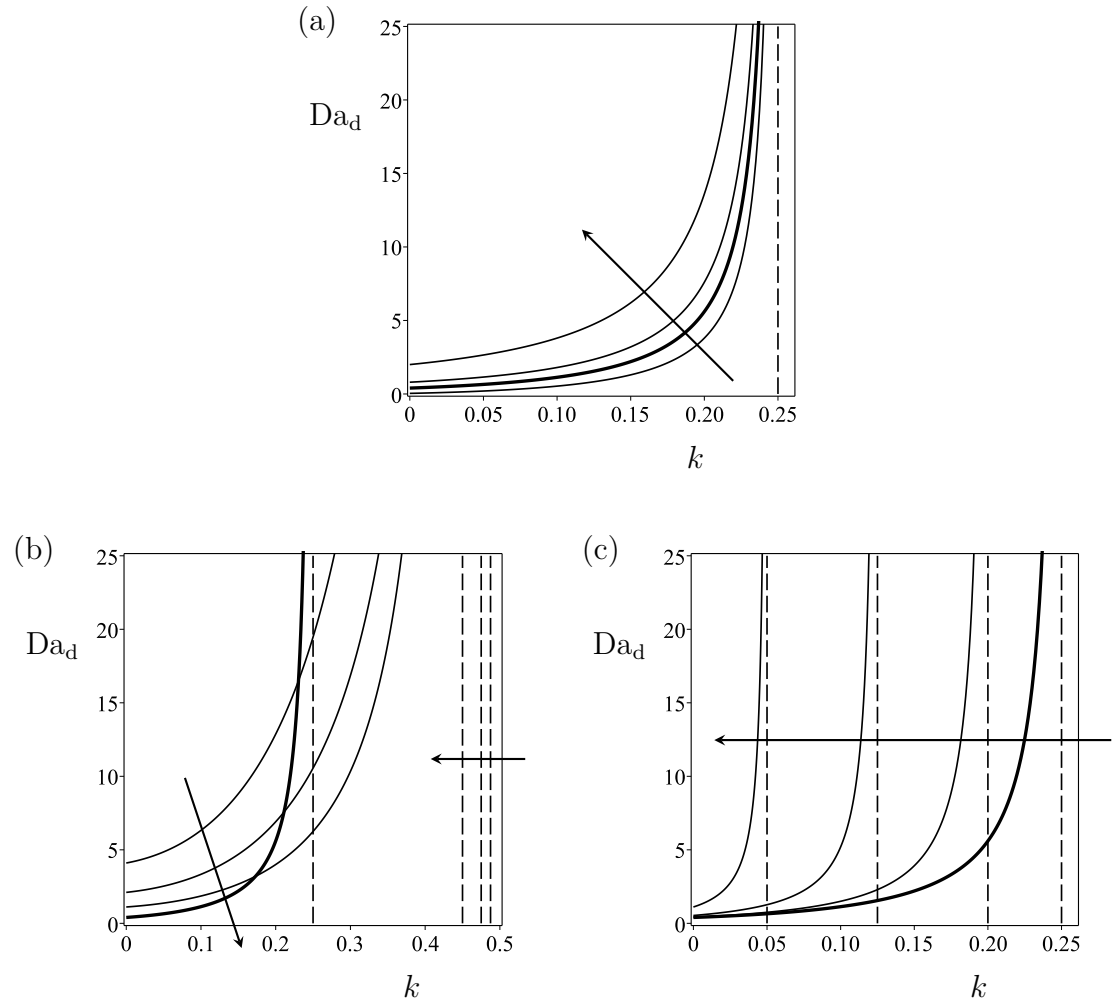

Figure 3.11: Marginal stability curves for the diffusive Damköhler number $\mathrm{Da_d}$ as a function of the wavenumber k in the infinite-depth limit $d \to \infty$, given by (3.5.9), for (a) $\mathrm{Da_a} = 0.005$, 0.05, 0.1, 0.25, (b) $K = 0.025$, 0.05, 0.1, 0.5, and (c) $K = 0.5$, 0.6, 0.75, 0.9. All other parameter values are given by Table 3.2, with $\theta = 1/(1-K)$, and where appropriate $\mathrm{Da_a} = 0.05$, $K = 0.5$. The thick solid curve corresponds to the reference case shown in Figure 3.9(b). In each plot, the arrow denotes the direction of increasing value of the variable.

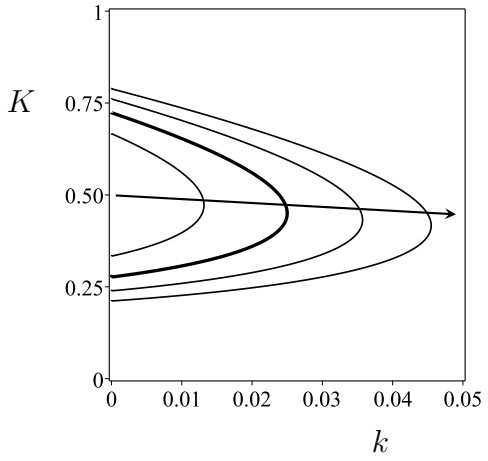

Figure 3.12: Marginal stability curves for the equilibrium rate constant K as a function of the wavenumber k in the limit $d \to \infty$, given as the solutions to (3.5.4) with $\omega = 0$, for $\delta = 9$, 10, 11, 12. All other parameter values are given by Table 3.2, with $\theta = 1/(1-K)$. The thick solid curve corresponds to the reference case shown in Figure 3.9(d). The arrow denotes the direction of increasing value of the variable.

3.5.2 Instability Mechanism

As we have seen thus far in section 3.5, a novel instability is predicted in a layer of anti-surfactant solution provided that certain conditions on the parameters (determined in the marginal stability analysis in section 3.5.1) are satisfied. The question therefore arises of what the mechanism of this instability is. In order for an instability to occur there must be some self-reinforcing physical mechanism, i.e., a positive feedback loop, in which growth causes further growth. Figure 3.13 shows a sketch of the mechanism of the instability. Since the solute is an anti-surfactant, regions of the free surface in which there is a high concentration will also be regions of high surface tension relative to the neighbouring free surface and, similarly, regions in which there is a low concentration will also be regions of low surface tension, relative to the neighbouring free surface. Since surface tension gradients cause fluid to flow along the free surface from regions of low surface tension to regions of high surface tension (i.e., the Marangoni effect), flow converges in the regions of high concentration. As the flow converges, it advects more solute into the already high concentration regions of the free surface which,

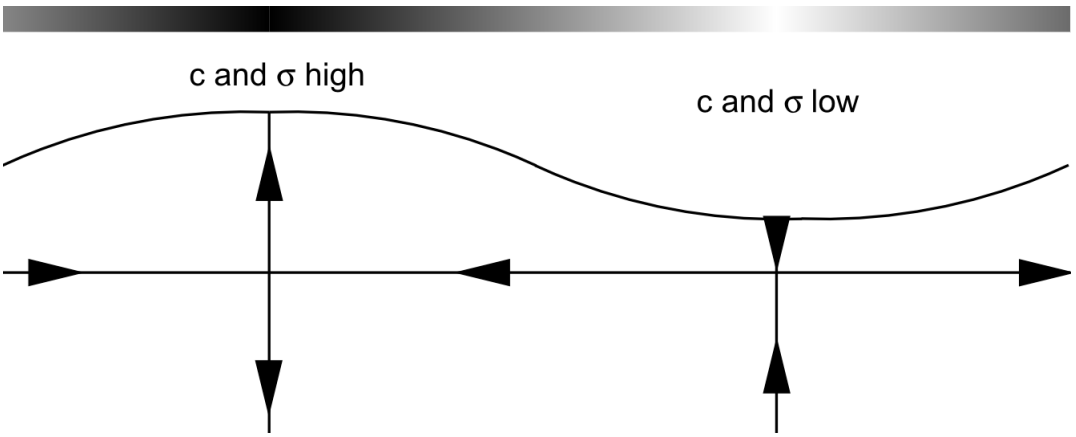

Figure 3.13: sketch of the mechanism of the instability, highlighting the fact that high concentrations correspond to high surface tension.

in turn, increases the surface tension further, and causes more flow convergence. This forms a positive feedback loop in which regions of high surface tension are reinforced to become regions of ever higher surface tension, i.e., to cause instability.

The occurrence of a linear instability naturally raises the question of the final (nonlinear) state towards which the perturbed system evolves. The instability is driven mainly by perturbations to the surface and bulk concentrations and, in fact, occurs even when the free surface is flat. We might speculate, therefore, that the first variables to grow beyond the linear regime will be one or both of the surface and bulk concentrations. The linear theory may possibly break down as the concentrations become large near the free surface because of, for example, packing effects on the free surface, changes in transport rates, or the linear bulk-surface flux no longer being applicable. Ultimately, this instability might manifest itself through precipitation of the solute at or near the free surface, and this would be the experimental hallmark of the instability, in situations where the bulk concentration is below the saturation concentration. In any case, a nonlinear stability calculation would be necessary in order to properly determine the nonlinear state to which the layer is evolving after the linear instability begins.

3.5.3 The Long-Wave Limit of the Infinite-Depth Problem

One particularly important feature of the infinite-depth problem that was made evident through the marginal stability analysis described in section 3.5.1, was that the onset of instability occurs in the long-wave limit $k \to 0$. Motivated by this, and further supported by the small range of k for which instability occurs, we now investigate this long-wave limit, in which the task of analysing the dispersion relation (3.5.4) becomes somewhat easier.

When $k = 0$, the dispersion relation (3.5.4) reduces to the conditions

$$\xi = 0 \qquad \text{or} \qquad \xi^2 + \mathrm{Da_d} K \xi + \mathrm{Da_a} = 0. \tag{3.5.14}$$

The former condition $\xi = 0$ leads simply to $\omega = 0$ and can therefore be discounted. The latter condition has no solutions for which $\Re(\xi) > 0$, i.e., no solutions with $\omega > 0$. Since the naïve approach of simply taking the limit $k \to 0$ does not pick up any of the interesting behaviour that has been seen throughout the previous section, we require a different ansatz. We therefore seek an asymptotic expansion of ξ in the dispersion relation (3.5.4) of the form $\xi \propto k^\alpha$ for some $\alpha > 0$ as $k \to 0$. Substituting this expansion into the dispersion relation (3.5.4) and seeking a consistent balance of terms, it is straightforward to show that $\alpha = 1$. This motivates the expansion

$$\xi = \xi_1 k + \xi_2 k^2 + O(k^3), \tag{3.5.15}$$

where $\Re(\xi_1) > 0$ so that the condition $\Re(\xi) > 0$ holds in the limit $k \to 0$, or equivalently so that $\omega > 0$ in this limit. Substitution of the expansion (3.5.15) into the dispersion relation (3.5.4) yields

$$\xi_1 = \frac{\mathrm{Da_d} K(1-K)}{2\mathrm{Da_a}}, \tag{3.5.16}$$

and

$$\xi_2 = -\frac{\mathrm{Da_d} K(1-K)^2(\mathrm{Da_d}^2 K^2 + \mathrm{Da_a}(\theta - 1))}{4\mathrm{Da_a}^3}. \tag{3.5.17}$$

When $0 < K < 1$ the coefficient ξ_1 is real and positive and so the expansion (3.5.15) remains consistent with the condition $\Re(\xi) > 0$. However, when $K > 1$

the expansion is no longer consistent with this condition. We therefore consider, for now, only the case $0 < K < 1$, corresponding to anti-surfactants. The case $K > 1$, i.e., the surfactant case, will be considered later.

Using (3.5.15), the expansion for the actual growth rate $\omega = \xi^2 - k^2$ (using the definition of ξ) becomes

$$\omega = \left(\frac{{\mathrm{Da_d}}^2 K^2 (1-K)^2}{4{\mathrm{Da_a}}^2} - 1 \right) k^2 - \frac{{\mathrm{Da_d}}^2 K^2 (1-K)^3 ({\mathrm{Da_d}}^2 K^2 + \mathrm{Da_a}(\theta - 1))}{4{\mathrm{Da_a}}^4} k^3 + O(k^4). \quad (3.5.18)$$

The condition $\omega > 0$ for the instability of long waves (i.e., in the limit $k \to 0$) is thus

$$\frac{{\mathrm{Da_d}}^2 K^2 (1-K)^2}{4{\mathrm{Da_a}}^2} > 1 \quad (3.5.19)$$

and, recalling that $0 < K < 1$, equation (3.5.19) reduces to

$$\delta = \frac{\mathrm{Da_d}}{\mathrm{Da_a}} > \frac{2}{K(1-K)}. \quad (3.5.20)$$

The condition (3.5.20) shows that one of the crucial parameters controlling stability is the ratio of the Damköhler numbers, $\delta = \mathrm{Da_d}/\mathrm{Da_a}$. This instability condition also shows that instability becomes more difficult to trigger as $K \to 0$ and as $K \to 1$, mirroring what was seen in the marginal stability plots and, in particular, in Figure 3.9(d).

When $\xi_2 > 0$, we can also obtain an estimate for the typical unstable wavenumber from (3.5.18), namely

$$k_{\mathrm{typ}} \simeq \frac{1 - \xi_1^2}{\xi_1 \xi_2} = \frac{2({\mathrm{Da_d}}^2 K^2 (1-K)^2 - 4{\mathrm{Da_a}}^2){\mathrm{Da_a}}^2}{{\mathrm{Da_d}}^2 K^2 (1-K)^3 ({\mathrm{Da_d}}^2 K^2 + \mathrm{Da_a}(\theta - 1))}. \quad (3.5.21)$$

Numerically, for the values of the parameters given by Table 3.2, k_{typ} is of the order of 0.04, corresponding to dimensional wavelengths of the order $2\pi L^*/k \simeq 5 \times 10^{-8}\,\mathrm{m}$. This is small, but remains significantly larger than the surface layer thickness $\eta^* = 10^{-9}\,\mathrm{m}$, and so the distinction between surface and bulk regions remains consistent.

We may rewrite the instability criterion (3.5.20) in terms of dimensional quantities as

$$\frac{\eta^* \Delta\sigma^*_{\mathrm{solv}}}{\mu^* \mathrm{D}^*_{\mathrm{b}}} > \frac{2}{K}, \quad (3.5.22)$$

where we have defined $\Delta\sigma^*_{\rm solv} = R^*T^*\eta^* c_{\rm i}^*(1-K)$ to be the difference between the equilibrium surface tension in the base state and the equilibrium surface tension of pure solvent. It is informative to rearrange (3.5.22) further, noting that in equilibrium experiments it is bulk quantities rather than surface quantities that would be measured, and to write (3.5.22) as

$$\frac{\Delta\sigma^*_{\rm solv}}{R^*T^*\mu^*{\rm D}^*_{\rm b}}\frac{{\rm d}\sigma^*_{\rm eq}}{{\rm d}c^*_{\rm eq}} > \frac{2(1-K)}{K}, \tag{3.5.23}$$

where in our linear model ${\rm d}\sigma^*_{\rm eq}/{\rm d}c^*_{\rm eq} = \Delta\sigma^*_{\rm solv}c_{\rm i}^*$. The left-hand side of (3.5.23) now consists solely of experimentally measurable quantities, while the right-hand side depends only on K, which in practice must be determined as a fitting parameter. It is worth noting that the magnitudes of the adsorption and desorption rate constants k_1^* and k_2^* do not affect the stability, since they enter (3.5.23) only through their ratio K.

3.5.4 The Limit of Small Damköhler Numbers in the Infinite-Depth Problem

The Damköhler numbers in the reference case for the infinite-depth problem (and for the general finite-depth problem) are not far below unity, and correspond to the upper limit of plausible values for the desorption rate constant k_2^*. Since this rate constant could be several orders of magnitude smaller than its upper value, it is of interest to consider the predictions of the stability analysis for $0 < K < 1$ as the Damköhler numbers become small, in the infinite-depth problem.

To obtain asymptotic results, we consider the limit in which both Damköhler numbers become small, while their ratio remains $O(1)$. Accordingly, we write ${\rm Da_d} = \delta{\rm Da_a}$, and consider the limit ${\rm Da_a} \to 0$ while $\delta = O(1)$. The dispersion relation (3.5.4) then becomes

$$2\xi^3 + 2\delta K{\rm Da_a}\xi^2 + \left[(1-K)(\theta-1)k + 2{\rm Da_a}\right]\xi - \delta K(1-K){\rm Da_a}k = 0. \tag{3.5.24}$$

We first consider a naïve expansion in which all quantities other than ${\rm Da_a}$ remain $O(1)$. Seeking an expansion of the form

$$\xi = \Omega_0 + \Omega_1{\rm Da_a} + O({\rm Da_a}^2), \tag{3.5.25}$$

where $\Re(\Omega_0) > 0$ is the condition that must be satisfied for instability to occur, and taking the limit $\mathrm{Da_a} \to 0$, we obtain the leading order equation

$$2\Omega_0^3 + (1-K)(\theta-1)k\Omega_0 = 0, \tag{3.5.26}$$

and omitting the case $\Omega_0 = 0$ since it does not satisfy the condition $\Re(\Omega_0) > 0$, equation (3.5.26) yields

$$\Omega_0^2 = \frac{(1-K)(1-\theta)}{2}k. \tag{3.5.27}$$

Since $0 < K < 1$, this is consistent with the condition $\Re(\Omega_0) > 0$ if and only if $\theta < 1$, and the corresponding asymptotic expansion for $\omega = \xi^2 - k^2$ is

$$\omega = \frac{(1-K)(1-\theta)}{2}k - k^2 + O(\mathrm{Da_a}). \tag{3.5.28}$$

Figure 3.14(a) shows a plot of the perturbation growth rates ω and illustrates how well the asymptotic result (3.5.28) captures the behaviour of ω as the Damköhler numbers become small. Although for the particular choice of $\delta = 5$ used in Figure 3.14(a), the system remains stable for small k, instability does occur for intermediate wavenumbers $k \simeq (1-K)(1-\theta)/4$, which in this case gives $k \simeq 0.125$.

The naïve expansion given by (3.5.25) is not consistent with the condition $\Re(\xi) > 0$ when $\theta \geq 1$, and as such we must seek alternative expansions to capture the behaviour in this regime. We therefore scale $k = {\mathrm{Da_a}}^{\alpha}\hat{k}$ for some $\alpha > 0$ and, motivated by the long-wave asymptotic result (3.5.18), we scale $\omega = {\mathrm{Da_a}}^{2\alpha}\hat{\omega}$, and therefore also scale $\xi = {\mathrm{Da_a}}^{\alpha}\hat{\xi}$. Substituting these scalings into the dispersion relation (3.5.24), we obtain

$$\begin{aligned} 2{\mathrm{Da_a}}^{3\alpha}\hat{\xi}^3 + 2\delta K{\mathrm{Da_a}}^{2\alpha+1}\hat{\xi}^2 + (1-K)(\theta-1){\mathrm{Da_a}}^{2\alpha}\hat{k}\hat{\xi} \\ + {\mathrm{Da_a}}^{\alpha+1}\left(2\hat{\xi} - \delta K(1-K)\hat{k}\right) = 0. \end{aligned} \tag{3.5.29}$$

Seeking a consistent balance of terms as $\mathrm{Da_a} \to 0$, we find that there are three possibilities for the value of α, namely $\alpha = 0$, $1/2$, and 1. The value $\alpha = 0$ corresponds to the naïve expansion which remains consistent for $\theta < 1$ and yields the asymptotic result (3.5.28). The value $\alpha = 1$ yields the leading order result

$$\hat{\xi}_0 = \frac{\delta K(1-K)\hat{k}}{(1-K)(\theta-1)\hat{k} + 2}, \tag{3.5.30}$$

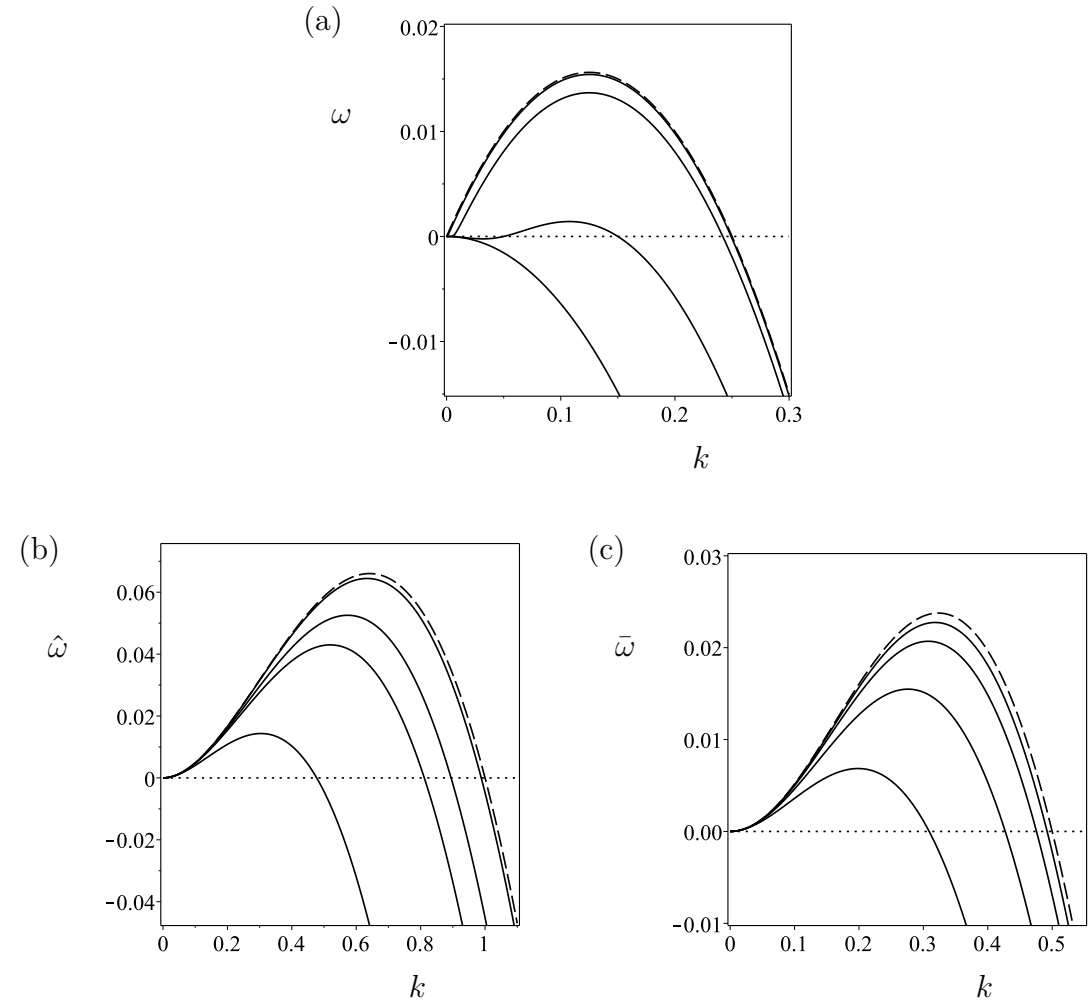

Figure 3.14: Growth rates of perturbations (a) ω, (a) $\hat{\omega}$, (a) $\bar{\omega}$ as a function of the wavenumber k in the infinite-depth regime for $K = 1/2$ and (a) $\theta = 0$, $\delta = 5$, $\mathrm{Da_d} = 1$, 0.1, 0.01, 0.001, (b) $\theta = 2$, $\delta = 10$, and $\mathrm{Da_d} = 0.5$, 0.1, 0.05, 0.005, (c) $\theta = 1$, $\delta = 10$, and $\mathrm{Da_d} = 0.1$, 0.1, 0.001, 0.0001, all shown solid, along with the small Damköhler number asymptotic results given by (a) equation (3.5.28), (b) equation (3.5.31), (c) equation (3.5.35), all shown dashed. The arrow denotes the direction of decreasing $\mathrm{Da_a}$.

which remains finite for $\hat{k}$ as long as $(1-K)(\theta-1) > 0$ and so, since $0 < K < 1$, the expansion with $\alpha = 1$ is consistent only if $\theta > 1$. The corresponding leading order expression for the actual growth rate $\hat{\omega} = \hat{\xi}^2 - \hat{k}^2$ is

$$\hat{\omega} = \left[\frac{\delta^2 K^2 (1-K)^2}{\left[(1-K)(\theta-1)\hat{k} + 2\right]^2} - 1 \right] \hat{k}^2. \tag{3.5.31}$$

Figure 3.14(b) shows a plot of the perturbation growth rates $\hat{\omega}$ and illustrates how well the asymptotic result (3.5.31) captures the behaviour of $\hat{\omega}$ as the Damköhler numbers become small.

When $\theta > 1$, equation (3.5.31) successfully captures the behaviour of $\hat{\omega}$ and, in particular, for small $\hat{k}$ it predicts instability precisely when (3.5.20) holds, and as $\hat{k} \to \infty$ the growth rate decays as $\hat{\omega} \sim -\hat{k}^2$, which is the pure diffusive mode of decay.

When $\theta = 1$, equation (3.5.31) fails to capture the decay terms which determine the position of the maximum of $\hat{\omega}$, and it is necessary to seek a different scaling of k and ξ. To this end, the third possible value of the exponent α is $\alpha = 1/2$; we use the scaling

$$k = \mathrm{Da_a}^{1/2} \bar{k}, \qquad \omega = \mathrm{Da_a} \bar{\omega}, \qquad \xi = \mathrm{Da_a}^{1/2} \bar{\xi}, \tag{3.5.32}$$

and seek the expansion

$$\bar{\xi} = \bar{\xi}_0 + \bar{\xi}_1 \mathrm{Da_a}^{1/2} + O(\mathrm{Da_a}). \tag{3.5.33}$$

Substituting this expansion into the dispersion relation (3.5.4), we obtain the depressed cubic equation

$$\bar{\xi}^3 + \bar{\xi} - \frac{1}{2}\delta K (1-K) \bar{k} = 0. \tag{3.5.34}$$

The real root of equation (3.5.34) may be found explicitly using Cardano's method, and the corresponding expression for the actual growth rate $\bar{\omega}$ is

$$\bar{\omega} = \left[\left(\frac{q}{2} + \sqrt{\frac{q^2}{4} + \frac{1}{27}} \right)^{1/3} + \left(\frac{q}{2} - \sqrt{\frac{q^2}{4} + \frac{1}{27}} \right)^{1/3} \right]^2 - \bar{k}^2 + O(\mathrm{Da_a}^{1/2}), \tag{3.5.35}$$

where we have defined $q = \delta K (1-K) \bar{k}/2$ to be the coefficient of $\bar{\xi}^0$ in equation (3.5.34).

Figure 3.14(c) shows a plot of the perturbation growth rates $\bar{\omega}$ and illustrates how well the asymptotic result (3.5.31) captures the behaviour of $\bar{\omega}$ as the Damköhler numbers become small.

In summary, we have shown that, while the stability of the system depends on the Damköhler numbers, in the limit in which both Damköhler numbers become small, while their ratio remains of order unity, the stability of the system depends instead on the parameter θ. For $\theta < 1$, so that the surface tension depends principally on the surface concentration, instabilities occur at wavenumbers of order unity, corresponding to preferred wavelengths of roughly an order of magnitude greater than the thickness of the surface layer, and can do so even when the system remains stable as $k \to 0$. In contrast, when $\theta \geq 1$, the preferred wavenumbers k decrease along with the Damköhler numbers; thus the long-wave stability criterion (3.5.20) continues to capture the behaviour of the system, and the preferred wavelengths of instabilities become much larger than the thickness of the surface layer.

3.5.5 The Infinite-Depth Limit, $d \to \infty$

In all of the previous parts of this section 3.5 we obtained results for the infinite-depth problem by *a priori* postulating an infinitely deep layer. Alternatively, we may seek asymptotic solutions to the general finite-depth problem in the infinite-depth limit $d \to \infty$. Solving the general finite-depth dispersion relation (3.3.29) numerically, we typically find that if $0 < K < 1$ then instability is possible for a range of small k values, whereas if $K > 1$ then no instability occurs. This is also typical of the infinite-depth problem. By postulating an infinitely deep layer, we obtained a simplified dispersion relation (3.5.4) and saw that the small-k expansion of ξ (and therefore of ω) is consistent only when $0 < K < 1$; we therefore focussed only on the anti-surfactant case. In this section, we also consider the surfactant case $K > 1$, in the limit as the depth of the layer becomes infinite, i.e., we take the limit $d \to \infty$ in equation (3.3.29).

The form of the exponential terms in equation (3.3.29) makes it natural to consider four distinguished limits, depending on the combination of k, kd, ξ, and

ξd that is taken to remain finite and non-zero in this limit.

Case 1: $\Re(\xi)$ and k remain finite and non-zero as $d \to \infty$

This is the case implicitly considered in all of the previous parts of section 3.5 by an *a priori* postulation of an infinitely deep body of fluid. In this limit we may approximate all of the hyperbolic terms in (3.3.29) by exponential terms. We must consider the cases $\Re(\xi) \lesseqgtr 0$ separately in order to discard the correct exponential terms; combining the results we find that the dispersion relation (3.3.29) reduces to

$$2\xi^3\mathrm{sgn}(\xi) + 2\mathrm{Da_d}K\xi^2 + [(1-K)(\theta-1)k + 2\mathrm{Da_a}]\,\mathrm{sgn}(\xi)\xi - \mathrm{Da_a}K(1-K)k + O\left(\mathrm{e}^{-2kd}, \mathrm{e}^{-2\mathrm{sgn}(\xi)\xi d}\right) = 0, \tag{3.5.36}$$

where $\mathrm{sgn}(\xi) = \pm 1$ if $\Re(\xi) \lesseqgtr 0$.

If $\Re(\xi) > 0$ then, as we have seen in section 3.5.3, only the regime $0 < K < 1$ permits consistent solutions for long waves. Alternatively, if $\Re(\xi) < 0$ then by defining $\xi' = -\xi$ we again find that there are consistent solutions for long waves only when $0 < K < 1$. We conclude that when $K > 1$, in order to find consistent solutions across all k we must consider a different distinguished limit.

Case 2: $\Re(\xi)$ and kd remain finite and non-zero as $d \to \infty$

We now consider the possibility that ξ remains of order unity (maintaining the possibility that $\omega = O(1)$) as $d \to \infty$, but that this occurs only for very long waves. We thus define $\kappa = kd$ and set $\kappa = O(1)$ as $d \to \infty$. Again considering the cases $\Re(\xi) \lesseqgtr 0$ separately we reduce the dispersion relation (3.3.29) to

$$\left(\xi^3 + \xi^2\mathrm{sgn}(\xi)\mathrm{Da_d}K + \mathrm{Da_a}\xi\right)(\cosh(\kappa)\sinh(\kappa) - \kappa) + O\left(\frac{1}{d}, \mathrm{e}^{-2\mathrm{sgn}(\xi)\xi d}\right) = 0. \tag{3.5.37}$$

Since we are not interested in the root corresponding to $\xi = 0$, and the factor $\cosh(\kappa)\sinh(\kappa) - \kappa)$ is strictly positive for $\kappa > 0$, we conclude that ξ must satisfy the quadratic equation

$$\xi^2 + \xi\mathrm{sgn}(\xi)\mathrm{Da_d}K + \mathrm{Da_a} = 0. \tag{3.5.38}$$

Again considering separately the cases $\mathrm{sgn}(\xi) = \pm 1$, we conclude that there are no consistent solutions in this distinguished limit for any positive value of K. In the case $\mathrm{sgn}(\xi) = 1$, equation (3.5.38) is a quadratic equation with all positive coefficients and therefore all roots have negative real part, inconsistent with the assumption that $\mathrm{sgn}(\xi) = 1$. In the case $\mathrm{sgn}(\xi) = -1$, all roots of equation (3.5.38) have positive real part, inconsistent with the assumption that $\mathrm{sgn}(\xi) = -1$.

Case 3: ξd and k remain finite and non-zero as $d \to \infty$

We now define $\Xi = \xi d$, where $\Xi = O(1)$. In this case the dispersion relation (3.3.29) reduces to

$$\begin{aligned}&\left[kd^2(1-K)(\theta-1) + 2\mathrm{Da_a}d^2 + 2\Xi^2\right]\Xi\sinh(\Xi)\\&+ \mathrm{Da_d}Kd\left[(K-1)kd^2 + 2\Xi^2\right]\cosh(\Xi) + O\left(\mathrm{e}^{-2kd}\right) = 0.\end{aligned} \tag{3.5.39}$$

As $d \to \infty$ the dominant terms are those in d^3, and so the dispersion relation reduces further to $\cosh(\Xi) = 0$, with solutions

$$\Xi = \left(n + \frac{1}{2}\right)\pi \qquad \text{for} \quad n \in \mathbb{Z}. \tag{3.5.40}$$

The solution for the actual growth rate is then

$$\omega = -k^2 - \left(n + \frac{1}{2}\right)^2 \frac{\pi^2}{d^2}, \tag{3.5.41}$$

which describes stable modes, independent of K and decaying a little faster than the rate $\omega = -k^2$ set by pure diffusion of a vertically constant perturbation. Crucially, when we take the limit $d \to \infty$ all of these modes collapse on to the pure diffusive mode. The loss of these modes represents a degeneracy in the problem, which is important only if no other modes exist.

Case 4: ξd and kd remain finite and non-zero as $d \to \infty$

In this final case, we set $\Xi = \xi d$ and $\kappa = kd$ as before, and the dispersion relation (3.3.29) reduces to

$$\mathrm{Da_d} K(K-1)\kappa \left[\sinh^2(\kappa) - \kappa^2\right] \cosh(\Xi) + 2\mathrm{Da_a} \left[\cosh(\kappa)\sinh(\kappa) - \kappa\right] \Xi \sinh(\Xi) + O\left(\frac{1}{d}\right) = 0. \quad (3.5.42)$$

Rearranging then yields

$$\Xi \tanh(\Xi) \sim \frac{\mathrm{Da_d} K(1-K)}{2\mathrm{Da_a}} \frac{\kappa\left(\sinh^2(\kappa) - \kappa^2\right)}{\cosh(\kappa)\sinh(\kappa) - \kappa}. \quad (3.5.43)$$

The function of κ on the right-hand side is strictly positive for $\kappa > 0$, so the sign of the left-hand side is identical to the sign of $1 - K$. Hence, it can be shown that for $0 < K < 1$ we obtain modes for which $\Xi \in \mathbb{R}_+$ and thus $\omega > -k^2$: these modes persist in the limit $d \to \infty$, although they occur at wavelengths that scale with d, while the growth rates scale with $1/d^2$. For $K > 1$, we must seek imaginary solutions for Ξ. We may write $\Xi = i\chi$ so that the left-hand side becomes $-\chi \tan(\chi)$, and so we obtain a spectrum of modes with $\omega \sim -\kappa^2/d^2 - \chi^2/d^2 < -k^2$.

The overall conclusion from this asymptotic analysis is that although the finite-depth stability problem is well posed for both surfactant and anti-surfactant solutions, the limit $d \to \infty$ is degenerate. Only a particular family of modes survives in this limit, and this family is available only for anti-surfactants, $0 < K < 1$, for which it provides the dominant mode.

The modes that degenerate in the limit $d \to \infty$ do so because their spatial scale is naturally set by the depth of the layer, and becomes ill-defined in this limit. In contrast, the bulk concentration field for the non-degenerating modes has a boundary layer structure and the depth of the layer becomes irrelevant. Since, from equation (3.3.5), the thickness of any concentration boundary layer must scale as $\xi = \sqrt{\omega + k^2}$, boundary layers can occur only when $\Re(\omega) > -k^2$, i.e., when the concentration perturbation is not decaying as rapidly as it would by pure diffusion. To resist this diffusive decay a destabilizing mechanism must

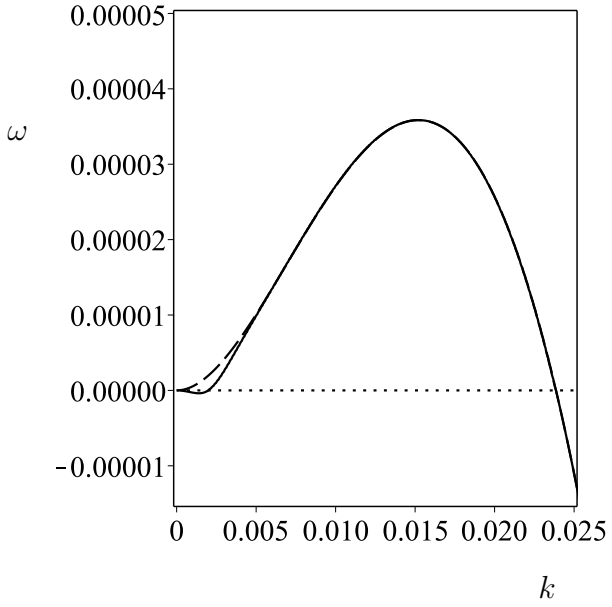

Figure 3.15: Growth rates of perturbations ω as a function of the wavenumber k in the infinite-depth regime (dash), and the general finite-depth regime with dimensionless layer depth $d = 10^3$ (solid), and with $K = 0.5$, $\theta = 1/(1-K) = 2$, and all other parameter values given by Table 3.2.

act near or at the free surface, and thus perturbations with this structure are available only for anti-surfactants.

3.6 General Finite-Depth Case

We now investigate the effects of finite depth on the stability and instability that has been analysed in the previous sections. The general-finite depth dispersion relation (3.3.29) is not analytically tractable, but may be readily solved numerically. For the remainder of this chapter we choose the velocity scale $U^* = U^*_{\mathrm{Ma}}$ and $L^* = L^*_{\mathrm{P_s}}$ so that $\mathrm{Ma} = \mathrm{P_s} = \mathrm{P_b} = 1$, unless otherwise stated.

Figure 3.15 shows a comparison between the growth rate of the unstable mode in the infinite-depth regime (dashed), and the finite-depth regime (solid) with a dimensionless layer depth $d = 10^3$, corresponding to a layer of dimensional depth $d^* = O(10^{-6}) - O(10^{-5})\,\mathrm{m}$. In particular, it shows that the infinite-depth regime is a good approximation to the more general finite-depth regime, even

for dimensional layer depths that might not intuitively be considered particularly large. The approximation offered by the infinite-depth regime performs well for any wavenumber k, with the exception of near $k = 0$, where the qualitative behaviour predicted by the infinite-depth regime is different from the qualitative behaviour seen in the finite-depth problem.

For small enough wavenumbers k, a layer of finite depth may also behave in an oscillatory manner, i.e., the growth rate ω will have a non-zero imaginary part. However, this oscillatory behaviour occurs only for wavenumbers that satisfy $kd \ll 1$, and is an inherently long-wave phenomenon. We therefore delay detailed discussion of the oscillatory behaviour until we have constructed the appropriate *thin film* approximation of our model, which we do in Chapter 4. In addition, a brief discussion of the oscillatory behaviour for a layer of general finite depth is given in Appendix A.

3.6.1 Marginal Stability Analysis: Effect of Finite Depth

In order to investigate the effects of finite depth on the stability of the fluid layer, we perform a marginal stability analysis similar to that in section 3.5.1, but with finite values of d. Assuming that the principle of exchange of stabilities holds, i.e., that $\omega = 0$ in the marginal state, we find that capillarity has no effect on the onset of instability. In other words, the capillary number will not appear in any calculations or results in this section, since it always appear multiplied by ω in the dispersion relation (3.3.29).

Figures 3.16–3.18 show marginal stability curves for several values of the dimensionless layer depth d (thin solid and thin dashed lines), along with the marginal curve in the infinite-depth case (thick solid), the latter of which corresponds exactly to the curves given in Figure 3.9.

Figures 3.16–3.18 show that for any finite value of d *above* a critical value, which we denote by d_{crit}, the maximum values of the corresponding marginal stability curves occur for $k \neq 0$. For $d \leq d_{\text{crit}}$, the maximum values occur at $k = 0$: the dashed curve in each of the plots given in Figures 3.16–3.18 corresponds to $d = d_{\text{crit}}$. The dotted curve tracks the maxima of each of the thin solid curves.

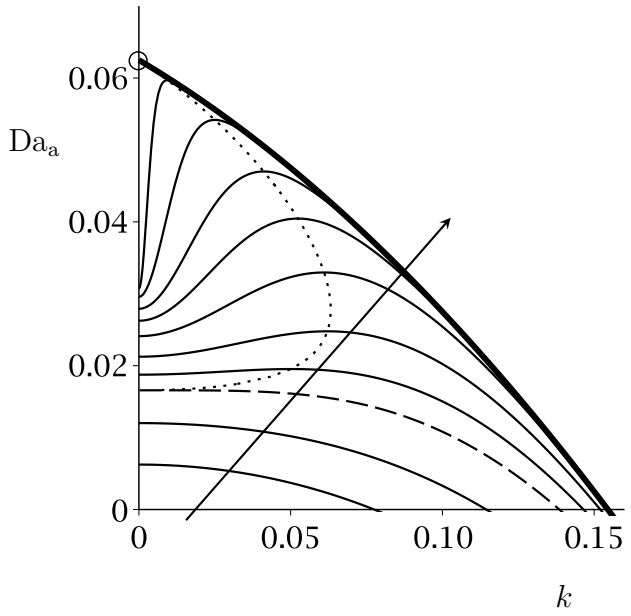

Figure 3.16: Marginal stability curves for the advective Damköhler number $\mathrm{Da_a}$ as a function of the wavenumber k as d is increased. Thin solid lines correspond to finite-values of d, the dashed line corresponds to $d = d_{\mathrm{crit}} \simeq 17$, the thick solid line corresponds to the singular limit $d \to \infty$, and the dotted line follows the maximum of the marginal stability curves. For each curve, $K = 0.5$, $\theta = 1$ and all other parameter values are given by Table 3.2. The arrow denotes the direction of increasing d, for $d = 10$, 13, 17.04 (dashed line), 20, 25, 30, 50, 75, 150, 500.

Finally, the thick solid curve corresponds to the infinite-depth limit $d \to \infty$.

As the asymptotic analysis presented in section 3.5.5 suggests, the limit $d \to \infty$ is degenerate, and does not behave as might naïvely be expected. The same is true in Figures 3.16–3.18 in which the limit $d \to \infty$ is singular. The value of each finite-d marginal curve (the thin solid curves) at $k = 0$ is monotonically increasing with d, and appears to converge to some limit as d becomes large. However, in the limit $d \to \infty$, the small k behaviour suddenly changes and the value at $k = 0$ in this limit is different from what the limiting value appears to be for large but finite values of d. The limit $d \to \infty$ is therefore singular, and this behaviour may be a manifestation of the degeneracy that is inherent in the infinite-depth limit.

Figure 3.16 shows the effect of finite depth on the marginal stability curve for

the advective Damköhler number $\mathrm{Da_a}$. For any finite d, the small k behaviour of $\mathrm{Da_a}$ is

$$\mathrm{Da_a} \sim \frac{1}{4}\mathrm{Da_d Ma}K(1-K) - \frac{\mathrm{Da_d}K}{d}. \tag{3.6.1}$$

Taking the limit $d \to \infty$ in (3.6.1), we see that

$$\mathrm{Da_a} \to \frac{1}{4}\mathrm{Da_d Ma}K(1-K), \tag{3.6.2}$$

and comparing this to the small k limit of $\mathrm{Da_a}$ obtained in the infinite-depth case given by (3.5.7), we see the singular behaviour of the large d limit. As d is increased, the system becomes more unstable, but the region of instability is limited by that of the infinite-depth case, i.e., the region cannot extend beyond the thick solid curve, as shown in Figure 3.9(a).

The dashed curve, corresponding to the value $d = d_{\mathrm{crit}}$ splits the curves below with $d < d_{\mathrm{crit}}$, which are qualitatively similar to the infinite-depth case, from those above with $d > d_{\mathrm{crit}}$, but excluding the case $d \to \infty$, in which the maxima occur for a non-zero value of k. The value of d_{crit} may be determined in the long-wave limit $k \to 0$ as the value of d which satisfies

$$\left.\frac{\partial^2 \mathrm{Da_a}}{\partial k^2}\right|_{k=0} = 0, \tag{3.6.3}$$

and while d_{crit} may easily be determined analytically, we omit the expression for brevity; in the case shown in Figure 3.16, this value is $d_{\mathrm{crit}} \simeq 17$. This corresponds to a dimensional layer depth of $d = O(10^{-8}) - -O(10^{-7})$m.

Figure 3.17 shows the effect of finite depth on the marginal stability curve for the diffusive Damköhler number $\mathrm{Da_a}$, and the description of Figure 3.16 also applies here. For any finite d, the long-wave $k \to 0$ behaviour of $\mathrm{Da_d}$ is

$$\mathrm{Da_d} \sim \frac{4\mathrm{Da_a}d}{K\left(\mathrm{Ma}d(1-K) - 4\right)}. \tag{3.6.4}$$

In the case shown in Figure 3.17, $d_{\mathrm{crit}} \simeq 12.1$.

Figure 3.18 shows the effect of finite depth on the marginal stability curve for the equilibrium rate constant K. The description of Figure 3.18 is qualitatively different from that of Figures 3.16 and 3.17. For any finite d, there is a "bubble" of instability that, depending on the particular value of each other parameter, may

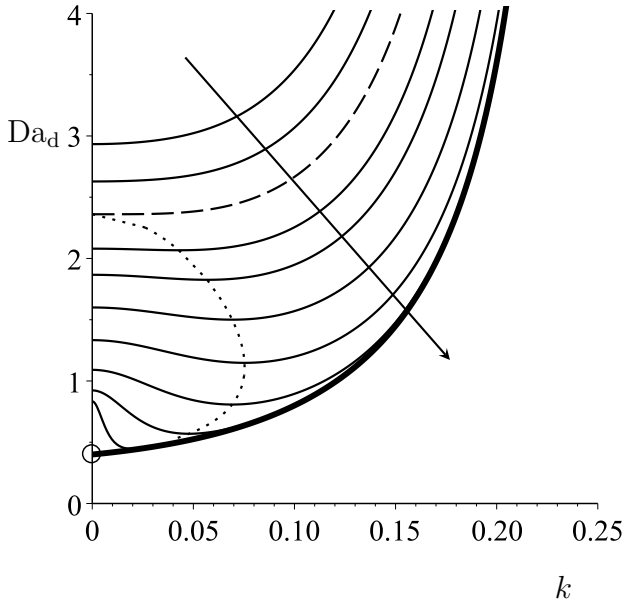

Figure 3.17: Marginal stability curves for the diffusive Damköhler number $\mathrm{Da_d}$ as a function of the wavenumber k as d is increased. Thin solid lines correspond to finite-values of d, the dashed line corresponds to $d = d_{\mathrm{crit}} \simeq 12.1$, the thick solid line corresponds to the singular limit $d \to \infty$, and the dotted line follows the maximum of the marginal curves. For each curve, $K = 0.5$, $\theta = 1$ and all other parameter values are given by Table 3.2. The arrow denotes the direction of increasing d, for $d = 10$, 13, 17.04 (dashed line), 20, 25, 30, 50, 75, 150, 500.

either be connected to the K-axis, or be completely detached from it. Choosing d such that there is a maximum for non-zero k in the $\mathrm{Da_a}$ marginal curve (or equivalently, a minimum for non-zero k in the $\mathrm{Da_d}$ marginal curve), there are values of $\mathrm{Da_a}$ such that perturbations with a small enough wavenumber k are stable, while a range of non-zero k is unstable. For example, choosing d such that the $\mathrm{Da_a}$ marginal curve is given by the top-most thin solid curve in Figure 3.16, for $\mathrm{Da_a} = 0.04$ the K marginal curve is a "detached bubble", such as the thin solid curves in Figure 3.18. On the other hand, if $\mathrm{Da_a} = 0.02$, then the K marginal is a "bubble" that touches the K-axis, such as the thick solid curve in Figure 3.18.

For any finite d, there will always be a maximum (or minimum) in each of the marginal curves that occurs at non-zero k. In particular, the maximum

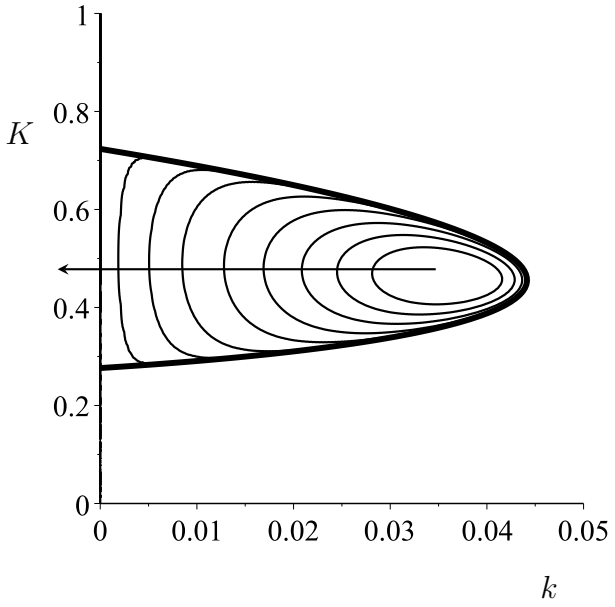

Figure 3.18: Marginal stability curves for the equilibrium rate constant K as a function of the wavenumber k as d is increased. Thin solid lines correspond to finite-values of d, and the thick solid line corresponds to the singular limit $d \to \infty$. For each curve, $\theta = 1$ and all other parameter values are given by Table 3.2. The arrow denotes the direction of increasing d, for $d = 15$, 20, 25, 30, 50, 75, 150, 500.

(minimum) will always occur at $k = O(1/d)$, as this is the magnitude of the wavenumber for which the infinite-depth regime cannot approximate the finite-depth regime particularly well. In the limit $d \to \infty$, the maximum (minimum) squeezes onto the vertical axis, and therefore occurs at $k = 0$. As mentioned previously, this singular behaviour may be a manifestation of the degeneracy present in the infinite-depth regime.

3.6.2 The Long-Wave Limit of the Finite-Depth Problem

For any finite value of the layer depth d the behaviour of the growth rate ω near $k = 0$ is different for the general finite-depth regime and the infinite-depth regime. To determine exactly what differences there are between these two regimes, we investigate the long-wave limit of the general finite-depth problem, and compare the behaviour that is obtained in this limit with that obtained in the corresponding limit of the infinite-depth regime, as given in section 3.5.

When $k = 0$, the dispersion relation (3.3.29) reduces to either

$$\omega = 0 \tag{3.6.5}$$

or

$$\frac{K\mathrm{Da_d}\sqrt{\omega}}{(\mathrm{Da_a} + \omega)} \cosh(\sqrt{\omega}d) + \sinh(\sqrt{\omega}d) = 0, \tag{3.6.6}$$

the latter of which has no solutions for which $\omega > 0$, but does have the solution $\omega = 0$ which we expect to be the value of the possibly unstable modes at $k = 0$. In the limit of infinite depth $d \to \infty$, equation (3.6.6) reduces to the second equation in (3.5.14) (with $\xi = \sqrt{\omega}$, and as long as $\omega = O(1)$), as expected.

Equation (3.6.6) has infinitely many solutions for which $\omega \leq 0$, corresponding to the infinite series of diffusive modes discussed in section 3.4.3, but modified by the layer depth, and by the bulk–surface flux, though it is not possible to obtain these solutions analytically.

We seek a naïve asymptotic expansion for ω of the form

$$\omega = \omega_2 k^2 + \omega_4 k^4 + O(k^5). \tag{3.6.7}$$

Substituting this ansatz into equation (3.6.6) and expanding for small k, we obtain two solutions for the leading order behaviour of ω, with one solution corresponding to the dominant mode, and the other to the possibly unstable sub-dominant mode.

As $k \to 0$, the dominant mode satisfies

$$\omega = \frac{d\mathrm{Da_a} + K\mathrm{Da_d}\,(1 - d\,(1 - K))}{d\mathrm{Da_a} + K\mathrm{Da_d}} k^2 + O(k^4), \tag{3.6.8}$$

and the sub-dominant mode satisfies

$$\omega = \frac{1}{12}\left(\frac{1}{\mathrm{Ca}} + 1 - K\right) \frac{4d\mathrm{Da_a} + K\mathrm{Da_d}\,(4 - d\,(1 - K))}{d\mathrm{Da_a} + K\mathrm{Da_d}\,(1 - d\,(1 - K))} k^4. \tag{3.6.9}$$

Figure 3.19 shows a comparison between the exact growth rates, given as solutions to (3.3.29), and the small k asymptotic approximation to the dominant and sub-dominant modes, given by (3.6.8) and (3.6.9), respectively.

From the leading order behaviour of the two modes that can be unstable, given in equations (3.6.8) and (3.6.9), it is trivial to determine when each of the

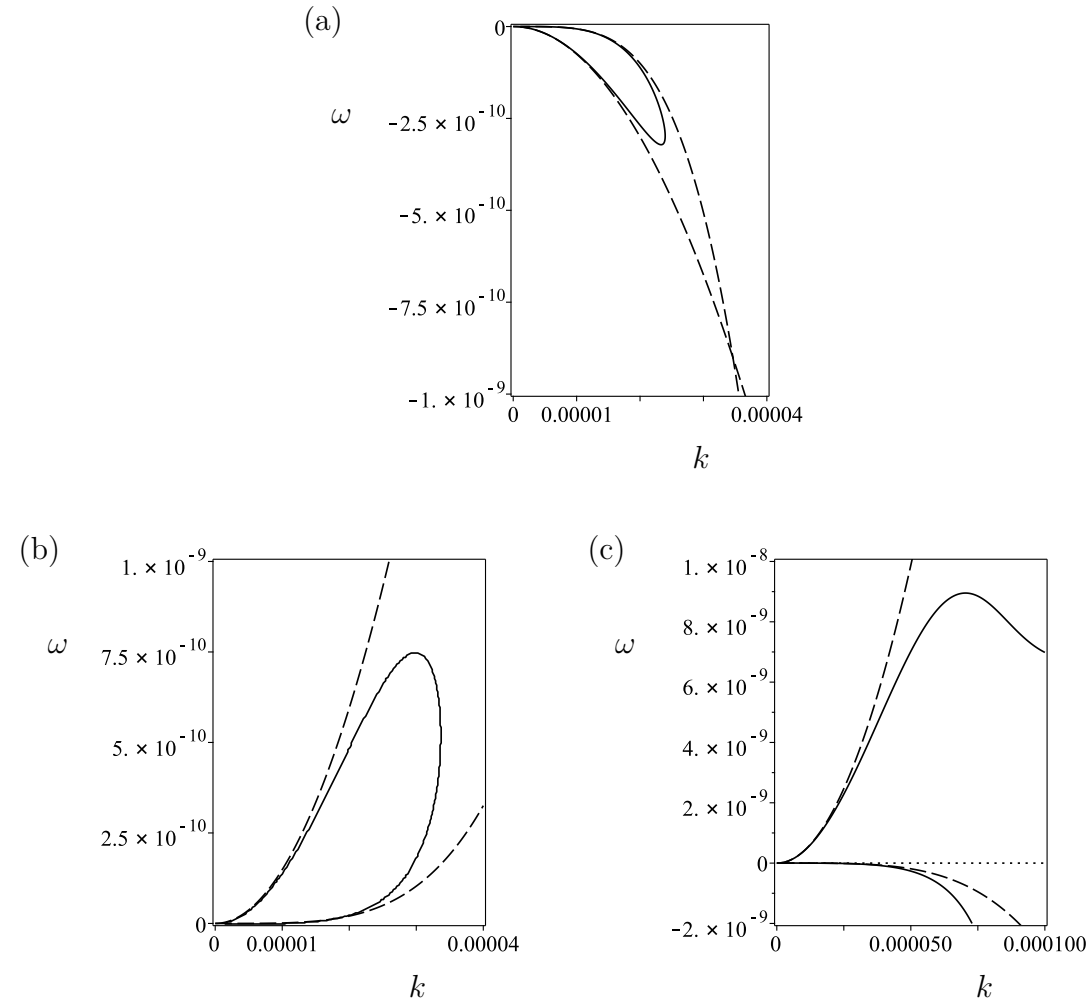

Figure 3.19: Comparison between the exact growth rates ω (solid) and the small k asymptotic approximation to the dominant and sub-dominant modes (dashed) in the case where (a) $\delta = 1 < \delta_{\text{crit}}$ so that both modes are stable, (b) $\delta_{\text{crit}} < \delta = 10 < \delta^*$, so that both modes are unstable, (c) $\delta = 20 > \delta^*$, so that only the dominant mode is stable. All other parameters are given in Table 3.2, with $d = 1000$, $K = 0.5$, $\theta = 1/(1-K) = 2$.

modes will become unstable upon varying each of the parameters. In particular, the value of the ratio $\delta = \mathrm{Da_d}/\mathrm{Da_a}$ required for instability is

$$\delta_{\mathrm{crit}} = \frac{d}{K\left(d(1-K)-1\right)} \tag{3.6.10}$$

for the dominant mode, and

$$\delta^* = \frac{4d}{K\left(d(1-K)-4\right)} \tag{3.6.11}$$

for the sub-dominant mode. For the parameter values given in Table 3.2, and for $d = 1000$, these critical values are $\delta_{\mathrm{crit}} \simeq 4.01$ ($\delta_{\mathrm{crit}} = 4$ in the limit $d \to \infty$), and $\delta^* \simeq 16.13$ ($= 16$ in the limit $d \to \infty$).

For $\delta < \delta_{\mathrm{crit}}$ the system is stable for small k, i.e., both modes are negative. For $\delta_{\mathrm{crit}} < \delta < \delta^*$ both modes are unstable, i.e., both modes are positive. For $\delta > \delta^*$, only the dominant mode is unstable.

In the infinite-depth limit it we showed that there is only one mode that can be unstable, and the critical value of δ required for instability is given by equation (3.5.20). In the limit as $d \to \infty$, equations (3.6.10)–(3.6.11) become

$$\delta_{\mathrm{crit}} = \frac{1}{K(1-K)}, \tag{3.6.12}$$

$$\delta^* = \frac{4}{K(1-K)}, \tag{3.6.13}$$

which are half and twice, respectively, of the value obtained in the infinite-depth limit, once again highlighting the singular nature of this limit.

It is also possible to obtain asymptotic approximations to the behaviour of the sub-dominant diffusive modes; however, since these modes are relatively uninteresting (i.e., always stable), we omit these approximations.

3.7 Summary

In this Chapter, we performed a linear stability analysis of the dimensionless system of equations describing the flow of a two-dimensional, initially quiescent layer of surfactant or anti-surfactant solution. In the special cases of a pure solvent and of a "perfectly soluble" anti-surfactant solution, or when the solute

is a surfactant, the system is unconditionally stable; this agrees with previous studies (see, for example, [35,66,107]). However, in the special case of an infinitely deep layer, and for a general finite-depth layer, of anti-surfactant solution, the layer can be linearly unstable to perturbations of certain wavenumbers. Assuming that the principle of exchange of stabilities holds, a marginal stability analysis was performed, and instability conditions on the dimensionless parameters in the system were derived. The effects of finite depth were considered when the principle of exchange of stabilities is assumed to hold and it was found that the region of instability in parameter space is largest in the infinite-depth limit. In section 3.5.2 we postulated a mechanism for the instability and noted that the system either the must move towards a nonlinear steady state, which could be determined through a nonlinear stability analysis, or that other factors must be important to the long time evolution of the system, such as gravity or inertia. Physically, this instability can occur even when there is no perturbation of the free surface itself, and we noted that one experimental hallmark could be the precipitation of solute at or near the free surface, even if no deformation of the free surface occurs.

Chapter 4

Thin-Film Formulation and Stability Analysis

4.1 Introduction

In this Chapter we formulate the model describing the evolution of a thin film of surfactant or anti-surfactant solution, and perform a linear stability analysis of an initially quiescent thin film, similar to the analysis performed in Chapter 3 for a layer of finite or infinite depth. In the following, the substrate is taken to be at $z^* = 0$, instead of at $z^* = -d^*$ as in the more general problem, and we choose the vertical length scale to be the typical layer depth. This allows us to write all length scales in terms of the aspect ratio and the horizontal length scale, both to be chosen at a later time. We also choose $\theta = 1/(1 - K)$ so that the surface tension depends solely on the surface excess of solute since, as Figure 3.9 shows, the value of θ does not significantly alter the results of the linear stability analysis, especially in the long-wave limit. It might therefore be reasonably expected that the value of θ matters even less in the thin-film limit.

The mathematical formulation of the model describing the flow of a thin film of fluid is somewhat different from the formulation of a model describing a layer of arbitrary depth and aspect ratio, such as we have done in Chapter 3, because the horizontal and vertical length scales of a thin film are necessarily different, which is not the case in the general formulation. There is a crucial small parameter,

namely the aspect ratio $\varepsilon = H^*/L^*$, which is the ratio of the vertical length scale H^* to the horizontal length scale L^*. For the general formulation we have implcitly chosen $\varepsilon = 1$, but to describe a thin film of fluid the appropriate choice is $\varepsilon \ll 1$, so that the horizontal length scale is much larger than the vertical length scale. This is the classical lubrication or thin-film approximation, a detailed discussion of which can be found in, for example, the review by Oron *et al.* [67].

4.2 Non-Dimensionalisation

Using natural choices, and with the general scalings (3.2.1) as a guide, we non-dimensionalise the system by

$$\begin{cases} (x^*, z^*, h^*) = (L^* x, \varepsilon L^* z, \varepsilon L^* h), \quad (u^*, w^*) = (U^* u, \varepsilon U^* w), \\ t^* = \dfrac{L^*}{U^*} t, \quad p^* = \dfrac{\mu^* U^*}{\varepsilon^2 L^*} p, \quad \mathbf{T}^* = \dfrac{\mu^* U^*}{\varepsilon^2 L^*} \mathbf{T}, \quad \sigma^* = \sigma^*_{\text{solv}} \sigma, \\ \Gamma^* = \eta^* c_{\text{i}}^* \Gamma, \quad c^* = c_{\text{i}}^* c, \quad s^* = \eta^* c_{\text{i}}^* s, \end{cases} \tag{4.2.1}$$

where L^* is the characteristic horizontal length scale, H^* is the characteristic vertical length scale, and U^* is the characteristic horizontal velocity scale. We have defined $\varepsilon = H^*/L^*$, the aspect ratio of the film, and will be taking the limit $\varepsilon \to 0$ in the usual thin-film approximation. The vertical velocity scale $W^* = \varepsilon U^*$ is a direct consequence of the continuity equation. As in the previous Chapter, the particular choice of U^* will follow either from the normal stress condition when we assume that mean surface tension is important and thus set an appropriate capillary number equal to unity, or from the tangential stress condition when we assume that surface tension gradients are important and thus set an appropriate Marangoni number equal to unity.

4.3 Geometry of the Free Surface

In the formulation of the present thin-film model three key geometrical quantities arise, namely the outward unit normal $\hat{\mathbf{n}}$ to the free surface, the unit tangent $\hat{\mathbf{t}}$ to the free surface (in the (x, z)-plane), and the surface gradient operator ∇_{s}.

Using (4.2.1), we obtain, at leading order in ε, expressions for each of these in turn, in the thin-film limit $\varepsilon \to 0$. We retain any higher order terms that might conceivably play a role at leading order; this is done *a posteriori*, as it is difficult to determine in advance which terms may appear in the leading order problem. To $O(\varepsilon)$ in the thin-film limit the unit normal becomes

$$\hat{\mathbf{n}} = \left(-\varepsilon \frac{\partial h}{\partial x}, 1\right) + O(\varepsilon^2), \tag{4.3.1}$$

and the unit tangent becomes

$$\hat{\mathbf{t}} = \left(1, \varepsilon \frac{\partial h}{\partial x}\right) + O(\varepsilon^2), \tag{4.3.2}$$

with which the surface gradient operator becomes

$$\nabla_{\mathrm{s}}^* = \frac{1}{L^*}\left[\left(\frac{\partial}{\partial x} + \frac{\partial h}{\partial x}\frac{\partial}{\partial z}, \varepsilon \frac{\partial h}{\partial x}\frac{\partial}{\partial x}\right) + O(\varepsilon^2)\right]. \tag{4.3.3}$$

4.4 Evolution of the Film Thickness

The first evolution equation we derive is that governing the evolution of the film thickness, $h^*(x^*, t^*)$. The general method of deriving this equation is as follows (see, for example, Craster and Matar [15] and/or Oron *et al.* [67]). From the z-component of the Navier–Stokes equation, along with the normal stress boundary conditions at the free surface, an expression for the leading order pressure $p^*(x^*, t^*)$, which will be independent of z^*, is obtained. Using this expression for the pressure and making use of the tangential stress boundary condition at the free surface, along with the no-slip and no-penetration conditions at the solid substrate, an expression for the leading order horizontal velocity $u^*(x^*, z^*, t^*)$ is obtained from the x-component of the Navier–Stokes equation. This expression for the horizontal velocity is then substituted into an integrated form of the kinematic condition, leading to the final evolution equation for the film thickness $h^*(x^*, t^*)$. In what follows, we go through this process in detail, first putting the equations and boundary conditions into dimensionless form.

4.4.1 Film Thickness: Governing Equations

The continuity equation (2.6.1) scales straightforwardly to give

$$\frac{\partial u}{\partial x} + \frac{\partial w}{\partial z} = 0. \tag{4.4.1}$$

The x-component of the Navier-Stokes equation becomes

$$\varepsilon^2 \left(\frac{\partial u}{\partial t} + u\frac{\partial u}{\partial x} + w\frac{\partial u}{\partial z} \right) = \frac{1}{\mathrm{Re}} \left(-\frac{\partial p}{\partial x} + \varepsilon^2 \frac{\partial^2 u}{\partial x^2} + \frac{\partial^2 u}{\partial z^2} \right), \tag{4.4.2}$$

where

$$\mathrm{Re} = \frac{\rho^* U^* L^*}{\mu^*} \tag{4.4.3}$$

is the Reynolds number. If the quantity $\varepsilon^2\mathrm{Re}$ (often called the *reduced Reynolds number*) satisfies $\varepsilon^2\mathrm{Re} \ll 1$, that is, if Re is not too large, then we are free to neglect all terms that are $O(\varepsilon^2)$ *and* all terms that are $O(\varepsilon^2\mathrm{Re})$; otherwise, if $\mathrm{Re} = O(\varepsilon^{-2})$ or larger, additional advective terms will have to be retained. If, for now, we assume that $\varepsilon^2\mathrm{Re} \ll 1$ (we will justify this in section 4.4.3), then the leading order x-component is obtained by neglecting any terms that are $O(\varepsilon^2)$ or smaller, giving

$$\frac{\partial p}{\partial x} = \frac{\partial^2 u}{\partial z^2}. \tag{4.4.4}$$

The z-component of the Navier–Stokes equation (2.6.2) is non-dimensionalised in the same way as the x-component to give

$$\varepsilon^4 \left(\frac{\partial w}{\partial t} + u\frac{\partial w}{\partial x} + w\frac{\partial w}{\partial z} \right) = \frac{1}{\mathrm{Re}} \left(-\frac{\partial p}{\partial z} + \varepsilon^4 \frac{\partial^2 w}{\partial x^2} + \varepsilon^2 \frac{\partial^2 w}{\partial z^2} \right), \tag{4.4.5}$$

Since we have assumed that $\varepsilon^2\mathrm{Re} \ll 1$, the leading order z-component is simply

$$\frac{\partial p}{\partial z} = 0. \tag{4.4.6}$$

4.4.2 Film Thickness: Boundary Conditions

The no-slip and no-penetration conditions (2.6.5) on the solid substrate are trivially scaled to

$$u = 0, \quad w = 0 \qquad \text{on} \quad z = 0. \tag{4.4.7}$$

The kinematic condition (2.6.8) also scales trivially to

$$\frac{\partial h}{\partial t} + u\frac{\partial h}{\partial x} = w \quad \text{on} \quad z = h. \tag{4.4.8}$$

As mentioned in Chapter 2, the kinematic condition (4.4.8) can also be written in its integrated form

$$\frac{\partial h}{\partial t} + \frac{\partial Q}{\partial x} = 0, \qquad \text{where} \qquad Q(x,t) = \int_0^{h(x,t)} u \, \mathrm{d}z, \tag{4.4.9}$$

with $Q = Q(x,t)$ denoting the dimensionless horizontal volume flux (per unit width in the y-direction) in the layer. This form of the kinematic condition is more convenient to use when we come to the final step in the derivation of the evolution equation for the film thickness.

The final two boundary conditions required are the normal and tangential stress balances. Both of these boundary conditions involve the total stress tensor $\mathbf{T}^*$, given in matrix form as

$$\mathbf{T}^* = \begin{bmatrix} -p^* + 2\mu^* \dfrac{\partial u^*}{\partial x^*} & \mu^* \left(\dfrac{\partial u^*}{\partial z^*} + \dfrac{\partial w^*}{\partial x^*} \right) \\ \mu^* \left(\dfrac{\partial u^*}{\partial z^*} + \dfrac{\partial w^*}{\partial x^*} \right) & -p^* + 2\mu^* \dfrac{\partial w^*}{\partial z^*} \end{bmatrix}. \tag{4.4.10}$$

Substituting the scalings (4.2.1) into $\mathbf{T}^*$ we obtain

$$\mathbf{T} = \begin{bmatrix} -p + 2\varepsilon^2 \dfrac{\partial u}{\partial x} & \varepsilon \dfrac{\partial u}{\partial z} + \varepsilon^3 \dfrac{\partial w}{\partial x} \\ \varepsilon \dfrac{\partial u}{\partial z} + \varepsilon^3 \dfrac{\partial w}{\partial x} & -p + 2\varepsilon^2 \dfrac{\partial w}{\partial z} \end{bmatrix}. \tag{4.4.11}$$

Retaining terms that are $O(1/\varepsilon^2)$ and $O(1/\varepsilon)$ since, *a posteriori*, these are the only terms that arise in the leading order problem, we write the scaled stress tensor as

$$\mathbf{T} = \begin{bmatrix} -p & \varepsilon \dfrac{\partial u}{\partial z} \\ \varepsilon \dfrac{\partial u}{\partial z} & -p \end{bmatrix} + O(\varepsilon^2). \tag{4.4.12}$$

The equation of state (2.6.12), recalling that we have set $\theta = 1/(1-K)$, is scaled to give

$$\sigma = 1 - \alpha\Gamma, \tag{4.4.13}$$

where

$$\Gamma = s - c \tag{4.4.14}$$

is the dimensionless form of the surface excess, and where we have defined

$$\alpha = \frac{R^* T^* \eta^* c_{\mathrm{i}}^*}{\sigma_{\mathrm{solv}}^*} \tag{4.4.15}$$

to be a dimensionless parameter controlling the importance of the variation of surface tension with the surface excess Γ, specifically $\mathrm{d}\sigma/\mathrm{d}\Gamma = -\alpha$. The leading order tangential stress balance at the free surface (2.6.7), using the identity $\hat{\mathbf{t}}\cdot\nabla_s = \hat{\mathbf{t}}\cdot\nabla$, becomes

$$\frac{\partial u}{\partial z} = -\mathrm{Ma}\left[\frac{\partial s}{\partial x} - \left(\frac{\partial h}{\partial x}\frac{\partial c}{\partial z} + \frac{\partial c}{\partial x}\right)\right] \tag{4.4.16}$$

at leading order, where

$$\mathrm{Ma} = \frac{\varepsilon R^* T^* \eta^* c_{\mathrm{i}}^*}{\mu^* U^*} \tag{4.4.17}$$

is the appropriate Marangoni number similar to that defined in (3.2.15), but with an extra factor of ϵ, reflecting the effect of the aspect ratio of the film on the relative strength of surface-tension-gradient forces. We assume that $\mathrm{Ma} = O(1)$, so that there is a non-trivial balance of terms in the tangential stress balance (4.4.16).

The leading order normal stress balance at the free surface (2.6.6) is

$$-p = \frac{1}{\mathrm{Ca}}\frac{\partial^2 h}{\partial x^2}\left(1 - \alpha\Gamma\right) \tag{4.4.18}$$

to leading order, where

$$\mathrm{Ca} = \frac{\mu^* U^*}{\varepsilon^3 \sigma_{\mathrm{solv}}^*} \tag{4.4.19}$$

is the appropriate capillary number. We may write the Marangoni number in terms of the capillary number as

$$\mathrm{Ma} = \frac{\alpha}{\varepsilon^2}\frac{1}{\mathrm{Ca}}. \tag{4.4.20}$$

In order to retain both mean surface tension and surface-tension-gradient effects at leading order, we require that both Ma and Ca be $O(1)$ which, from (4.4.20), is consistent only when $\alpha = O(\varepsilon^2)$, which is reasonable when the typical concentration is $c_{\mathrm{i}}^* = O(1)\,\mathrm{mol\,m^{-3}}$. In other words to retain both effects to leading

order, we require that the variation of surface tension is small; physically, this is generally true, regardless of the underlying mechanism of surface-tension variation. Thus, if we assume that $\alpha = O(\varepsilon^2)$, then the leading order normal stress balance (4.4.18) becomes

$$-p = \frac{1}{\mathrm{Ca}} \frac{\partial^2 h}{\partial x^2}. \tag{4.4.21}$$

Note that, because the variation in surface tension is small, this leading order boundary condition now contains no effects of the variation of surface tension, and only the effects of mean surface tension appear.

4.4.3 Film Thickness: Dimensionless Numbers

Throughout this scaling process we have made assumptions concerning the sizes of dimensionless parameters. In particular, we have assumed that $\varepsilon^2\mathrm{Re} \ll 1$, $\mathrm{Ma} = O(1)$, and $\mathrm{Ca} = O(1)$. In order to determine values for these numbers we must choose a specific velocity scale, which we do by setting $\mathrm{Ca} = 1$, giving $U^* = \varepsilon^3 \sigma^*_{\mathrm{solv}}/\mu$. Using the values given in Table 2.3, and choosing a typical horizontal length scale to be, say, $L^* = 10^{-2}\,\mathrm{m}$, the reduced Reynolds number is

$$\varepsilon^2\mathrm{Re} = \frac{\varepsilon^5 \sigma^*_{\mathrm{solv}} \rho^* L^*}{\mu^{*2}} \simeq \varepsilon^5 \times 10^6. \tag{4.4.22}$$

Thus, choosing an aspect ratio of $\varepsilon \ll 0.1$ ensures that $\varepsilon^2\mathrm{Re} \ll 1$, and justifies neglect of $O(\varepsilon^2\mathrm{Re})$ terms in the Navier–Stokes equation. Taking an aspect ratio of $\varepsilon = 10^{-2}$ for the moment, the Marangoni number is

$$\mathrm{Ma} = \frac{\alpha}{\varepsilon^2} = \frac{R^* T^* \eta^* c^*_{\mathrm{i}}}{\sigma^*_{\mathrm{solv}} \varepsilon^2} \simeq c^*_{\mathrm{i}} \times \left(1\,\mathrm{m}^3\,\mathrm{mol}^{-1}\right). \tag{4.4.23}$$

Thus, for $\mathrm{Ma} = O(1)$ we require that the base-state (or initial) bulk concentration is $c^*_{\mathrm{i}} = O(1)\ \mathrm{mol\,m^{-3}}$.

4.4.4 Film Thickness: Evolution Equation

Now that we have dealt with the thin-film reduction of the hydrodynamic equations and boundary conditions, we combine these into a single PDE governing the evolution of the film thickness. For the remainder of this section we will switch

to suffix notation for partial derivatives. For ease of reference, a summary of the pertinent leading order equations and boundary conditions using this notation is as follows. Recall that we have now chosen the horizontal velocity scale to be such that Ca = 1.

Equations

- Conservation of mass,

$$h_t + Q_x = 0. \tag{4.4.24}$$

- Navier–Stokes equation, x-component,

$$p_x = u_{zz}. \tag{4.4.25}$$

- Navier–Stokes equation, z-component,

$$p_z = 0. \tag{4.4.26}$$

Boundary Conditions

- No slip,

$$u = 0 \qquad \text{on} \quad z = 0. \tag{4.4.27}$$

- No penetration,

$$w = 0 \qquad \text{on} \quad z = 0. \tag{4.4.28}$$

- Normal stress balance,

$$p = -h_{xx} \qquad \text{on} \quad z = h. \tag{4.4.29}$$

- Tangential stress balance,

$$u_z = -\mathrm{Ma}\left[s_x - (c_x + h_x c_z)\right] \qquad \text{on} \quad z = h. \tag{4.4.30}$$

Equation (4.4.26) shows that the pressure is independent of z to leading order; then the normal stress boundary condition (4.4.29) gives

$$p = -h_{xx} \tag{4.4.31}$$

throughout the layer. Substituting this expression for p into the x-component of the Navier–Stokes equation (4.4.25) and applying the no-slip condition (4.4.27) we obtain

$$u = -\frac{h_{xxx}}{2}z^2 + Az, \tag{4.4.32}$$

where the unknown function $A(x,t)$ appears as a consequence of the integration. Applying the tangential stress balance boundary condition (4.4.30) to determine A, we obtain

$$u = h_{xxx}z\left(h - \frac{1}{2}z\right) - z\mathrm{Ma}\Big[s_x - (c_x + h_x c_z)\Big]. \tag{4.4.33}$$

The flux is then

$$Q = \int_0^h u\,\mathrm{d}z = \frac{1}{3}h_{xxx}h^3 - \frac{\mathrm{Ma}}{2}h^2\Big[s_x - (c_x + h_x c_z)\Big]. \tag{4.4.34}$$

Substituting this into (4.4.24) we obtain

$$h_t + \left\{\frac{h_{xxx}h^3}{3} - \frac{\mathrm{Ma}h^2}{2}\left[s_x - (c_x + h_x c_z)\right]\right\}_x = 0, \tag{4.4.35}$$

which is the evolution equation for the film thickness.

4.5 Evolution of Surface Concentration

We now derive the equation describing the evolution of the surface concentration, $s(x,t)$. Substituting the scalings (4.2.1) into (2.4.4), and using the geometric quantities outlined in section 4.3, we obtain

$$s_t + (us)_x = \frac{1}{\mathrm{P_s}}s_{xx} + \mathrm{Da_a}\left(Kc - s\right), \tag{4.5.1}$$

where

$$\mathrm{P_s} = \frac{U^*L^*}{\mathrm{D_s^*}} = \frac{\varepsilon^3 L^*\sigma^*_{\mathrm{solv}}}{\mathrm{D_s^*}\mu^*} \tag{4.5.2}$$

is a surface Péclet number,

$$\mathrm{Da_a} = \frac{k_2^*L^*}{U^*} = \frac{k_2^*L^*\mu^*}{\varepsilon^3\sigma^*_{\mathrm{solv}}} \tag{4.5.3}$$

is an advective Damköhler number, and

$$K = \frac{k_1^*}{k_2^*} \tag{4.5.4}$$

is an equilibrium rate constant. All three parameters $\mathrm{P_s}$, $\mathrm{Da_a}$, and K are assumed to be $O(1)$. When evaluated at the free surface, the horizontal velocity (4.4.33) yields

$$u|_{z=h} = \frac{1}{2}h_{xxx}h^2 - \mathrm{Ma}h\left[s_x - (c_x + h_x c_z)\right]. \tag{4.5.5}$$

Thus the equation governing the evolution of the surface concentration is

$$s_t + \left\{\frac{1}{2}h_{xxx}h^2 s - \mathrm{Ma}hs\left[s_x - (c_x + h_x c_z)\right]\right\}_x - \frac{1}{\mathrm{P_s}}s_{xx} - \mathrm{Da_a}\left(Kc - s\right) = 0. \tag{4.5.6}$$

4.5.1 Evolution of Surface Concentration: Dimensionless Numbers

Similarly to how dimensionless parameters were treated in section 4.4.3, we have made the assumptions that $\mathrm{P_s} = O(1)$ and $\mathrm{Da_a} = O(1)$, so that there is a non-trivial balance of terms at leading order. Again, using the values given in Table 2.3, and taking the horizontal velocity scale based on $\mathrm{Ca} = 1$, the surface Péclet number is

$$\mathrm{P_s} = \frac{\varepsilon^3 L^* \sigma^*_{\mathrm{solv}}}{\mathrm{D}^*_{\mathrm{s}}\mu^*} \simeq 7, \tag{4.5.7}$$

and so $\mathrm{P_s}$ can safely be considered $O(1)$. However, the advective Damköhler number is

$$\mathrm{Da_a} = \frac{k_2^* \mu^* L^*}{\varepsilon^3 \sigma^*_{\mathrm{solv}}} \simeq 10^{15}, \tag{4.5.8}$$

which is very much larger than unity. Since $\mathrm{Da_a}$ represents the ratio of the rate of solute desorption to the rate of advection of solute, this suggests that solute desorption occurs on a much shorter time scale than solute advection. Notwithstanding the fact that $\mathrm{Da_a}$ is very large, in the spirit of existing surfactant-based models (see, for example, [40, 45]), we proceed, for now, under the assumption that $\mathrm{Da_a} = O(1)$. While $\mathrm{Da_a}$ will be formally treated as $O(1)$ for the time being, we will also analyse the limit as $\mathrm{Da_a} \to \infty$, in which the system is always in surface–bulk equilibrium. In this limit, which we consider in section 4.12, no oscillatory behaviour (such as that discussed in Appendix A) is possible, and so we consider both the case of finite $\mathrm{Da_a}$ and the large $\mathrm{Da_a}$ limit.

4.6 Evolution of Bulk Concentration

The final governing equation is that describing the evolution of the bulk concentration. Using the scalings (4.2.1) the bulk concentration evolution equation (2.6.3) becomes

$$\frac{\partial c}{\partial t} + u\frac{\partial c}{\partial x} + w\frac{\partial c}{\partial z} = \frac{1}{\mathrm{P_b}}\left(\frac{\partial^2 c}{\partial x^2} + \frac{1}{\varepsilon^2}\frac{\partial^2 c}{\partial z^2}\right), \tag{4.6.1}$$

where

$$\mathrm{P_b} = \frac{U^* L^*}{\mathrm{D_b^*}} = \frac{\varepsilon^3 L^* \sigma^*_{\mathrm{solv}}}{\mathrm{D_b^*}\mu^*} \tag{4.6.2}$$

is a bulk Péclet number. Since $\mathrm{D_s^*}$ and $\mathrm{D_b^*}$ are of similar magnitude (see discussion in section 2.5), $\mathrm{P_s}$ and $\mathrm{P_b}$ are of similar magnitude and so, in particular, $\mathrm{P_b}$ is $O(1)$. The substrate boundary condition (2.6.9) trivially becomes

$$\frac{\partial c}{\partial z} = 0 \quad \text{on} \quad z = 0. \tag{4.6.3}$$

The flux boundary condition (2.6.10) becomes

$$\frac{1}{\varepsilon^2}\frac{\partial c}{\partial z} - \frac{\partial h}{\partial x}\frac{\partial c}{\partial x} + O(\varepsilon^2) = -\,\mathrm{Da_d}\,(Kc - s)\,, \tag{4.6.4}$$

where

$$\mathrm{Da_d} = \frac{k_2^* \eta^* L^*}{\varepsilon \mathrm{D_b^*}} \tag{4.6.5}$$

is a diffusive Damköhler number, formally treated as $O(1)$ for the time being.

Proceeding naively, and recalling that $\mathrm{P_b} = O(1)$, we neglect all $O(\varepsilon^2)$ terms to obtain the following leading order system:

$$\frac{\partial^2 c}{\partial z^2} = 0, \tag{4.6.6}$$

$$\frac{\partial c}{\partial z} = 0 \quad \text{on} \quad z = 0, \tag{4.6.7}$$

$$\frac{\partial c}{\partial z} = 0 \quad \text{on} \quad z = h. \tag{4.6.8}$$

It is trivial to see that c is independent of z to leading order, i.e., the leading order bulk concentration is uniform across the layer and is therefore given by

some function $c = c_0(x,t)$. In order to determine c_0 it is necessary to go to higher order; to do this we expand the bulk concentration according to

$$c(x,z,t) = c_0(x,t) + \varepsilon^2 c_1(x,z,t) + O(\varepsilon^4), \tag{4.6.9}$$

that is, the bulk concentration is uniform across the layer to leading order in ε^2, with an $O(\varepsilon^2)$ correction which captures the z-variation (i.e., concentration gradients) across the layer. The expansion (4.6.9) is often presented as a separate ansatz (see, for example, [40, 45, 107]) and is sometimes called the *rapid vertical diffusion* assumption but, in fact, emerges here naturally, without any additional assumptions. Note that we must also expand h, u, and w in a similar way, but the expansions of these variables have no bearing on the resulting leading order system.

Substituting (4.6.9) into the evolution equation (4.6.1) and the two boundary conditions (4.6.3) and (4.6.4), and neglecting $O(\varepsilon^2)$ terms, the leading order system is

$$\frac{\partial c_0}{\partial t} + u\frac{\partial c_0}{\partial x} = \frac{1}{\mathrm{P_b}}\left(\frac{\partial^2 c_0}{\partial x^2} + \frac{\partial^2 c_1}{\partial z^2}\right), \tag{4.6.10}$$

$$\frac{\partial c_1}{\partial z} = 0 \quad \text{on} \quad z = 0, \tag{4.6.11}$$

$$\frac{\partial c_1}{\partial z} = \frac{\partial h}{\partial x}\frac{\partial c_0}{\partial x} - \mathrm{Da_d}\left(Kc_0 - s\right) \quad \text{on} \quad z = h. \tag{4.6.12}$$

Typically in the literature (see, for example, [15, 40]), the next step is to depth-average equation (4.6.10), i.e., to integrate each term across the layer and then divide by the depth of the layer. The reasoning that is usually given for this is to remove the z-dependence from the equation, but this is a misleading explanation. What we are actually doing is *solving* this system for c_1 and this solution delivers the evolution equation for the unknown leading order bulk concentration. Integrating (4.6.10) across the layer, keeping in mind that c_0 is independent of z, we obtain

$$\int_0^h \frac{\partial^2 c_1}{\partial z^2}\,\mathrm{d}z = \int_0^h \left\{\mathrm{P_b}\left(\frac{\partial c_0}{\partial t} + u\frac{\partial c_0}{\partial x}\right) - \frac{\partial^2 c_0}{\partial x^2}\right\}\mathrm{d}z. \tag{4.6.13}$$

The left-hand side of (4.6.13) integrates trivially and allows us to apply the two boundary conditions directly, while on the right-hand side of (4.6.13) the only function with z-dependence is the velocity u which integrates to yield the volume

flux Q given by (4.4.34). Note that c_1 will no longer appear in the problem, and so the equation obtained involves only the leading order bulk concentration c_0. Performing the integration we obtain

$$\left.\frac{\partial c_1}{\partial z}\right|_{z=h} - \left.\frac{\partial c_1}{\partial z}\right|_{z=0} = \mathrm{P_b}\left(h\frac{\partial c_0}{\partial t} + Q\frac{\partial c_0}{\partial x}\right) - h\frac{\partial^2 c_0}{\partial x^2}. \tag{4.6.14}$$

Applying the two boundary conditions (4.6.11) and (4.6.12) gives the evolution equation for c_0 that we seek:

$$\frac{\partial h}{\partial x}\frac{\partial c_0}{\partial x} - \mathrm{Da_d}\left(Kc_0 - s\right) = \mathrm{P_b}\left(h\frac{\partial c_0}{\partial t} + Q\frac{\partial c_0}{\partial x}\right) - h\frac{\partial^2 c_0}{\partial x^2}. \tag{4.6.15}$$

Writing equation (4.6.15) in a form more readily comparable with those appearing in the literature (e.g., [40]), the evolution of the leading order bulk concentration is determined by

$$\mathrm{P_b}\left\{h\frac{\partial c_0}{\partial t} + \left[\frac{1}{3}h\frac{\partial^3 h}{\partial x^3}h^3 - \frac{\mathrm{Ma}}{2}h^2\left(\frac{\partial s}{\partial x} - \frac{\partial c_0}{\partial x}\right)\right]\frac{\partial c_0}{\partial x}\right\} - \frac{\partial}{\partial x}\left(h\frac{\partial c_0}{\partial x}\right) + \mathrm{Da_d}\left(Kc_0 - s\right) = 0. \tag{4.6.16}$$

4.6.1 Evolution of Bulk Concentration: Dimensionless Numbers

We have once again assumed that the dimensionless numbers in the previous section are of order unity, i.e., that $\mathrm{P_b} = O(1)$ and $\mathrm{Da_d} = O(1)$. Since $\mathrm{P_b} \simeq \mathrm{P_s}$, we immediately have that $\mathrm{P_b} = O(1)$. Using the values given in Table 2.3, we have

$$\mathrm{Da_d} = \frac{k_2^* \eta^* L^*}{\varepsilon \mathrm{D_b^*}} \simeq 10^{11}, \tag{4.6.17}$$

which is very much larger than $O(1)$, as was the case with $\mathrm{Da_a}$. This large value of $\mathrm{Da_d}$ also has a similar interpretation to the large value of $\mathrm{Da_a}$: sorptive effects are much faster than diffusion of solute. Also, similarly to the way in which we treat $\mathrm{Da_a}$, in the spirit of existing surfactant-based models, we proceed, for now, under the assumption that $\mathrm{Da_d} = O(1)$, but will also analyse the limit $\mathrm{Da_d} \to \infty$ in due course.

4.7 Summary of the Thin-Film Equation

A summary of the leading order system of evolution equations for a thin film of surfactant or anti-surfactant solution is given below. Governing the evolution of the film thickness $h(x,t)$ we have

$$h_t + \left[\frac{h_{xxx}h^3}{3} - \frac{\mathrm{Ma}h^2}{2}\left(s-c\right)_x\right]_x = 0, \tag{4.7.1}$$

governing the evolution of the surface concentration $s(x,t)$ we have

$$s_t + \left[\frac{1}{2}h_{xxx}h^2 s - \mathrm{Ma}hs\left(s-c\right)_x\right]_x - \frac{1}{\mathrm{P_s}}s_{xx} - \mathrm{Da_a}\left(Kc-s\right) = 0, \tag{4.7.2}$$

and governing the evolution of the (leading order) bulk concentration $c(x,t)$ we have

$$\mathrm{P_b}\left(hc_t + \left[\frac{1}{3}h_{xxx}h^3 - \frac{\mathrm{Ma}}{2}h^2\left(s-c\right)_x\right]c_x\right) - \left(hc_x\right)_x + \mathrm{Da_d}\left(Kc-s\right) = 0. \tag{4.7.3}$$

Note that we have dropped the subscript on c_0 for simplicity of notation and so, hereafter, any c appearing denotes the leading order bulk concentration, which is uniform across the fluid layer.

We also summarise the definitions of all of the dimensionless parameters, and the values that we take for them in general, in Table 4.1. Note that the values taken for $\mathrm{Da_a}$ and $\mathrm{Da_d}$ are significantly smaller than the values that were calculated in sections 4.5.1 and 4.6.1, respectively. These particular values are chosen to be on the low end of the possible values, and are for illustrative purposes; increasing the values of these Damköhler numbers further does not qualitatively change any results and only causes numerical calculations to become more difficult.

4.8 Linear Stability Analysis of a Thin Film

We now perform a linear stability analysis of the thin-film equations (4.7.1)–(4.7.3). As in Chapter 3, the base state is taken to be a quiescent layer with a flat free surface, and with both the bulk and the surface concentrations constant

Parameter	**Expression**	**Value Taken**
U^*	$\dfrac{\varepsilon^3 \sigma^*_{\mathrm{solv}}}{\mu^*}$	$O(10^{-7})\,\mathrm{m\,s^{-1}}$
H^*	d^*	$O(10^{-4})\,\mathrm{m}$
ε	$\dfrac{H^*}{L^*}$	$O(10^{-3})$
$\mathrm{P_b}$	$\dfrac{U^* L^*}{\mathrm{D_b^*}}$	10
$\mathrm{P_s}$	$\dfrac{U^* L^*}{\mathrm{D_s^*}}$	10
$\mathrm{Da_a}$	$\dfrac{k_2^* L^*}{U^*}$	10^5
$\mathrm{Da_d}$	$\dfrac{k_2^* \eta^* L^*}{\varepsilon \mathrm{D_b^*}}$	10^6
Ca	1	1
Ma	$\dfrac{\varepsilon R^* T^* \eta^* c_{\mathrm{i}}^*}{\mu^* U^*}$	10

Table 4.1: Dimensionless parameters in the thin-film limit and the values that will be taken for each using Table 2.1. The horizontal velocity scale U^* is chosen such that $\mathrm{Ca} = 1$, and the vertical length scale H^* is chosen such that $d = 1$.

and at their equilibrium values. Again, we make use of the usual normal mode ansatz of the type (3.3.1), namely,

$$h(x,t) = 1 + \epsilon\alpha(t)\exp(ikx), \tag{4.8.1}$$

$$s(x,t) = K + \epsilon\gamma(t)\exp(ikx), \tag{4.8.2}$$

$$c(x,t) = 1 + \epsilon\beta(t)\exp(ikx), \tag{4.8.3}$$

where $\alpha(t)$, $\gamma(t)$, and $\beta(t)$ are the amplitudes of the perturbations to the film thickness, the surface concentration, and the bulk concentration, respectively, to obtain the leading order (in the limit $\varepsilon \to 0$) linear system

$$\frac{\mathrm{d}\alpha}{\mathrm{d}t} = -\frac{1}{3}k^4\alpha(t) - \frac{\mathrm{Ma}}{2}k^2\gamma(t) + \frac{\mathrm{Ma}}{2}k^2\beta(t), \tag{4.8.4}$$

$$\frac{\mathrm{d}\gamma}{\mathrm{d}t} = -\frac{K}{2}k^4\alpha(t) - \left(\mathrm{Ma}Kk^2 + \frac{1}{\mathrm{P_s}}k^2 + \mathrm{Da_a}\right)\gamma(t) + K\left(\mathrm{Ma}k^2 + \mathrm{Da_a}\right)\beta(t), \tag{4.8.5}$$

$$\frac{\mathrm{d}\beta}{\mathrm{d}t} = \frac{\delta\mathrm{Da_a}}{\mathrm{P_b}}\gamma(t) - \left(\frac{1}{\mathrm{P_b}}k^2 + \frac{K\delta\mathrm{Da_a}}{\mathrm{P_b}}\right)\beta(t), \tag{4.8.6}$$

where again $\delta = \mathrm{Da_d}/\mathrm{Da_a}$. In general, equations (4.8.4)–(4.8.6) have solutions

$$\begin{bmatrix}\alpha(t)\\ \gamma(t)\\ \beta(t)\end{bmatrix} = A_1\mathbf{v}_1\exp(\omega_1 t) + A_2\mathbf{v}_2\exp(\omega_2 t) + A_3\mathbf{v}_3\exp(\omega_3 t), \tag{4.8.7}$$

where the A_i are constants of integration, and the $\mathbf{v}_i$ are the eigenvectors of the linear system, with corresponding eigenvalues ω_1, ω_2, and ω_3, which will be analysed in detail in section 4.9.

As discussed in Chapter 3, a layer of anti-surfactant solution can be unstable if certain conditions on the parameters are satisfied. This is also true for a thin film, though the parameter values for which instability occurs are different because of the different definitions of many of the parameters. For now, we will simply give the values of each of the ω_i in equation (4.8.7) as illustrative solutions to the linear thin-film problem. Note that the ω_i are, in general, complex; this is true in general and the occurrence of oscillatory behaviour in the finite-depth case is discussed in Appendix A, where we demonstrate that oscillatory behaviour is an inherently long-wave phenomenon

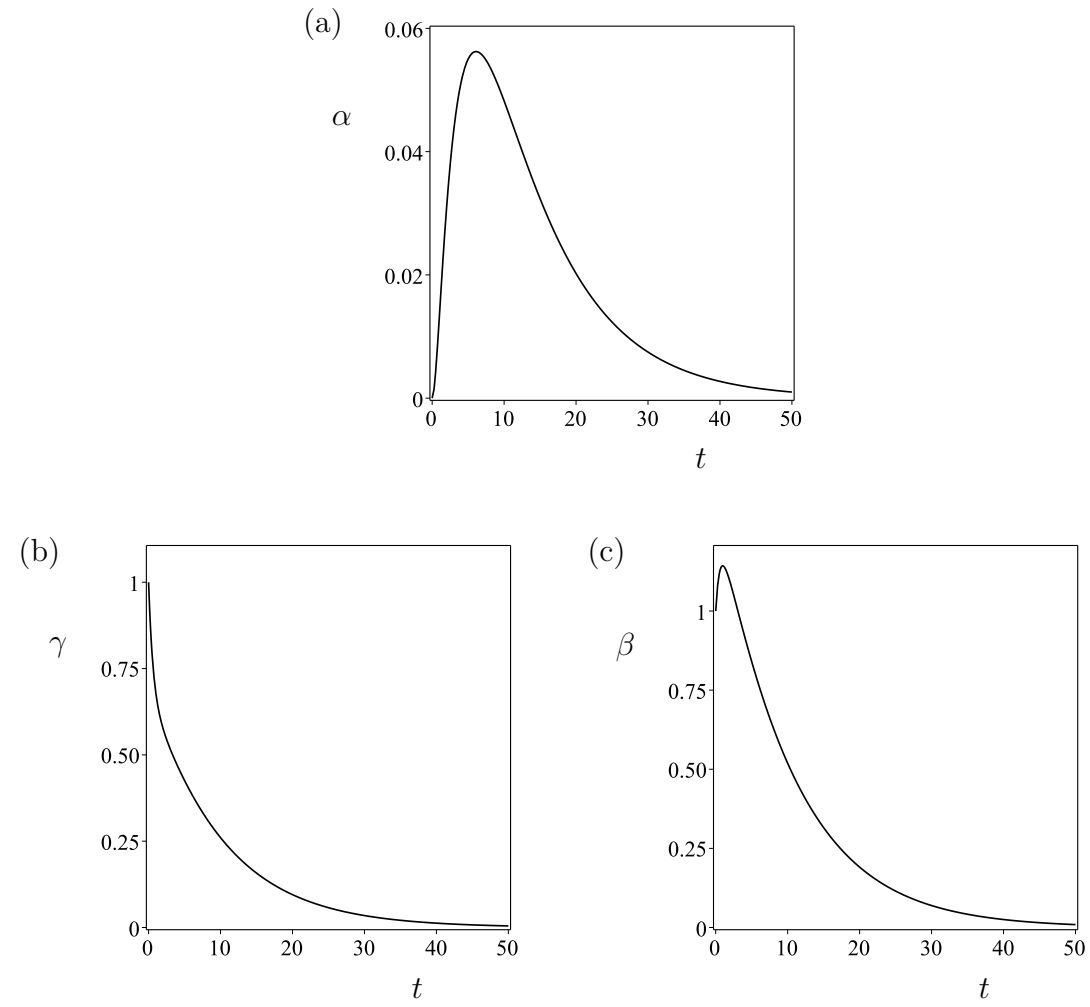

Figure 4.1: Amplitude of the perturbation to (a) the film thickness, (b) the surface concentration, and (c) the bulk concentration, for the linear theory with initial condition $\alpha(0) = 0$, $\gamma(0) = 1$, $\beta(0) = 1$, and where $\mathrm{Ma} = 0.1$, $\mathrm{P_s} = 10$, $\mathrm{P_b} = 10$, $\mathrm{Da_a} = 1$, $\mathrm{Da_d} = 10$.

Figures 4.1–4.3 show plots of the solutions (4.8.7) for the amplitudes $\alpha(t)$, $\gamma(t)$, and $\beta(t)$, in each case the initial condition being chosen to be $\alpha(0) = 0$, $\gamma(0) = 1$, and $\beta(0) = 1$. In Figure 4.1 we have chosen parameter values such that the system is monotonically stable and, in particular, we have chosen $\mathrm{Ma} = 0.1$. In Figure 4.2 we have chosen parameter values such that the system is stable, but oscillates around the equilibrium state and, in particular, have chosen $\mathrm{Ma} = 1$. In Figure 4.3 we have chosen parameter values such that the system is monotonically unstable and, in particular, have chosen $\mathrm{Ma} = 4$. In each of Figures 4.1–4.3 we

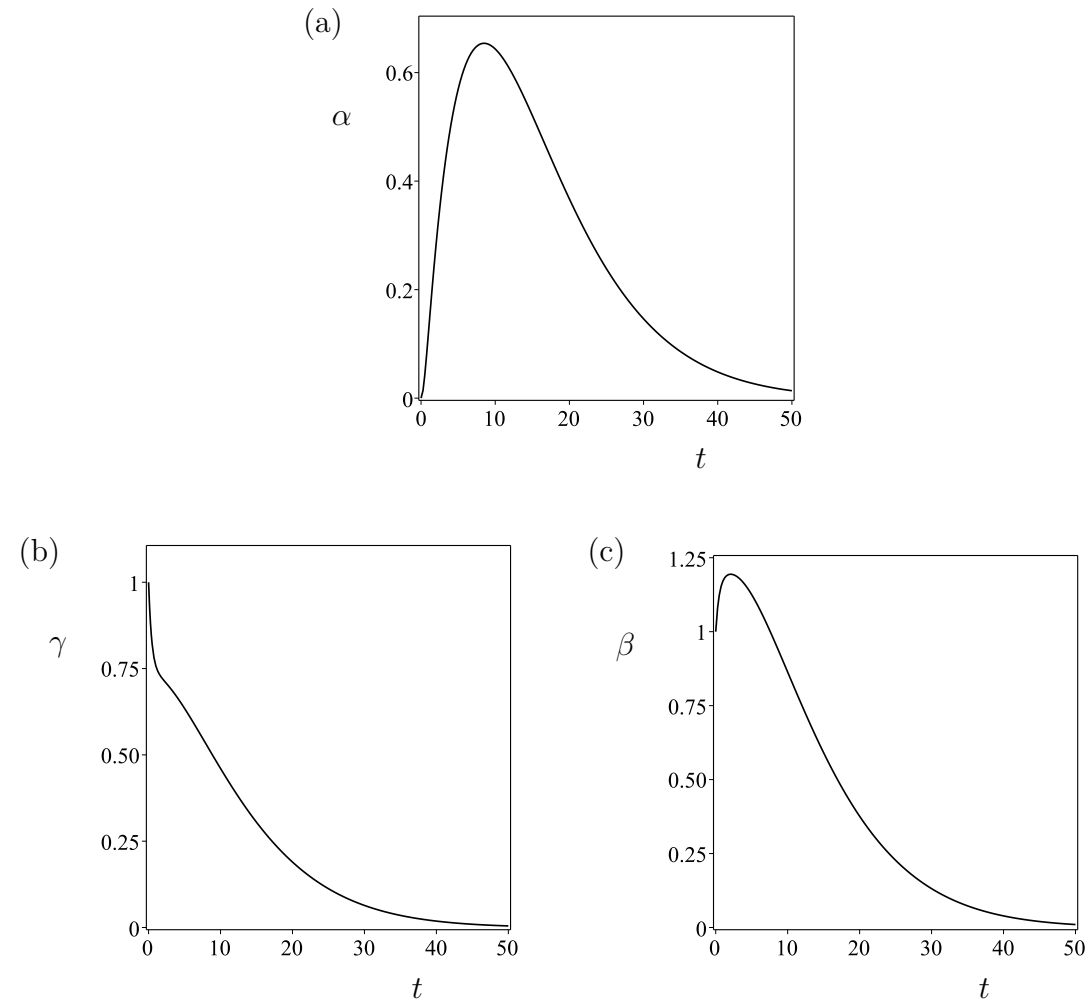

Figure 4.2: As in 4.1, except that Ma = 1.

have set $\mathrm{Da_a} = 1$ and $\mathrm{Da_d} = 10$, in order to delineate the early time evolution from the late time evolution. While these values of the Damköhler numbers are small compared to the values they might take in reality, the solutions do not qualitatively depend of the values of the Damköhler numbers, provided that they are finite (as we will discuss in section 4.12).

In Figures 4.1–4.3, there is a relatively rapid initial change in the amplitudes $\gamma(t)$ and $\beta(t)$, which occurs over a dimensionless time scale of $O(1/\mathrm{Da_a})$ (which is an $O(1)$ timescale for our choice of $\mathrm{Da_a} = 1$). This initial behaviour is due to the effects of the surface–bulk flux, which ensures that the surface and the bulk concentrations will remain close to surface–bulk equilibrium.

In the case shown in Figure 4.1, corresponding to Ma = 0.1, the solution to

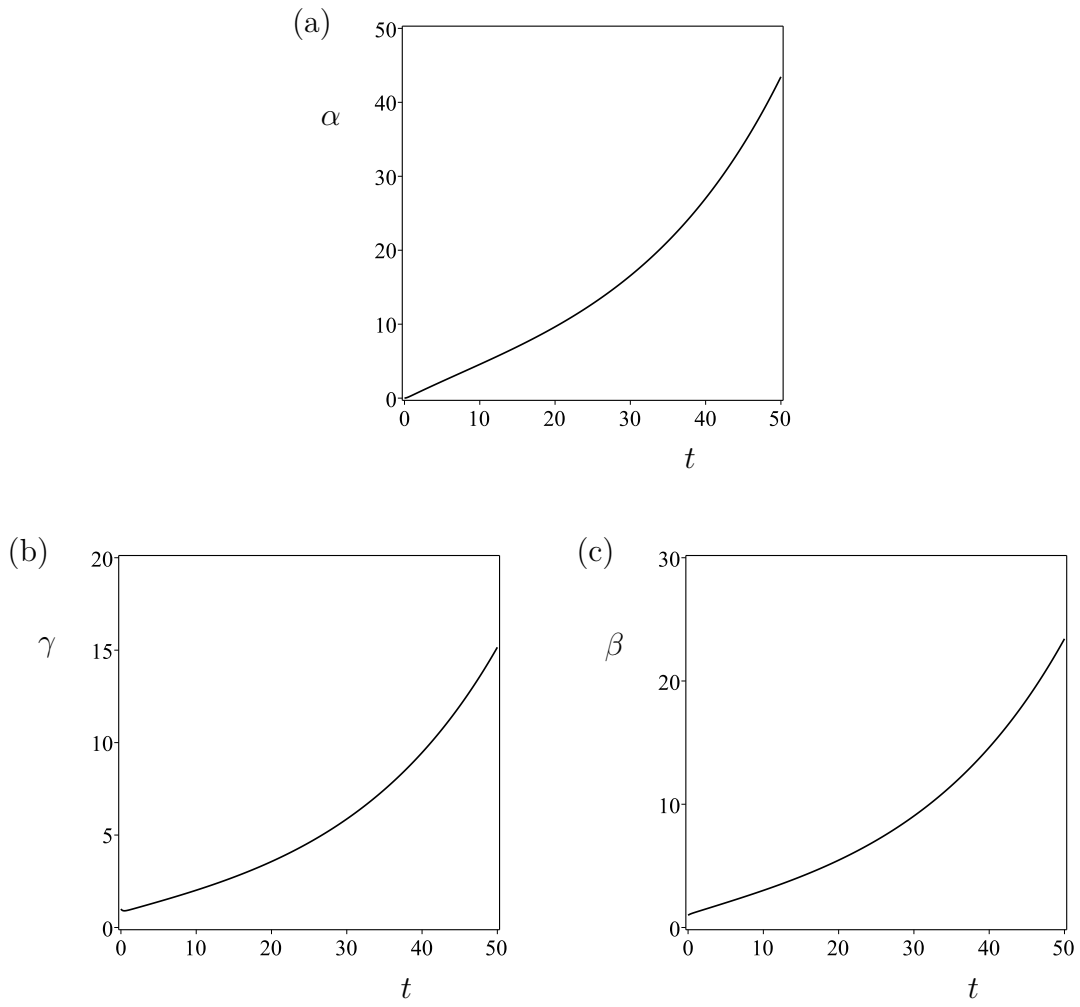

Figure 4.3: As in 4.1, except that Ma = 1.

the linear system (4.8.4)–(4.8.6) is

$$\alpha(t) \simeq 0.16\exp(-0.1t) - 0.18\exp(-0.3t) + 0.02\exp(-1.7t), \tag{4.8.8}$$

$$\gamma(t) \simeq 0.72\exp(-0.1t) - 0.04\exp(-0.3t) + 0.32\exp(-1.7t), \tag{4.8.9}$$

$$\beta(t) \simeq 1.45\exp(-0.1t) - 0.15\exp(-0.3t) - 0.3\exp(-1.7t), \tag{4.8.10}$$

where all three eigenvalues are real and negative, i.e., the system is monotonically stable. The solutions (4.8.8)–(4.8.10) make explicit the behaviour of the system: at short times, all three modes are important, but the mode corresponding to the eigenvalue $\omega_3 \simeq -2.3$ becomes negligible after a short time. Physically, this rapidly decaying mode represents the initial decay caused by the flux of solute. Increasing the Damköhler numbers, that is, increasing the rate at which surface–

bulk equilibrium is established, causes this mode to decay even faster, but does not change the qualitative behaviour of the system. In equation (4.8.10) the coefficient of the rapidly decaying mode is negative, which explains the short period of transient growth seen in Figure 4.1(c). After this short timescale, only the modes with $\omega = \omega_1 \simeq -0.1$ and $\omega = \omega_2 \simeq= -0.3$ are non-negligible, thereafter only the mode with $\omega = \omega_1$ is important, and corresponds to the long-time evolution of the system. Since ω_1 is real and negative, the imposed perturbation to the system will decay monotonically for long time.

Figures 4.1 and 4.2 also show that the amplitudes $\alpha(t)$ and $\beta(t)$ undergo some transient growth before settling down in their long-time monotonic decay. The increase in $\alpha(t)$ is caused by the Marangoni effect induced by the imposed concentration gradients in the initial condition. The increase in $\beta(t)$ is due to the transfer of solute from the surface to the bulk, as mentioned above.

In the case shown in Figure 4.2, corresponding to $\mathrm{Ma} = 1$, the solution to the linear system (4.8.4)–(4.8.6) is

$$\alpha(t) \simeq (-0.11\cos(0.04t) + 5.98\sin(0.04t))\exp(-0.12t) + 0.11\exp(-2.3t), \tag{4.8.11}$$

$$\gamma(t) \simeq (0.74\cos(0.04t) + 2.27\sin(0.04t))\exp(-0.12t) + 0.26\exp(-2.3t), \tag{4.8.12}$$

$$\beta(t) \simeq (1.15\cos(0.04t) + 4.82\sin(0.04t))\exp(-0.12t) - 0.15\exp(-2.3t), \tag{4.8.13}$$

where there is a pair of complex conjugate eigenvalues with $\Re(\omega_1) = \Re(\omega_2) \simeq -0.12$. Since ω_1 and ω_2 are complex but with negative real part the perturbation decays for long time, but oscillates about the equilibrium position as it does so. This happens over a much longer timescale than we have plotted in Figure 4.2, but would be imperceptible even if the plot range were to be extended. Similarly to the case in which $\mathrm{Ma} = 0.1$, the mode with the largest eigenvalue $\omega = \omega_3 \simeq -2.3$ is rapidly decaying, and will be negligible after a short time, after which the oscillatory modes with $\omega = \omega_1$ and $\omega = \omega_2$ dominate for all time. There is also similar transient growth in the amplitudes $\alpha(t)$ and $\beta(t)$, as in the previous case.

In the case shown in Figure 4.3, corresponding to Ma = 4, the solution to the linear system (4.8.4)–(4.8.6) is

$$\alpha(t) \simeq 4.18\exp(0.05t) - 4.31\exp(-0.07t) + 0.13\exp(-4.0t), \tag{4.8.14}$$

$$\gamma(t) \simeq 1.46\exp(0.05t) - 0.64\exp(-0.07t) + 0.18\exp(-4.0t), \tag{4.8.15}$$

$$\beta(t) \simeq 2.25\exp(0.05t) - 1.20\exp(-0.07t) - 0.05\exp(-4.0t), \tag{4.8.16}$$

where there is one positive eigenvalue $\omega_1 \simeq 0.05$, meaning that the system is unstable. At short times, all three modes are important, but the mode corresponding to the largest eigenvalue $\omega_3 \simeq -4.0$ rapidly decays. There is also some transient decay of the perturbations $\alpha(t)$ and $\gamma(t)$ due to the positive coefficients of the mode corresponding to the largest eigenvalue $\omega_3 \simeq -4.0$.

4.9 Thin-Film Stability Analysis: Dispersion Relation

Figures 4.1–4.3 offer only illustrations of the type of behaviour that the solutions (4.8.7) may have. We now investigate exactly what regions of parameter space lead to particular types of behaviour, be it monotonic or oscillatory in nature, or whether the system is stable or unstable.

As in Chapter 3, setting the determinant of the coefficient matrix of the system (4.8.4)–(4.8.6) to zero yields a dispersion relation from which we may obtain the growth rate ω of perturbations of wavenumber $k > 0$. In the thin-film regime, this dispersion relation is simply a cubic polynomial equation in the growth rate ω:

$$\omega^3 + f_2\omega^2 + f_1\omega + f_0 = 0, \tag{4.9.1}$$

where the coefficient f_i for $i = 0, 1, 2$ are real-valued functions of the wavenumber k and of the dimensionless parameters left in the equations, specifically

$$f_0 = \frac{k^6}{12\mathrm{P_b}\mathrm{P_s}}\Big[(\mathrm{MaP_s}K + 4)k^2 + 4\mathrm{P_s}\mathrm{Da_a} + 4K\mathrm{Da_d} + \mathrm{MaP_s}\mathrm{Da_d}K(K-1)\Big], \tag{4.9.2}$$

$$f_1 = \frac{k^2}{12\mathrm{P_b P_s}}\Big\{(\mathrm{MaP_s P_b}K + 4\mathrm{P_s} + 4\mathrm{P_b})k^4 + \left[12(\mathrm{MaP_s}K + 1) + 4\mathrm{P_s}(\mathrm{Da_d}K + \mathrm{P_b Da_a})\right]k^2 + 12\left(\mathrm{P_s Da_a} + K\mathrm{Da_d} + \mathrm{MaP_s Da_d}K(K-1)\right)\Big\}, \quad (4.9.3)$$

$$f_2 = \frac{1}{12\mathrm{P_b P_s}}\Big[4\mathrm{P_s P_b}k^4 + 12(\mathrm{MaP_s P_b}K + \mathrm{P_s} + \mathrm{P_b})k^2 + 12\mathrm{P_s}(\mathrm{P_b Da_a} + K\mathrm{Da_d})\Big]. \quad (4.9.4)$$

It should be noted that (4.9.1) can be obtained directly from the general finite-depth dispersion relation (3.3.29) as follows. If we temporarily label all parameters appearing in (3.3.29), including the wavenumber and growth rate, with a subscript 'g' (for "general"), and similarly label their thin-film counterparts with a subscript 't' (for "thin"), then we may write all of the 'g' parameters in terms of the 't' parameters and the aspect ratio ε as follows:

$$\begin{cases} \mathrm{Ma_g} = \varepsilon^2 \mathrm{Ma_t}, \quad \mathrm{Ca_g} = \mathrm{Ca_t}, \quad \mathrm{P_{s,g}} = \varepsilon^{-3}\ell \mathrm{P_{s,t}}, \\ \mathrm{Da_{a,g}} = \varepsilon^3 \ell \mathrm{Da_{a,t}}, \quad \mathrm{Da_{d,g}} = \varepsilon\ell \mathrm{Da_{d,t}}, \quad \mathrm{P_{b,g}} = \varepsilon^{-3}\ell \mathrm{P_{b,t}}, \\ k_\mathrm{g} = \ell k_\mathrm{t}, \quad d_\mathrm{g} = \frac{\varepsilon}{\ell} d_\mathrm{t}, \quad \omega_\mathrm{g} = \varepsilon^3 \ell \omega_\mathrm{t}, \end{cases} \quad (4.9.5)$$

where $\ell = L_g/L_t$ is the ratio of horizontal length scales between the general finite-depth and thin-film problems; also although $d_\mathrm{t} = 1$, it has been retained in the above expression for d_g for clarity. Substituting (4.9.5) into (3.3.29) and expanding for small ε, the leading order dispersion relation is exactly (4.9.1) with f_i for $i = 0, 1, 2$ given by (4.9.2)–(4.9.4). Note that the ratio ℓ cancels out completely from the 't' dispersion relation, and thus does not appear in (4.9.1).

Since the dispersion relation (4.9.1) is a cubic polynomial in ω, the roots may be obtained explicitly, but they cannot be written in any particularly useful form; however, we can say something about the nature of the three roots.

4.10 Thin-Film Stability Analysis: Marginal Stability and Oscillatory Behaviour

We now further investigate the stability of the thin-film system, and elucidate which parameter regimes will lead to, for example, oscillatory behaviour, or to instability. To do so, as in Chapter 3, we plot stability diagrams in which all but one dimensionless number is held fixed, and we allow only the wavenumber and the remaining dimensionless parameter to vary; this allows us to plot curves in parameter–wavenumber space and determine which regions lead to stability or instability, and to monotonic or oscillatory behaviour. Unlike in Chapter 3, we do not assume that the principle of exchange of stabilities holds, and ω can therefore take complex values.

Since the dispersion relation (4.9.1) is cubic in the growth rate ω, we may make use of the cubic discriminant [116], defined as

$$\Delta = 18 f_2 f_1 f_0 - 4 f_2^3 f_0 + f_2^2 f_1^2 - 4 f_1^3 - 27 f_0^2. \tag{4.10.1}$$

Wherever Δ is positive (4.9.1) will have three real and distinct roots, i.e., perturbations will grow or decay monotonically in time. Wherever Δ is negative (4.9.1) will have one purely real root, and a pair of complex conjugate roots; thus the system will behave in an oscillatory fashion if the complex roots are dominant, and in a monotonic fashion if the real root is dominant. Wherever Δ is zero (4.9.1) will have repeated real roots and, again, the system will behave in a monotonic fashion. Using Δ, then, we may determine regions in which ω is real and those in which ω is complex. It turns out to be the case that one mode (say, ω_3) is always real and negative, and is always sub-dominant to the other two modes. Thus, whenever complex roots occur, the dominant behaviour will be oscillatory in nature.

In order to distinguish between the two possibilities in the stability diagrams, to be shown in Figures 4.4–4.9, we will denote regions in which ω is complex (i.e., in which $\Delta < 0$) by grey shading. In addition, we also plot solid curves corresponding to marginal stability curves, that is, the curves on which $\Re(\omega) = 0$.

Within the grey region the marginal curves are given by $f_2 f_1 - f_0 = 0$, while outside the grey region, the marginal curves are given by $f_0 = 0$. This can be seen by substituting $\omega = \alpha + i\beta$ into (4.9.1) and equating real and imaginary parts. Equating the imaginary parts gives

$$\beta\left(3\alpha^2 + 2f_2\alpha + f_1 - \beta^2\right) = 0, \tag{4.10.2}$$

while equating the real parts gives

$$\alpha^3 + f_2\alpha^2 + f_1\alpha + f_0 - \beta^2(3\alpha + f_2) = 0. \tag{4.10.3}$$

Solving equation (4.10.2) for β we see that either $\beta = 0$ or $\beta^2 = 3\alpha^2 + 2f_2\alpha + f_1$. When $\beta = 0$, i.e., when ω is purely real, the condition $\Re(\omega) = \alpha = 0$ is equivalent to the condition $f_0 = 0$, which is seen by setting $\alpha = \beta = 0$ in equation (4.10.3). The case $\beta = 0$ corresponds to the condition that must be satisfied outside the grey region discussed above. If, instead, we set $\beta^2 = 3\alpha^2 + 2f_2\alpha + f_1 \neq 0$ in (4.10.3) then the condition $\Re(\omega) = \alpha = 0$ is equivalent to the condition $f_2 f_1 - f_1 = 0$. The case $\beta^2 = 3\alpha^2 + 2f_2\alpha + f_0$ corresponds to the condition that must be satisfied inside the grey region. Crossing a solid curve, i.e., crossing a marginal stability curve, shifts the system between stable and unstable states.

In addition, we plot a dashed curve, also given by $f_0 = 0$, which corresponds to the boundary between regions in which there are two unstable modes and regions in which there is only one unstable mode.

The curves and shading described above will, in general, divide wavenumber–parameter space into five distinct regions, labelled U_1, U_2, U_3, S_4, S_5, where U denotes a region in which the system is unstable, and S one in which the system is stable. The meaning and interpretation of each of the five regions, in terms of stable/unstable, real/complex, and the number of unstable roots, if indeed there are any, are given in Table 4.2.

We now present these stability diagrams for each of the parameters in turn, holding fixed all other parameters at reference values given by Table 4.1.

In each of the Figures 4.4–4.9 below, there are two or more plots: part (b) always shows the marginal stability curve over the whole range of possibly unstable wavenumbers, while part (a) shows a zoom in to the small wavenumber

Region	Stability	Nature	Number of unstable roots
U_1	Unstable	Monotonic	1
U_2	Unstable	Monotonic	2
U_3	Unstable	Oscillatory	2
S_4	Stable	Oscillatory	0
S_5	Stable	Monotonic	0

Table 4.2: Definition and interpretation of the regions U_1, U_2, U_3, S_4, and S_5 depending on the roots of (4.9.1).

detail that is not apparent on the larger scale, with the exception of Figure 4.9, in which both (a) and (b) are zoomed in to the small-k detail and (c) is the larger view. Note that in all cases the box used to show the "zooming in" process is not drawn to scale.

4.10.1 Stability Diagram: Marangoni Number Ma

To begin, we fix all of the parameters at their reference values given by Table 4.1, with the exception of the Marangoni number Ma and the wavenumber k, and plot the regions defined in Table 4.2 in the k–Ma plane. We will use this stability diagram, and the associated analysis, to define and quantify certain critical values of Ma denoted $\mathrm{Ma}_{\mathrm{crit}}$ and Ma^*. Figure 4.4 shows the marginal stability diagram for the Marangoni number and shows the positions of the critical values $\mathrm{Ma}_{\mathrm{crit}}$, Ma^*, and $k_{\max}$.

We define $\mathrm{Ma}_{\mathrm{crit}}$ to be the smallest value of Ma for which instability may occur; for $\mathrm{Ma} < \mathrm{Ma}_{\mathrm{crit}}$ the system is stable for all wavenumbers, although the growth rates may, in general, be complex, and so oscillatory levelling is possible, except for the special case $\mathrm{Ma} = 0$, for which the levelling will be monotonic for any wavenumber k.

We also define Ma^* ($> \mathrm{Ma}_{\mathrm{crit}}$) to be the value of Ma above which only *one* unstable mode exists. For $\mathrm{Ma}_{\mathrm{crit}} < \mathrm{Ma} < \mathrm{Ma}^*$ the system is unstable and the growth rates will be complex for some finite range of wavenumbers, with both ω_1

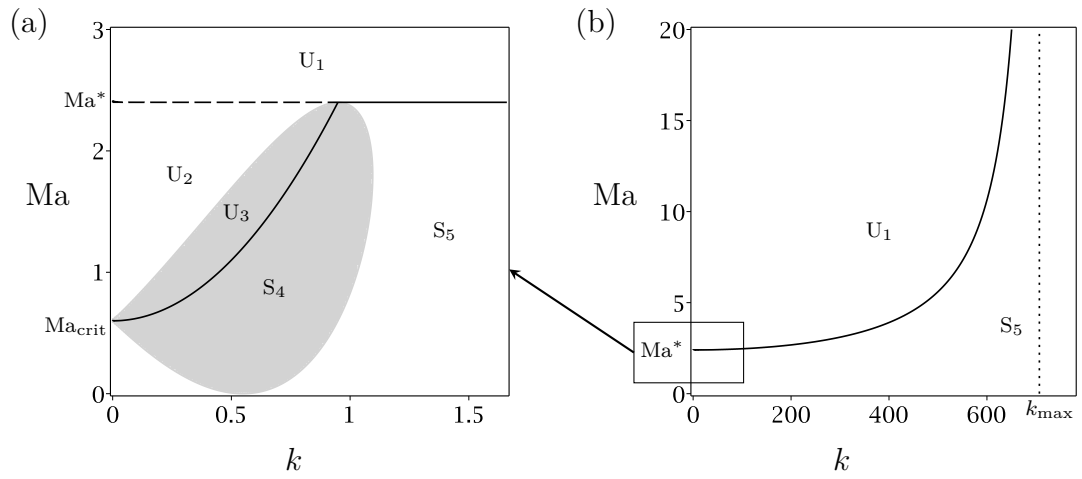

Figure 4.4: Stability diagram for the Marangoni number Ma as a function of the wavenumber k. Part (a) shows a zoom in to the small-k detail of (b). The parameters values used are given in Table 4.1.

and ω_2 having positive real part. For $\mathrm{Ma} > \mathrm{Ma}^*$ the system is unstable and the growth rates are all purely real, with only ω_1 being positive for some finite range of wavenumbers. Both of these critical values of Ma will be quantified later.

At $\mathrm{Ma} = 0$, since the k-axis lies only in region S_5, the system is stable and behaves monotonically for all wavenumbers. The grey region touches the line $\mathrm{Ma} = 0$ at exactly one point (i.e., the boundary of the grey region is tangent to the line $\mathrm{Ma} = 0$).

For $0 < \mathrm{Ma} < \mathrm{Ma}_{\mathrm{crit}}$, the system remains stable, but now there is a band of wavenumbers for which oscillatory stability (i.e., overstability) occurs.

At $\mathrm{Ma} = \mathrm{Ma}_{\mathrm{crit}}$, the system is marginally stable for $k = 0$ and stable for all non-zero k, meaning that the longest-wave perturbation neither grows nor decays. It is interesting to note that the grey region touches the Ma-axis at exactly $\mathrm{Ma} = \mathrm{Ma}_{\mathrm{crit}}$: the onset of instability is therefore oscillatory. Since inside the grey region the solid marginal curve is given by $f_2 f_1 - f_0 = 0$, we may explicitly determine the value of $\mathrm{Ma}_{\mathrm{crit}}$ by looking at the small-k behaviour of the marginal curve, which is

$$\mathrm{Ma} = \mathrm{Ma}_{\mathrm{crit}} + O(k^2), \tag{4.10.4}$$

where

$$\mathrm{Ma}_{\mathrm{crit}} = \frac{K\mathrm{Da}_{\mathrm{d}} + \mathrm{P}_{\mathrm{s}}\mathrm{Da}_{\mathrm{a}}}{\mathrm{P}_{\mathrm{s}}\mathrm{Da}_{\mathrm{d}}K\left(1-K\right)}, \tag{4.10.5}$$

so that $\mathrm{Ma}_{\mathrm{crit}} = 0.6$ for the parameter values given by Table 4.1. As in the infinite-depth case studied in section 3.5, the expression (4.10.5) for $\mathrm{Ma}_{\mathrm{crit}}$ shows that instability becomes more difficult to trigger as $K \to 1$, and as $K \to 0$. Equation (4.10.5) also shows that the Damköhler numbers enter the value of $\mathrm{Ma}_{\mathrm{crit}}$ only through the ratio $\delta = \mathrm{Da}_{\mathrm{d}}/\mathrm{Da}_{\mathrm{a}}$, again mirroring the infinite-depth case.

For $\mathrm{Ma}_{\mathrm{crit}} < \mathrm{Ma} < \mathrm{Ma}^*$ we may draw a horizontal line of constant Ma in Figure 4.4, and move along this line with k increasing from $k = 0$. For the longest waves (i.e., the smallest values of k), the system is in region U_2 and is therefore unstable, with two monotonically unstable modes. Increasing k the systems moves into region U_3, in which it has two unstable but oscillatory modes for a range of values of k, before crossing the solid curve and moving into region S_4, corresponding to a stable, albeit oscillatory, regime. Finally, increasing k further we enter region S_5 and the system becomes monotonically stable as k continues to increase without bound.

For $\mathrm{Ma} = \mathrm{Ma}^*$ the system has one unstable mode and one marginally stable mode, both monotonic for $k = 0$. Increasing k follows the same description as the previous case when $\mathrm{Ma}_{\mathrm{crit}} < \mathrm{Ma} < \mathrm{Ma}^*$. The dashed curve in Figure 4.4 is given by $f_0 = 0$ and so we may look at the small-k behaviour of the marginal curve in order to determine Ma^*, i.e.,

$$\mathrm{Ma} = \mathrm{Ma}^* + O(k^2), \tag{4.10.6}$$

where

$$\mathrm{Ma}^* = \frac{4\left(K\mathrm{Da}_{\mathrm{d}} + \mathrm{P}_{\mathrm{s}}\mathrm{Da}_{\mathrm{a}}\right)}{\mathrm{P}_{\mathrm{s}}\mathrm{Da}_{\mathrm{d}}K\left(1-K\right)} = 4\mathrm{Ma}_{\mathrm{crit}}, \tag{4.10.7}$$

so that $\mathrm{Ma}^* = 2.4$ for the parameter values given in Table 4.1. In particular, it is interesting to note the simple relationship between Ma^* and $\mathrm{Ma}_{\mathrm{crit}}$, namely that $\mathrm{Ma}^* = 4\mathrm{Ma}_{\mathrm{crit}}$

For $\mathrm{Ma} > \mathrm{Ma}^*$ the system is monotonically unstable for sufficiently small values of k lying in region U_1, and stable for sufficiently large values of k lying in region S_5. In this case varying Ma causes much more dramatic changes in the

magnitude of ω than in the case $\mathrm{Ma} < \mathrm{Ma}^*$. For $\mathrm{Ma} < \mathrm{Ma}^*$ the range of unstable wavenumbers grows as Ma increases and, while this is the still the case for $\mathrm{Ma} > \mathrm{Ma}^*$, in the latter case, the range of unstable wavenumbers becomes very large compared to the former case. Indeed, even increasing Ma to, say, $1.01\mathrm{Ma}^*$ extends the range of unstable wavenumbers from between $k = 0$ and $k \simeq 0.95$ when $\mathrm{Ma} = \mathrm{Ma}^* = 2.4$, to between $k = 0$ and $k \simeq 61$ when $\mathrm{Ma} = 1.01\mathrm{Ma}^* = 2.424$. As Ma is increased the range of unstable wavenumbers increases further, but it does not do so without limit: there is a maximum wavenumber, denoted by $k_{\max}$, above which the system is unconditionally stable; this maximum wavenumber is shown as a dotted line in Figure 4.4(b) and corresponds to the k at which the Ma marginal curve blows up, namely

$$k_{\max} = \sqrt{\mathrm{Da_d}\,(1 - K)} \tag{4.10.8}$$

for $K < 1$. We recall that for $K > 1$, the roots of the dispersion relation (4.9.1) are always negative, and so instability is impossible and there is therefore no equivalent of $k_{\max}$.

Other interesting features of Figure 4.4(a) are, for example, the maximum wavenumber for which oscillatory behaviour is possible, and the maximum wavenumber for which two unstable modes may be present. Unfortunately, it has proved impossible to obtain analytical expressions for these special wavenumbers.

4.10.2 Stability Diagram: Surface Péclet Number $\mathrm{P_s}$

The stability diagram for the surface Péclet number $\mathrm{P_s}$ is qualitatively very similar to that for the Marangoni number that we have just discussed, and is shown in Figure 4.5. We define $\mathrm{P_{s,crit}}$ and $\mathrm{P_s}^*$ in an analogous way to how we have defined $\mathrm{Ma_{crit}}$ and Ma^*, i.e., they are the minimum value of $\mathrm{P_s}$ required for instability and for a single unstable mode, respectively.

Since the qualitative description of Figure 4.5 is very similar to that of Figure 4.4, we discuss only the differences. Aside from differences in the particular expression for the critical numbers $\mathrm{P_{s,crit}}$, $\mathrm{P_s}^*$ and $k_{\max}$, the grey region denoting complex values of ω now stretches much further to the right, i.e., to much larger

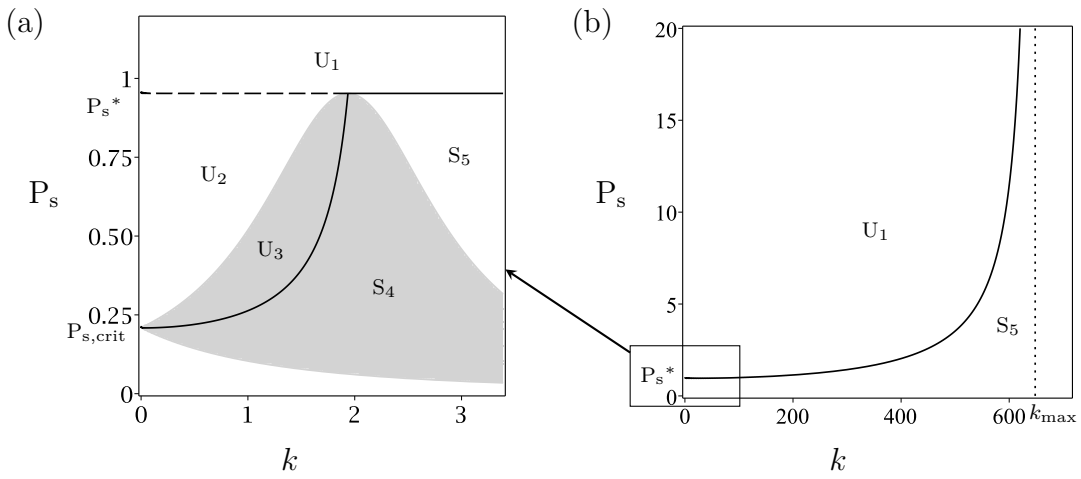

Figure 4.5: Stability diagram for the surface Péclet number $\mathrm{P_s}$ as a function of the wavenumber k. In (a) is shown a zoom in to the small-k detail of (b). The parameters values used are given in Table 4.1.

values of k. While the grey region in Figure 4.4 ended somewhere in the vicinity of $k = 1$, the grey region in Figure 4.5 extends to almost $k = 20$, and narrows as it does; at $k \simeq 19$ it is necessary that $\mathrm{P_s} = O(10^{-4})$ in order to be inside the grey region. Figure 4.6 shows a plot of the grey region in its entirety, confirming what has been said above.

The critical minimum value of $\mathrm{P_s}$ required for instability is given by

$$\mathrm{P_{s,crit}} = \frac{\mathrm{Da_d}}{\mathrm{MaDa_d}K(1-K) - 4\mathrm{Da_a}}, \tag{4.10.9}$$

so that $\mathrm{P_{s,crit}} \simeq 0.23$ for the parameter values given by Table 4.1. Similarly to $\mathrm{Ma_{crit}}$ given in (4.10.5), equation (4.10.9) shows that the ratio $\delta = \mathrm{Da_d}/\mathrm{Da_a}$ is important (as opposed to the values of the individual Damköhler numbers) to triggering instability. Equation (4.10.9) also shows that instability becomes easier to trigger as Ma is increased, with $\mathrm{P_{s,crit}} \to 0$ as $\mathrm{Ma} \to \infty$.

The minimum value of $\mathrm{P_s}$ required to switch between one and two unstable modes is

$$\mathrm{P_s}^* = \frac{4\mathrm{Da_d}}{\mathrm{MaDa_d}K(1-K) - 4\mathrm{Da_a}} = 4\mathrm{P_{s,crit}}, \tag{4.10.10}$$

so that $\mathrm{P_s}^* \simeq 0.92$ for the parameter values given by Table 4.1. Interestingly we have the same simple relationship between $\mathrm{P_s}^*$ and $\mathrm{P_{s,crit}}$ as we had between Ma^*

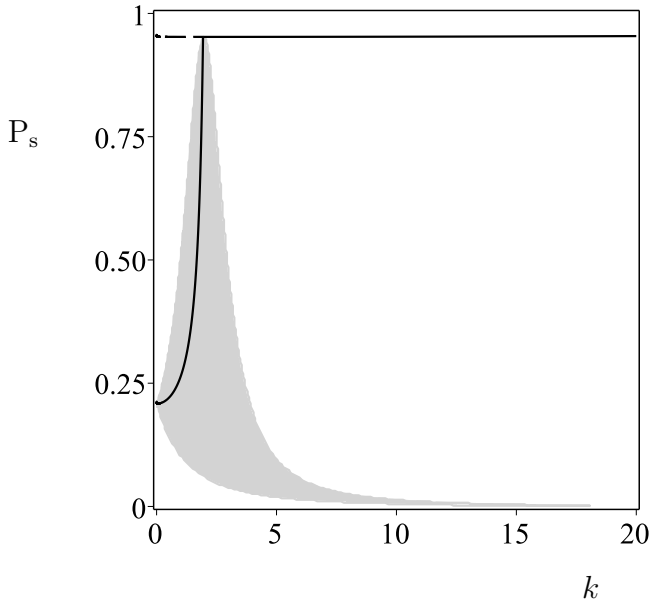

Figure 4.6: As Figure 4.5, but showing the region of complex ω in its entirety.

and $\mathrm{Ma}_{\mathrm{crit}}$, namely that ${P_s}^* = 4P_{s,\mathrm{crit}}$, perhaps suggesting that there is a deeper connection between the two critical values.

Finally, the maximum unstable wavenumber is

$$k_{\max} = \sqrt{\frac{\mathrm{MaDa_d}K(1-K) - 4\mathrm{Da_a}}{\mathrm{Ma}K}}, \tag{4.10.11}$$

and this recovers the equivalent result from the previous case (4.10.8) in the limit $\mathrm{Ma} \to \infty$, as expected.

4.10.3 Stability Diagram: Diffusive Damköhler Number $\mathrm{Da_d}$

The stability diagram for the diffusive Damköhler number $\mathrm{Da_d}$, shown in Figure 4.7, is qualitatively very similar to the previous two cases described in sections 4.10.1 and 4.10.2, but with one difference. Whereas the previous two cases had a wavenumber $k_{\max}$ beyond which instability is impossible, this case does not. With all other parameters fixed, any wavenumber may be unstable, provided that $\mathrm{Da_d}$ is sufficiently large. Apart from this, the description of Figure 4.4 and 4.5 given in section 4.10.1 applies to Figure 4.7.

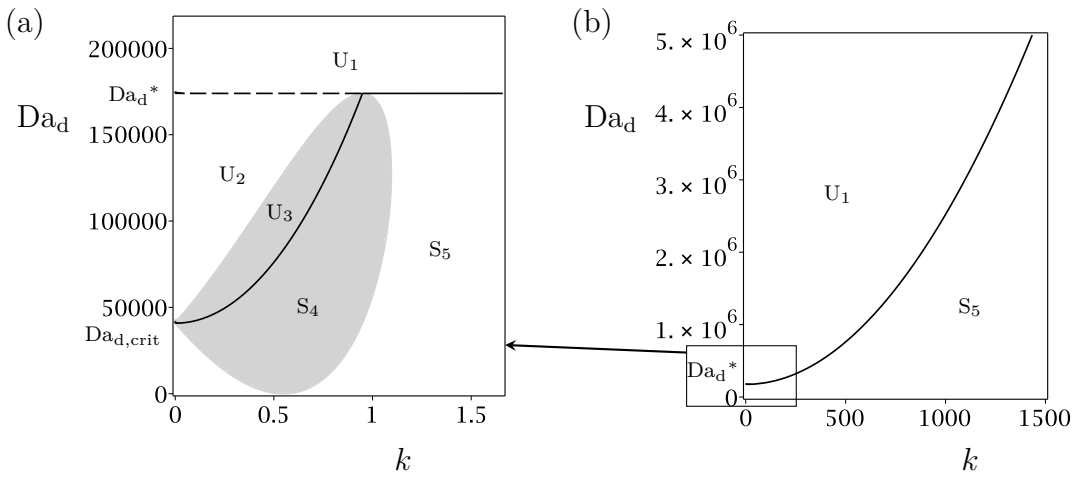

Figure 4.7: Stability diagram for the diffusive Damköhler number $\mathrm{Da_d}$ as a function of the wavenumber k. In (a) is shown a zoom in to the small-k detail of (b). The parameters values used are given in Table 4.1..

The minimum critical value of $\mathrm{Da_d}$ required for instability can again be found by considering the limit $k \to 0$, and is given by

$$\mathrm{Da_{d,crit}} = \frac{\mathrm{P_s Da_a}}{K\left[\mathrm{MaP_s}\left(1-K\right)-4\right]}, \tag{4.10.12}$$

so that $\mathrm{Da_{d,crit}} \simeq 4.7 \times 10^4$ for the parameter values given in Table 4.1. The minimum value of $\mathrm{Da_d}$ required for there to be only one unstable mode can also be found by considering the limit $k \to 0$, and is given by

$$\mathrm{Da_d}^* = \frac{4\mathrm{P_s Da_a}}{K\left[\mathrm{MaP_s}\left(1-K\right)-4\right]} = 4\mathrm{Da_{d,crit}}, \tag{4.10.13}$$

Again, we notice that $\mathrm{Da_d}^* = 4\mathrm{Da_{d,crit}}$. As mentioned above, there is no equivalent of $k_{\max}$ in this case since the curve $f_0 = 0$ is simply quadratic in k, and is given by

$$\mathrm{Da_d} = \frac{\mathrm{P_s Da_a}}{K\left(\mathrm{MaP_s}\left(1-K\right)-4\right)} + \frac{K\mathrm{MaP_s}+4}{K\left(\mathrm{MaP_s}\left(1-K\right)-4\right)}k^2. \tag{4.10.14}$$

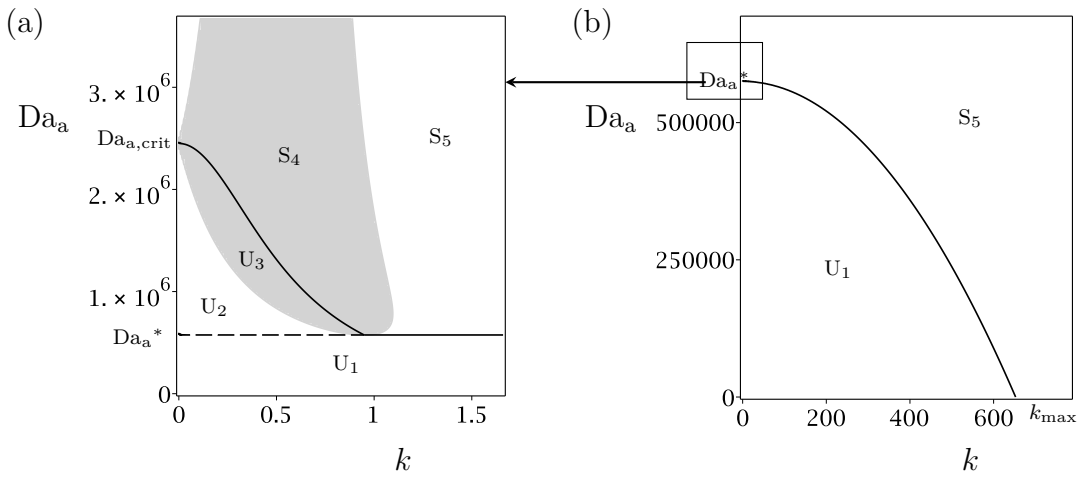

Figure 4.8: Stability diagram for the advective Damköhler number $\mathrm{Da_a}$ as a function of the wavenumber k. In (a) is shown a zoom in to the small-k detail of (b). The parameters values used are given in Table 4.1.

4.10.4 Stability Diagram: Advective Damköhler Number $\mathrm{Da_a}$

The stability diagram for the advective Damköhler number $\mathrm{Da_a}$ is qualitatively different from those we have described thus far. The three parameters that we have considered so far in this section have all been *destabilising*; as Ma, $\mathrm{P_s}$, or $\mathrm{Da_d}$ are increased, the system becomes more unstable. This is in contrast with the parameters $\mathrm{Da_a}$, which is *stabilising*; increasing $\mathrm{Da_a}$ makes the system more stable. In terms of the stability diagram, this essentially flips the picture upside-down compared to those in the previous three cases, with the unstable region lying *below* some critical value. Instead of a critical *minimum* value of $\mathrm{Da_a}$ that is required for instability, there is a critical *maximum* value, i.e., above the value $\mathrm{Da_{a,crit}}$ the system is stable for all k, and below $\mathrm{Da_{a,crit}}$ the system is unstable for a range of k. As in the previous cases, we may obtain an exact expression for $\mathrm{Da_{a,crit}}$ by taking the limit $k \to 0$, in which we obtain

$$\mathrm{Da_{a,crit}} = \frac{\mathrm{Da_d} K \left[\mathrm{MaP_s}\left(1-K\right)-1\right]}{\mathrm{P_s}}, \tag{4.10.15}$$

so that $\mathrm{Da_{a,crit}} \simeq 2.4 \times 10^6$ for the parameter values given by Table 4.1.

Similarly, there is a maximum value of $\mathrm{Da_a}$ required for there to be only one

unstable mode, that is, below the value $\mathrm{Da_a}^*$ there will be one unstable mode, and above the system will either have two unstable modes (if $\mathrm{Da_a} < \mathrm{Da_{a,crit}}$) or will be stable (if $\mathrm{Da_a} > \mathrm{Da_{a,crit}}$). By taking the limit $k \to 0$ we may obtain an explicit expression for $\mathrm{Da_a}^*$, namely

$$\mathrm{Da_a}^* = \frac{4\mathrm{Da_d}K\left[\mathrm{MaP_s}\left(1-K\right)-1\right]}{\mathrm{P_s}}, \tag{4.10.16}$$

so that $\mathrm{Da_a}^* \simeq 0.6 \times 10^6$ for the parameter values given by Table 4.1, and we notice that $\mathrm{Da_a}^* = \mathrm{Da_{d,crit}}/4$, which is "upside down" compared to the previous results.

Finally, there is a maximum unstable wavenumber $k_{\max}$, but instead of being a point of blow-up in the $\mathrm{Da_a}$ marginal curve, it is instead the zero of the $\mathrm{Da_a}$ marginal curve, i.e., the value of k for which $f_0 = 0$, and is given by

$$k_{\max} = \sqrt{\frac{\mathrm{Da_d}K\left[\mathrm{MaP_s}\left(1-K\right)\right]}{\mathrm{MaP_s}K+4}}. \tag{4.10.17}$$

4.10.5 Stability Diagram: Equilibrium Rate Constant K

The final stability diagram we consider is that for the equilibrium rate constant K. Figure 4.9 shows the stability diagram for K, with Figure 4.9(c) showing the stability diagram over the whole range of unstable wavenumbers, and Figures 4.9(a) and 4.9(b) showing a zoom in of the small-k behaviour of the top and bottom portions of the solid curve, respectively.

The most striking feature of the large-scale plot shown in Figure 4.9(c) is the significant qualitative difference from the corresponding plots shown in the previous sections (i.e., from Figures 4.4(b)–4.8(b)). Instead of the monotonic behaviour that is shown in the previous figures, with the unstable region above the solid curves (or below in the case of $\mathrm{Da_a}$), and the stable region below (or above in the case of $\mathrm{Da_a}$), the unstable region in Figure 4.9(c) lies in a "bubble" enclosed by the solid curves. However, It is clear that, while the picture may appear somewhat different at first, the fine detail is similar to what we have already seen. Near $K = K_{\mathrm{crit}}^-$, varying K causes the system to behave in the same manner as, for example, varying Ma in Figure 4.4: increasing K destabilises the

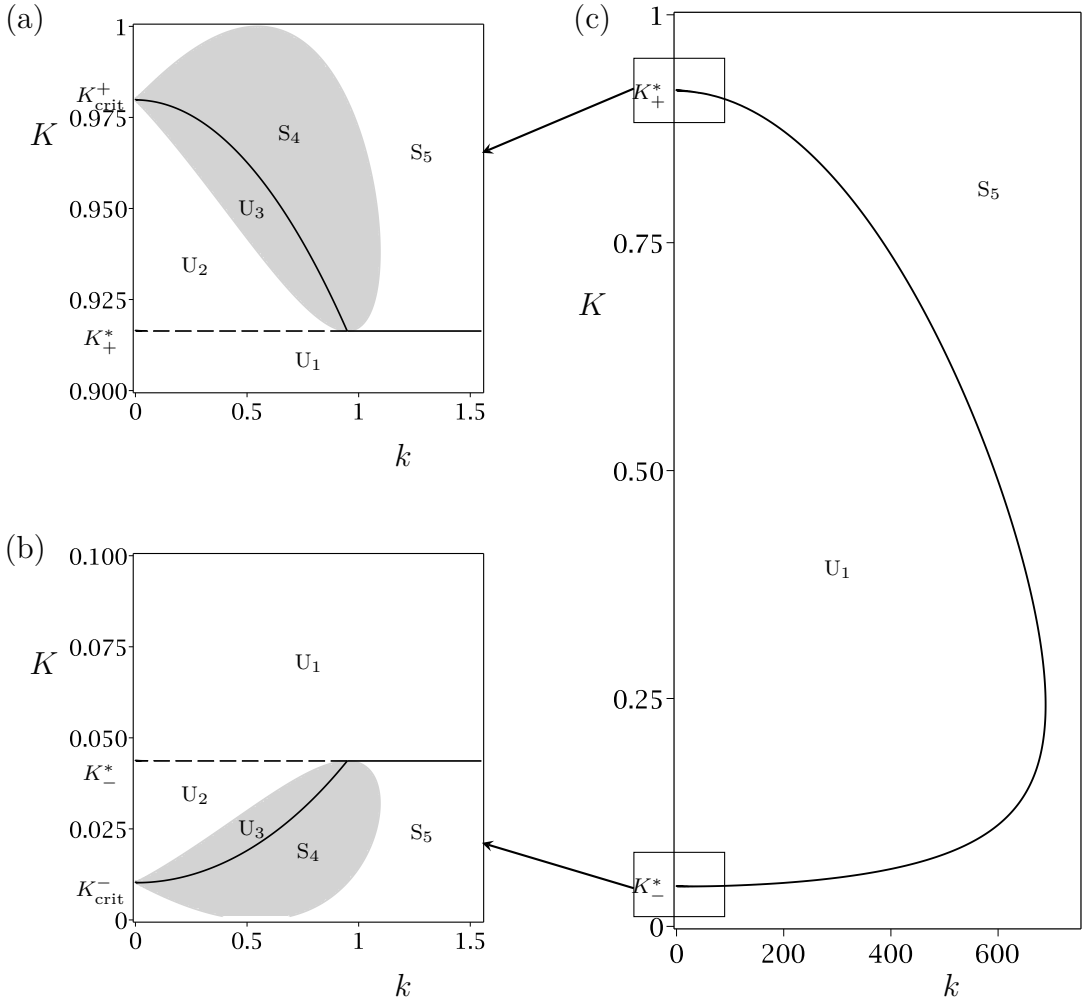

Figure 4.9: Stability diagram for the equilibiurm rate constant K as a function of the wavenumber k. In (a) and (b) are shown zooms in to the small-k details of (c). The parameters values used are given in Table 4.1.

system, and the description is very similar to that given in sections 4.10.1–4.10.3. On the other hand, near $K = K^+_{\rm crit}$, varying K causes the system to behave in the same manner as $\mathrm{Da_a}$ in Figure 4.8: increasing K stabilises the system, and the description is very similar to that given in section 4.10.4.

The maximum and minimum values of K required to switch between one and two unstable modes are given by

$$K^*_\pm = \frac{\mathrm{Da_d}\left(\mathrm{MaP_s}-4\right) \pm \sqrt{{\mathrm{Da_d}}^2\left(\mathrm{MaP_s}-4\right)^2 - 16{\mathrm{MaP_s}}^2\mathrm{Da_d}\mathrm{Da_a}}}{2\mathrm{MaP_s}\mathrm{Da_d}}, \qquad (4.10.18)$$

and the critical maximum and minimum values of K required for instability are

given by

$$K^{\pm}_{\text{crit}} = \frac{\text{Da}_\text{d}\left(\text{MaP}_\text{s} - 1\right) \pm \sqrt{{\text{Da}_\text{d}}^2\left(\text{MaP}_\text{s} - 1\right)^2 - 4{\text{MaP}_\text{s}}^2\text{Da}_\text{d}\text{Da}_\text{a}}}{2\text{MaP}_\text{s}\text{Da}_\text{d}}. \qquad (4.10.19)$$

Additionally, there exists a maximum unstable wavenumber k_{max}, but we have been unable to obtain an analytical expression for this special wavenumber.

4.11 Thin-Film Stability Analysis: Growth Rates

Figures 4.10 and 4.11 show illustrative plots of $\Re(\omega_1)$ and $\Re(\omega_2)$ (we omit ω_3 for now, since it is always sub-dominant to the other two modes, i.e., it is always more negative than the other two roots), when the Marangoni number Ma is varied, from zero to above the critical value at $\text{Ma} = \text{Ma}^*$. The thick solid curves represent $\Re(\omega_1)$ when ω_1 is purely real, the thin solid curves represent $\Re(\omega_2)$ when ω_2 is purely real, and the dashed curves represent $\Re(\omega_1)$ and $\Re(\omega_2)$ when both ω_1 and ω_2 have non-zero imaginary part. On the thick and the thin solid curves, the perturbations to the system will either grow or decay monotonically, depending on the sign of the dominant (i.e., the least negative value of) ω. However, on the dashed curve, the perturbation will grow or decay in an oscillatory manner, depending on the sign of $\Re(\omega)$.

Figure 4.10 shows illustrative plots of the growth rate ω for $\text{Ma} < \text{Ma}^*$. Figure 4.10(a) shows a plot of ω_1 and ω_2 when $\text{Ma} = 0$, and corresponds exactly to the thin-film limit of the Orchard mode of levelling (thin solid line) given by (3.4.3), and the pure-diffusive mode (thick solid line) given by (3.4.7). Figure 4.10(b) shows the corresponding plot for $0 < \text{Ma} < \text{Ma}_{\text{crit}}$ and illustrates the situation in which the system is stable, but with oscillatory decay for a finite range of wavenumbers. Figure 4.10(c) shows how the system behaves at exactly $\text{Ma} = \text{Ma}_{\text{crit}}$, with oscillatory decay for a finite range of wavenumbers from $k = 0$. This value of Ma is the lowest for which instability is seen and demonstrates that the onset of instability is oscillatory and occurs in the long-wave limit corresponding to $k = 0$. Figure 4.10(d) shows the situation for $\text{Ma}_{\text{crit}} < \text{Ma} < \text{Ma}^*$, in which the system is unstable for a finite range of wavenumbers, and demonstrates that

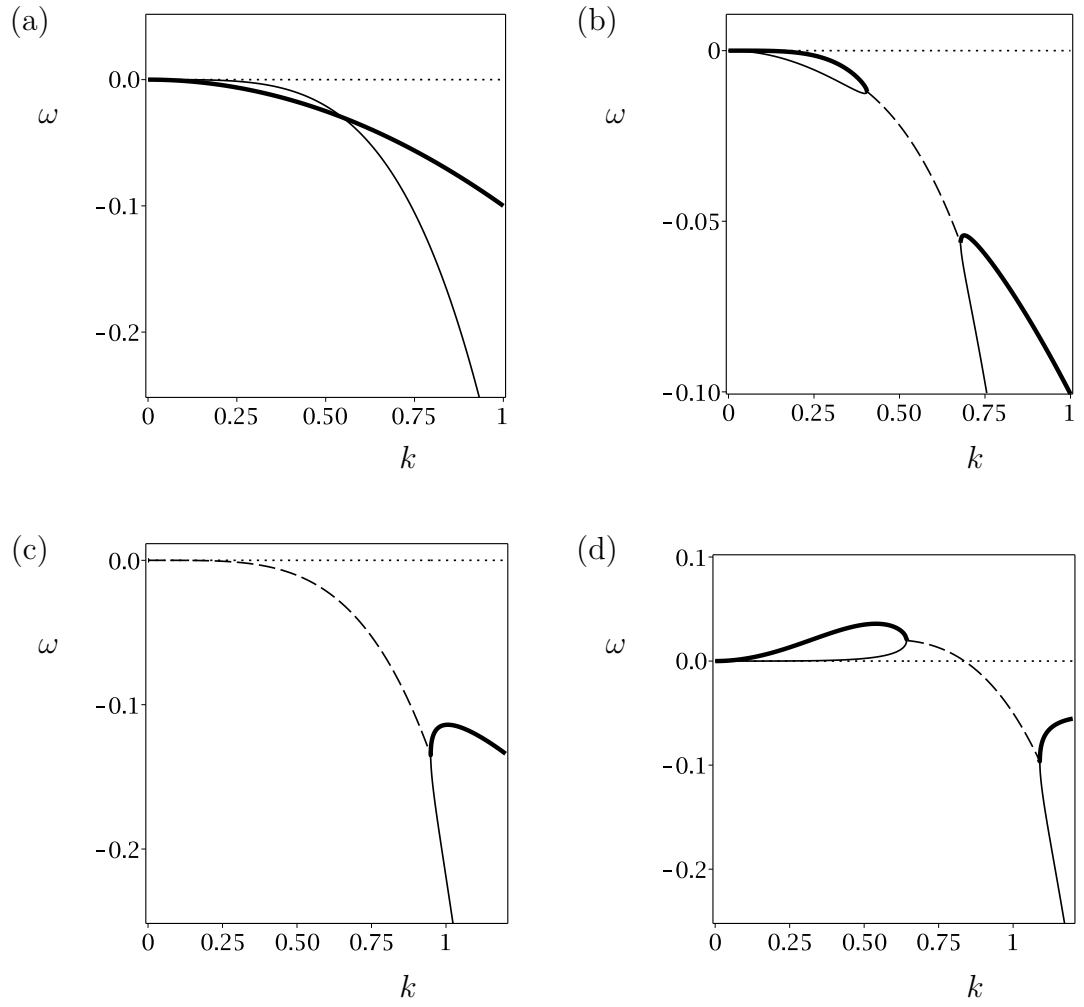

Figure 4.10: Illustrative plots of $\Re(\omega_1)$ and $\Re(\omega_2)$ when Ma is varied, but below the value of $\mathrm{Ma}^* = 2.4$, for the parameter values given in Table 4.1, and (a) $\mathrm{Ma} = 0$, (b) $\mathrm{Ma} = 0.1$ (so that $0 < \mathrm{Ma} < \mathrm{Ma}_{\mathrm{crit}} = 0.6$), (c) $\mathrm{Ma} = \mathrm{Ma}_{\mathrm{crit}} = 0.6$, (d) $\mathrm{Ma} = 2$ (so that $0.6 = \mathrm{Ma}_{\mathrm{crit}} < \mathrm{Ma} < \mathrm{Ma}^* = 2.4$). The thick solid lines represent ω_1, the thin solid line represents ω_2, the dashed line denotes the real part of ω_1 and ω_2 when the imaginary part is non-zero, and the dotted line is simply $\omega = 0$.

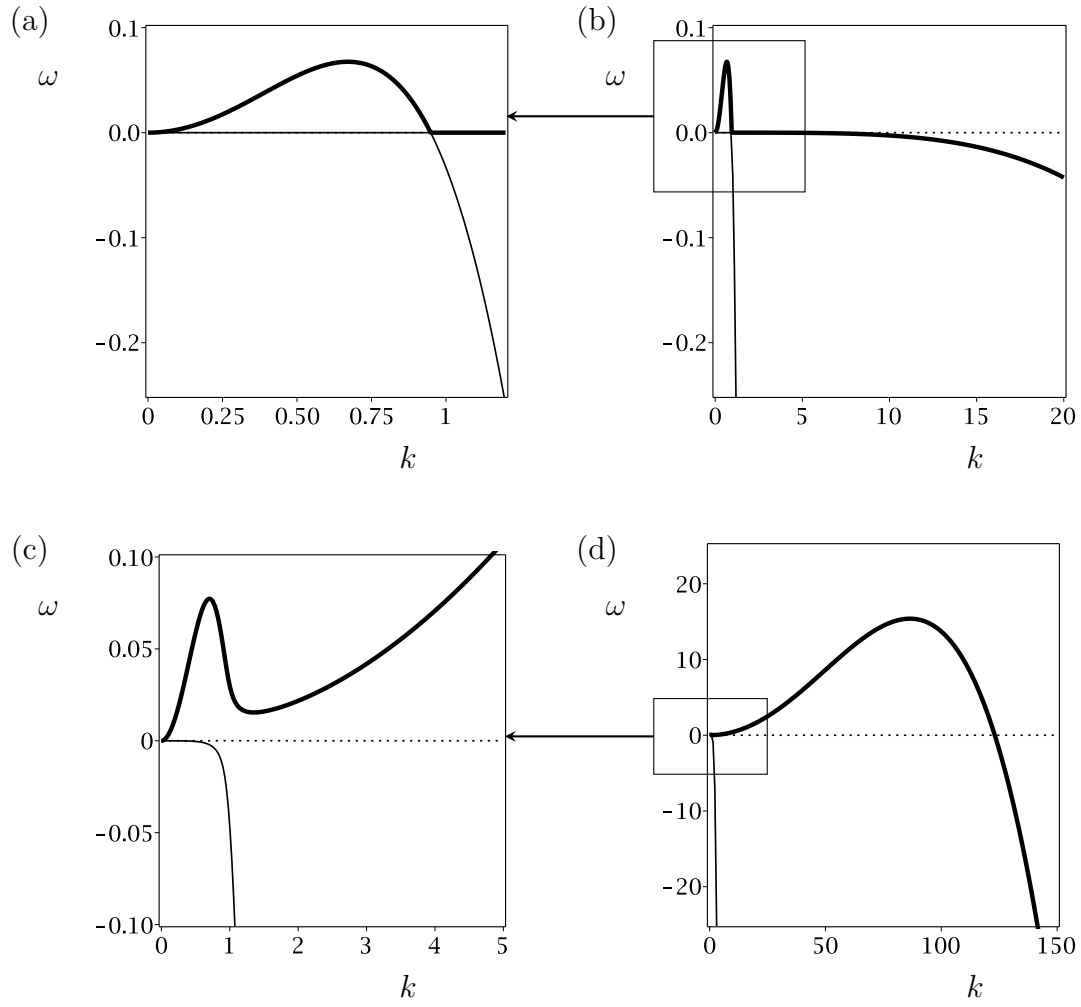

Figure 4.11: Illustrative plots of $\Re(\omega_1)$ and $\Re(\omega_2)$ when Ma is varied, but at or above the value of $\mathrm{Ma}^* = 2.4$, for the parameter values given in Table 4.1, and (a) $\mathrm{Ma} = \mathrm{Ma}^* = 2.4$, zoomed in, (b) $\mathrm{Ma} = \mathrm{Ma}^* = 2.4$, (c) $\mathrm{Ma} = 2.5$ (so that $\mathrm{Ma} > \mathrm{Ma}^* = 2.4$), zoomed in, (d) $\mathrm{Ma} = 2.5$ (so that $\mathrm{Ma} > \mathrm{Ma}^* = 2.4$). The thick solid lines represent ω_1, the thin solid line represents ω_2, the dashed line denotes the real part of ω_1 and ω_2 when the imaginary part is non-zero, and the dotted line is simply $\omega = 0$.

both monotonic and oscillatory instability are possible.

Figure 4.11 shows illustrative plots for $\mathrm{Ma} \geq \mathrm{Ma}^*$. Both Figure 4.11(a) and 4.11(b) show the growth rates $\Re(\omega_1)$ and $\Re(\omega_2)$ when $\mathrm{Ma} = \mathrm{Ma}^*$, with (a) zoomed in to show the small-k detail. When $\mathrm{Ma} = \mathrm{Ma}^*$, the system switches from having two unstable modes to having one unstable mode, and so this is also the value of Ma at which the growth rates can no longer be complex, i.e., at or above $\mathrm{Ma} = \mathrm{Ma}^*$ the system behaves in a monotonically unstable fashion. Figures 4.11(c) and 4.11(d) illustrate how the system behaves when $\mathrm{Ma} > \mathrm{Ma}^*$. Just above $\mathrm{Ma} = \mathrm{Ma}^*$, a small variation of Ma causes a large variation in not only the magnitude of the growth rates, but also the width of the range of unstable wavenumbers. This rapid change in the monotonically unstable behaviour of the system becomes less pronounced as Ma is increased further from $\mathrm{Ma} = \mathrm{Ma}^*$ and there is a maximum unstable wavenumber $k_{\max}$ beyond which the system is always stable, regardless of the value of Ma, which is given by $k = k_{\max}$.

4.12 Thin Film Stability: Large Damköhler Numbers Limit

In practice, as we have already seen in sections 4.5.1 and 4.6.1, the numerical values of $\mathrm{Da_d}$ and $\mathrm{Da_a}$ are very large relative to all other parameters in the thin-film problem. In fact, the values of the Damköhler numbers given in Table 4.1 that we consider in the previous sections are, if anything, on the *low* side of what is possible, as they assume only moderately fast flux kinetics [11]. We are, therefore, motivated to look at the limit of large Damköhler numbers, i.e., the limit $\mathrm{Da_d}, \mathrm{Da_a} \to \infty$.

From the stability analysis of the infinite-depth regime in section 3.5 and the stability analysis of the thin-film problem in the previous section we suspect that it is the ratio $\delta = \mathrm{Da_d}/\mathrm{Da_a}$ that is important rather than the individual values of $\mathrm{Da_d}$ and $\mathrm{Da_a}$. Thus, we consider the distinguished limit $\mathrm{Da_d} \to \infty$, $\mathrm{Da_a} \to \infty$ in which $\delta = \mathrm{Da_d}/\mathrm{Da_a} = O(1)$ is held fixed. We must be careful, however, to scale k and ω appropriately in order for the large Damköhler numbers expansion

of (4.9.1) to lead to consistent solutions for ω.

From the analysis in the preceding sections, we have seen that the maximum possibly unstable wavenumber is always proportional to $\sqrt{\mathrm{Da_a}}$ (see equations (4.10.8), (4.10.11), (4.10.17)), and so the appropriate scaling of k is $k = \sqrt{\mathrm{Da_a}}\hat{k}$, where $\hat{k}$ is $O(1)$.

To determine the appropriate scaling for ω, we substitute $k = \sqrt{\mathrm{Da_a}}\hat{k}$ and $\omega = {\mathrm{Da_a}}^{\alpha}\hat{\omega}$, along with $\mathrm{Da_d} = \delta\mathrm{Da_a}$, into the dispersion relation (4.9.1) to obtain

$$g_1{\mathrm{Da_a}}^4\omega + g_2{\mathrm{Da_a}}^{2+\alpha} + g_3{\mathrm{Da_a}}^{3+\alpha} + g_4{\mathrm{Da_a}}^{1+2\alpha} = 0, \tag{4.12.1}$$

where the g_i for $i = 1, 2, 3, 4$ are functions of the other parameters, including $\hat{k}$ and $\hat{\omega}$. By seeking the dominant balances in equation (4.12.1) in the limit $\mathrm{Da_a} \to \infty$, we find that the only consistent choices for α are $\alpha = 2$ and $\alpha = 1$, and these choices lead to different solutions for $\hat{\omega}$.

Substituting the former solution, namely $\omega = {\mathrm{Da_a}}^2\hat{\omega}$, along with our chosen scaling for $k = \sqrt{\mathrm{Da_a}}\hat{k}$ into the dispersion relation (4.9.1), writing $\mathrm{Da_d} = \delta\mathrm{Da_a}$, and expanding for $\mathrm{Da_a} \to \infty$, we find that the leading order dispersion relation is

$$\hat{\omega}^2\left(3\hat{\omega} + \hat{k}^4\right) = 0, \tag{4.12.2}$$

from which we obtain $\hat{\omega} = -\hat{k}^4/3$, which is exactly the long–wave limit of the Orchard levelling mode (3.4.3).

If we instead use the latter solution, namely $\omega = \mathrm{Da_a}\hat{\omega}$, we obtain the leading order dispersion relation

$$\begin{aligned} &4\mathrm{P_s}\mathrm{P_b}\hat{\omega}^2 + \left[\left(\mathrm{Ma}\mathrm{P_b}\mathrm{P_s}K + 4\left(\mathrm{P_b} + \mathrm{P_s}\right)\right)\hat{k}^2 + 4\mathrm{P_s}\left(\delta K + \mathrm{P_b}\right)\right]\hat{\omega} \\ &\qquad + \hat{k}^2\left[\left(\mathrm{Ma}\mathrm{P_s}K + 4\right)\hat{k}^2 - \left(\mathrm{Ma}\mathrm{P_s}\delta K\left(1 - K\right) - 4\left(\delta K + \mathrm{P_s}\right)\right)\right] = 0. \end{aligned} \tag{4.12.3}$$

Figure 4.12 shows plots comparing the appropriately scaled exact solutions of the dispersion relation (4.9.1), along with the corresponding leading order asymptotic approximation $\omega = \mathrm{Da_a}\hat{\omega}$ with $\hat{\omega}$ obtained from (4.12.3) for large but finite values of $\mathrm{Da_a}$. In all three cases shown the large-$\mathrm{Da_a}$ asymptotic solutions capture the dominant mode fairly well, except near $k = 0$ where the long wave detail present

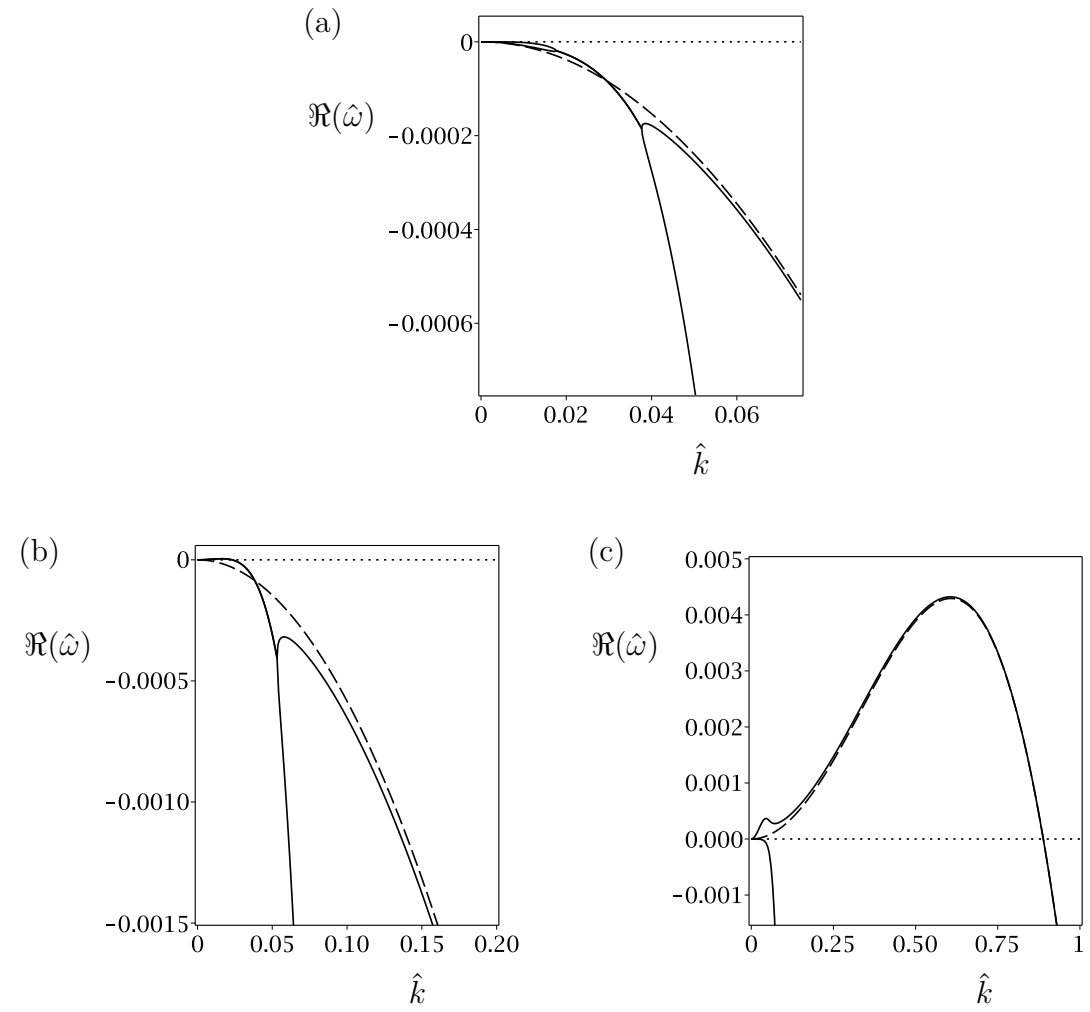

Figure 4.12: Typical plots of the exact value of (solid), and the large Damköhler number asymptotic approximation to (dashed) $\Re(\hat{\omega}(\hat{k}))$, for the parameter values given in Table 4.1, and (a) $\mathrm{Ma} = 0.1$, (b) $\mathrm{Ma} = 1$, (c) $\mathrm{Ma} = 3$.

in the full thin-film solutions disappears. In particular, the system does not behave in an oscillatory fashion in the limit $\mathrm{Da_a}$, $\mathrm{Da_d} \to \infty$.

To expand upon this last point: for any finite values of $\mathrm{Da_a}$, $\mathrm{Da_d}$, the system may behave in either a monotonic or an oscillatory fashion, but the regions of long-wave detail near $k = 0$ shown in Figures 4.4–4.9(a) along with Figure 4.9(b) become smaller and the regions of monotonic behaviour become larger as $\mathrm{Da_a}$ and $\mathrm{Da_d}$ are increased, and the regions of complex behaviour vanish in the limit $\mathrm{Da_a} \to \infty$. In practice, the values of the Damköhler numbers are large but finite, and so, in reality, the fine detail will always be present in a small region near

$k = 0$.

We may show explicitly from equations (4.7.1)–(4.7.3) that no oscillatory behaviour is possible in the limit $\mathrm{Da_a} \to \infty$, and also show that there is a separation of timescales into an early timescale, of $O(1/\mathrm{Da_a})$, over which the flux acts, and a longer timescale over which capillarity, diffusion and the Marangoni effect act. To do so, we define a new timescale $t = {\mathrm{Da_a}}^{-\alpha}\tau$, where $\tau = O(1)$ and we take the limit $\mathrm{Da_a} \to \infty$, with all other parameters remaining $O(1)$. Substituting this new timescale into equations (4.7.1)–(4.7.3), and expanding h, s and c as power series in the small parameter $1/\mathrm{Da_a} \ll 1$, namely,

$$h = h_0 + {\mathrm{Da_a}}^{-\alpha} h_1 + O({\mathrm{Da_a}}^{-2\alpha}), \tag{4.12.4}$$

$$s = s_0 + {\mathrm{Da_a}}^{-\alpha} s_1 + O({\mathrm{Da_a}}^{-2\alpha}), \tag{4.12.5}$$

$$c = c_0 + {\mathrm{Da_a}}^{-\alpha} c_1 + O({\mathrm{Da_a}}^{-2\alpha}), \tag{4.12.6}$$

we obtain

$$\frac{\partial h_0}{\partial \tau} + {\mathrm{Da_a}}^{-\alpha}\left\{\frac{\partial h_1}{\partial \tau} + \frac{\partial}{\partial x}\left[\frac{1}{3\mathrm{Ca}}\frac{\partial^3 h_0}{\partial x^3}h_0^3 - \frac{\mathrm{Ma}}{2}h_0^2\frac{\partial}{\partial x}(s_0 - c_0)\right]\right\} + O({\mathrm{Da_a}}^{-2\alpha}) = 0, \tag{4.12.7}$$

$$\underbrace{\frac{\partial s_0}{\partial \tau}} + {\mathrm{Da_a}}^{-\alpha}\left\{\frac{\partial s_1}{\partial \tau} + \frac{\partial}{\partial x}\left[\frac{1}{2\mathrm{Ca}}\frac{\partial^3 h_0}{\partial x^3}h_0^2 s_0 - \mathrm{Ma}h_0 s_0\frac{\partial}{\partial x}(s_0 - c_0)\right] - \frac{1}{\mathrm{P_s}}\frac{\partial^2 s_0}{\partial x^2}\right\} - \underbrace{{\mathrm{Da_a}}^{1-\alpha}(Kc_0 - s_0)} - {\mathrm{Da_a}}^{1-2\alpha}(Kc_1 - s_1) + O({\mathrm{Da_a}}^{-2\alpha}) = 0, \tag{4.12.8}$$

$$\underbrace{h_0\frac{\partial c_0}{\partial \tau}} + {\mathrm{Da_a}}^{-\alpha}\left\{h_0\frac{\partial c_1}{\partial \tau} + h_1\frac{\partial c_0}{\partial x} + \left[\frac{1}{3\mathrm{Ca}}\frac{\partial^3 h_0}{\partial x^3}h_0^3 - \mathrm{Ma}h_0^2\frac{\partial}{\partial x}(s_0 - c_0)\right]\frac{\partial c_0}{\partial x} - \frac{1}{\mathrm{P_s}}\frac{\partial}{\partial x}\left(h_0\frac{\partial c_0}{\partial x}\right)\right\} + \underbrace{\delta{\mathrm{Da_a}}^{1-\alpha}(Kc_0 - s_0)} + \delta{\mathrm{Da_a}}^{1-2\alpha}(Kc_1 - s_1) + O({\mathrm{Da_a}}^{-2\alpha}) = 0. \tag{4.12.9}$$

In order to balance the underbraced terms to leading order (for a non-trivial balance of terms), we require that $\alpha = 1$, in which case the leading order system

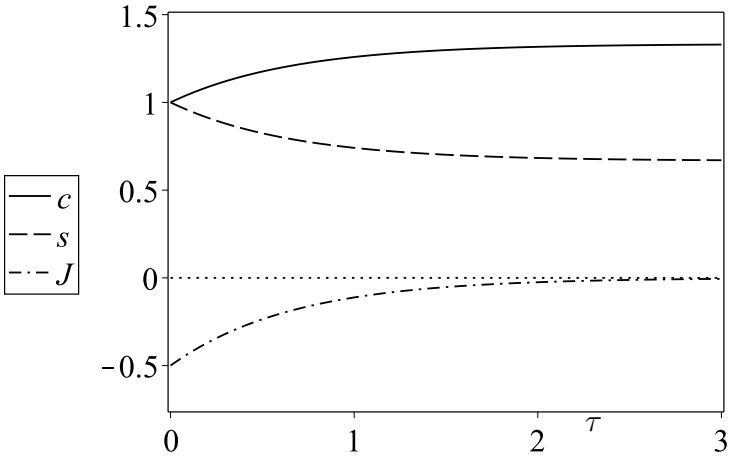

Figure 4.13: Evolution towards $J = 0$ of the leading order surface concentration (dashed line), the bulk concentration (solid line), and the flux $J = Kc_0 - s_0$ (dash-dot line), for an anti-surfactant with $K = 1/2$, and where the initial condition is $s = 1$, $c = 1$.

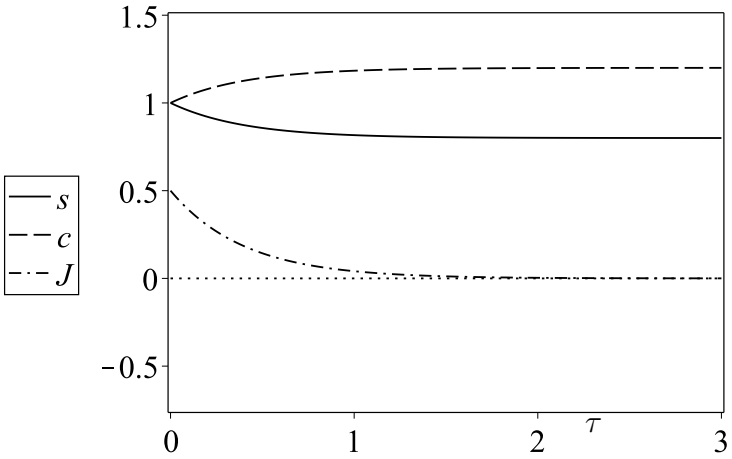

Figure 4.14: Evolution towards $J = 0$ of the leading order surface concentration (dashed line), the bulk concentration (solid line), and the flux $J = Kc_0 - s_0$ (dash-dot line), for a surfactant with $K = 3/2$, and where the initial condition is $s = 1$, $c = 1$.

reduces dramatically to

$$\frac{\partial h_0}{\partial \tau} = O(\frac{1}{\mathrm{Da_a}}), \tag{4.12.10}$$

$$\frac{\partial s_0}{\partial \tau} = Kc_0 - s_0 + O(\frac{1}{\mathrm{Da_a}}), \tag{4.12.11}$$

$$h_0 \frac{\partial c_0}{\partial \tau} = -\left(Kc_0 - s_0\right) + O(\frac{1}{\mathrm{Da_a}}), \tag{4.12.12}$$

which has the leading order solution

$$h_0 = 1, \tag{4.12.13}$$

$$s_0 = \frac{1}{1+K}\left[K(c_{\mathrm{IC}} + s_{\mathrm{IC}}) - (Kc_{\mathrm{IC}} - s_{\mathrm{IC}})\mathrm{e}^{-(1+K)t}\right], \tag{4.12.14}$$

$$c_0 = \frac{1}{1+K}\left[c_{\mathrm{IC}} + s_{\mathrm{IC}} + (Kc_{\mathrm{IC}} - s_{\mathrm{IC}})\mathrm{e}^{-(1+K)t}\right], \tag{4.12.15}$$

where the subscript IC denotes the initial condition, which may be a function of x, and the initial condition for the film thickness is $h = 1$.

The leading order solution given by (4.12.13)–(4.12.15) makes clear how the system (4.7.1)–(4.7.3) evolves at early times. The free surface undergoes only small $O(1/\mathrm{Da_a})$ changes in shape over this short timescale, and the surface and bulk concentrations move towards surface–bulk equilibrium, i.e., move towards the state in which $J = Kc_0 - s_0 = 0$, and they both do so monotonically. Figure 4.13 shows the evolution towards $J = 0$ of the leading order surface concentration (dashed line), the bulk concentration (solid line), and the flux $J = Kc_0 - s_0$ (dash-dot line), for an anti-surfactant with $K = 1/2$, and where the initial condition is $s = 1$, $c = 1$. Figure 4.14 shows the corresponding plot for a surfactant with $K = 3/2$.

If the initial condition is such that the surface and bulk concentrations are not in equilibrium, then there will be growth in growth in one of them and decay in the other depending on the sign of $J = Kc_0 - s_0$. Figure 4.13 demonstrates that when $J < 0$ initially, there will be growth in the bulk concentration, whereas Figure 4.14 demonstrates that when $J > 0$ initially, there will be growth in the surface concentration. Note that in any physical system there will be small $O(1/\mathrm{Da_a})$ changes in the film thickness, surface concentration, and bulk concentration due to capillarity, diffusion, and the Marangoni effect, corresponding to the first order solution in the limit $\mathrm{Da_a} \to \infty$.

4.13 Summary

In this Chapter, we investigated the behaviour of a thin film of surfactant or anti-surfactant solution by assuming that the aspect ratio of the layer was small, i.e., by making a classical lubrication approximation. Closure of the leading order problem for the evolution of the bulk concentration required going to higher order in the small aspect ratio limit. We also performed a linear stability analysis similar to that performed in Chapter 3, and found that a thin film of anti-surfactant solution is unstable to perturbations of certain wavenumbers. Stability diagrams for each of the dimensionless parameters were produced, showing the regions of instability, and also showing the regions in which oscillatory behaviour occurs. Furthermore, in the limit of fast bulk–surface flux, there is a separation of timescales with a short timescale over which the surface and bulk concentrations come into surface–bulk equilibrium, and a long timescale over which capillarity, diffusion, and the Marangoni effect are dominant.

Chapter 5

Non-Linear Dynamics of a Thin Film: Numerical Solutions

5.1 Introduction

In Chapter 4 we formulated the nonlinear equations describing the flow of thin films of surfactant or anti-surfactant solutions, but thus far have analysed only their linear stability. In this Chapter we focus on the nonlinear dynamics of thin films described by equations (4.7.1)–(4.7.3) and, in particular, obtain numerical solutions.

In section 5.2, we introduce the numerical scheme that will be used to integrate equations (4.7.1)–(4.7.3) numerically.

In section 5.3, we obtain numerical results for the evolution of a sinusoidally perturbed layer, both within and outwith the linear regime, in order to validate the results of Chapter 4. We compare these numerical results with the linear theory described in Chapter 4, and see that the linear theory performs well even for perturbations with $O(1)$ amplitudes.

Finally, in section 5.4, we consider the evolution of a layer in which a localized amount of surfactant or anti-surfactant is initially added to the surface or bulk of the fluid, and find that there is a separation of timescales. Specifically, there is a short timescale over which the flux acts to bring the surface and bulk concentrations into equilibrium, and a long timescale over which capillarity, diffusion, and

the Marangoni effect dominate.

5.2 Numerical Scheme

In order to obtain numerical solutions to the nonlinear equations (4.7.1)–(4.7.3), we used the finite-element package COMSOL Multiphysics [13]. The system of equations were solved numerically in COMSOL using three one-dimensional, time-dependent, "General PDE" modules. The "General PDE" module of COMSOL solves equations in the flux-conservative form

$$e_a \frac{\partial^2 \mathbf{u}}{\partial t^2} + d_a \frac{\partial \mathbf{u}}{\partial t} + \frac{\partial \mathbf{\Gamma}}{\partial x} = \mathbf{f}, \tag{5.2.1}$$

where e_a is a so-called "mass coefficient" matrix ($e_a \equiv 0$ in all cases we consider), d_a is a so-called "damping coefficient" matrix, $\mathbf{u} = \mathbf{u}(x,t)$ is the unknown (in general, vector-valued) function, $\mathbf{\Gamma} = \mathbf{\Gamma}(\mathbf{u}, \mathbf{u}_x, \mathbf{u}_{xx})$ is a flux of $\mathbf{u}$, and $\mathbf{f} = \mathbf{f}(\mathbf{u})$ is a source term. In order to solve equations (4.7.1)–(4.7.3) in COMSOL, we must therefore write them in the flux-conservative form (5.2.1), i.e.,

$$\frac{\partial h}{\partial t} + \frac{\partial}{\partial x}\left[\frac{h_{xxx}h^3}{3} - \frac{\mathrm{Ma}h^2}{2}(s-c)_x\right] = 0, \tag{5.2.2}$$

$$\frac{\partial s}{\partial t} + \frac{\partial}{\partial x}\left[\frac{h_{xxx}h^2 s}{3} - \frac{\mathrm{Ma}hs}{2}(s-c)_x\right] = \frac{1}{\mathrm{P_s}}s_{xx} + \mathrm{Da_a}\left(Kc - s\right), \tag{5.2.3}$$

$$h\frac{\partial c}{\partial t} - \frac{1}{\mathrm{P_b}}\frac{\partial}{\partial x}\left(hc_x\right) = -\left(\frac{h_{xxx}h^3}{3} - \frac{\mathrm{Ma}h^2}{2}(s-c)_x\right)c_x - \delta\mathrm{Da_a}\left(Kc - s\right). \tag{5.2.4}$$

An idiosyncrasy of COMSOL (among other numerical packages) is that any variable can be differentiated a maximum of twice, and so the h_{xxx} terms in each of these equations cannot be handled directly by COMSOL. To circumvent this difficulty we make the substitution $P = h_{xx}$, so that all h_{xxx} terms are now P_x terms and, in COMSOL, we simply create a vector equation in $\mathbf{u} = [h, P]^{\mathrm{T}}$ in lieu of the scalar equation for h, of the form given by (5.2.1), where

$$e_a = \begin{bmatrix} 0 & 0 \\ 0 & 0 \end{bmatrix}, \tag{5.2.5}$$

$$d_a = \begin{bmatrix} 1 & 0 \\ 0 & 0 \end{bmatrix}, \tag{5.2.6}$$

$$\mathbf{\Gamma} = \left[\frac{P_x h^3}{3} - \frac{\mathrm{Ma} h^2}{2} \left(s - c \right)_x, h_x \right]^{\mathrm{T}}, \tag{5.2.7}$$

$$\mathbf{f} = [0, P]^{\mathrm{T}}. \tag{5.2.8}$$

The geometry, boundary conditions, mesh size, and length of simulation time will vary depending on the particular simulations that are being done and are therefore chosen on a case-by-case basis. COMSOL uses variable time step methods, and so only the start and end times must be specified.

5.3 Comparison Between the Nonlinear and Linear Results

We first compare the results from the linear stability calculation, as described in section 4.8, with the results obtained by direct numerical simulation of the full nonlinear system given by equations (4.7.1)–(4.7.3). We will compare the results of the nonlinear theory with those of the linear theory when the thin film is subjected to perturbations of small amplitude relative to the base-state values of h, s and c, i.e., to perturbations in the linear regime, and also to larger perturbations that are of the same order as the base state values, i.e., to perturbations outwith the linear regime.

Equations (4.7.1)–(4.7.3) are solved using COMSOL, as described in section 5.2. We take the initial condition

$$h = 1, \quad s = K + \epsilon \cos(x), \quad c = 1 + \epsilon \cos(x), \tag{5.3.1}$$

i.e., we add a perturbation of wavenumber $k = 1$ and of initial amplitude ϵ to the constant base state values of s and c, which is a specific choice of the wavenumber and the aspect ratio used in the more general treatment in the linear stability analysis performed in Chapters 3 and 4. The computational domain is the interval $[0, 2\pi]$, i.e., one wavelength long, and periodic boundary conditions are imposed at the two endpoints. A mesh of twenty uniformly spaced points is sufficient to resolve the features that occur in the evolution of the system and allows for short computation times of approximately 2 seconds. Any increase in the mesh

density does not offer any noticeable increase in quality and only serves to increase computation time; for this simple problem, the computation time remains at this "baseline" value of 2 seconds until the mesh is made up of approximately 5000 points for small values of ϵ, or 2000 points for larger values of ϵ, and at these mesh densities the computation time is approximately doubled to 4 seconds.

To obtain the linear behaviour of the full nonlinear system, we solve three coupled ODEs for the amplitude of perturbations in the limit $\epsilon \to 0$ (as discussed in Chapter 4), namely equations (4.8.4)–(4.8.6).

Figures 5.1–5.4 show comparisons between the numerical solutions of the full nonlinear problem, which are shown solid, and the linear problem, which are shown dashed, where we have plotted the value of the solution at the origin minus the value of the constant initial condition of (a) the film thickness, (b) the surface concentration, and (c) the bulk concentration, as a measure of the amplitude of the perturbations. In Figures 5.1–5.3 the initial perturbation has amplitude $\epsilon = 0.01$, whereas in Figure 5.4 the initial perturbation has amplitude $\epsilon = 0.5$. The dashed lines in each of Figures 5.1–5.3 are the solutions to the linearised problem presented in Figures 4.1–4.3.

In general, for all three of Figures 5.1–5.3, the solutions to the linearised problem are good approximations to the solutions of the full nonlinear problem. It is apparent from Figure 5.3 that, in the unstable case (corresponding to $\mathrm{Ma} = 4$ in this particular illustration), the linear approximation does not do particularly well at long times as nonlinear effects begin to dominate. While the linear theory performs worse for the large-amplitude initial perturbation shown in Figure 5.4 than it does for the small-amplitude initial perturbation presented in Figure 5.2, it still performs well, with the maximum error less than 10% in each of h, s, and c.

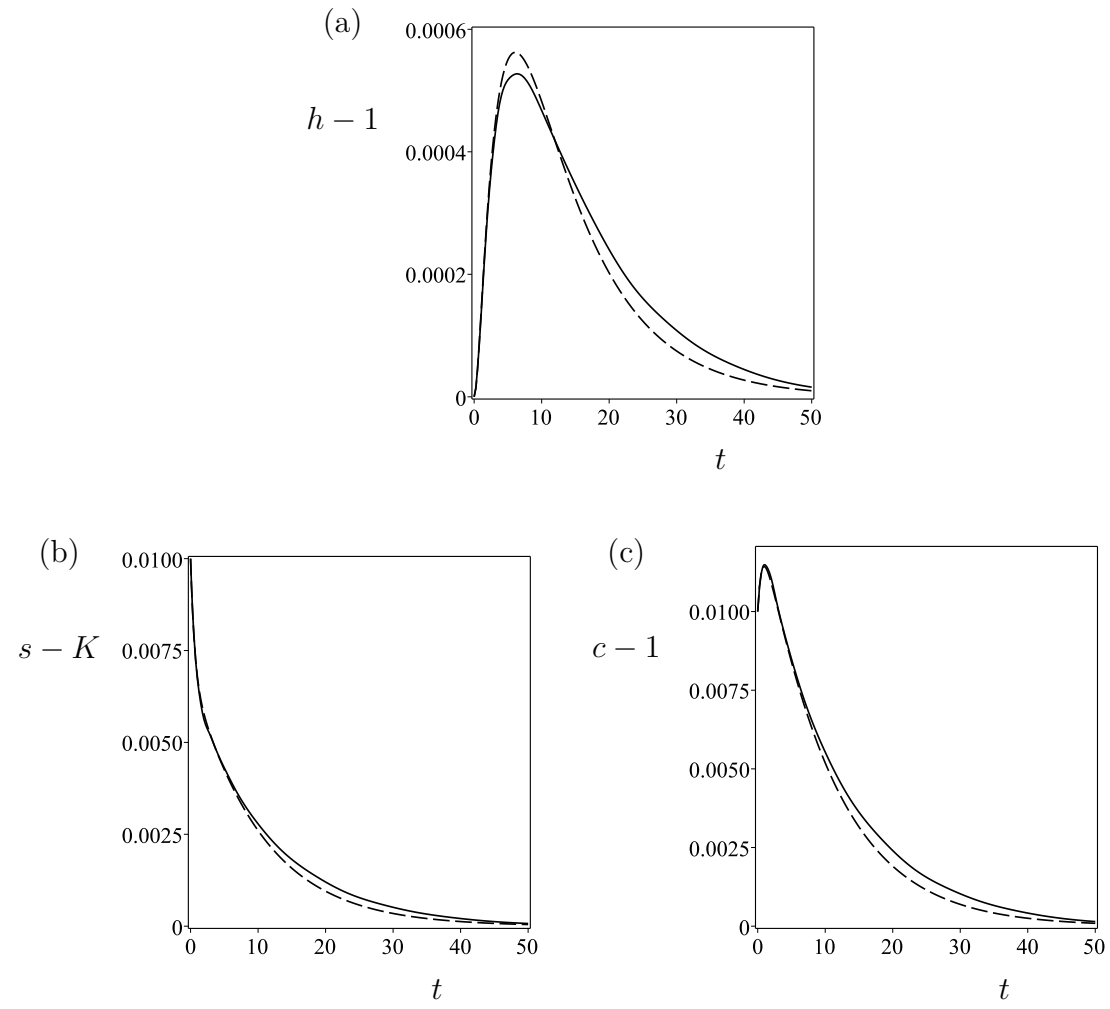

Figure 5.1: The value of the solution at the origin minus the value of the constant initial condition for (a) the film thickness, (b) the surface concentration, and (c) the bulk concentration, as a measure of the amplitude of the perturbations. The numerical results are shown for the linear theory (solid lines) and the nonlinear theory (dashed lines), where $\mathrm{Ma} = 0.1$, $\mathrm{Ca} = 1$, $\mathrm{P_s} = 10$, $\mathrm{P_b} = 10$, $\mathrm{Da_a} = 1$, $\mathrm{Da_d} = 10$, and $\epsilon = 0.01$.

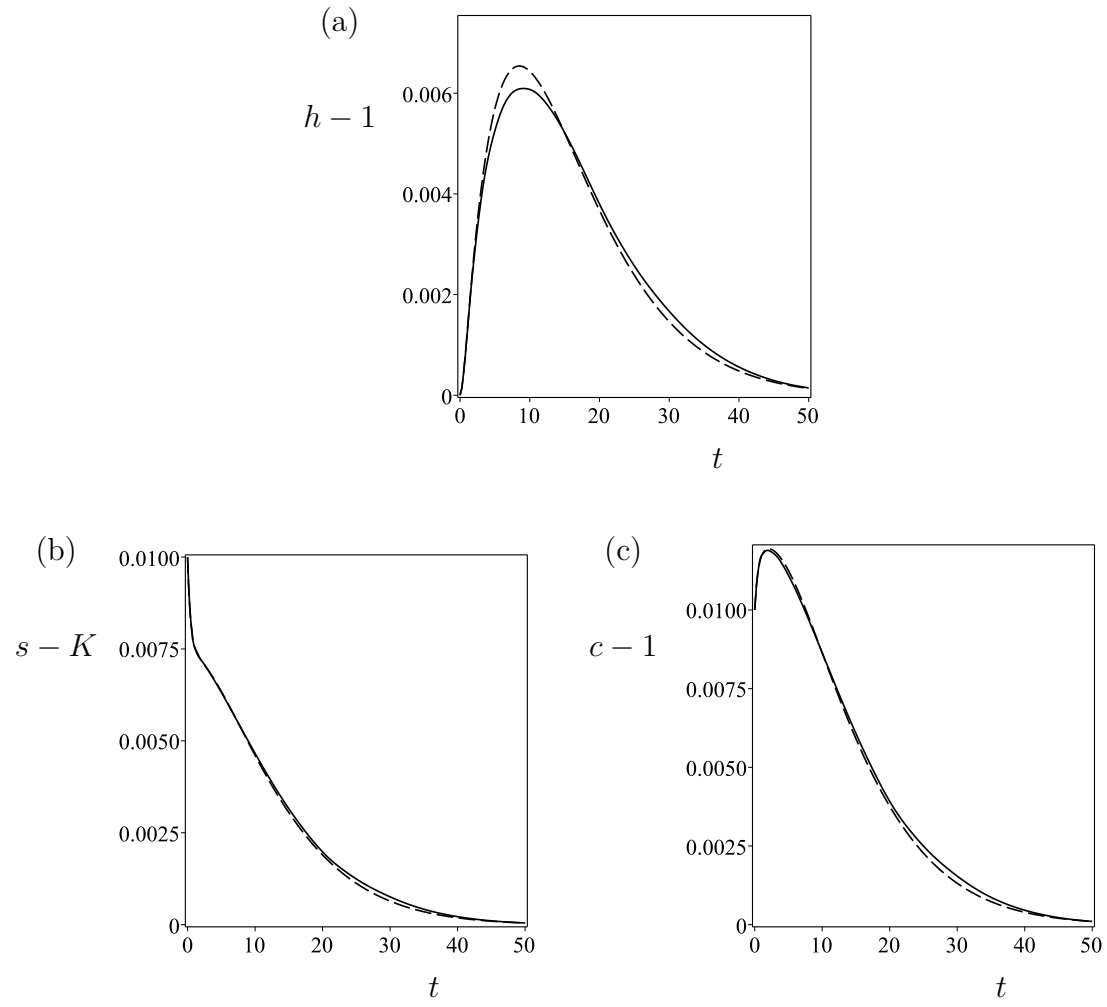

Figure 5.2: As in Figure 5.1, except that Ma = 1.

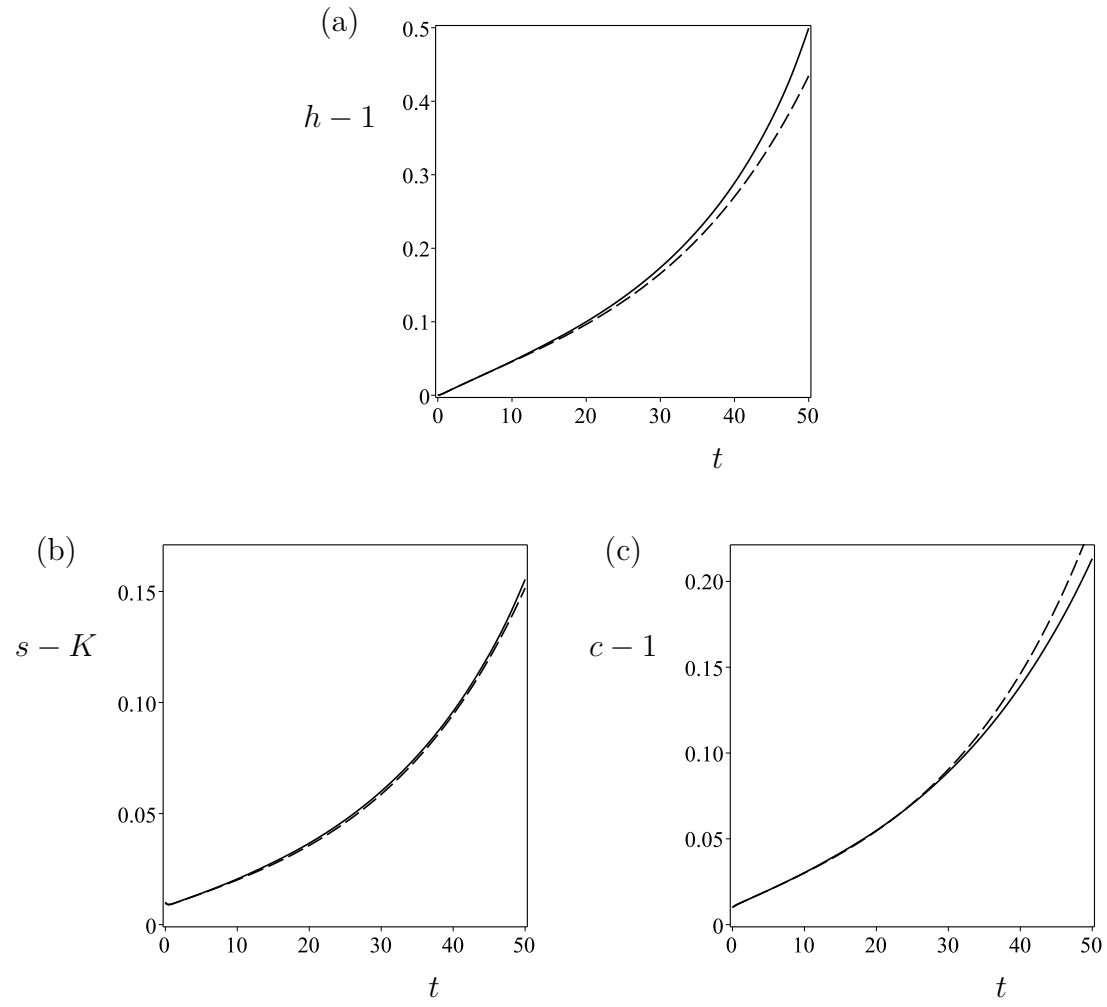

Figure 5.3: As in Figure 5.1, except that Ma = 4.

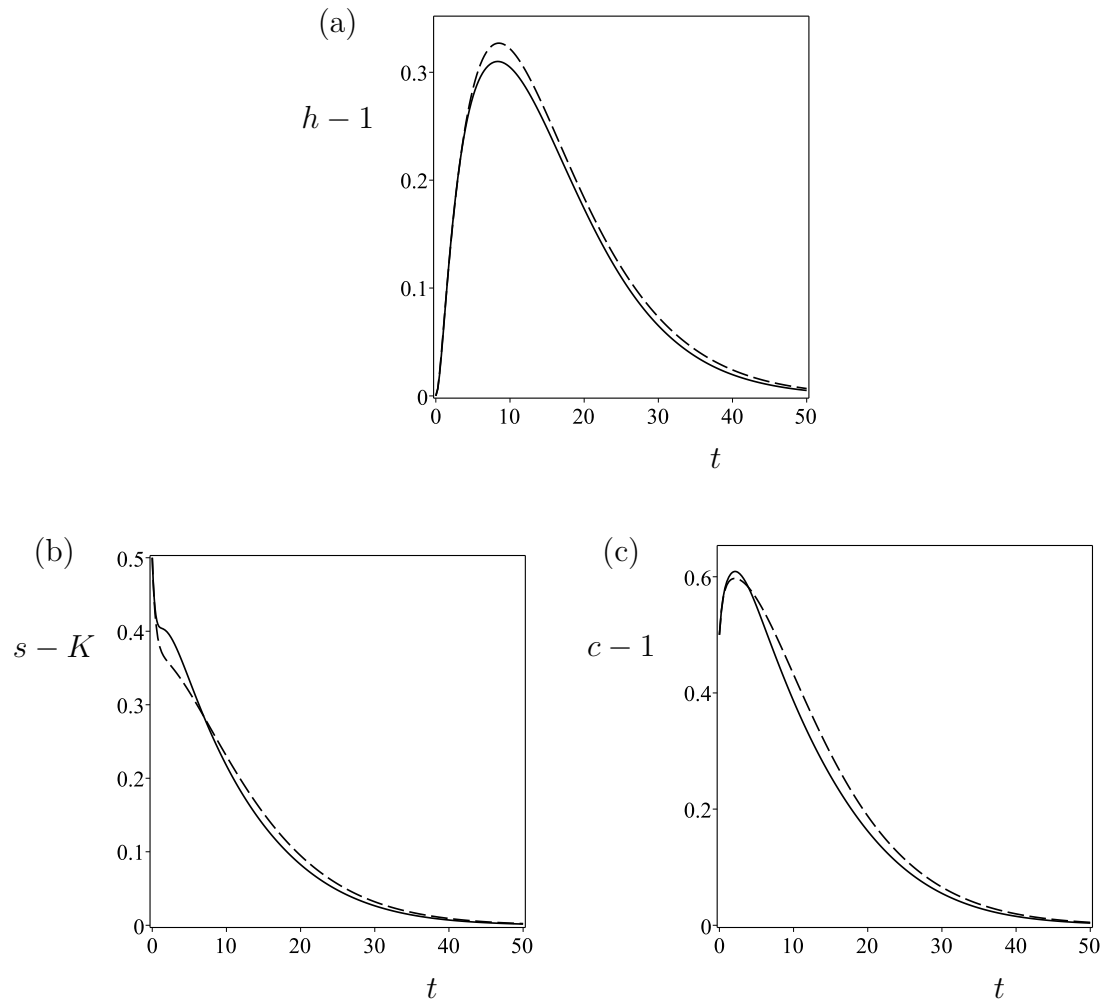

Figure 5.4: As in Figure 5.1, except that Ma = 1 and $\epsilon = 0.5$

5.4 Local Disturbances to the Surface or Bulk Concentration

At the end of section 5.3, we considered the evolution of the nonlinear system given by equation (4.7.1)–(4.7.3) when subjected to *periodic* disturbances of large initial amplitude on a spatially periodic domain. We now consider *local* disturbances to the surface or bulk concentrations, where a large amplitude non-periodic disturbance, i.e., where the disturbance amplitude is comparable in magnitude to the base state values of h, s, and c, and is imposed in some small region of the surface or bulk of the fluid.

We consider four cases: two in which the local disturbance is to the surface

concentration for both surfactants and anti-surfactants, and two in which the local disturbance is to the bulk concentration for both surfactants and anti-surfactants. Since these four cases are very closely related, we will describe only the first in detail, and then discuss only the differences between the first and the other three.

5.4.1 Local Disturbance to the Surface Concentration of Anti-Surfactant ($K < 1$)

The first case we investigate in detail is that in which anti-surfactant ($K < 1$) is added to the free surface. The initial condition is

$$h = 1, \quad c = 1, \quad s = K + 0.5\exp(-x^2), \tag{5.4.1}$$

that is the local disturbance to the surface concentration is simply a Gaussian pulse with initial amplitude 0.5. The spatial domain is taken to be the interval $[-60, 60]$ (which is long enough for edge effects from the boundaries to be negligible). As discussed in section 4.12, there are two distinct timescales in this problem: a short timescale of $O(1/\mathrm{Da_a})$, over which the flux acts to bring the surface and bulk concentration into equilibrium, and in which there is only a small $O(1/\mathrm{Da_a})$ deformation of the free surface, and a long $O(1)$ timescale, over which the Marangoni effect, capillarity, and diffusion all act, and over which there are $O(1)$ changes in all of h, s, and c. We consider these timescales separately in the following numerical solutions.

(a) Early $O(1/\mathrm{Da_a})$ Time Evolution: Flux and Free Surface Depression

The first phase of evolution over the short $O(1/\mathrm{Da_a})$ timescale is dominated by a single physical effect: the flux of solute between the surface and the bulk regions of the fluid layer. This flux causes significant $O(1)$ changes in s and c, while both the Marangoni effect and capillarity cause small $O(1/\mathrm{Da_a})$ changes in h, as discussed in section 4.12.

Initially, s is larger than the equilibrium value of $s = K$, and is largest at the origin. Therefore, there are surface tension gradients, with the surface tension lowest at the origin. Since the Marangoni effect acts to move fluid from the region

of low surface tension, i.e., near the origin, to regions of higher surface tension, i.e., away from the origin, there is therefore an outward Marangoni flow, moving fluid away from the origin (to the right for $x > 0$, and to the left for $x < 0$), and a small $O(1/\mathrm{Da_a})$ depression forms in the free surface, as discussed in section 4.12.

As the Marangoni effect casues a depression to form in the initially flat free surface, the surface–bulk flux simultaneously acts to bring s and c into surface–bulk equilibrium. This equilibrium state is such that $Kc = s$, with $K < 1$ since the solute is an anti-surfactant, and the surface tension is *increased* in regions of high concentration, rather than being decreased as it was initially at $t = 0$, when the surface concentration was larger than Kc. This causes the initial outward (i.e., away from the origin) Marangoni flow to reverse and become an inward (i.e., towards the origin) Marangoni flow. This inward flow causes the initial depression in the free surface to fill in and become a peak.

Figures 5.5(a) shows the evolution of h over the early $O(1/\mathrm{Da_a})$ timescale. The initially flat free surface (shown solid) is deformed due to the flow induced by the Marangoni effect, with a small $O(1/\mathrm{Da_a})$ depression forming initially, which later fills in and becomes a peak due to the reversal in the direction of the Marangoni flow. Dimensionally, this deformation of the free surface is of the order $10^{-6}\,\mathrm{m}$.

Figures 5.5(b) and (c) show the evolution of s and c, respectively, over the early timescale. The initial $O(1)$ disturbance to s reduces because of the flux of solute from the surface to the bulk, with a corresponding increase in c, as the system moves into surface–bulk equilibrium.

(b) Late $O(1)$ Time Evolution: Transient Growth and Ultimate Decay

After the early $O(1/\mathrm{Da_a})$ timescale described above, the system has reached surface-bulk equilibrium, and any changes to s and c are due solely to diffusion and advection. The peak of the free surface that formed and began to grow during the early time evolution continues to grow up to some maximum height while, simultaneously, diffusion begins to reduce concentration gradients. The growth of the peak of the free surface continues until diffusion has reduced concentration gradients sufficiently to allow capillarity to counter the Marangoni-flow-induced

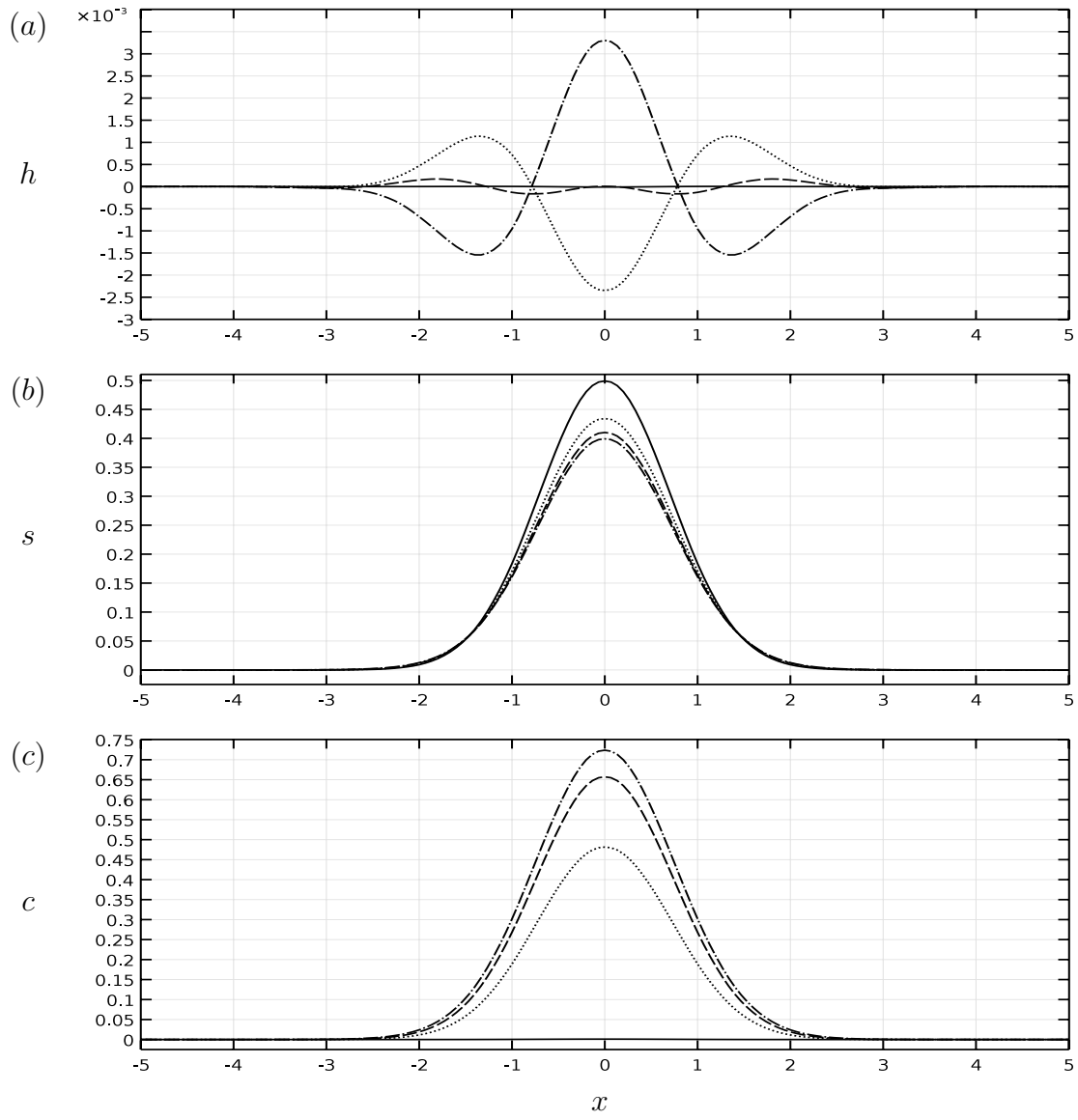

Figure 5.5: Evolution of (a) the film thickness, (b) the surface concentration s, (c) the bulk concentration c, over the early $O(1/\mathrm{Da_a})$ timescale for an anti-surfactant with $K = 0.5$ added to the surface concentration, and for Ma = 1, Ca = 1, $\mathrm{P_s} = \mathrm{P_b} = 1$, $\mathrm{Da_a} = 100$, $\mathrm{Da_d} = 1000$, for times $t = 0$ (solid), 0.004 (dotted), 0.008 (dashed), 0.012 (dash-dot).

growth. This is not to say that the direction of the Marangoni flow again reverses, but instead that the direction of the *net* flow reverses from an inward flow to an outward flow; the sign of the Marangoni contribution to the velocity of the fluid does not change. Ultimately, the layer returns to its equilibrium state, with capillarity levelling the free surface, and diffusion flattening the surface and bulk concentration profiles.

Figure 5.6(a) shows the evolution of h over the long $O(1)$ timescale. The peak of the free surface grows until approximately $t \simeq 3$, at which time the tendency for capillarity to level the free surface balances the tendency of the Marangoni effect to cause growth. Specifically, at $t \simeq 3$, the net inward flow that causes the growth of the film thickness switches to a net outward flow, and causes the free surface to move back towards its flat equilibrium position. Dimensionally, the deformation of the free surface is of the order 10^{-4}m at its maximum.

Figure 5.7 shows a plot of the gradient of the velocity evaluated at the origin. In particular, it shows that the velocity gradient is positive for early times (which corresponds to *net outward* flow), but switches sign at an $O(1/\mathrm{Da_a})$ time, as described in the discussion of the early time evolution in the previous subsection, due to the reversal of the direction of the *Marangoni* flow. For a finite $O(1)$ range of times, the velocity gradient is negative (which corresponds to *net inward* flow), but once again switches sign at approximately $t \simeq 3$, after which time there is a net outward flow, and this outward flow now persists for all time as the layer levels. We omit plots of the evolution of the film thickness over these long times, as this regime is relatively uninteresting.

Figures 5.6(b) and (c) show the evolution of s and c over the $O(1)$ timescale. The only physical effects at play in these evolutions are diffusion and advection, the net effect of which is simply to cause the concentrations to flatten over time, though, again, we do not plot the decay over these long times.

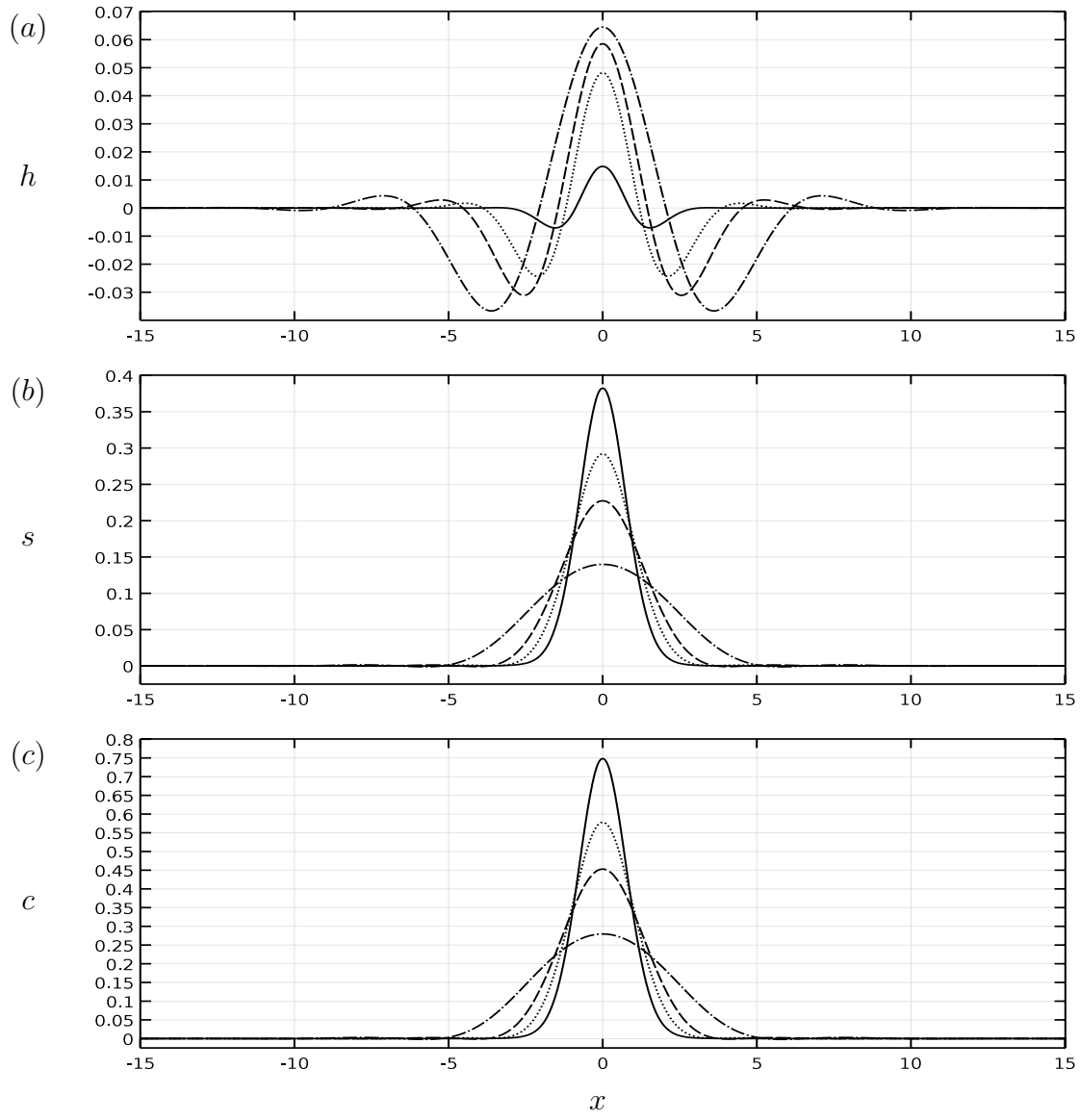

Figure 5.6: Evolution of (a) the film thickness, (b) the surface concentration s, (c) the bulk concentration c, over timescales longer than $O(1/\mathrm{Da_a})$ for an anti-surfactant with $K = 0.5$ added to the surface concentration, and for $\mathrm{Ma} = 1$, $\mathrm{Ca} = 1$, $\mathrm{P_s} = \mathrm{P_b} = 1$, $\mathrm{Da_a} = 100$, $\mathrm{Da_d} = 1000$, for times $t = 0.1$ (solid), 0.5 (dotted), 1 (dashed), 3 (dash-dot).

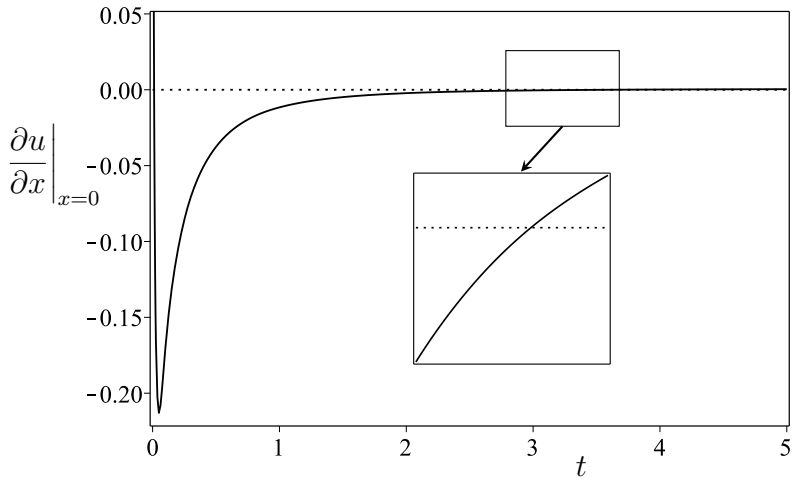

Figure 5.7: Evaluation of the gradient of velocity at the origin for a localised disturbance of anti-surfactant with $K = 0.5$ added to the surface, and for Ma = 1, Ca = 1, $\mathrm{P_s} = \mathrm{P_b} = 1$, $\mathrm{Da_a} = 100$, $\mathrm{Da_d} = 1000$. Inset is a zoom in to the $O(1)$ time at which there is a sign change of the gradient.

5.4.2 Local Disturbance to the Surface Concentration of Surfactant ($K > 1$)

We now investigate the case in which surfactant ($K > 1$) is added to the free surface. The initial condition is again given by (5.4.1). This case is different from the previous case in which anti-surfactant was added to the surface in that the Marangoni flow generated by the concentration gradients does not reverse once the surface and bulk concentrations have equilibrated. The depression that forms in the free surface therefore does not become a peak and, instead, the depression itself grows in magnitude, similar to the growth of the peak in the previous case.

(a) Early $O(1/\mathrm{Da_a})$ Time Evolution

As in the previous case, the evolution of the system over the early $O(1/\mathrm{Da_a})$ timescale is dominated by the flux of solute, with small changes in the film thickness. Since the surface concentration is initially large at the origin, there are surface tension gradients, with surface tension lowest at the origin, and thus an outward Marangoni flow develops, and causes a depression to form in the free sur-

face. Unlike the previous case, however, when s and c have reached surface-bulk equilibrium, the surface tension gradients do switch in sign and surface tension remains lowest at the origin, since the solute is a surfactant. There is therefore no reversal in the direction of the Marangoni flow, and the depression that forms in the free surface remains a depression.

Figure 5.8(a) shows the evolution of the film thickness over the short $O(1/\mathrm{Da_a})$ timescale. The outward Marangoni flow causes a depression to form in the free surface, which remains for the entirety of this early time period, rather than switching to a peak as in the previous case.

Figures 5.8(b) and (c) show the evolution of the surface and bulk concentrations over this short timescale. Both s and c behave in the same qualitative manner as in the previous case. Note that since the solute is a surfactant, the surface concentration will always remain larger than the bulk concentration.

(b) Late $O(1)$ Time Evolution

As with all of the cases considered in this section, there is a period of transient growth in the film thickness, though, in this case, and differently from the previous case, it is a *depression* of the free surface that grows, as there was no peak formed, as described in the early-time subsection. This growth continues until approximately $t \simeq 4$, at which time the net outward flow causing the depression to grow becomes a net inward flow in the same manner as the previous case. Figure 5.9 shows the evolution of the film thickness, the surface concentration, and the bulk concentration, respectively, until the period of transient growth ends.

5.4.3 Local Disturbance to the Bulk Concentration of Anti-Surfactant ($K < 1$)

We now investigate the case in which anti-surfactant ($K < 1$) is added to the bulk concentration. This case is essentially an "upside down" version of the previous case (i.e., the case in which surfactant is added to the surface concentration). Instead of a depression that forms, grows, and ultimately decays, there is a *peak*

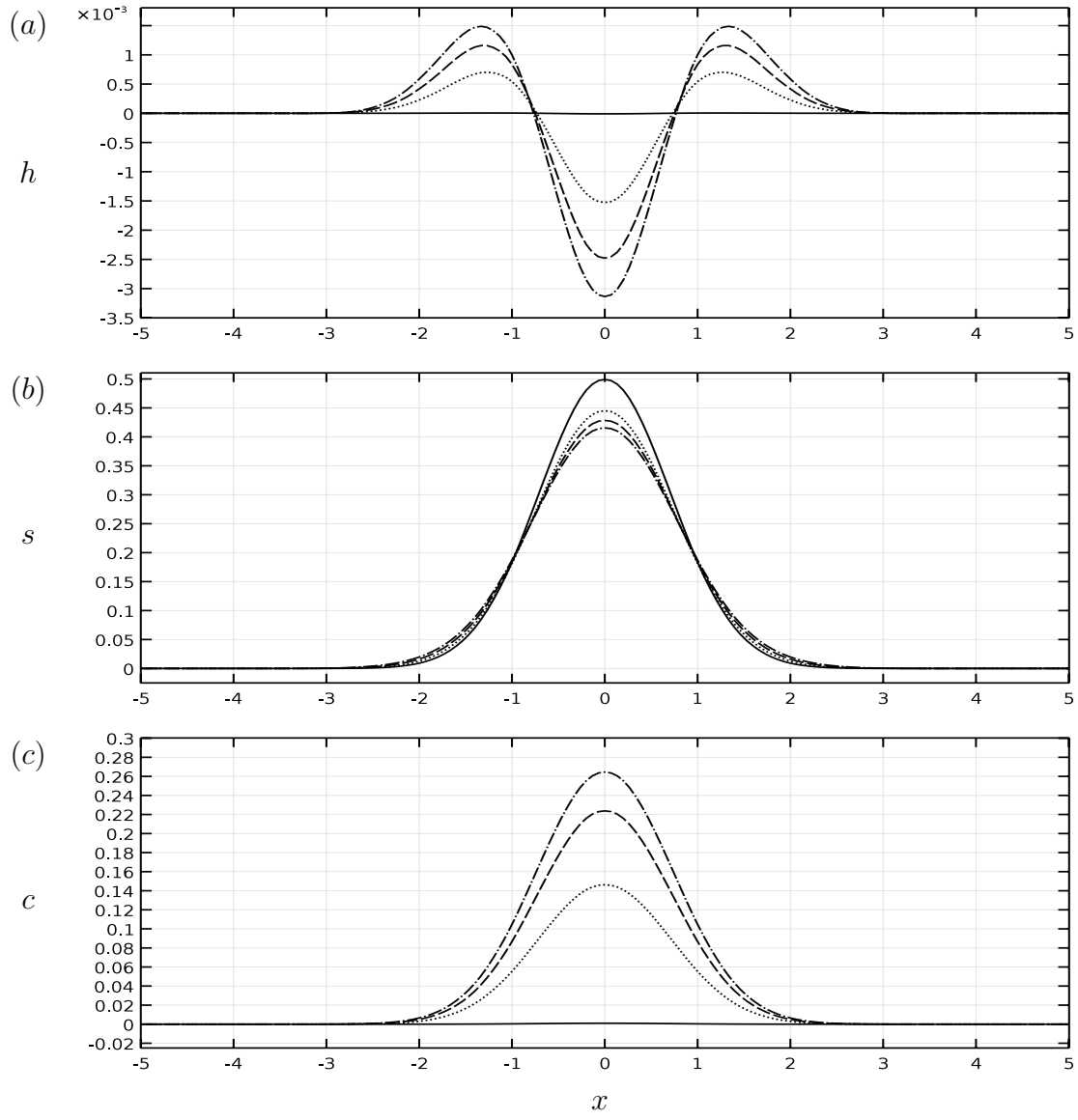

Figure 5.8: As in Figure 5.5 except that $K = 1.5$.

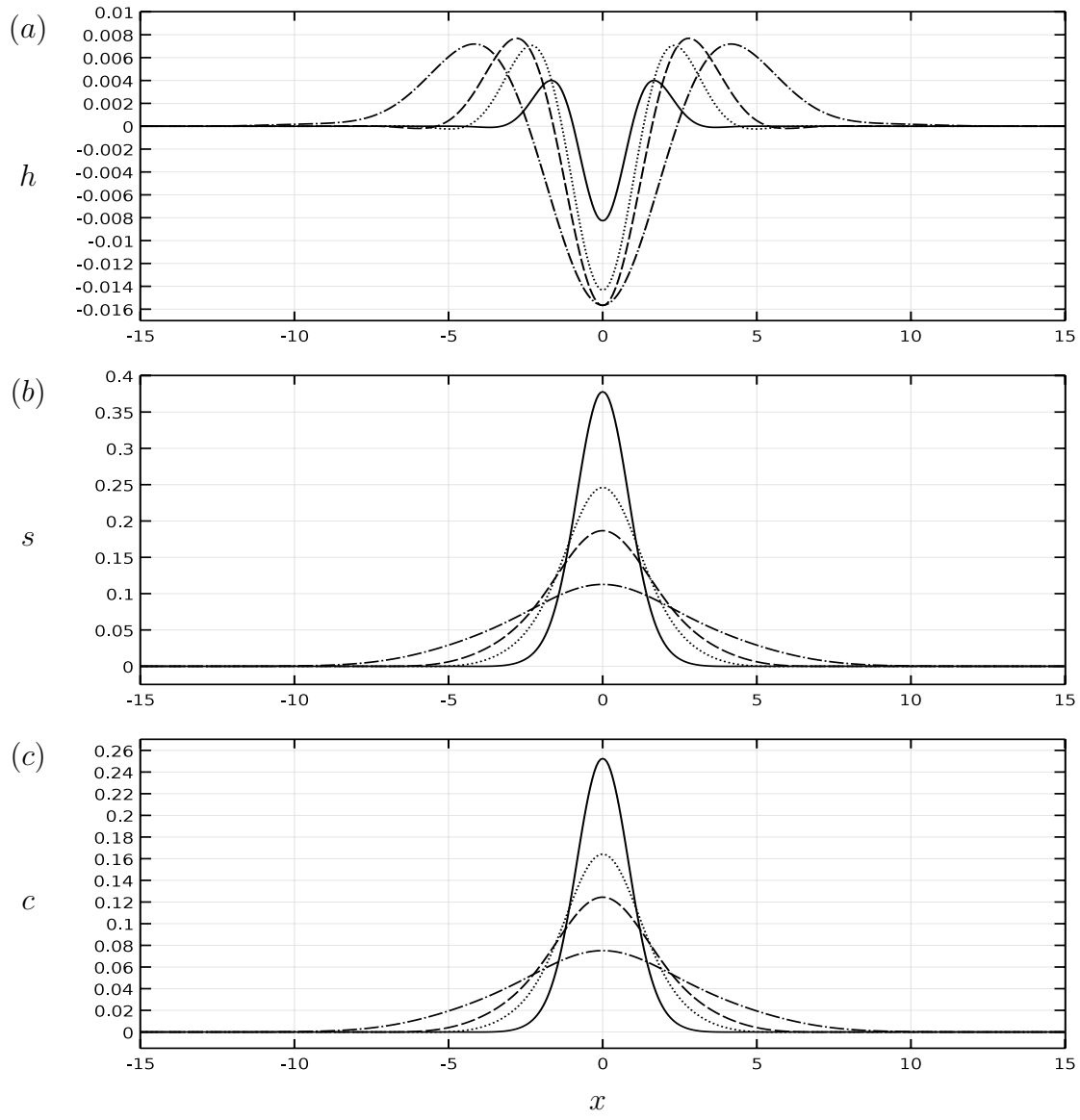

Figure 5.9: As in Figure 5.6, except that $K = 1.5$.

that forms, grows, and ultimately decays. This is what might have been expected, since in both cases the departure of surface tension from its equilibrium state does not change sign, i.e., surface tension is either always decreased or always increased relative to the equilibrium, and cannot switch between the two.

(a) Early $O(1/\mathrm{Da_a})$ Time Evolution

Since the initial disturbance is to the bulk concentration, the surface tension is largest at the origin, and there is therefore an inward Marangoni flow which causes a peak to form on the free surface. After the surface and bulk concentrations have come into surface–bulk equilibrium, the surface tension remains largest at the origin, and so the inward Marangoni flow remains throughout the early time evolution.

Figure 5.10 shows the evolution of the film thickness, surface concentration, and bulk concentration over this early $O(1/\mathrm{Da_a})$ timescale, showing the peak that forms in the free surface, and the changes due to the surface-bulk equilibration of the surface and bulk concentrations.

(b) Late $O(1)$ Time Evolution

Figures 5.11 shows the evolution of the film thickness, surface concentration, and bulk concentration, respectively, over the $O(1)$ timescale. Over these longer times, the peak of the free surface grow to a maximum at approximately $t = 4$. Beyond this, capillarity and diffusion act to bring the system back to equilibrium.

5.4.4 Local Disturbance to the Bulk Concentration of Surfactant $(K > 1)$

The final case we investigate is that in which a surfactant is added to the bulk concentration. This case is essentially an "upside down" version of the first case that we considered (i.e., the case in which an anti-surfactant is added to the surface concentration). Instead of a depression that forms, then flips to become a

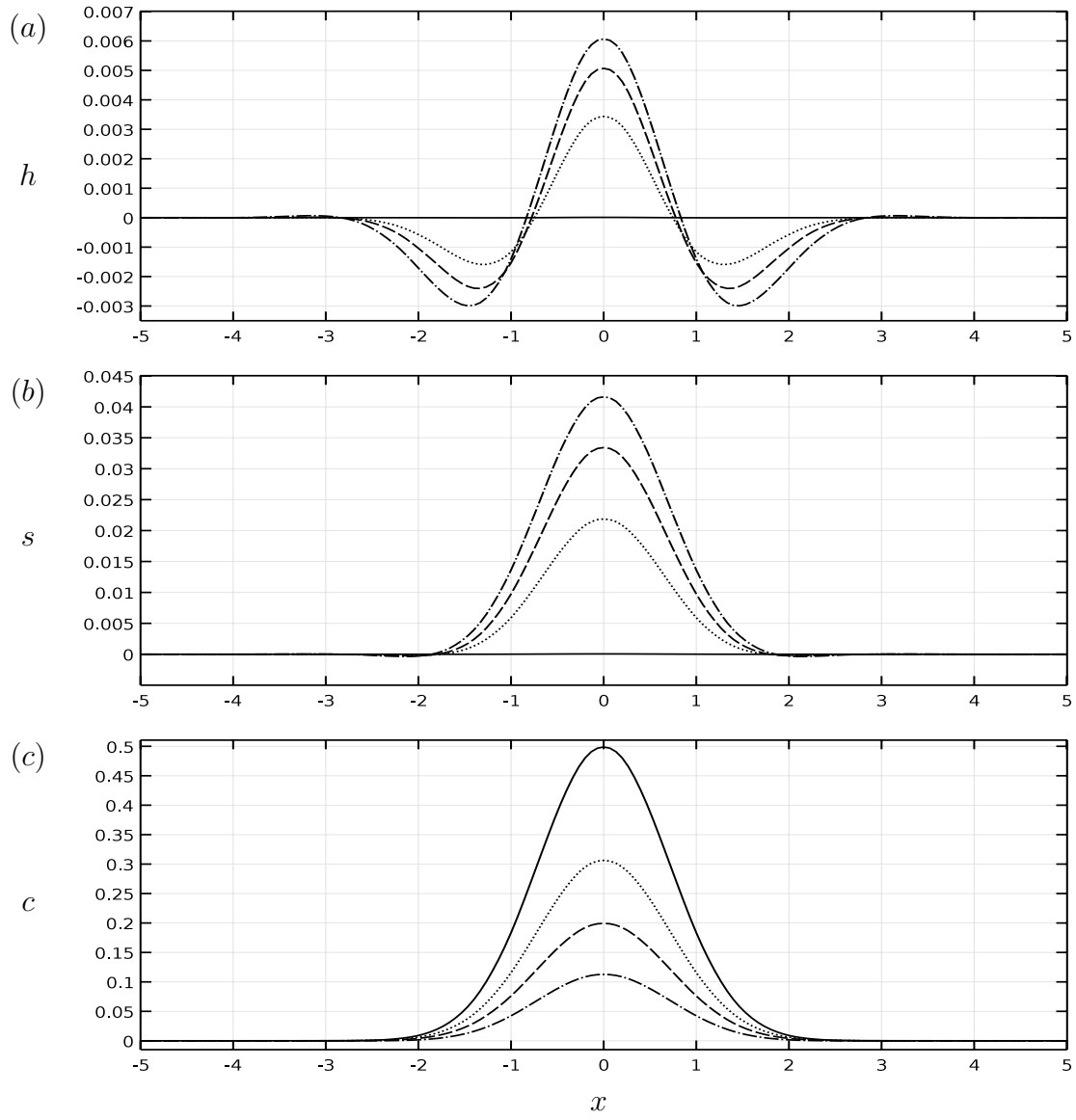

Figure 5.10: Evolution of (a) the film thickness, (b) the surface concentration s, (c) the bulk concentration c, over the early $O(1/\mathrm{Da_a})$ timescale for a surfactant with $K = 0.5$ added to the bulk concentration, and for Ma = 1, Ca = 1, $\mathrm{P_s} = \mathrm{P_b} = 1$, $\mathrm{Da_a} = 100$, $\mathrm{Da_d} = 1000$, for times $t = 0$ (solid), 0.004 (dotted), 0.008 (dashed), 0.012 (dash-dot).

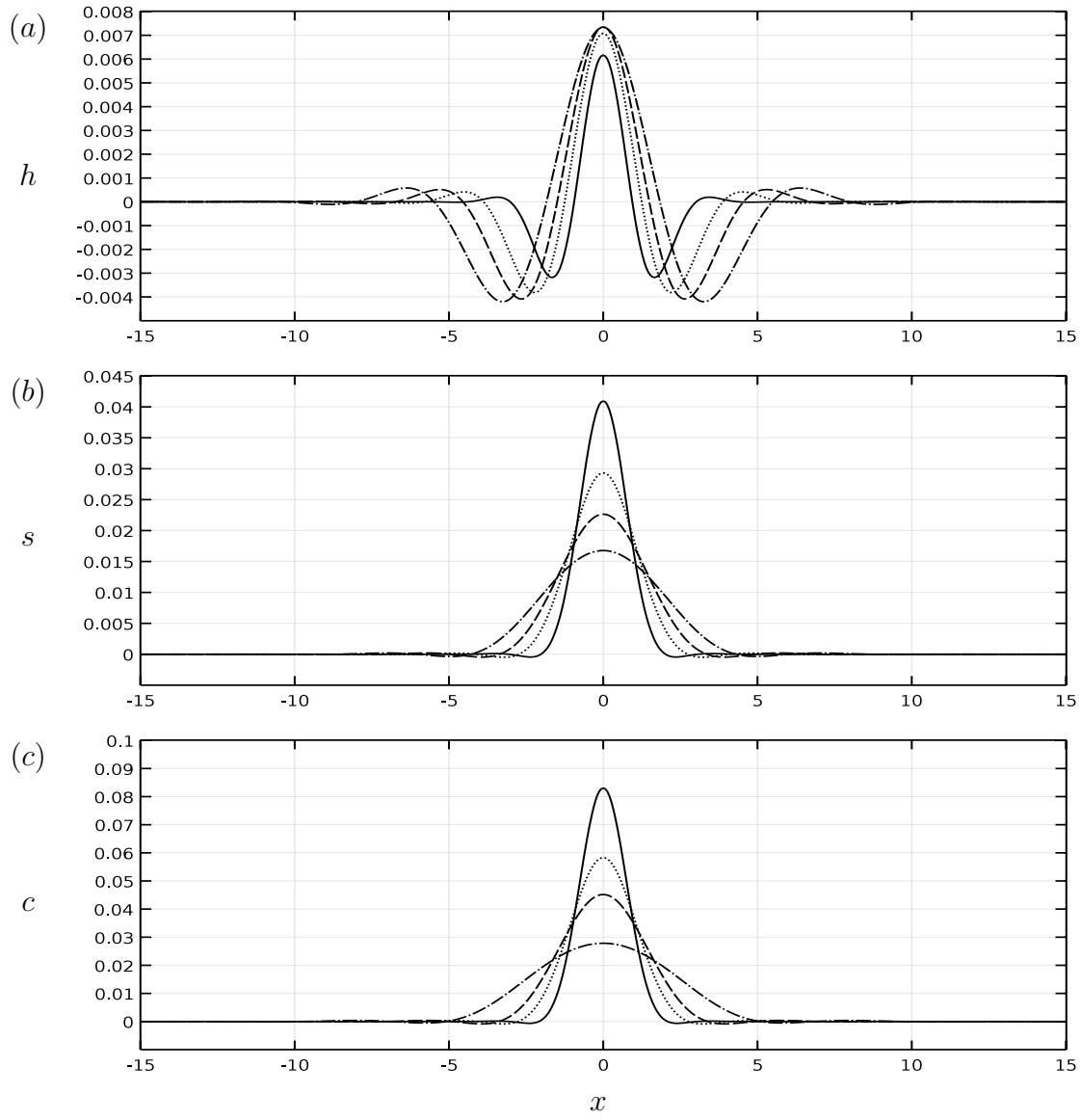

Figure 5.11: Evolution of (a) the film thickness, (b) the surface concentration s, (c) the bulk concentration c, over the early $O(1/\mathrm{Da_a})$ timescale for a surfactant with $K = 0.5$ added to the bulk concentration, and for Ma = 1, Ca = 1, $\mathrm{P_s} = \mathrm{P_b} = 1$, $\mathrm{Da_a} = 100$, $\mathrm{Da_d} = 1000$, for times $t = 0$ (solid), 0.1 (dotted), 0.5 (dashed), 4 (dash-dot).

peak, which then grows and ultimately decays, in this case a peak forms, then flips to become a depression, which grows and ultimately decays. This is what might have been expected since in both cases there is a change in sign of the departure of the surface tension from its equilibrium state (i.e., the surface tension switches from being largest at the origin initially to lowest at the origin in surface–bulk equilibrium in the case discussed in section 5.4.1, and vice versa in this case).

(a) Early $O(1/\mathrm{Da_a})$ Time Evolution

Since the initial disturbance is to the bulk concentration, the surface tension is increased at the origin, and an inward Marangoni flow causes a peak to form in the free surface. After the surface and bulk concentrations have come into surface–bulk equilibrium, the surface tension switches from being increased to decreased at the origin, and a reversal of Marangoni flow from an inward flow to an outward flow occurs. This causes the peak of the free surface to flip to become a depression, which then grows.

Figures 5.12 shows the evolution of the film thickness, surface concentration, and bulk concentration over the early $O(1/\mathrm{Da_a})$ timescale, and showing the formation in the peak of the free surface that becomes a depression, and also show the changes due to surface–bulk equilibration of the surface and bulk concentrations.

(b) Late $O(1)$ Time Evolution

Figures 5.13 shows the evolution of the film thickness, surface concentration, and bulk concentration, respectively, over the $O(1)$ timescale. Over these longer times, the depression in the free surface grows, to a maximum at approximately $t \simeq 4$. Beyond this, capillarity and diffusion act to bring the system back to equilibrium.

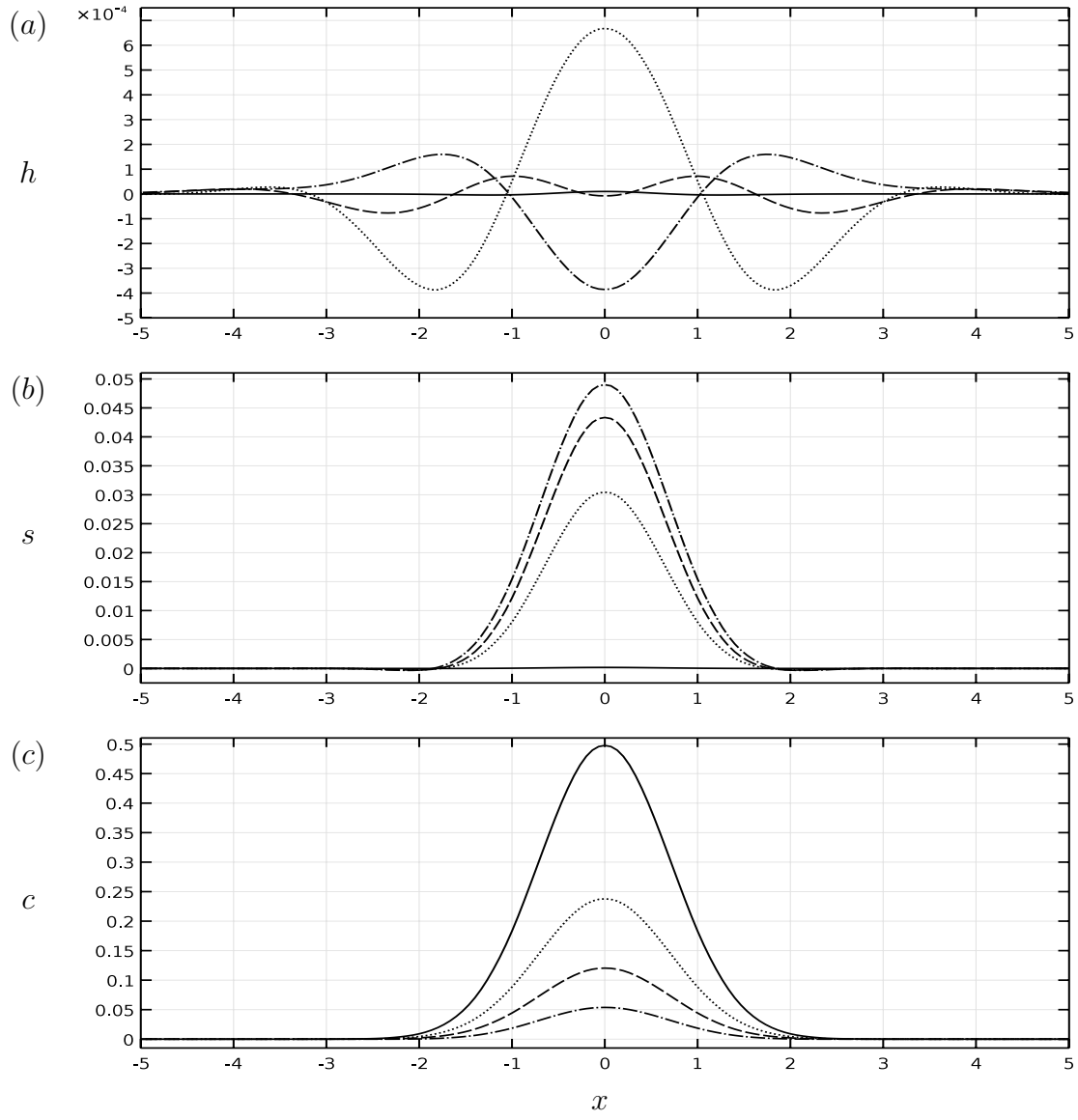

Figure 5.12: As in Figure 5.10, except that $K = 1.5$.

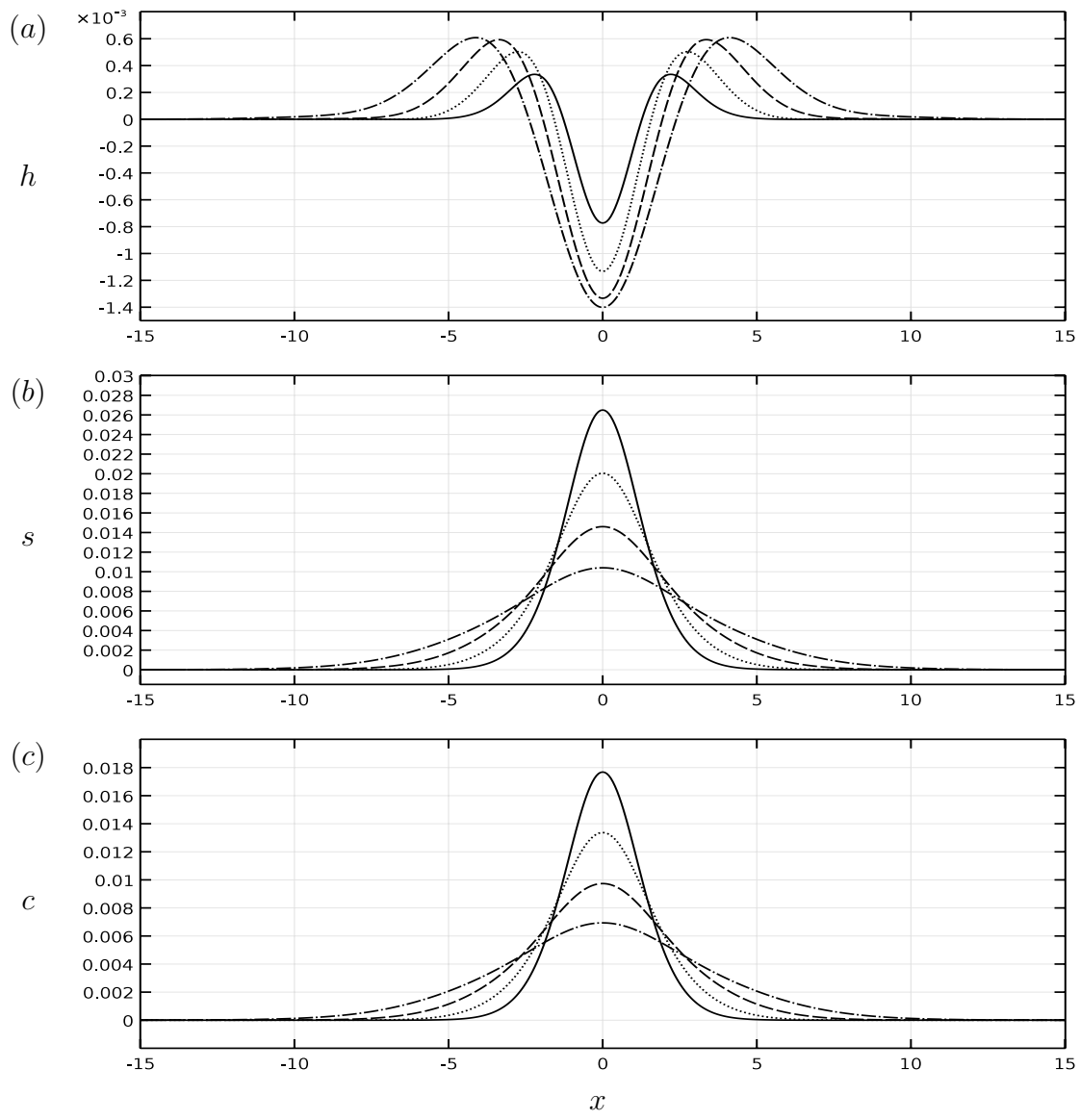

Figure 5.13: As in Figure 5.11, except that $K = 1.5$.

5.5 Summary

In this Chapter, we numerically integrated the thin-film equations derived in Chapter 4. In particular, we confirmed the results of the linear stability analysis performed in Chapter 4, and demonstrated that the linear theory performs well even for perturbations that are $O(1)$. We also considered the problem of adding a large amount of surfactant or anti-surfactant to a small region of either the surface or the bulk of an otherwise pure solvent. Transient growth of either a peak or a depression in the free surface occurs, depending on whether the solute is a surfactant or an anti-surfactant, and on whether the solute is added to the surface or the bulk, but the free surface deformation is typically small (of the order 1-100 microns). These results could readily be tested experimentally and indeed such experiments have been carried out for insoluble surfactants (see, for example, [24]). For perturbations to the bulk concentration, without disturbing the surface concentration or the free surface itself, one can imagine, for example, lacing the substrate with the solute before adding the solvent, or having the solute in some form of inert, but soluble, capsule which releases when triggered to do so.

Chapter 6

Non-Linear Dynamics of a Thin Film: Analytical Solutions

6.1 Introduction

In this Chapter we seek analytical solutions to the equations describing the flow of a thin film of surfactant or anti-surfactant solution in the special cases of an insoluble surfactant (where $c \equiv 0$, as in section 3.4.2) and a 'perfectly soluble' anti-surfactant (where $s \equiv 0$, as in section 3.4.3). In section 6.2, we focus on "perfectly soluble" anti-surfactants and seek solutions to a family of Riemann problems in which there is a discontinuity in the initial condition. In section 6.5, we seek similarity solutions for an insoluble surfactant, where we recover the similarity solution obtained by Jensen and Grotberg [39] and extend their results to include different scalings of the film thickness, and for a "perfectly soluble" anti-surfactant, where we find a doubly-infinite family of new similarity solutions.

The equations that we will use in section 6.2 (i.e., equations (6.2.3) and (6.2.4)) were first solved by Howison *et al.* [35] in the context of drying paint films, though they reached these equation through a different process. Howison *et al.* demonstrated that one can obtain implicit solutions to these equations, and used these solutions to show that when a sinusoidal distribution of "perfectly soluble" anti-surfactant (the resin in the paint) is added to a flat layer, the film thickens at the peaks of the concentration distribution and thins at the troughs.

This leads to the formation of a shock in the film thickness in finite time at the peaks of the concentration distribution. It is also possible to obtain solutions to these equations in parametric form for sufficiently well-behaved initial conditions, which we do in Appendix C.

6.2 A Family of Simple-Wave Solutions for a "Perfectly Soluble" Anti-Surfactant

The equations that describe the flow of a "perfectly soluble" anti-surfactant solution (where $s \equiv 0$, as in section 3.4.3) can be solved analytically when diffusion and capillarity are neglected. In fact, these equations can be written in characteristic form, enabling us to use the powerful method of characteristics [95, 117] to solve problems in which the initial condition may be discontinuous — so-called Riemann problems. In this section we demonstrate this approach by solving a family of Riemann problems that resemble the classical dam-break problem (see, e.g., Whitham [117]), or the classical Stoker problem [95], but where the driving force is not gravity, but a spatially non-uniform shear stress due to concentration gradients. In particular, we will consider initial conditions in which there is a discontinuity at a single point (the origin, for convenience) in both the film thickness and the concentration gradient.

6.2.1 The Governing Equations in Characteristic Form

We begin by rewriting the governing equations in characteristic form, so that we may employ the method of characteristics [117] to obtain solutions. Beginning from equations (4.7.1) and (4.7.3) (with $s \equiv 0$), we take the limits $\mathrm{Ca} \to \infty$ so that capillarity is neglected, $\mathrm{P_b} \to \infty$ so that diffusion is neglected, and $K \to 0$ so that the solute is completely excluded from the free surface. We also choose the velocity scale to be $U^* = U^*_{\mathrm{Ma}}$ so that $\mathrm{Ma} = 1$. Under the above assumptions, we obtain the reduced pair of equations

$$\frac{\partial h}{\partial t} + \frac{1}{2}\frac{\partial}{\partial x}(h^2 \frac{\partial c}{\partial x}) = 0, \tag{6.2.1}$$

$$\frac{\partial c}{\partial t} + \frac{1}{2} h \left(\frac{\partial c}{\partial x} \right)^2 = 0. \tag{6.2.2}$$

Differentiating (6.2.2) with respect to x and making the substitution $\partial c/\partial x = b$, where $b(x,t)$ denotes the gradient of the concentration of solute, we obtain the equations

$$\frac{\partial h}{\partial t} + \frac{1}{2} \frac{\partial}{\partial x}(h^2 b) = 0, \tag{6.2.3}$$

$$\frac{\partial b}{\partial t} + \frac{1}{2} \frac{\partial}{\partial x}(h b^2) = 0. \tag{6.2.4}$$

Note that, because of the Marangoni effect, a positive (negative) value of b corresponds to a positive (negative) shear stress at the free surface of the film which drives the fluid to the right (left).

The system of nonlinear equations given by (6.2.3) and (6.2.4) is purely hyperbolic, and so may be written in characteristic form with Riemann invariants $r_\pm = h b^{\pm 1}$, which are constant along the characteristic curves in the (x,t)-plane with slopes given by the eigenvalues $\lambda_\pm = hb(1 \pm \frac{1}{2})$. Thus

$$\frac{\mathrm{d}}{\mathrm{d}t}(r_+) = \frac{\mathrm{d}}{\mathrm{d}t}(hb) = 0, \tag{6.2.5}$$

$$\frac{\mathrm{d}}{\mathrm{d}t}(r_-) = \frac{\mathrm{d}}{\mathrm{d}t}\left(\frac{h}{b}\right) = 0 \tag{6.2.6}$$

on the characteristic curves given by

$$\frac{\mathrm{d}x}{\mathrm{d}t} = \lambda_\pm = hb\left(1 \pm \frac{1}{2}\right). \tag{6.2.7}$$

With the governing equations (6.2.1) and (6.2.2) written in the characteristic form (6.2.5)–(6.2.7), we are now able to solve a family of Riemann problems in which there is a discontinuity in the initial conditions for the film thickness h and/or the concentration gradient b. Specifically, we consider situations in which an initial discontinuity separates two otherwise uniform regions in each of which h and b are constant. Without loss of generality, we take the initial discontinuity to be at $x = 0$, and so take the initial conditions at $t = 0$ to be

$$\begin{cases} h = h_\mathrm{L}, \quad b = b_\mathrm{L} \quad \text{for} \quad x < 0, \\ h = h_\mathrm{R}, \quad b = b_\mathrm{R} \quad \text{for} \quad x > 0, \end{cases} \tag{6.2.8}$$

where, in general, none of the prescribed constants $h_{\rm L}$, $h_{\rm R}$, $b_{\rm L}$ and $b_{\rm R}$ are equal, and the subscripts R and L denote initial quantities to the right and to the left of the initial discontinuity, i.e., for $x > 0$ and $x < 0$, respectively. Note that since b is initially piecewise constant, c will be initially piecewise linear, and hence if $b_{\rm L} > 0$ and/or $b_{\rm R} < 0$ then c will be initially negative (which is, of course, unphysical) as $x \to -\infty$ and/or $x \to \infty$. Thus in these cases the present analysis is strictly only a local (rather than a global) one. However, as we shall show, in all cases the present analysis gives valuable insight into the surprisingly complicated dynamics that can arise from an initial discontinuity.

6.3 The "dry-bed" problem

In this section we consider the "dry-bed" problem in which $h_{\rm L} > 0$ but $h_{\rm R} = b_{\rm R} = 0$, so that the region $x > 0$ is initially dry.

In order to construct solutions for h and b, we consider the characteristics in the (x,t)-plane given by (6.2.7). There are two characteristics emanating from any initial point $(x,0)$, which we label as $C_\pm$, corresponding to the eigenvalues $\lambda_\pm$, respectively, and we use the superscripts R and L to denote characteristics emanating from the right and from the left of the initial discontinuity, i.e., from $x > 0$ and $x < 0$, respectively.

For $x > 0$ we have $h = b \equiv 0$ at $t = 0$, and so the $C_\pm^{\rm R}$ characteristics coincide and are simply vertical straight lines given by

$$C_\pm^{\rm R} : \; x = x_\pm^{\rm R}, \tag{6.3.1}$$

where $x_\pm^{\rm R}$ is a constant that labels each of the characteristics. On the other hand, for $x < 0$ we have $h = h_{\rm L}$ and $b = b_{\rm L}$ at $t = 0$, and so the $C_\pm^{\rm L}$ characteristics are inclined straight lines given by

$$C_+^{\rm L} : \; x = \frac{3}{2} h_{\rm L} b_{\rm L} t + x_+^{\rm L}, \tag{6.3.2}$$

$$C_-^{\rm L} : \; x = \frac{1}{2} h_{\rm L} b_{\rm L} t + x_-^{\rm L}, \tag{6.3.3}$$

where $x_\pm^{\rm L}$ are constants that label each of the characteristics. Evidently, the slopes of the $C_\pm^{\rm L}$ (but not the $C_\pm^{\rm R}$) characteristics depend on the values and signs of $h_{\rm L}$

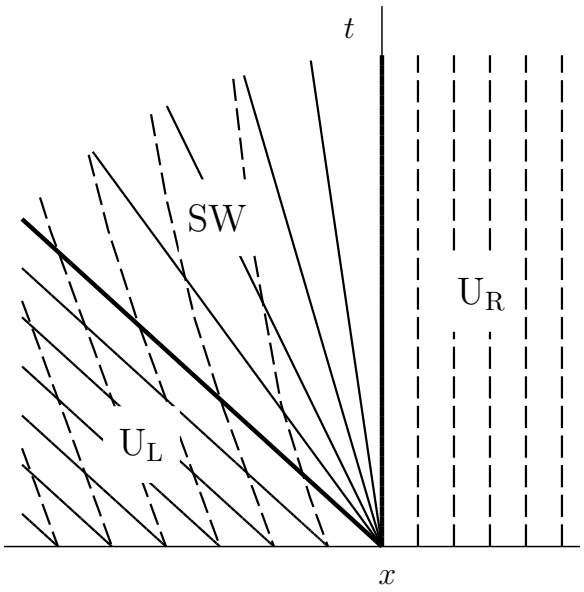

Figure 6.1: The typical arrangement of the characteristics in the (x,t)-plane for the dry-bed problem with $b_{\mathrm{L}} < 0$. Three separate regions are identified, namely a uniform region to the left (labelled $\mathrm{U_L}$), a uniform region to the right (labelled $\mathrm{U_R}$), and a simple-wave region (labelled SW). The dashed lines correspond to the $C_{\pm}^{\mathrm{R}}$ characteristics in region $\mathrm{U_R}$ and the C_{-}^{L} characteristics in region $\mathrm{U_L}$, the thin solid lines correspond to the C_{+}^{L} characteristics in region $\mathrm{U_L}$ and the C_{+} characteristics which form the expansion fan in region SW, and the thick solid lines represent the limiting characteristics which form the boundaries of region SW.

and b_{L}. Physically, since h is a thickness, we are restricted to positive values of h_{L}, but, since b is a concentration gradient, b_{L} can be either positive or negative, and we now consider these possibilities in turn.

6.3.1 The dry-bed problem with $b_{\mathrm{L}} < 0$

Firstly, consider the case $b_{\mathrm{L}} < 0$ in which a negative concentration gradient drives the fluid to the left. In this case, the $C_{\pm}^{\mathrm{L}}$ characteristics have a negative slope, and hence the information carried by these characteristics propagates to the left.

Figure 6.1 shows the typical arrangement of the characteristics in the (x,t)-plane in this case. Three separate regions are identified, namely a uniform region to the left (labelled $\mathrm{U_L}$), a uniform region to the right (labelled $\mathrm{U_R}$), and a simple-

wave region (labelled SW). The dashed lines correspond to the $C_{\pm}^{\mathrm{R}}$ characteristics in region $\mathrm{U_R}$ and the C_{-}^{L} characteristics in region $\mathrm{U_L}$, the thin solid lines correspond to the C_{+}^{L} characteristics in region $\mathrm{U_L}$ and the C_{+} characteristics which form the expansion fan in region SW, and the thick solid lines represent the limiting characteristics which form the boundaries of region SW. We now construct the solutions that hold in each of these regions.

Region $\mathrm{U_L}$ corresponds to the uniform region of undisturbed fluid to the left, i.e., extending to $x \to -\infty$, with the right-hand boundary of region $\mathrm{U_L}$ being the limiting C_{+}^{L} characteristic, i.e., the straight line given by (6.3.2) with $x_{+}^{\mathrm{L}} = 0$. The solutions for h and b in region $\mathrm{U_L}$ are therefore simply

$$h = h_{\mathrm{L}}, \quad b = b_{\mathrm{L}} \, (< 0) \quad \text{for} \quad x \leq \frac{3}{2} h_{\mathrm{L}} b_{\mathrm{L}} t \, (< 0). \tag{6.3.4}$$

The corresponding solution for c is obtained by integrating $\partial c / \partial x = b_{\mathrm{L}}$ with respect to x and (6.2.2) with respect to t to obtain

$$c = c_{\mathrm{L}} + b_{\mathrm{L}} x - \frac{1}{2} h_{\mathrm{L}} {b_{\mathrm{L}}}^2 t \quad \text{for} \quad x \leq \frac{3}{2} h_{\mathrm{L}} b_{\mathrm{L}} t \, (< 0), \tag{6.3.5}$$

where c_{L} is a constant of integration.

Similarly, region $\mathrm{U_R}$ corresponds to the uniform region with no fluid to the right of $x = 0$, i.e., extending from $x = 0$ to $x \to \infty$. The solutions for h, b and c in region $\mathrm{U_R}$ are therefore simply

$$h \equiv 0, \quad b \equiv 0, \quad c \equiv 0 \quad \text{for} \quad x \geq 0. \tag{6.3.6}$$

The C_{-}^{L} characteristics emanating from region $\mathrm{U_L}$ intersect the limiting C_{+}^{L} characteristic, and then enter region SW. Since these characteristics carry the same value of $r_{-} = r_{-}^{\mathrm{L}}$ in both regions, we have

$$\frac{h}{b} = \frac{h_{\mathrm{L}}}{b_{\mathrm{L}}} \quad \text{in region SW.} \tag{6.3.7}$$

Furthermore, since each C_{+} characteristic carries a constant value of r_{+}, we also have

$$hb = k \quad \text{in region SW} \tag{6.3.8}$$

for some constant k that is different on each C_{+} characteristic in region SW. Solving equations (6.3.7) and (6.3.8) shows that both h and b are constant along

any given C_+ characteristic in region SW. Thus λ_+ must be constant for any value of k and, from (6.2.7), the C_+ characteristics in region SW must be straight lines through the origin of the (x,t)-plane with slopes depending on the value of k. These C_+ characteristics form the expansion fan in region SW shown in Figure 6.1. Furthermore, since all C_+ characteristics are straight lines, we may write

$$\frac{\mathrm{d}x}{\mathrm{d}t} = \frac{x}{t} = \frac{3}{2}hb. \tag{6.3.9}$$

Solving equations (6.3.7) and (6.3.9), we find the simple-wave solutions for h and b in region SW to be

$$h = \sqrt{\frac{2h_{\mathrm{L}}x}{3b_{\mathrm{L}}t}}, \quad b = -\sqrt{\frac{2b_{\mathrm{L}}x}{3h_{\mathrm{L}}t}}\,(<0), \tag{6.3.10}$$

where we have chosen the signs of the square roots appearing in h and b appropriately.

The corresponding simple-wave solution for c in region SW which is continuous with the solution in region $\mathrm{U_L}$ across the limiting C_+^{L} characteristic, i.e., across $x = 3h_{\mathrm{L}}b_{\mathrm{L}}t/2$, is

$$c = c_{\mathrm{L}} + \left(\frac{2}{3}\right)^{3/2}\sqrt{\frac{b_{\mathrm{L}}x^3}{h_{\mathrm{L}}t}}. \tag{6.3.11}$$

The presence of the arbitrary constant, namely c_{L}, in the solution for c reflects the fact that adding a uniform amount of solute to the film has no effect on the dynamics of the system, i.e., only gradients in the concentration of solute affect the behaviour of the film.

Figure 6.2 shows typical plots of the exact solutions given by (6.3.4)–(6.3.6), (6.3.10) and (6.3.11), and, in particular, shows the uniform solutions to the right and to the left and the simple-wave solutions that connect them. Since b is always negative, the negative concentration gradient always drives the fluid to the left, advecting the solute with it. Note that, since gravity, capillarity and diffusion effects have all been neglected, there is no physical mechanism to drive the fluid rightwards, and so the initially dry region $x > 0$ always remains dry.

We also sought numerical solutions of the system of equations (4.7.1) and (4.7.3) (with $s \equiv 0$ and in the limit $K \to 0$), with finite (but large) values of Ca and $\mathrm{P_b}$ (specifically, both were taken to be 10^4), and compared these numerical

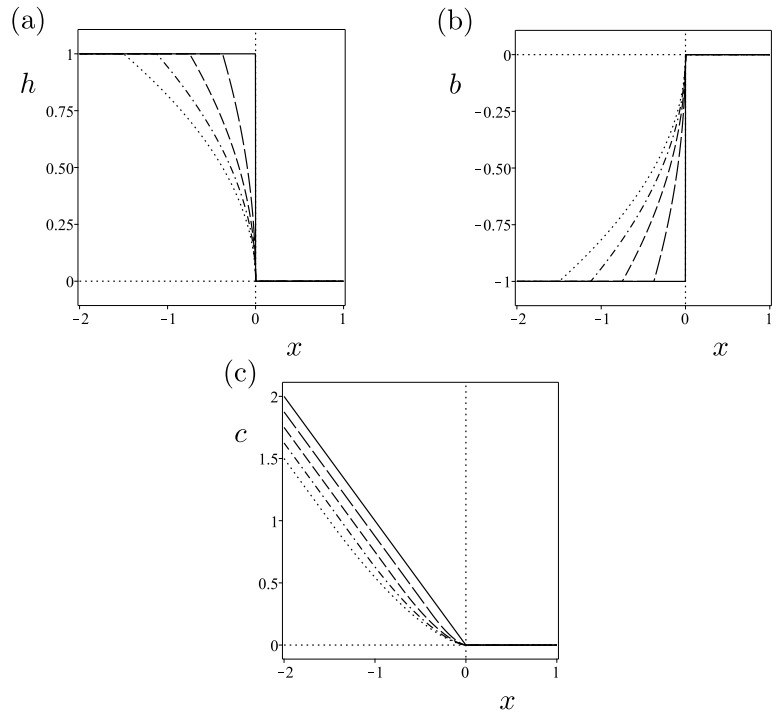

Figure 6.2: Exact solutions of the dry-bed problem with $b_{\mathrm{L}} < 0$ given by equations (6.3.4)–(6.3.6), (6.3.10) and (6.3.11) for (a) h, (b) b and (c) c with initial conditions (6.2.8), where $h_{\mathrm{R}} = 0$, $b_{\mathrm{R}} = 0$, $h_{\mathrm{L}} = 1$, $b_{\mathrm{L}} = -1$ and $c_{\mathrm{L}} = 0$, for $t = 0, 0.25, 0.5, 0.75, 1$ (solid to dotted lines, respectively).

solutions with the analytical simple-wave solutions obtained earlier and shown in Figure 6.2. The initial conditions for h and c are piecewise constant and piecewise linear, respectively, as given by equation (6.2.8), and are smoothed by COMSOL such that they each have at least continuous first and second derivatives by smoothly interpolating over a small range of x around the discontinuity. The initial conditions, before smoothing, are

$$h = \begin{cases} h_L & \text{for} \quad x < 0, \\ 0 & \text{for} \quad x > 0, \end{cases} \qquad c = \begin{cases} b_L(x - x_0) & \text{for} \quad x < 0, \\ x_0 & \text{for} \quad x > 0, \end{cases} \qquad \text{at} \quad t = 0, \tag{6.3.12}$$

where x_0 is a positive constant (chosen to be $x_0 = 10$ so that $c > 0$ in the computational domain). The computational domain was chosen to be the interval $[-30, 1]$, so that there were no significant edge effects from the left-hand boundary, and, since both h and c remain constant to the right of the initial discontinuity,

only a relatively small portion of $x > 0$ needs to be simulated. A uniform mesh of 3000 points was used, in order to resolve any sharp transitions between the two uniform solutions that occur for early times. The simulation was run for 20 units of dimensionless time, and used COMSOL's built in variable-time-step methods. The typical computation times were approximately 15 seconds.

Figures 6.3 and 6.4 show the numerically calculated solutions of equations (4.7.1) and (4.7.3) subject to the initial condition (6.3.12). As time increases, the initial condition "spreads", but only to the left, which is consistent with the analytical simple-wave solutions obtained in this section for the dry-bed case with $r_- = 0$. In order to compare these numerical solutions directly with the analytical solutions, we rescale the spatial variable in both the analytical and the numerical solutions to be the simple wave variable $\xi = x/t$.

Figures 6.5 and 6.6 show a comparison between the numerical solution plotted using $\xi = x/t$ (shown solid), and the analytical solution (shown dashed). There is very good agreement between the numerical and analytical solutions for both h and b, except near the left edge of region SW. These differences are due to the smoothing associated with the small, but not entirely negligible, effects of diffusion and capillarity in equations (4.7.1) and (4.7.3).

6.3.2 The dry-bed problem with $b_{\mathrm{L}} > 0$

Secondly, consider the case $b_{\mathrm{L}} > 0$ in which a positive concentration gradient drives the fluid to the right. In this case, the $C_{\pm}^{\mathrm{R}}$ characteristics, given by (6.3.1), are again vertical straight lines, but the $C_{\pm}^{\mathrm{L}}$ characteristics, given by (6.3.2) and (6.3.3), now have a positive slope. The C_+ and C_- characteristics therefore intersect at the origin of the (x,t)-plane, meaning that shocks form instantly (i.e., at $t = 0$) in both h and b at $x = 0$, and for $t > 0$ these shocks propagate with some speed $\dot{x}_{\mathrm{s}}$. The speed of the shocks $\dot{x}_{\mathrm{s}}$ is determined by the Rankine–Hugoniot shock conditions [117] for this problem, namely

$$\dot{x}_{\mathrm{s}} \left[\!\left[h\right]\!\right] = \frac{1}{2}\left[\!\left[h^2 b\right]\!\right], \tag{6.3.13}$$

$$\dot{x}_{\mathrm{s}} \left[\!\left[b\right]\!\right] = \frac{1}{2}\left[\!\left[h b^2\right]\!\right], \tag{6.3.14}$$

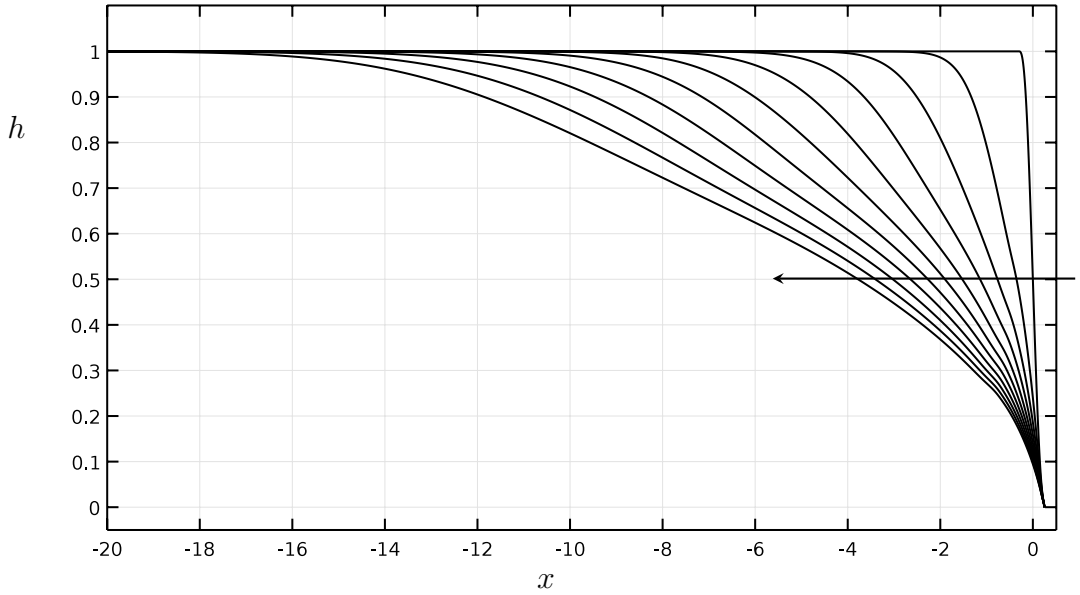

Figure 6.3: Numerically calculated solutions for the film thickness h in the dry-bed problem when $h_R = b_R \equiv 0$, $b_L = -1$, $h_L = 1$. The arrow denotes the direction of increasing time.

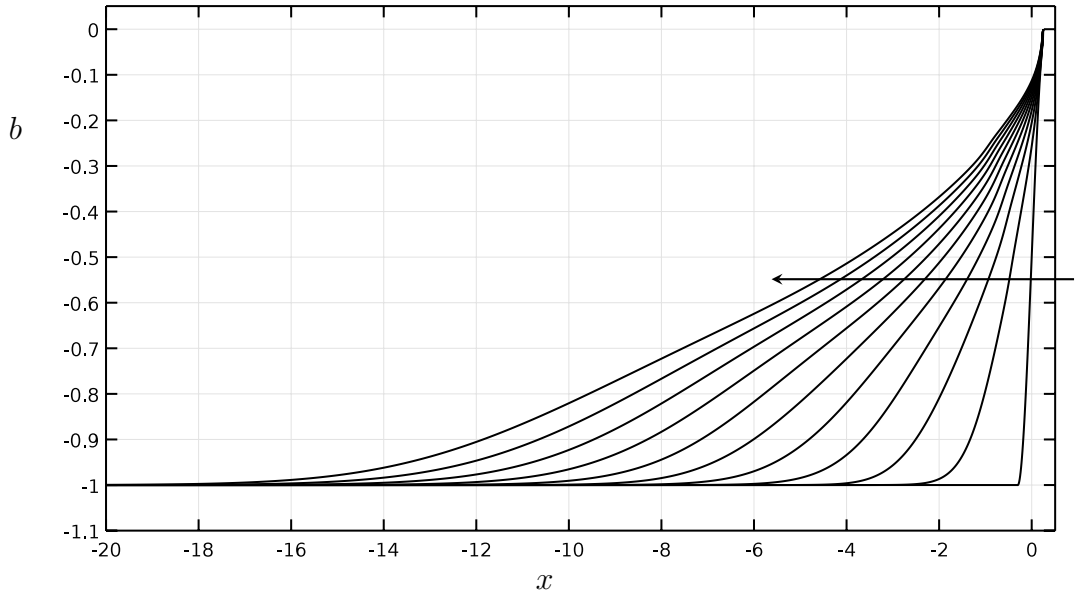

Figure 6.4: As in Figure 6.3 but showing the concentration gradient b.

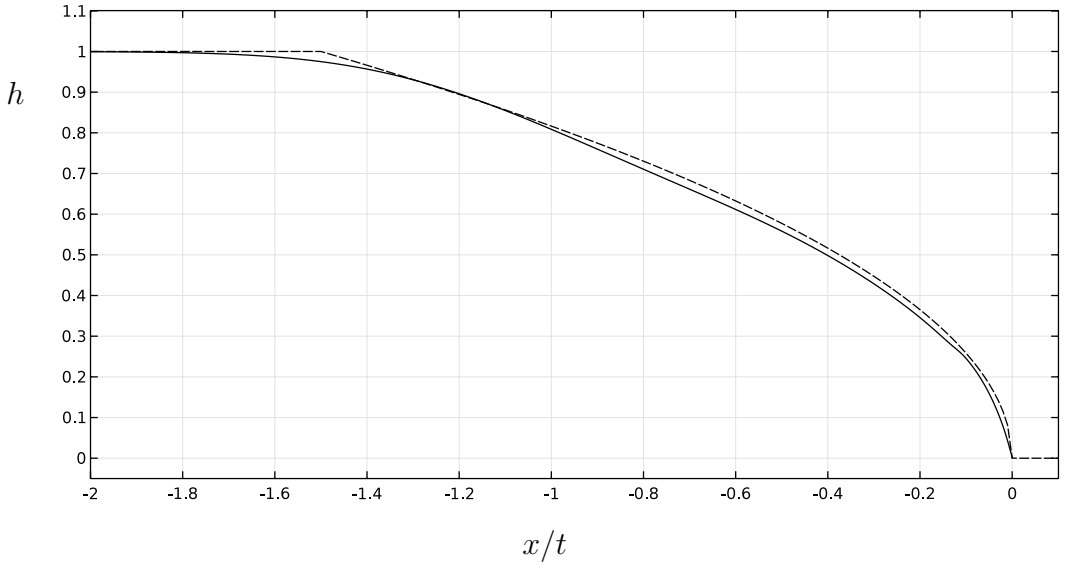

Figure 6.5: Comparison between the numerical solution (shown solid) and the analytical solution (shown dashed) for the film thickness h in the dry-bed problem when $h_R = b_R \equiv 0$, $b_L = -1$, $h_L = 1$, $t = 10$.

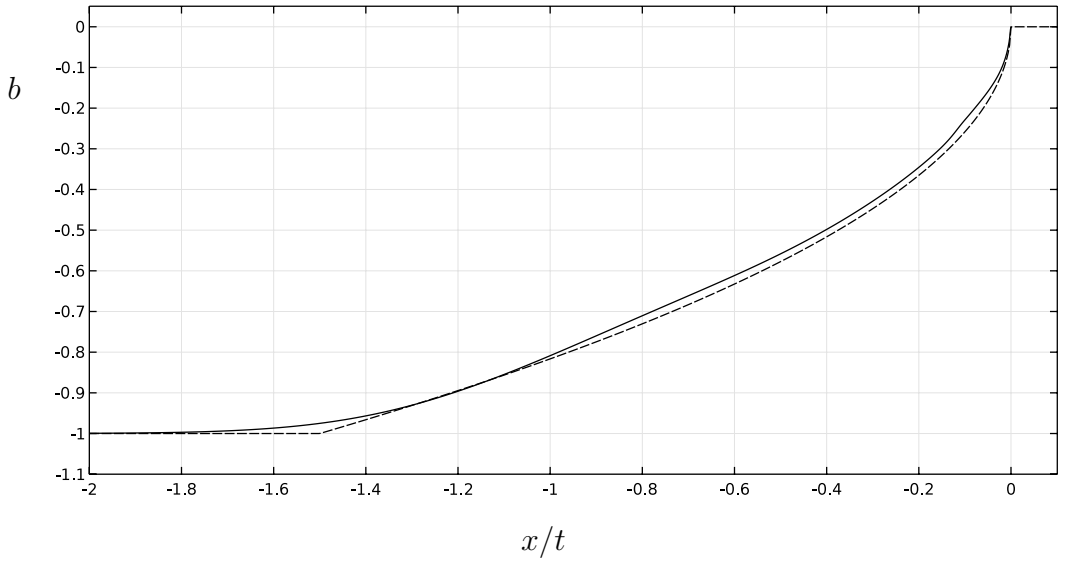

Figure 6.6: As in Figure 6.5 but showing the concentration gradient b.

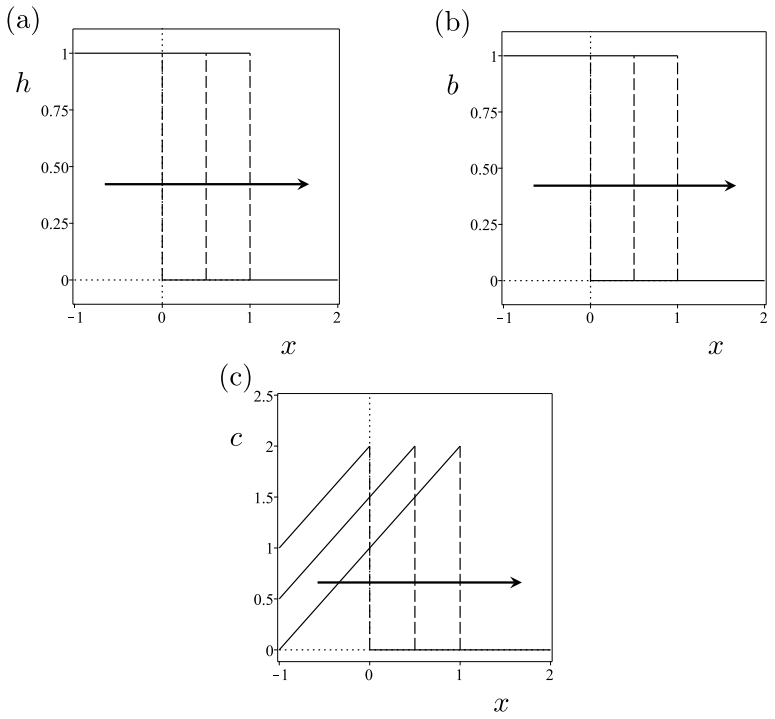

Figure 6.7: Exact solutions of the dry-bed problem with $b_{\mathrm{L}} > 0$ given by equation (6.3.16) for (a) h, (b) b and (c) c with initial conditions (6.2.8), where $h_{\mathrm{R}} = 0$, $b_{\mathrm{R}} = 0$, $h_{\mathrm{L}} = 1$, $b_{\mathrm{L}} = 1$ and $c_{\mathrm{L}} = 2$, for $t = 0, 1, 2$. The arrows indicate the rightwards propagation of the shocks, which are indicated with dashed lines.

where the notation $[\![u]\!]$ denotes the jump in the quantity u across the shock. Solving (6.3.13) and/or (6.3.14) yields

$$\dot{x}_{\mathrm{s}} = \frac{1}{2} h_{\mathrm{L}} b_{\mathrm{L}} \, (> 0), \tag{6.3.15}$$

showing that the location of the shocks is given by the limiting C_{-}^{L} characteristic. It is then straightforward to obtain the solutions for h, b and c, namely

$$\begin{cases} h = h_{\mathrm{L}}, \quad b = b_{\mathrm{L}} \, (> 0), \quad c = c_{\mathrm{L}} + b_{\mathrm{L}} x - \frac{1}{2} h_{\mathrm{L}} {b_{\mathrm{L}}}^2 t & \text{for} \quad x < \frac{1}{2} h_{\mathrm{L}} b_{\mathrm{L}} t \, (> 0), \\ h \equiv 0, \quad b \equiv 0, \quad c \equiv 0 & \text{for} \quad x > \frac{1}{2} h_{\mathrm{L}} b_{\mathrm{L}} t \, (> 0), \end{cases} \tag{6.3.16}$$

which simply represent uniform solutions for h and b and a linear solution for c, terminated by shocks that propagate rightwards at constant speed $\dot{x}_{\mathrm{s}}$ given by (6.3.15).

Figure 6.7 shows typical plots of the exact solutions given by (6.3.16), and, in particular, shows the rightwards propagation of the shocks. Note that, unlike

in the case $b_{\mathrm{L}} < 0$ shown on Figure 6.2, in this case the positive concentration gradient provides a physical mechanism that can drive the fluid rightwards into the initially dry region $x > 0$.

6.4 The "wet-bed" problem

In this section we consider the "wet-bed" problem in which $h_{\mathrm{L}} > 0$ and $h_{\mathrm{R}} > 0$, so that there is initially fluid everywhere. Since there are now four (rather than two) free parameters, there are more cases to consider than for the dry-bed problem. However, for brevity, in the present work we consider only two of the more interesting cases, in both of which $h_{\mathrm{L}} > h_{\mathrm{R}} > 0$, $b_{\mathrm{L}} < 0$ and $b_{\mathrm{R}} < 0$. These cases are somewhat analogous to the cases of subcritical and supercritical flow, respectively, in, for example, the classical dam-break problem [117]. In particular, in section 6.4.1 we consider the case $h_{\mathrm{L}}b_{\mathrm{L}} < h_{\mathrm{R}}b_{\mathrm{R}}$, and show that the solution to this problem resembles that of the classical Stoker problem [95] in which a simple-wave solution continuously connects two uniform regions, the rightmost of which is connected by a shock to a further uniform region, while in section 6.4.2 we consider the case $h_{\mathrm{L}}b_{\mathrm{L}} > h_{\mathrm{R}}b_{\mathrm{R}}$, and show that the solution to this problem consists of three uniform regions connected by two shocks. In both cases, like in the dry-bed problem discussed in section 6.3.1, since b is always negative, the negative concentration gradient always drives the fluid to the left, and so the solution in the region $x > 0$ always remains at its initial values.

6.4.1 Wet-bed problem with $h_{\mathrm{L}}b_{\mathrm{L}} < h_{\mathrm{R}}b_{\mathrm{R}}$

Firstly, we consider the case $h_{\mathrm{L}}b_{\mathrm{L}} < h_{\mathrm{R}}b_{\mathrm{R}}$. For $x > 0$ we have $h = h_{\mathrm{R}}$ and $b = b_{\mathrm{R}}$ at $t = 0$, and so the $C^{\mathrm{R}}_{\pm}$ characteristics are straight lines given by

$$C^{\mathrm{R}}_{+} : \; x = \frac{3}{2}h_{\mathrm{R}}b_{\mathrm{R}}t + x^{\mathrm{R}}_{+} \tag{6.4.1}$$

$$C^{\mathrm{R}}_{-} : \; x = \frac{1}{2}h_{\mathrm{R}}b_{\mathrm{R}}t + x^{\mathrm{R}}_{-}, \tag{6.4.2}$$

where $x^{\mathrm{R}}_{\pm}$ are constants that label each of the characteristics. For $x < 0$ we have $h = h_{\mathrm{L}}$ and $b = b_{\mathrm{L}}$ at $t = 0$, and so the $C^{\mathrm{L}}_{\pm}$ characteristics are, as in the

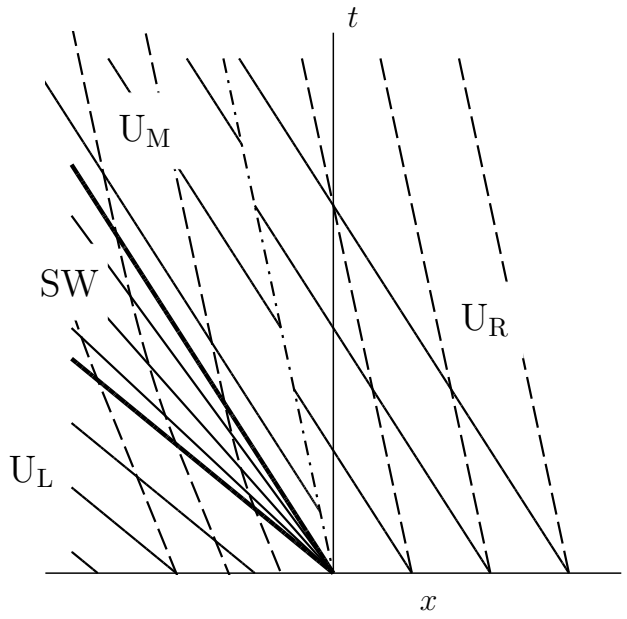

Figure 6.8: The typical arrangement of the characteristics in the (x,t)-plane for the wet-bed problem with $h_{\mathrm{L}} > h_{\mathrm{R}} > 0$, $b_{\mathrm{L}} < 0$, $b_{\mathrm{R}} < 0$ and $h_{\mathrm{L}}b_{\mathrm{L}} < h_{\mathrm{R}}b_{\mathrm{R}}$. In addition to two uniform regions and one simple-wave region similar to those that occur in the dry-bed problem (again labelled $\mathrm{U_L}$, $\mathrm{U_R}$ and SW, respectively), an additional "middle" uniform region (labelled $\mathrm{U_M}$), not present in the dry-bed problem, that connects the simple-wave solutions in region SW to the uniform solutions in region $\mathrm{U_R}$ via a shock (indicated with the dash-dot line) is also identified.

dry-bed problem, straight lines given by (6.3.2) and (6.3.3). From the forms of these characteristics, it is clear that if the constraint $h_{\mathrm{L}}b_{\mathrm{L}} < h_{\mathrm{R}}b_{\mathrm{R}}$ did *not* hold, then the slope of the C_+^{R} characteristics would be shallower than that of the C_+^{L} characteristics, and the C_+ characteristics would therefore intersect at the origin of the (x,t)-plane, meaning that shocks would form instantly in both h and b at $x = 0$. This is the situation considered in section 6.4.2.

Figure 6.9 shows the typical arrangement of the characteristics in the (x,t)-plane for the wet-bed problem in the case $h_{\mathrm{L}}b_{\mathrm{L}} < h_{\mathrm{R}}b_{\mathrm{R}}$. In addition to two uniform regions and one simple-wave region similar to those that occur in the dry-bed problem (again labelled $\mathrm{U_L}$, $\mathrm{U_R}$ and SW, respectively), an additional "middle" uniform region (labelled $\mathrm{U_M}$), not present in the dry-bed problem, that connects the simple-wave solutions in region SW to the uniform solutions in

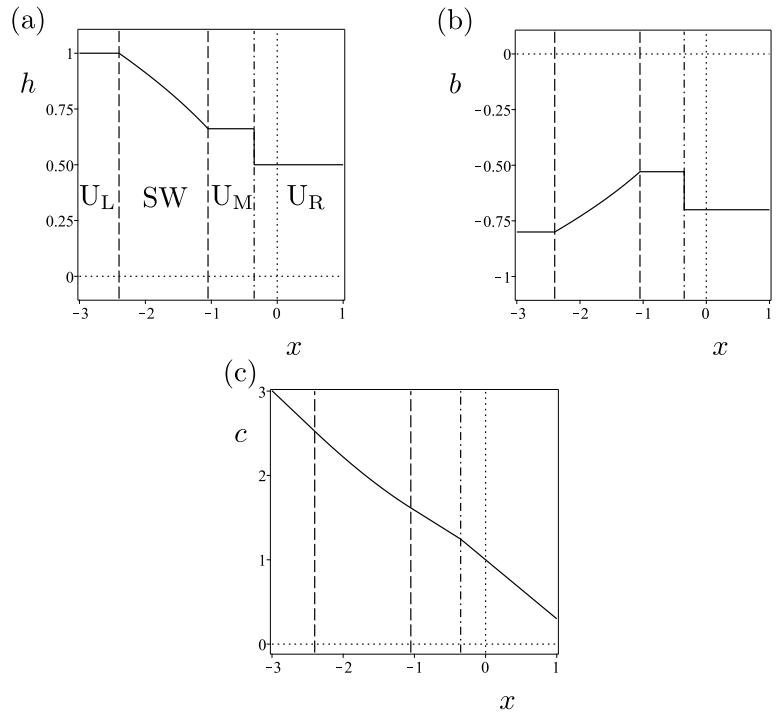

Figure 6.9: Exact solutions of the wet-bed problem with $h_{\rm L} > h_{\rm R} > 0$, $b_{\rm L} < 0$, $b_{\rm R} < 0$ and $h_{\rm L} b_{\rm L} < h_{\rm R} b_{\rm R}$ given by (6.3.10), (6.3.11), (6.4.3), (6.4.4), (6.4.9) and (6.4.10) for (a) h, (b) b and (c) c, where $h_{\rm L} = 1$, $b_{\rm L} = -0.8$, $h_{\rm R} = 0.5$, $b_{\rm R} = -0.7$ and $c_{\rm L} = 1$, at $t = 2$. The boundaries between the regions are indicated with dashed lines, except for the locations of the shocks at the boundary between regions $\mathrm{U_M}$ and $\mathrm{U_R}$, which are indicated with dash-dot lines.

region $\mathrm{U_R}$ via a shock (indicated with the dash-dot line) is also identified. We now construct the solutions that hold in each of these regions.

The solutions for h, b and c in the uniform regions $\mathrm{U_L}$ and $\mathrm{U_R}$ are simply

$$h = h_{\rm L}, \quad b = b_{\rm L}\,(<0), \quad c = c_{\rm L} + b_{\rm L} x - \frac{1}{2} h_{\rm L} {b_{\rm L}}^2 t \quad \text{for} \quad x \leq \frac{3}{2} h_{\rm L} b_{\rm L} t\,(<0) \tag{6.4.3}$$

and

$$h = h_{\rm R}, \quad b = b_{\rm R}\,(<0), \quad c = c_{\rm R} + b_{\rm R} x - \frac{1}{2} h_{\rm R} {b_{\rm R}}^2 t \quad \text{for} \quad x \geq \frac{3}{2} h_{\rm R} b_{\rm R} t\,(<0), \tag{6.4.4}$$

respectively, where $c_{\rm L}$ and $c_{\rm R}$ are constants of integration.

As in the dry-bed problem, the $C_-^{\rm L}$ characteristics emanating from region $\mathrm{U_L}$ enter region SW, and so the solutions for h and b in this region are precisely the same as those in the dry-bed problem given by (6.3.10) and (6.3.11), respectively.

However, unlike in the dry-bed problem, the right-hand boundary of region SW is not simply the vertical line $x = 0$, but now must be found as part of the solution. Using the solutions for h and b in region SW, the C_-^{L} characteristics in this region satisfy

$$\frac{\mathrm{d}x}{\mathrm{d}t} = \frac{x}{3t}, \tag{6.4.5}$$

and hence are given by

$$t = \beta x^3, \tag{6.4.6}$$

where $\beta\,(< 0)$ is a constant of integration which must be negative in order that the C_-^{L} characteristics be continuous across the boundary between regions $\mathrm{U_L}$ and SW. After passing through region SW, the C_-^{L} characteristics eventually intersect the boundary between regions SW and $\mathrm{U_M}$, and then enter region $\mathrm{U_M}$. Since these characteristics carry the same value of $r_- = r_-^{\mathrm{L}}$ in both regions, we have

$$\frac{b}{h} = \frac{b_{\mathrm{L}}}{h_{\mathrm{L}}} \quad \text{in region } \mathrm{U_M}. \tag{6.4.7}$$

However, there are no solutions for the uniform values of h and b in region $\mathrm{U_M}$, denoted by h_{M} and b_{M}, that are continuous with the solutions in region $\mathrm{U_R}$ given by (6.4.4), and so there must be shocks in h and b at the boundary between regions $\mathrm{U_M}$ and $\mathrm{U_R}$. The uniform values of h and b on either side of the shocks are related by the shock conditions (6.3.13) and (6.3.14), which, along with (6.4.7), give three simultaneous (nonlinear) algebraic equations for three unknowns, namely the shock speed $\dot{x}_{\mathrm{s}}$, h_{M} and b_{M}. Solving these equations yields

$$\dot{x}_{\mathrm{s}} = \frac{1}{2} h_{\mathrm{R}} b_{\mathrm{R}}\,(< 0), \tag{6.4.8}$$

showing that the location of the shocks is given by the limiting C_-^{R} characteristic, and the uniform solutions for h and b in region $\mathrm{U_M}$, namely

$$h_{\mathrm{M}} = \sqrt{\frac{h_{\mathrm{L}} h_{\mathrm{R}} b_{\mathrm{R}}}{b_{\mathrm{L}}}}, \quad b_{\mathrm{M}} = -\sqrt{\frac{h_{\mathrm{R}} b_{\mathrm{L}} b_{\mathrm{R}}}{h_{\mathrm{L}}}}\,(< 0). \tag{6.4.9}$$

The solution for c in region $\mathrm{U_M}$, denoted by c_{M}, which is continuous with the solution in region SW is

$$c_{\mathrm{M}} = c_{\mathrm{L}} + \sqrt{\frac{h_{\mathrm{R}} b_{\mathrm{L}} b_{\mathrm{R}}}{h_{\mathrm{L}}}} \left(\frac{h_{\mathrm{R}} b_{\mathrm{R}} t}{2} - x \right). \tag{6.4.10}$$

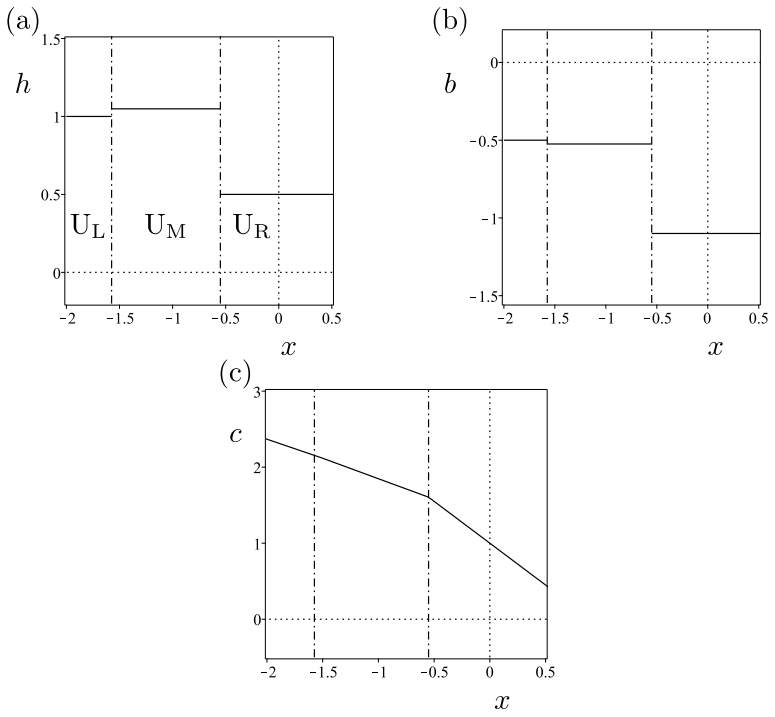

Figure 6.10: Exact solutions of the wet-bed problem with $h_{\mathrm{L}} > h_{\mathrm{R}} > 0$, $b_{\mathrm{L}} < 0$, $b_{\mathrm{R}} < 0$ and $h_{\mathrm{L}} b_{\mathrm{L}} > h_{\mathrm{R}} b_{\mathrm{R}}$ given by (6.4.3), (6.4.4), (6.4.9) and (6.4.10) for (a) h, (b) b and (c) c, where $h_{\mathrm{L}} = 1$, $b_{\mathrm{L}} = -0.5$, $h_{\mathrm{R}} = 0.5$, $b_{\mathrm{R}} = -1.1$ and $c_{\mathrm{L}} = 1$, at $t = 1$. The shocks at the boundaries between regions $\mathrm{U_L}$ and $\mathrm{U_M}$ and between regions $\mathrm{U_M}$ and $\mathrm{U_R}$ are indicated with dash-dot lines.

Requiring that the solution for c (but not, of course, the solutions for h and b) is also continuous across the boundary between regions $\mathrm{U_M}$ and $\mathrm{U_R}$, i.e., across $x = \frac{1}{2} h_{\mathrm{R}} b_{\mathrm{R}} t$, shows that $c_{\mathrm{R}} = c_{\mathrm{L}}$, i.e., that, as in the dry-bed case, there is a single arbitrary constant, namely c_{L}, in the solution for c which has no effect on the dynamics of the system.

Figure 6.9 shows typical plots of the exact solutions for h, b and c given by (6.3.10), (6.3.11), (6.4.3), (6.4.4), (6.4.9) and (6.4.10). In particular, Figure 6.9 shows that the solutions for both h and b are continuous everywhere except for shocks at the boundary between region $\mathrm{U_M}$ and region $\mathrm{U_R}$, which propagate leftwards into the region $x < 0$ at constant speed $\dot{x}_{\mathrm{s}}$ given by (6.4.8).

6.4.2 Wet-bed problem with $h_{\mathrm{L}}b_{\mathrm{L}} > h_{\mathrm{R}}b_{\mathrm{R}}$

Secondly, we consider the case $h_{\mathrm{L}}b_{\mathrm{L}} > h_{\mathrm{R}}b_{\mathrm{R}}$, i.e., the case in which the C_+ characteristics intersect at the origin of the (x,t)-plane, meaning that shocks form instantly in both h and b at $x = 0$. In fact, it is immediately apparent that in this case there must be *two* shocks (rather than just one shock) in both h and b. Specifically, since the values h_{L}, b_{L}, h_{R} and b_{R} are all prescribed, a single shock in both h and b would introduce only a single unknown (namely, the single shock speed), leading to an over-determined system, and so a second shock with a second shock speed must also occur in both h and b.

Proceeding along the same lines as in the cases discussed previously, we find that the solution in this case consists of the uniform regions $\mathrm{U_L}$ and $\mathrm{U_R}$ in which the solutions for h, b and c are again given by (6.4.3) and (6.4.4) separated from a middle uniform region $\mathrm{U_M}$ in which the solutions for h, b and c are again given by (6.4.9) and (6.4.10). Solving the appropriate shock conditions yields

$$\dot{x}_{\mathrm{s}}^{\mathrm{LM}} = \frac{1}{2}\left(h_{\mathrm{L}}b_{\mathrm{L}} + h_{\mathrm{R}}b_{\mathrm{R}} - \sqrt{h_{\mathrm{L}}h_{\mathrm{R}}b_{\mathrm{L}}b_{\mathrm{R}}}\right) (< 0) \tag{6.4.11}$$

and

$$\dot{x}_{\mathrm{s}}^{\mathrm{MR}} = \frac{1}{2}h_{\mathrm{R}}b_{\mathrm{R}}\,(< 0), \tag{6.4.12}$$

where $\dot{x}_{\mathrm{s}}^{\mathrm{LM}}$ and $\dot{x}_{\mathrm{s}}^{\mathrm{MR}}$ denote the speeds of the shocks at the boundaries of regions $\mathrm{U_L}$ and $\mathrm{U_M}$ and regions $\mathrm{U_M}$ and $\mathrm{U_R}$, respectively. Note that $|\dot{x}_{\mathrm{s}}^{\mathrm{LM}}| > |\dot{x}_{\mathrm{s}}^{\mathrm{MR}}|$, and so the middle region gets monotonically wider as t increases, and, in particular, the shocks never collide. Furthermore, comparing the solutions in the three different regions reveals that whereas the value of b_{M} always lies between b_{L} and b_{R}, the value of h_{M} is always greater than *both* h_{L} and h_{R}, i.e., that the film is always thickest in the middle region.

Figure 6.10 shows typical plots of the exact solutions for h, b and c given by (6.4.3), (6.4.4), (6.4.9) and (6.4.10). In particular, Figure 6.10 shows that the solutions for both h and b are uniform everywhere except at the shocks, which propagate leftwards into the region $x < 0$ at constant speeds $\dot{x}_{\mathrm{s}}^{\mathrm{LM}}$ and $\dot{x}_{\mathrm{s}}^{\mathrm{MR}}$ given by (6.4.11) and (6.4.12), respectively. Figure 6.10 also shows that the film is thickest in the middle region between the two shocks.

6.5 Similarity Solutions

It is well known that equations governing the flow of thin films of fluid can, in some regimes, admit *similarity* (or, synonymously, *self-similar*) solutions, i.e., the solution for any time $t = t_1$ is simply an appropriately rescaled version of the solution for any other time $t = t_2$ (see, for example, Barenblatt [5]).

Unfortunately, the governing equations that arose in Chapters 4 and 5, i.e., equations (4.7.1)–(4.7.3), do not, in general, admit similarity solutions. However, in certain simplified regimes in which some physical effects are neglected, similarity solutions can be found that either represent the true long-time asymptotic behaviour of the system, or are valid in some range of intermediate times. In particular, we will see that, when the flux of solute is retained in the problem (i.e., when $\mathrm{Da_a} \neq 0$ and $\mathrm{Da_d} \neq 0$), no similarity solutions of the specific type that we seek can exist. In addition we will see that, when capillarity and solute diffusion are retained, the similarity solutions that we obtain can be either long-time or intermediate-time asymptotic solutions, depending on the values of the exponents in the similarity transformation.

In this section, we investigate several simplified regimes that admit similarity solutions. To do this, we first use a general similarity transformation to transform the system of PDEs governing the evolution of a thin film of surfactant- or anti-surfactant-laden fluid, without neglecting any of the physics. From these transformed equations, we investigate special cases in which exact similarity solutions can be obtained, and investigate the times for which we expect these solutions to be valid.

6.5.1 Similarity Transformation

We seek solutions to equations (4.7.1)–(4.7.3), when they are transformed according the following similarity transformation with general constant exponents α, β, γ, and ζ:

$$h(x,t) = \hat{h}(\xi)t^{\alpha}, \quad s(x,t) = \hat{s}(\xi)t^{\gamma}, \quad c(x,t) = \hat{c}(\xi)t^{\beta}, \quad \xi = xt^{\zeta}, \tag{6.5.1}$$

where ξ is the independent similarity variable. Substituting (6.5.1) into the PDEs (4.7.1)–(4.7.3) yields

$$\underbrace{\alpha\hat{h}+\zeta\xi\hat{h}'}+\left[\frac{1}{3\mathrm{Ca}}\hat{h}'''\hat{h}^3t^{3\alpha+4\zeta+1}-\frac{\mathrm{Ma}}{2}\hat{h}^2\hat{s}'t^{\alpha+2\zeta+\gamma+1}+\frac{\mathrm{Ma}}{2}\hat{h}^2\hat{c}'t^{\alpha+2\zeta+\beta+1}\right]'=0, \tag{6.5.2}$$

$$\underbrace{\gamma\hat{s}+\zeta\xi\hat{s}'}+\left[\frac{1}{2\mathrm{Ca}}\hat{h}'''\hat{h}^2\hat{s}t^{3\alpha+4\zeta+1}-\mathrm{Ma}\hat{h}\hat{s}\hat{s}'t^{\alpha+2\zeta+\gamma+1}+\mathrm{Ma}\hat{h}\hat{s}\hat{c}'t^{\alpha+2\zeta+\beta+1}\right]'$$
$$-\frac{1}{\mathrm{P_s}}\hat{s}''t^{2\zeta+1}-\mathrm{Da_a}K\hat{c}t^{\beta-\gamma+1}+\mathrm{Da_a}\hat{s}t^1=0, \tag{6.5.3}$$

$$\underbrace{\hat{h}\left(\beta\hat{c}+\zeta\xi\hat{c}'\right)}+\left[\frac{1}{3\mathrm{Ca}}\hat{h}'''\hat{h}^3t^{3\alpha+4\zeta+1}-\frac{\mathrm{Ma}}{2}\hat{h}^2\hat{s}'t^{\alpha+2\zeta+\gamma+1}+\frac{\mathrm{Ma}}{2}\hat{h}^2\hat{c}'t^{\alpha+2\zeta+\beta+1}\right]\hat{c}'$$
$$-\frac{1}{\mathrm{P_b}}\left(\hat{h}\hat{c}'\right)'t^{2\zeta+1}-\delta\mathrm{Da_d}K\hat{c}t^{1-\alpha}+\delta\mathrm{Da_d}\hat{s}t^{\gamma-\beta-\alpha+1}=0, \tag{6.5.4}$$

where the prime denotes differentiation with respect to ξ and the underbraced terms are the transformed time derivatives $\partial/\partial t$) . In addition to these equations we also require that the change in the total mass of solute in the system balances the amount of solute (if any) that is being added or removed from the system by any means. The total mass of solute in the system at any instant, which we denote by $M(t)$, is given by

$$M(t)=\int_{-\infty}^{+\infty}(\delta s+hc)\,\mathrm{d}x, \tag{6.5.5}$$

which, under the transformation (6.5.1), becomes

$$Qt^m=\int_{-\infty}^{+\infty}\left(\delta\hat{s}t^{\gamma-\zeta}+\hat{h}\hat{c}t^{\alpha+\beta-\zeta}\right)\mathrm{d}\xi, \tag{6.5.6}$$

where we have written $M(t)=Qt^m$. When $m=0$, the total mass of solute remains constant for all time; when $m>0$ the total mass of solute increases over time; when $m<0$ the total mass of solute decreases over time.

Balancing terms in each of equations (6.5.2)–(6.5.4) and (6.5.6) yields conditions on the values of the exponents that must be satisfied. Many different combinations of balancing terms could be analysed, and a detailed discussion of every case is not presented here. Instead, we consider only an interesting subset of the possible problems; even this subset contains rich mathematical and physical

problems. In particular, we consider only those regimes in which the underbraced terms in equations (6.5.2)–(6.5.4) are balanced by some of the other terms. This precludes any solutions in which the bulk–surface flux of solute is retained, since it is impossible to balance the flux term proportional to s in equation (6.5.3), which scale with t^1, with the time derivatives, which scale with t^0.

6.5.2 Similarity Solution for an Insoluble Surfactant

In order to demonstrate that our model recovers the behaviour of the similarity solutions that occur for classical insoluble surfactants, we first consider one particular similarity solution that was first obtained by Jensen and Grotberg [39], and provide a generalisation. To model an insoluble surfactant solution we set $\hat{c} \equiv 0$, and $\mathrm{Da_a} = 0$ in equations (6.5.2)–(6.5.4) so that the bulk concentration is zero, and no surface concentration is transferred to the bulk. We also choose $\delta = 1$ and $\beta = 0$ without loss of generality, and choose the characteristic velocity scale to be $U^* = U^*_{\mathrm{Ma}}$ so that $\mathrm{Ma} = 1$. For the time being, we also take the limits $\mathrm{Ca} \to \infty$ and $\mathrm{P_s} \to \infty$ so that both capillarity and diffusion are neglected, but we will discuss later the appropriateness of neglecting these terms.

With the above assumptions the governing ODEs (6.5.2) and (6.5.3) become

$$\alpha\hat{h} + \zeta\xi\hat{h}' - \frac{1}{2}\left(\hat{h}^2\hat{s}'\right)' t^{\alpha+2\zeta+\gamma+1} = 0, \tag{6.5.7}$$

$$\gamma\hat{s} + \zeta\xi\hat{s}' - \left(\hat{h}\hat{s}\hat{s}'\right)' t^{\alpha+2\zeta+\gamma+1} = 0, \tag{6.5.8}$$

along with the conservation of solute (6.5.6), which now states

$$Qt^m = \int_{-\infty}^{+\infty} \hat{s}t^{\gamma-\zeta}\,\mathrm{d}\xi. \tag{6.5.9}$$

Balancing terms in each of equations (6.5.7)–(6.5.9) yields two conditions on the exponents, namely

$$\alpha + 2\zeta + \gamma + 1 = 0 \tag{6.5.10}$$

from both (6.5.7) and (6.5.8), and

$$\gamma - \zeta = m \tag{6.5.11}$$

from (6.5.9). Solving these two conditions for γ and ζ, we obtain

$$\gamma = \frac{1}{3}\left(2m - \alpha - 1\right), \tag{6.5.12}$$

$$\zeta = -\frac{1}{3}\left(m + \alpha + 1\right), \tag{6.5.13}$$

and with these the governing equations (6.5.7) and (6.5.8) become

$$\alpha\hat{h} - \frac{1}{3}\left(m + \alpha + 1\right)\xi\hat{h}' - \frac{1}{2}\left(\hat{h}^2\hat{s}'\right)' = 0, \tag{6.5.14}$$

$$\frac{1}{3}\left(2m - \alpha - 1\right)\hat{s} - \frac{1}{3}\left(m + \alpha + 1\right)\xi\hat{s}' - \left(\hat{h}\hat{s}\hat{s}'\right)' = 0. \tag{6.5.15}$$

Equations (6.5.14) and (6.5.15) are generalisations to non-zero values of α of the corresponding equations obtained by Jensen and Grotberg [39]: by setting $\alpha = 0$, one obtains exactly their equations (3.8), with a and b given by their equations (3.4a).

With γ and ζ given by (6.5.12) and (6.5.13), respectively, the coefficient of the diffusion term in equations (6.5.2) and (6.5.3) that we have neglected thus far is

$$\frac{1}{\mathrm{P_s}}t^{r_\mathrm{d}}, \tag{6.5.16}$$

and the coefficient of the capillarity term in equations (6.5.2) and (6.5.3) that we have neglected thus far is

$$\frac{1}{\mathrm{Ca}}t^{r_\mathrm{c}}, \tag{6.5.17}$$

where

$$r_\mathrm{d} = -\frac{1}{3}\left(2\alpha + 2m - 1\right) \tag{6.5.18}$$

and

$$r_\mathrm{c} = \frac{1}{3}\left(5\alpha - 4m - 1\right), \tag{6.5.19}$$

and by looking at the signs and magnitudes of r_d and r_c, we may determine the values of α and m for which capillarity and diffusion will be negligible for long time, or will eventually dominate.

Figure 6.11 shows a plot of the lines $r_\mathrm{d} = 0$ and $r_\mathrm{c} = 0$ in (α, m) parameter space, with r_d and r_c given by (6.5.18) and (6.5.19), respectively, for an insoluble surfactant solution (as considered by Jensen and Grotberg [39]). In regions 1 and

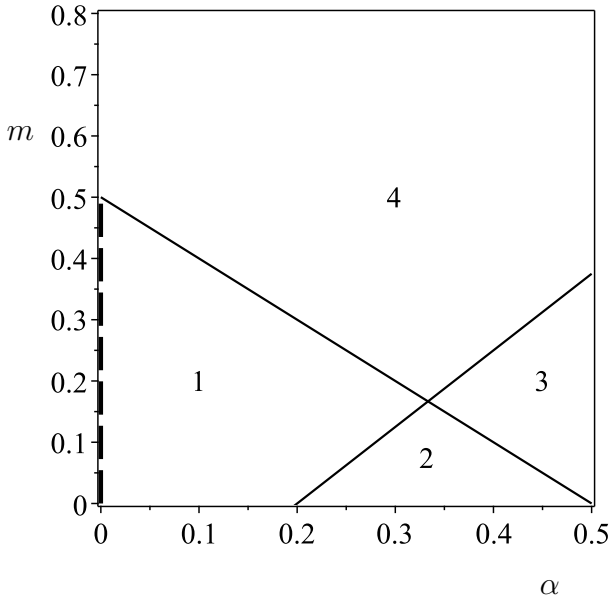

Figure 6.11: A plot of the lines $r_{\mathrm{d}} = 0$ and $r_{\mathrm{c}} = 0$ in (α, m) parameter space, with r_{d} and r_{c} given by (6.5.18) and (6.5.19), respectively, for an insoluble surfactant solution (as considered by Jensen and Grotberg [39]). In regions 1 and 2 diffusion will eventually dominate over the Marangoni effect; in regions 2 and 3 capillarity will eventually dominate over the Marangoni effect; in region 4 diffusion and capillarity will eventually be negligible. The thick dashed line lies in region 1 and corresponds to the values of α and m that were considered by Jensen and Grotberg [39].

2, $r_{\mathrm{d}} > 0$ and so diffusion will dominate over the Marangoni effect at times longer than $t = O(\mathrm{P_s}^{1/r_{\mathrm{d}}})$. In regions 2 and 3, $r_{\mathrm{c}} > 0$ and so capillarity will dominate over the Marangoni effect at times longer than $t = O(\mathrm{Ca}^{1/r_{\mathrm{c}}})$. In region 4, $r_{\mathrm{d}} < 0$ and $r_{\mathrm{c}} < 0$, and so both diffusion and capillarity will be negligible for long times. Therefore, equations (6.5.14) and (6.5.15) will describe the true long-time asymptotic behaviour of the system for choices of α and m in region 4, but will be only an intermediate-time description for values of α and m lying in any of the other three regions.

The thick dashed line in Figure 6.11 corresponds to the values of m considered by Jensen and Grotberg [39] (recall they only considered the special case $\alpha = 0$), and so, in particluar, their similarity solutions are valid only during an intermediate range of times. Specifically, taking the values of Ca and $\mathrm{P_s}$ from Figure

2 in Jensen and Grotberg [39], diffusion will dominate for (dimensionless) times longer than $t = O(500^3) = O(10^8)$ (corresponding to $t^* = O(10^6)$ s in dimensional time using the scaling in [39]), while capillarity will be negligible for long times.

We now briefly recap the similarity solution obtained by Jensen and Grotberg [39] for the spreading of a two-dimensional "planar strip" of insoluble surfactant, from an initial localised disturbance, similar to the problems discussed in section 5.4 of this thesis. For this particular problem, which is only one of several treated by Jensen and Grotberg [39], we choose $\alpha = 0$, so that a constant film thickness in the original (x, t) variables corresponds to a constant film thickness in the transformed variables (we assume that the layer is flat at infinity), and also choose $m = 0$ so that the total mass of solute is constant. With these assumptions the exponents become $\gamma = -1/3$, $\zeta = -1/3$, and equations (6.5.14)–(6.5.15) reduce to

$$\frac{1}{3}\xi\hat{h}' + \frac{1}{2}\left(\hat{h}^2\hat{s}'\right)' = 0, \tag{6.5.20}$$

$$\frac{1}{3}\left(\xi\hat{s}'\right)' + \left(\hat{h}\hat{s}\hat{s}'\right)' = 0; \tag{6.5.21}$$

we investigate solutions that are symmetric about $\xi = 0$, and so we take $\xi \geq 0$. As in Jensen and Grotberg [39], we seek a solution to (6.5.20) and (6.5.21) with a shock at $\xi = \xi_{\mathrm{s}}$, at which there is/are discontinuities in $\hat{h}$ and $\hat{s}'$.

We first rescale the system so that the shock position is $\hat{\xi} = 1$, by rescaling $\hat{s}$ and ξ according to

$$\hat{s} = \xi_{\mathrm{s}}^2\bar{s}, \quad \xi = \xi_{\mathrm{s}}\bar{\xi}, \tag{6.5.22}$$

where, from (6.5.9),

$$\xi_{\mathrm{s}} = \left(\frac{Q}{\displaystyle\int_0^\infty \bar{s}\,\mathrm{d}\bar{\xi}}\right)^{\frac{1}{3}} \tag{6.5.23}$$

is the position of the shock before rescaling. Note that the position of the shock depends on the initial mass of solute in the system: the larger the initial mass of solute, the further right of the origin the shock will be.

Following Jensen and Grotberg [39], to the right of the shock, i.e., for $\bar{\xi} > 1$, we take the solution to be $\hat{h} = 1$, $\bar{s} = 0$, and just to the left of the shock, i.e., for

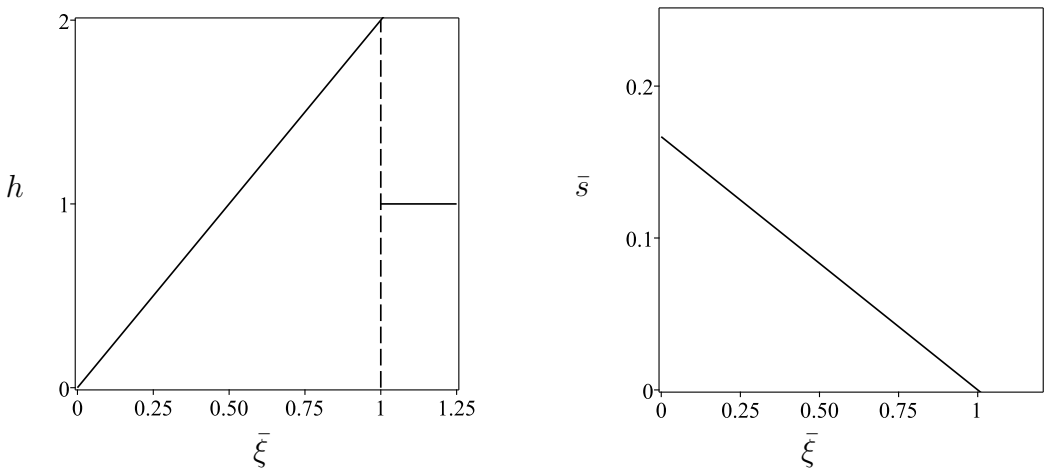

Figure 6.12: Similarity solution (6.5.25) obtained by Jensen and Grotberg [39]. The dashed vertical line denotes the position of the shock at $\hat{\bar{\xi}} = 1$.

$0 < \bar{\xi} < 1$, we impose the boundary conditions

$$\hat{h} = 2, \quad \bar{s}' = -\frac{1}{6} \quad \text{at} \quad \bar{\xi} = 1^{-}. \tag{6.5.24}$$

Note that Jensen and Grotberg [39] state that these boundary conditions are arrived at by integrating equations (6.5.20) and (6.5.21) across the shock, but we were unable to repeat this process. Instead we obtained these boundary conditions by solving the shock condition corresponding to equation (6.5.20), and by expanding equation (6.5.21) just to the left of the shock.

The solution to equations (6.5.20) and (6.5.21) subject to the boundary conditions (6.5.24) is

$$\hat{h} = 2\bar{\xi}, \quad \bar{s} = \frac{1}{6}(1 - \bar{\xi}) \quad \text{for} \quad 0 < \bar{\xi} < 1. \tag{6.5.25}$$

Figure 6.12 shows the similarity solution (6.5.25) first obtained by Jensen and Grotberg [39]. The dashed vertical line denotes the position of the shock at $\hat{\bar{\xi}} = 1$, with the similarity solution valid to the left of the shock, and a uniform solution to the right of the shock.

We compared the similarity solution given by (6.5.25) with numerical solutions to the full nonlinear equations governing the flow of an insoluble surfactant solution, i.e., equations (4.7.1)–(4.7.2) with $c \equiv 0$ and $\mathrm{Da_a} = 0$, using the finite

element package COMSOL. Following Jensen and Grotberg [39], we took the initial conditions for these computations to be

$$h = 1, \quad \bar{s} = \frac{1}{2}\left[1 - \tanh\left(\frac{\hat{\xi} - \xi_0}{\xi_w}\right)\right], \tag{6.5.26}$$

where ξ_0 and ξ_w are constants, and the boundary conditions

$$h = 1, \quad h_x = 0, \quad \bar{s} = 0 \tag{6.5.27}$$

at the right-hand boundary of the numerical domain, and

$$h_x = 0, \quad h_{xxx} = 0, \quad \bar{s}_x = 0 \tag{6.5.28}$$

at the left-hand boundary of the numerical domain. Equations (6.5.27) ensure that the solutions remain approximately constant far from the initial disturbance, and equations (6.5.28) are regularity conditions. The numerical domain itself was chosen to be the interval $[0, 30]$, split into 201 evenly spaced grid points. The simulation was begun at $t = 1$ (an arbitrary choice: since we wish to plot solutions using the similarity variable $\xi = x/t^{\frac{1}{3}}$, any sufficiently small $t > 0$ such that capillarity and diffusion are still negligible would do), and was run for an intermediate time range (typically from $t = 1$ to $t = 1000$) since for the particular choices $m = \alpha = 0$, diffusion will eventually dominate the solution. Typical computation times were approximately 20 seconds.

Figures 6.13 and 6.14 show plots of the evolution of the film thickness h and the surface concentration s, respectively, for the spreading of insoluble surfactant in original (x, t) variables. Initially there are gradients of surface tension, with the surface tension lowest at the origin. Thus an outward (i.e., away from $x = 0$) Marangoni flow is generated and the fluid spreads outwards. As the fluid spreads, a front forms and moves rightwards as $t^{\frac{1}{3}}$. Simultaneously, the surface concentration is advected away from the origin and also spreads as $t^{\frac{1}{3}}$.

Figures 6.15 and 6.16 show the corresponding plots of the evolutions of the film thickness h and the surface concentration s, respectively, for the spreading of a planar strip of insoluble surfactant, plotted in similarity variables $(\bar{\xi}, t)$, along with the similarity solution (6.5.25) obtained by Jensen and Grotberg [39]. There

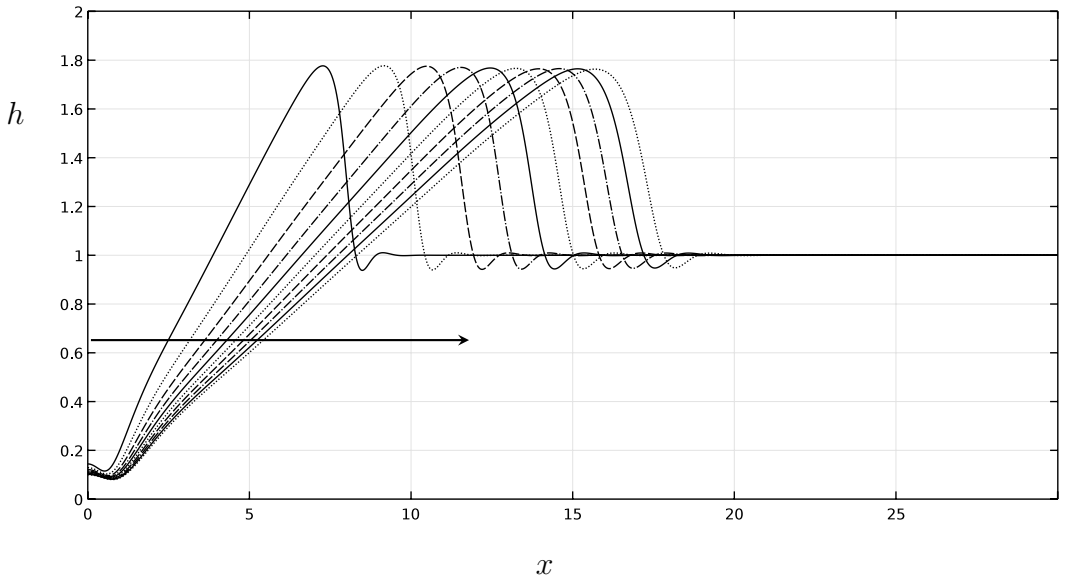

Figure 6.13: Numerically calculated evolution of the film thickness h for the spreading of insoluble surfactant (as first analysed by Jensen and Grotberg [39]) in original (x, t) variables when Ma $= 1$, Ca $= 10^4$, $\mathrm{P_s} = 10^4$, $\xi_0 = 0$, $\xi_w = 10$, simulated between $t = 10^2$ and $t = 10^3$ in steps of 10^2. The arrow denotes the direction of increasing time.

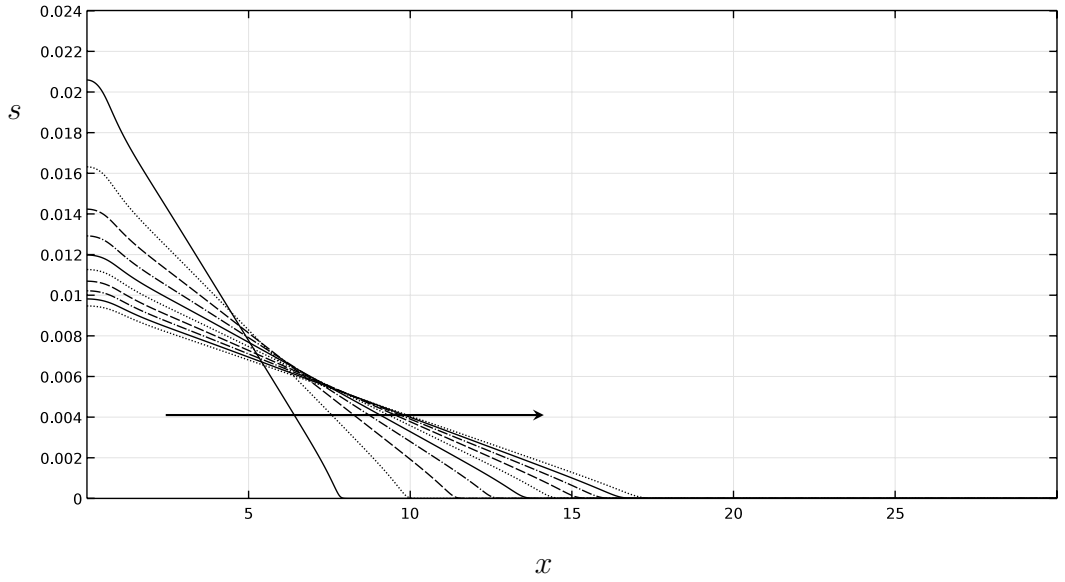

Figure 6.14: Numerically calculated evolution of the surface concentration s for the spreading of insoluble surfactant (as first analysed by Jensen and Grotberg [39]) in original (x, t) variables when Ma $= 1$, Ca $= 10^4$, $\mathrm{P_s} = 10^4$, $\xi_0 = 0$, $\xi_w = 10$, simulated between $t = 10^2$ and $t = 10^3$ in steps of 10^2. The arrow denotes the direction of increasing time.

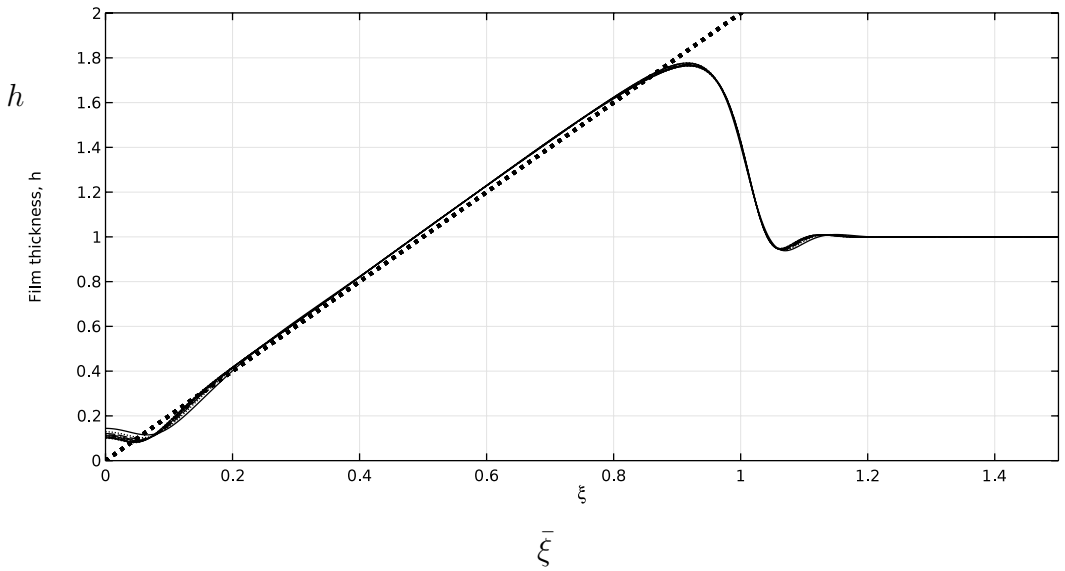

Figure 6.15: As Figure 6.13, but plotted in similarity variables (ξ, t). The dotted line denotes the similarity solution as shown in Figure 6.12.

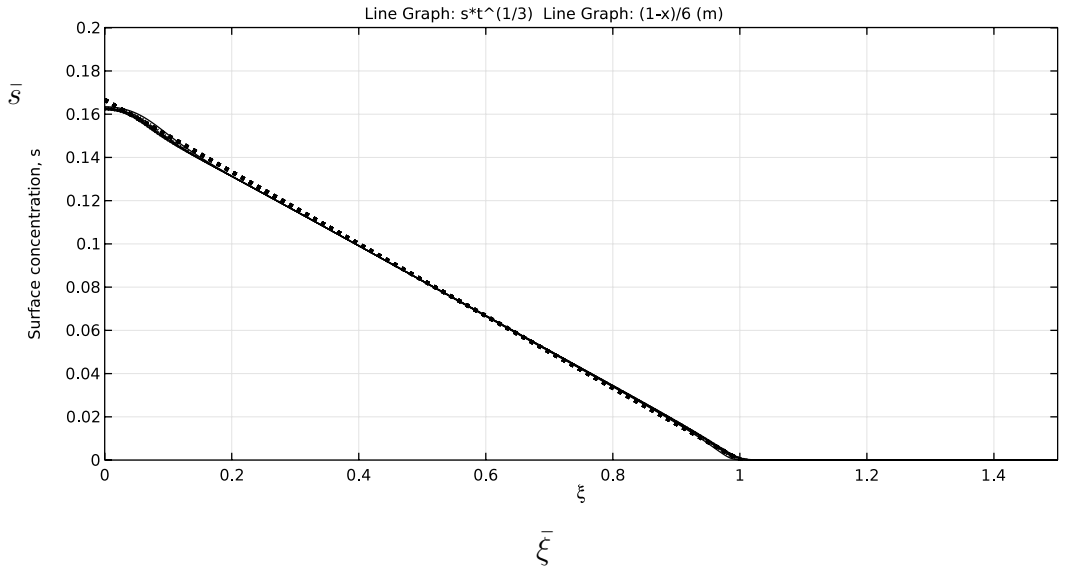

Figure 6.16: As Figure 6.14, but plotted in similarity variables (ξ, t). The dotted line denotes the similarity solution as shown in Figure 6.12.

is good agreement between the two solutions, but, as might have been expected, there are transition regions near $\xi = 0$ and $\xi = 1$, due to the effects of the boundary conditions on the left, and due to weak diffusion and weak capillarity on the right, in the numerical simulations. We remark here that the numerical solutions calculated using COMSOL more accurately match the analytical similarity solutions than those calculated by Jensen and Grotberg [39] for the same values of $\mathrm{P_s}$ and Ca. A better match would, of course, be possible by increasing the values of Ca and $\mathrm{P_s}$ further, but the slight improvement gained in doing so does not outweigh the increased computation time required.

For a much fuller account of the spreading of a local disturbance of insoluble surfactant, including generalisations to different geometries and different values of m, see the original paper by Jensen and Grotberg [39].

6.5.3 Similarity Solutions: "Perfectly Soluble" Anti-surfactant

We now revisit the problem of a "perfectly soluble" anti-surfactant. The equations solved in section 6.2, i.e., equations (6.2.1) and (6.2.2), also admit similarity solutions. For now, as in the insoluble surfactant case considered in the previous section, we take the limits $K \to 0$, $s \equiv 0$ (and by extension setting the exponent $\gamma = 0$ without loss of generality), $\mathrm{Ca} \to \infty$, and $\mathrm{P_b} \to \infty$, in equations (6.5.2)–(6.5.4) (or, alternatively, we simply transform equations (6.2.1)–(6.2.2)). Under these assumptions the governing equations (6.5.2)–(6.5.4) become

$$\alpha\hat{h} + \zeta\xi\hat{h}' + \frac{1}{2}\left(\hat{h}^2\hat{c}'\right)' t^{\alpha+2\zeta+\beta+1} = 0, \tag{6.5.29}$$

$$\beta\hat{c} + \zeta\xi\hat{c}' + \frac{1}{2}\hat{h}\left(\hat{c}'\right)^2 t^{\alpha+2\zeta+\beta+1} = 0, \tag{6.5.30}$$

along with the conservation of solute (6.5.6), which now states

$$Qt^m = \int \hat{h}\hat{c}t^{\alpha+\beta-\zeta}\,\mathrm{d}\xi. \tag{6.5.31}$$

Again, we will shortly describe the regions in parameter space in which these equations describe the true long-time behaviour of the system, and in which regions they describe only some intermediate-time evolution. Balancing the terms

in equations (6.5.29)–(6.5.31) yields two conditions on the exponents, namely

$$\alpha + 2\zeta + \beta + 1 = 0, \tag{6.5.32}$$

from both (6.5.29) and (6.5.30), and

$$\alpha + \beta - \zeta = m \tag{6.5.33}$$

from (6.5.31). Solving these two conditions for β and ζ, we obtain

$$\beta = \frac{1}{3}\left(2m - 1 - 3\alpha\right) \tag{6.5.34}$$

$$\zeta = -\frac{1}{3}\left(m + 1\right), \tag{6.5.35}$$

and with these the governing equations (6.5.29) and (6.5.30) become

$$\alpha\hat{h} - \frac{1}{3}\left(m+1\right)\xi\hat{h}' + \frac{1}{2}\left(\hat{h}^2\hat{c}'\right)' = 0, \tag{6.5.36}$$

$$\frac{1}{3}\left(2m - 1 - 3\alpha\right)\hat{c} - \frac{1}{3}\left(m+1\right)\xi\hat{c}' + \frac{1}{2}\hat{h}\left(\hat{c}'\right)^2 = 0. \tag{6.5.37}$$

With β and ζ given by (6.5.34) and (6.5.35), respectively, the coefficient of the diffusion term that we have neglected in equations (6.5.2) and (6.5.4) thus far is

$$\frac{1}{\mathrm{P_b}} t^{r_\mathrm{d}}, \tag{6.5.38}$$

and the coefficient of the capillarity term that we have neglected in equations (6.5.2) and (6.5.4) thus far is

$$\frac{1}{\mathrm{Ca}} t^{r_\mathrm{c}}, \tag{6.5.39}$$

where

$$r_\mathrm{d} = \frac{1}{3}\left(1 - 2m\right) \tag{6.5.40}$$

and

$$r_\mathrm{c} = \frac{1}{3}\left(9\alpha - 4m - 1\right), \tag{6.5.41}$$

and by looking at the signs and magnitudes of r_d and r_c, we may determine the values of α and β for which capillarity and diffusion will be negligible for long time, or eventually dominate the solution.

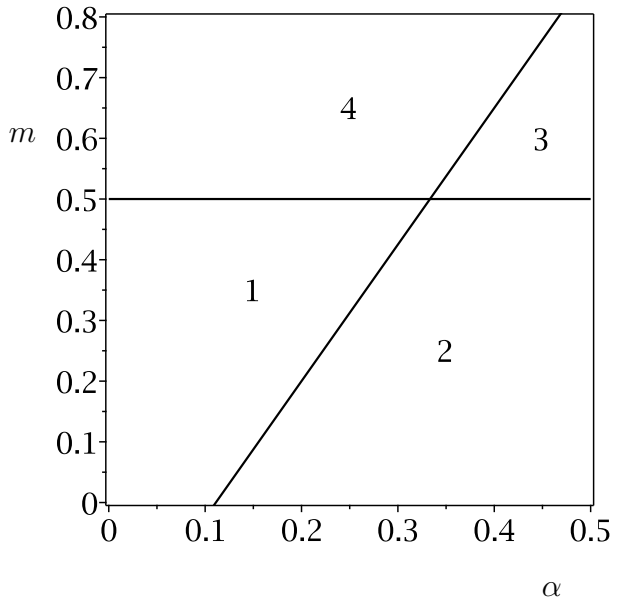

Figure 6.17: A plot of the lines $r_{\mathrm{d}} = 0$ and $r_{\mathrm{c}} = 0$ in (α, m) parameter space, with r_{d} and r_{c} given by (6.5.40) and (6.5.41), respectively, for a "perfectly soluble" anti-surfactant. In regions 1 and 2 diffusion will eventually dominate over the Marangoni effect; in regions 2 and 3 capillarity will eventually dominate over the Marangoni effect; in region 4 diffusion and capillarity will eventually be negligible.

Figure 6.17 shows a plot of the lines $r_{\mathrm{d}} = 0$ and $r_{\mathrm{c}} = 0$ in (α, m) parameter space, with r_{d} and r_{c} given by (6.5.40) and (6.5.41), respectively, for a "perfectly soluble" anti-surfactant, and corresponds to Figure 6.11. Thus, the regions marked represent the same as they did in Figure 6.11 and, in particular, equations (6.5.29) and (6.5.30) will describe the true long-time behaviour of the system for values of α and m in region 4.

We now proceed to find a general solution to equations (6.5.36) and (6.5.37). Solving (6.5.37) for $\hat{h}$, we obtain

$$\hat{h} = \frac{2}{3}\frac{(m+1)\,\xi\hat{c}' + (3\alpha + 1 - 2m)\,\hat{c}}{(\hat{c}')^2}, \tag{6.5.42}$$

as long as $\hat{c}' \neq 0$ (we are not interested in singular solutions for which c is constant, since we are focussing on the effect of concentration gradients). Substituting this

solution for $\hat{h}$ into (6.5.37) yields an ODE for $\hat{c}$ only, namely

$$(m+1)(6\alpha+2-m)\xi(\hat{c}')^3 - 3(3\alpha+1-2m)^2\hat{c}^2\hat{c}'' + (3\alpha+1-2m)(9\alpha+4-2m)\hat{c}(\hat{c}')^2 - 2(m+1)(3\alpha+1-2m)\xi\hat{c}\hat{c}'\hat{c}'' = 0. \quad (6.5.43)$$

We then make equation (6.5.43) autonomous by means of the substitution $\xi = \pm e^{\lambda}$ so that $\hat{c}(\xi) = \hat{c}(\lambda)$, $\hat{c}' = \pm e^{-\lambda}\hat{c}_\lambda$, and $\hat{c}'' = e^{-2\lambda}(\hat{c}_{\lambda\lambda} - \hat{c}_\lambda)$, and hence equation (6.5.43) becomes

$$(m+1)(6\alpha+2-m)\hat{c}_\lambda^3 + 3(3\alpha+2)(3\alpha+1-2m)\hat{c}\hat{c}_\lambda^2 - 3(3\alpha+1-2m)^2\hat{c}^2\hat{c}_{\lambda\lambda} + 3(3\alpha+1-2m)^2\hat{c}^2\hat{c}_\lambda - 2(m+1)(3\alpha+1-2m)\hat{c}\hat{c}_\lambda\hat{c}_{\lambda\lambda} = 0. \quad (6.5.44)$$

This may now be transformed into a first order equation through the substitution $\hat{c}_\lambda = p$, so that $\hat{c}_{\lambda\lambda} = pp_{\hat{c}}$, and, recalling that $\hat{c}' \neq 0$ and therefore $p \neq 0$, solving for $p_{\hat{c}}$ yields

$$p_{\hat{c}} = \frac{(m+1)(6\alpha+2-m)p^2 + 3(3\alpha+2)(3\alpha+1-2m)\hat{c}p + 3(3\alpha+1-2m)^2\hat{c}^2}{2(m+1)(3\alpha+1-2m)\hat{c}p + 3(3\alpha+1-2m)^2\hat{c}^2}, \quad (6.5.45)$$

where we now require that $3\alpha + 1 - 2m \neq 0$ (which is equivalent to saying that the exponent $\beta \neq 0$). Finally, equation (6.5.45) may be made separable through the substitution $p(\hat{c}) = \hat{c}q(\hat{c})$, which yields

$$q + \hat{c}q_{\hat{c}} = f(q), \quad (6.5.46)$$

where

$$f(q) = \frac{(m+1)(6\alpha+2-m)q^2 + 3(3\alpha+2)(3\alpha+1-2m)q + 3(3\alpha+1-2m)^2}{2(m+1)(3\alpha+1-2m)q + 3(3\alpha+1-2m)^2}, \quad (6.5.47)$$

and equation (6.5.46) is now easily solved to obtain $\hat{c}$ in terms of a parameter q which may, in general, take any real value.

Integrating equation (6.5.46) yields

$$\int \frac{d\hat{c}}{\hat{c}} = \int \frac{dq}{f(q) - q}, \quad (6.5.48)$$

which gives $\hat{c}$ parametrically in terms of q:

$$\hat{c}(q) = c_0 \left[(m+1)\, q + 3\alpha + 1 - 2m\right]^{\frac{1}{3}(3\alpha+1-2m)} \left[mq + 3\alpha + 1 - 2m\right]^{-\frac{(m-2)(3\alpha+1-2m)}{3m}}, \tag{6.5.49}$$

where c_0 is a constant of integration. We may also find ξ parametrically in terms of q by noting that

$$\hat{c}_\lambda = p \iff \frac{\mathrm{d}\lambda}{\mathrm{d}\hat{c}} = \frac{1}{p} \iff \lambda = \int \frac{\mathrm{d}\hat{c}}{p} = \int \frac{\mathrm{d}\hat{c}}{q\hat{c}} = \int \frac{\mathrm{d}q}{q\,(f(q) - q)}, \tag{6.5.50}$$

which may be evaluated to give an expression for λ in terms of q, from which we obtain

$$\xi = \mathrm{e}^{\lambda} = \xi_0 q \left[(m+1)\, q + 3\alpha + 1 - 2m\right]^{-\frac{1}{3}(m+1)} \left[mq + 3\alpha + 1 - 2m\right]^{\frac{1}{3}(m-2)}, \tag{6.5.51}$$

where ξ_0 is a constant. Substitution of (6.5.49) and (6.5.51) into (6.5.42) yields an expression for $\hat{h}$ in terms of q, namely

$$\hat{h} = h_0 \left[(m+1)\, q + 3\alpha + 1 - 2m\right]^{-\alpha} \left[mq + 3\alpha + 1 - 2m\right]^{\frac{(m-2)(3\alpha+1)}{3m}}, \tag{6.5.52}$$

where $h_0 = 2\xi_0/(3c_0)$.

To summarise, we have solved equations (6.5.36) and (6.5.37) through a number of substitutions to obtain solutions for $\hat{h}(\xi)$ and $\hat{c}(\xi)$ parametrically in terms of a parameter q, namely the solutions (6.5.49), (6.5.51), and (6.5.52).

We will now consider two interesting special cases of these solutions by choosing particular values of α and m. The first of these will be an intermediate-time asymptotic solution, and the second will be the long-time asymptotic solution. Since the constants of integration in these solutions appear only as multiplicative factors, we may normalise the solutions by rescaling, i.e., we define

$$\hat{X} = \frac{\xi}{\xi_0}, \quad \hat{H} = \frac{\hat{h}}{h_0}, \quad \hat{C} = \frac{\hat{c}}{c_0}, \tag{6.5.53}$$

with the corresponding solution in the original (x, t) variables, namely

$$X = \frac{\xi}{\xi_0} t^{\frac{1}{3}}, \quad H = \frac{\hat{h}}{h_0}, \quad C = \frac{\hat{c}}{c_0} t^{\frac{1}{3}}, \tag{6.5.54}$$

where the hat denotes functions of the similarity variable; functions of the original variables are unadorned.

(a) The case $\alpha = 0$ and $m = 0$

A natural case to start with is when both free exponents are zero, i.e., $m = \alpha = 0$. Note that this places the solution in region 1 in Figure 6.17, so that the solution will be valid only for an intermediate range of times, until a dimensionless time of $t = O({\mathrm{P_s}}^3)$. When $m = 0$, so that no solute is being added or removed from the system, and $\alpha = 0$, the solutions for $\xi(q)$, $\hat{h}(q)$ and $\hat{c}(q)$, given by (6.5.51), (6.5.52), and (6.5.49), respectively, become

$$\hat{X} = q(q+1)^{-\frac{1}{3}}, \tag{6.5.55}$$

$$\hat{H} = \exp\left(-\frac{2}{3}q\right), \tag{6.5.56}$$

$$\hat{C} = (q+1)^{\frac{1}{3}} \exp\left(\frac{2}{3}q\right). \tag{6.5.57}$$

Figure 6.18 shows plots of the normalised film thickness $\hat{H}$ and normalised bulk concentration $\hat{C}$ as functions of the normalised similarity variable $\hat{X}$ for a 'perfectly soluble' anti-surfactant with $\alpha = 0$ and $m = 0$. The solution for the film thickness resembles a classical dam-break problem, such as the dry-bed problem considered in section 6.2. The shape of $\hat{C}$, increasing from left to right, shows that the fluid is being pulled from left to right due to the increasing gradients of surface tension caused by the increasing bulk concentration. This may be shown explicitly by transforming the solutions back into original variables, namely,

$$X = q(q+1)^{-\frac{1}{3}} t^{\frac{1}{3}}, \tag{6.5.58}$$

$$H = \exp\left(-\frac{2}{3}q\right), \tag{6.5.59}$$

$$C = (q+1)^{\frac{1}{3}} \exp\left(\frac{2}{3}q\right) t^{\frac{1}{3}}, \tag{6.5.60}$$

which makes it apparent that, as t increases, both H and C stretch horizontally, while C will also stretch vertically. Figure 6.19 shows these solutions as time increases.

Asymptotically, as $\hat{X} \to 0$, $\hat{H}$ and $\hat{C}$ satisfy

$$\hat{H} \sim 1 - \frac{2}{3}\hat{X} + \frac{8}{81}\hat{X}^3, \tag{6.5.61}$$

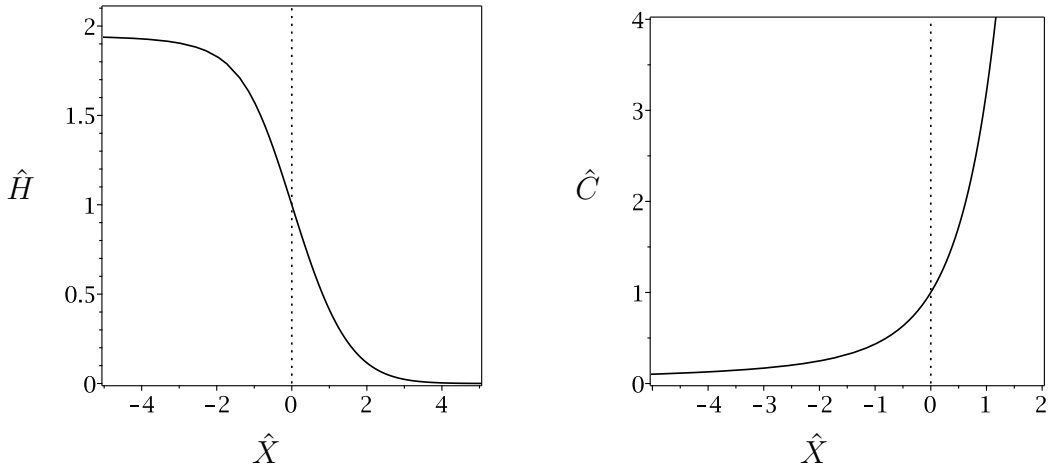

Figure 6.18: The normalised film thickness $\hat{H}$ given by (6.5.56) and normalised bulk concentration $\hat{C}$ given by (6.5.57) as functions of the normalised similarity variable $\hat{X}$ given by (6.5.55), for a "perfectly soluble" anti-surfactant with $\alpha = 0$ and $m = 0$.

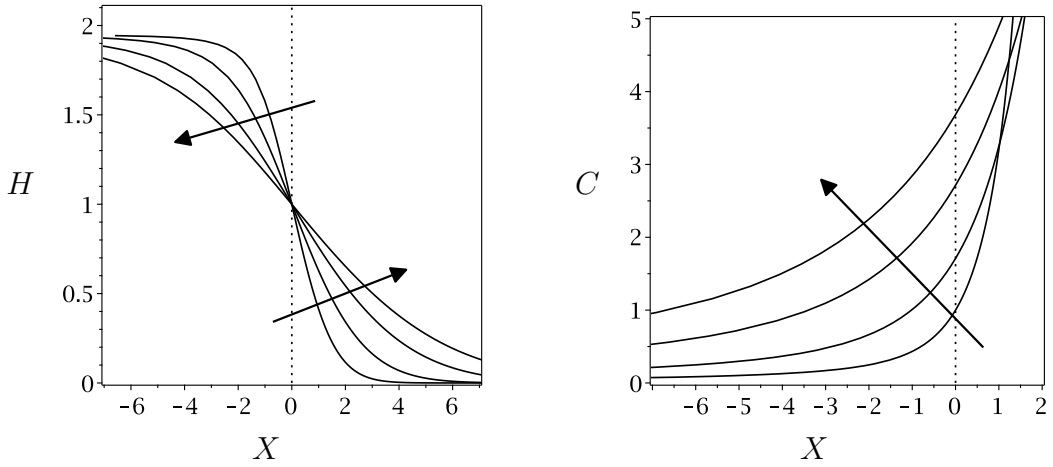

Figure 6.19: The normalised film thickness H given by (6.5.58) and normalised bulk concentration C given by (6.5.59) as functions of the normalised original variables (X, t), with X given by (6.5.60), for a "perfectly soluble" anti-surfactant with $\alpha = 0$ and $m = 0$, for $t = 1$, 5, 20, 50 and the arrow denotes increasing t.

$$\hat{C} \sim 1 + \hat{X} + \frac{2}{3}\hat{X}^2 + \frac{1}{3}\hat{X}^3, \tag{6.5.62}$$

while as $\hat{X} \to +\infty$,

$$\hat{H} \sim \exp\left(-\frac{2}{3}\hat{X}^{\frac{3}{2}} - \frac{1}{3}\right), \tag{6.5.63}$$

$$\hat{C} \sim \hat{X}^{\frac{1}{2}} \exp\left(\frac{2}{3}\hat{X}^{\frac{3}{2}} + \frac{1}{3}\right), \tag{6.5.64}$$

and, finally, as $\hat{X} \to -\infty$,

$$\hat{H} \sim \frac{\exp\left[\frac{2}{3}\left(3\hat{X}^3 + 2\right)\right]}{3\hat{X}}, \tag{6.5.65}$$

$$\hat{C} \sim \frac{1}{\exp\left(\frac{2}{3}\right)\hat{X}}. \tag{6.5.66}$$

Figures 6.20–6.22 show comparisons between the exact solutions, given parametrically by (6.5.55)–(6.5.57), and their asymptotic approximations in the limits $\hat{X} \to 0$, $\hat{X} \to +\infty$, and $\hat{X} \to -\infty$, respectively, given by (6.5.61)–(6.5.66).

(b) The case $\alpha = 0$ and $m = 1$

We now consider the case in which solute is being added to the system linearly with time, i.e., $\alpha = 0$ and $m = 1$, so that the total mass of solute is increasing as t^1. Note that the values $\alpha = 0$ and $m = 1$ lie in region 6 in Figure 6.17, and so the solution represents the true long-time asymptotic behaviour of the system.

When $\alpha = 0$ and $m = 1$, the solutions for $\xi(q)$, $\hat{h}(q)$, and $\hat{c}(q)$ (normalised as in the previous case) become

$$\hat{X} = q\,(2q-1)^{-\frac{2}{3}}\,(q-1)^{-\frac{1}{3}}\,, \tag{6.5.67}$$

$$\hat{H} = (q-1)^{-\frac{1}{3}}\,, \tag{6.5.68}$$

$$\hat{C} = (2q-1)^{-\frac{1}{3}}\,(q-1)^{-\frac{1}{3}}\,. \tag{6.5.69}$$

Figure 6.23 shows plots of the normalised film thickness $\hat{H}$ and bulk concentration $\hat{C}$ as functions of the normalised similarity variable $\hat{X}$, for a "perfectly soluble" anti-surfactant with $\alpha = 0$ and $m = 1$. In original variables, these solutions are

$$X = q\,(2q-1)^{-\frac{2}{3}}\,(q-1)^{-\frac{1}{3}}\,t^{\frac{2}{3}}, \tag{6.5.70}$$

$$H = (q-1)^{-\frac{1}{3}}\,, \tag{6.5.71}$$

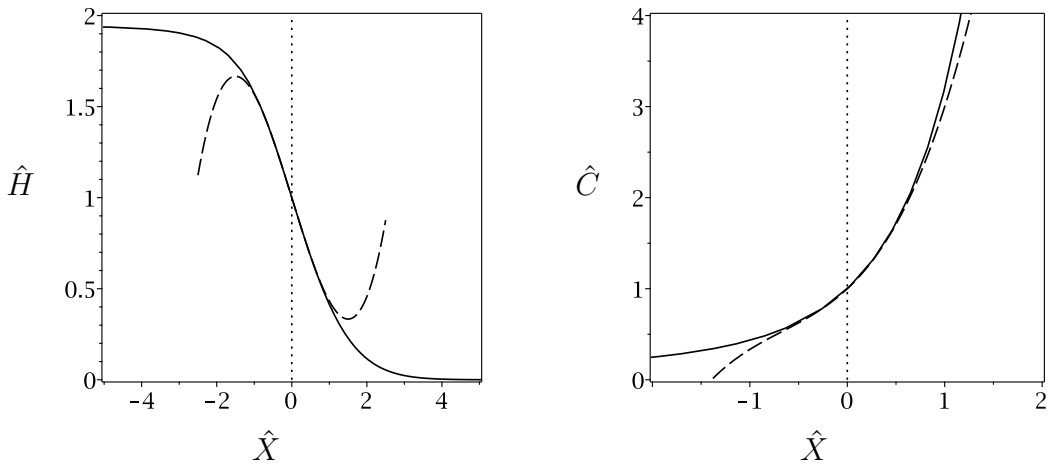

Figure 6.20: Comparison between the exact solutions for the film thickness $\hat{H}(\hat{X})$ and bulk concentration $\hat{C}(\hat{X})$, shown with solid lines, given parametrically by (6.5.55)–(6.5.57), and their asymptotic approximations in the limit $\hat{X} \to 0$, shown with dashed lines, given by (6.5.61) and (6.5.62), respectively, for a "perfectly soluble" anti-surfactant with $\alpha = 0$ and $m = 1$.

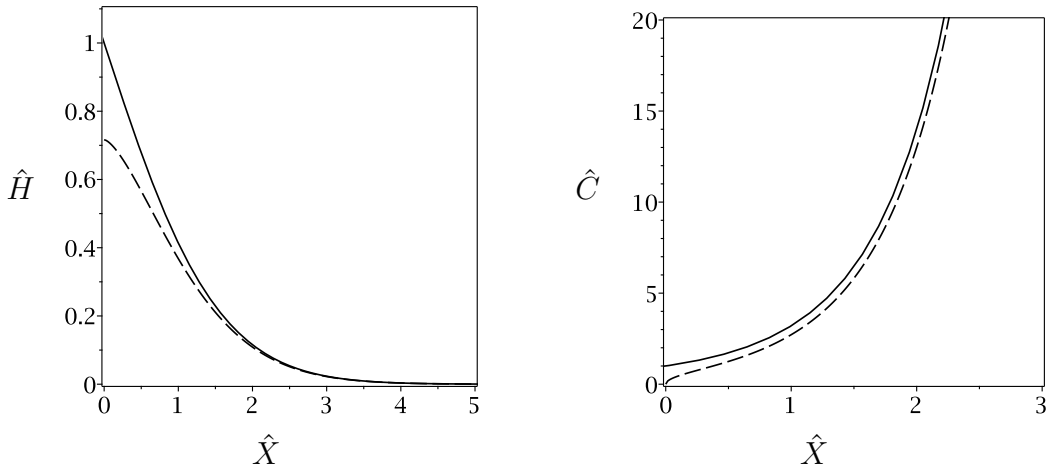

Figure 6.21: Comparison between the exact solutions for the film thickness $\hat{H}(\hat{X})$ and bulk concentration $\hat{C}(\hat{X})$, shown with solid lines, given parametrically by (6.5.55)–(6.5.57), and their asymptotic approximations in the limit $\hat{X} \to +\infty$, shown with dashed lines, given by (6.5.63) and (6.5.64), respectively, for a "perfectly soluble" anti-surfactant with $\alpha = 0$ and $m = 1$.

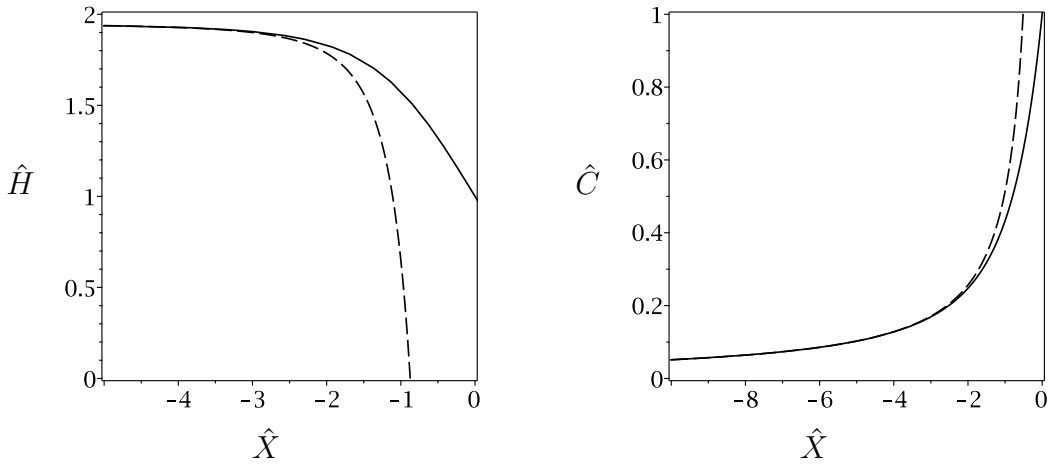

Figure 6.22: Comparison between the exact solutions for the film thickness $\hat{H}(\hat{X})$ and bulk concentration $\hat{C}(\hat{X})$, shown with solid lines, given parametrically by (6.5.55)–(6.5.57), and their asymptotic approximations in the limit $\hat{X} \to -\infty$, shown with dashed lines, given by (6.5.65) and (6.5.66), respectively, for a "perfectly soluble" anti-surfactant with $\alpha = 0$ and $m = 1$..

$$C = (2q-1)^{-\frac{1}{3}} (q-1)^{-\frac{1}{3}} t^{-\frac{1}{3}}, \tag{6.5.72}$$

showing that both H and C will move rightwards, and C will decrease as time increases. Figure 6.24 shows that this is indeed the case. Asymptotically, as $\hat{X} \to +\infty$, $\hat{H}$ and $\hat{C}$ satisfy

$$\hat{H} \sim \hat{X}, \tag{6.5.73}$$

$$\hat{C} \sim \hat{X}, \tag{6.5.74}$$

and as $\hat{X} \to 2^{-\frac{2}{3}}$ (in which limit both $\hat{H}$ and $\hat{C}$ become zero),

$$\hat{H} \sim 3^{\frac{1}{3}} 2^{-\frac{1}{9}} \left(-2^{-\frac{2}{3}} + \hat{X}\right)^{\frac{1}{3}}, \tag{6.5.75}$$

$$\hat{C} \sim 3^{\frac{2}{3}} 2^{-\frac{14}{9}} \left(-2^{-\frac{2}{3}} + \hat{X}\right)^{\frac{2}{3}}. \tag{6.5.76}$$

Figures 6.25 and 6.26 show comparisons between the exact solutions, given parametrically by (6.5.67)–(6.5.69), and their asymptotic approximations in the limits $\hat{X} \to +\infty$ and $\hat{X} \to 2^{-\frac{2}{3}}$, respectively, given by (6.5.73)–(6.5.76).

Physically, this solution could be interpreted as a local solution near the contact line of a contracting drop or a growing hole in a thin film of anti-surfactant

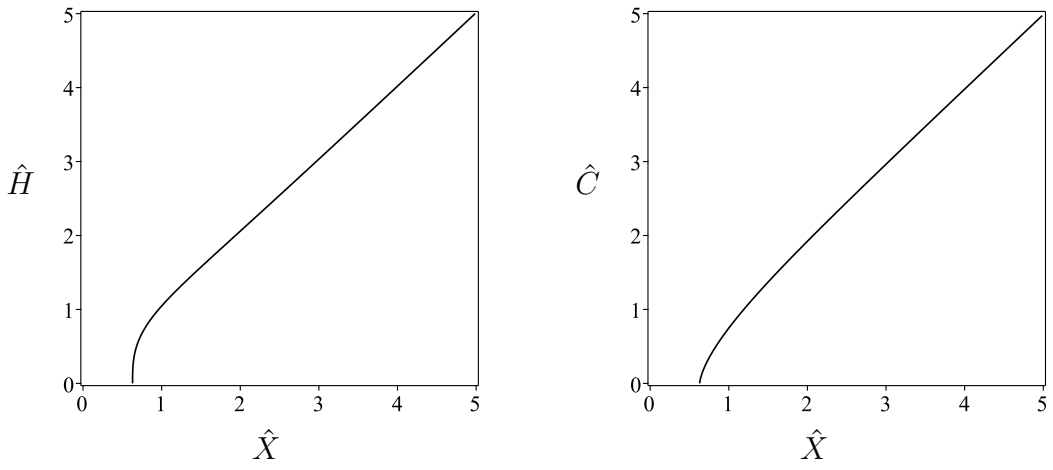

Figure 6.23: The normalised film thickness $\hat{H}$ given by equation (6.5.68) and normalised bulk concentration $\hat{C}$ given by equation (6.5.69) as functions of the normalised similarity variable $\hat{X}$ given by equation (6.5.67) for a "perfectly soluble" anti-surfactant with $\alpha = 0$ and $m = 1$.

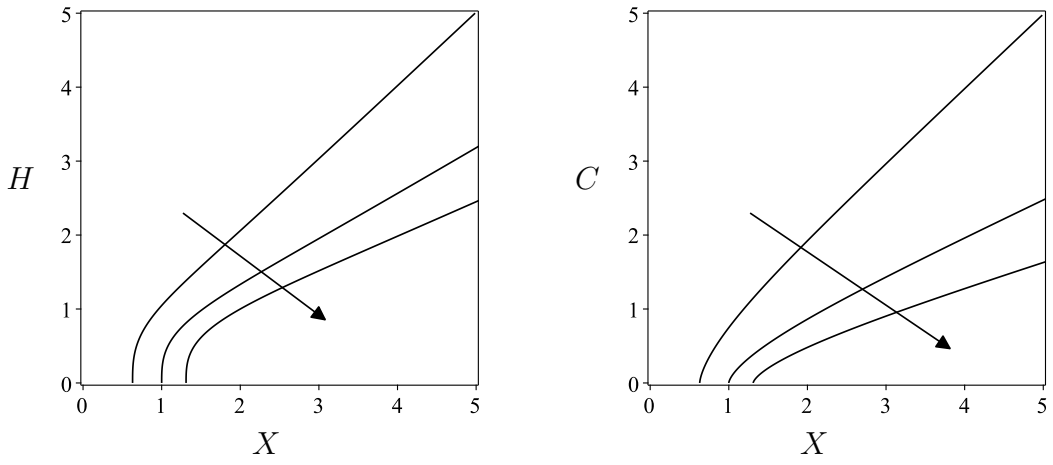

Figure 6.24: The normalised film thickness H given by equation (6.5.71) and normalised bulk concentration C given by equation (6.5.72) for a "perfectly soluble" anti-surfactant with $\alpha = 0$ and $m = 1$ for $t = 1$, 2, 3. The arrow denotes the direction of increasing time.

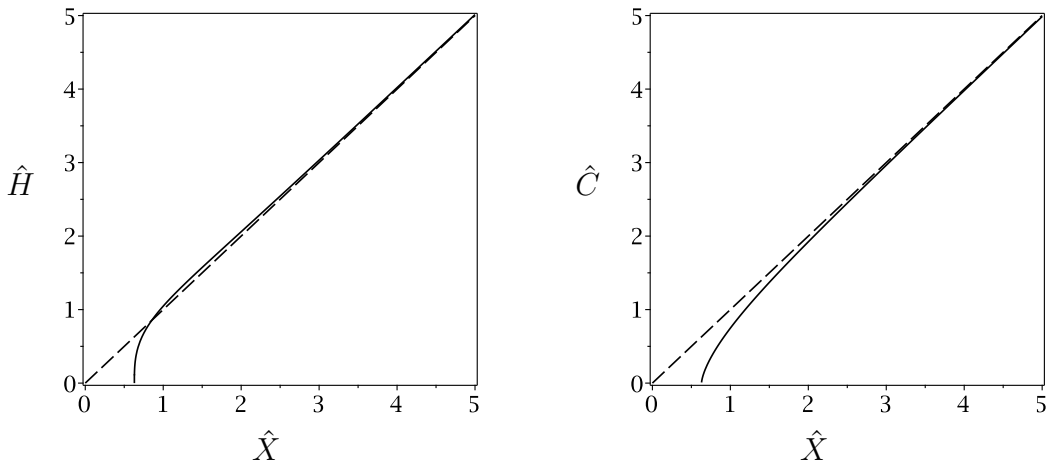

Figure 6.25: Comparison between the exact solutions for the film thickness $\hat{H}(\hat{X})$ and bulk concentration $\hat{C}(\hat{X})$, shown as solid lines, given parametrically by (6.5.67)–(6.5.69) and their asymptotic approximations in the limit $\hat{X} \to +\infty$, shown by dashed lines, given by (6.5.73) and (6.5.74), respectively, for a "perfectly soluble" anti-surfactant with $\alpha = 0$ and $m = 1$.

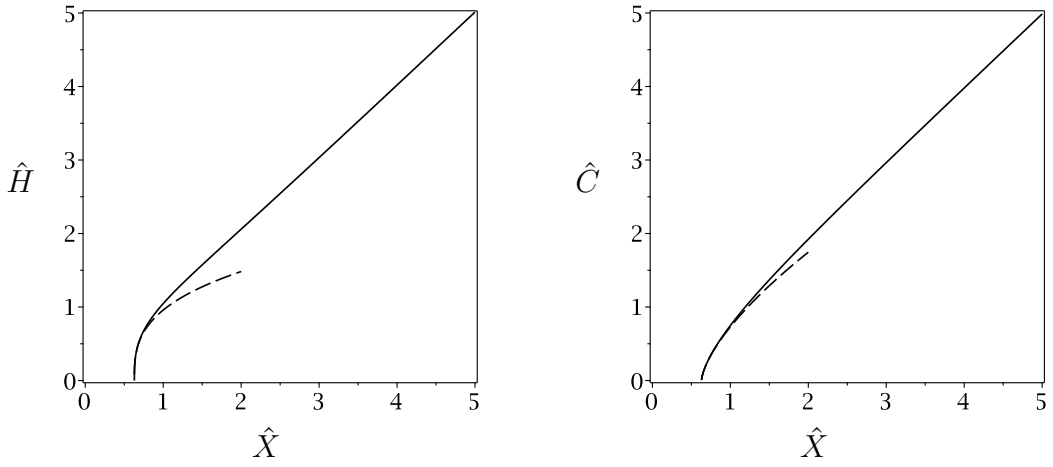

Figure 6.26: Comparison between the exact solutions for the film thickness $\hat{H}(\hat{X})$ and bulk concentration $\hat{C}(\hat{X})$, shown as solid lines, given parametrically by (6.5.67)–(6.5.69) and their asymptotic approximations in the limit $\hat{X} \to 2^{-\frac{2}{3}}$, shown by dashed lines, given by (6.5.75) and (6.5.76), respectively, for a "perfectly soluble" anti-surfactant with $\alpha = 0$ and $m = 1$.

solution, and would need to be matched to some outer solution away from the contact line if a global solution was desired.

It is possible to eliminate q from the solutions (6.5.67)–(6.5.69) and to write $\hat{X}$ and $\hat{C}$ parametrically in terms of the film thickness $\hat{H}$, namely

$$\hat{X} = \frac{\left(\hat{H}^3 + 1\right)}{\left(\hat{H}^3 + 2\right)^{\frac{2}{3}}}, \quad \hat{C} = \frac{\hat{H}^3}{\left(\hat{H}^3 + 2\right)^{\frac{1}{3}}}. \tag{6.5.77}$$

From these expression it is easy to obtain information about the behaviour near the contact line. Since $\hat{H} = 0$ at the contact line we see that $\hat{C} = 0$ at the same point, so there is no solute outside of the drop or in the expanding hole, and the position of the contact line is at $\hat{X} = 2^{-\frac{2}{3}}$. Transforming this position back into original variables yields $X = 2^{-\frac{2}{3}} t^{\frac{2}{3}}$, showing that the contact line moves rightwards as $t^{\frac{2}{3}}$.

One worry, of course, is that there is no equation built into the model to describe the movement of a contact line, and that the point where $\hat{H} = 0$ seen in Figures 6.23 and 6.24 should not move because of the well known contact-line singularity (also known as the Huh and Scriven paradox) [36], where the force required to move the free surface at the contact line is infinite. However, for this particular case, we can readily calculate the force $\mathbf{F}$ on the substrate due to the fluid, namely

$$\mathbf{F} = \int_{x_c}^{L} \mathbf{T} \cdot \mathbf{n} \, \mathrm{d}x, \tag{6.5.78}$$

where x_c is the position of the contact line, and $L > x_c$ is some point away from the contact line. The stress tensor $\mathbf{T}$ is given by (4.4.12), and the velocity and pressure (from equations (4.4.31) and (4.4.33) when surface tension is neglected, and for a 'perfectly soluble' anti-surfactant) are simply

$$u = \frac{\partial c}{\partial x} z, \quad p = p_0. \tag{6.5.79}$$

Using these it is trivial to show that the force required to move the substrate, which is equivalent to moving the contact line, is finite at the contact line, and thus the contact line is able to move as shown in Figures 6.23 and 6.24.

6.6 Summary

In this Chapter, we found analytical solutions to the thin-film equations derived in Chapter 4 in the asymptotic regime in which the Marangoni effect dominates over capillarity and diffusion, and the solute is a "perfectly soluble" anti-surfactant. By employing the method of characteristics, we found solutions to problems with discontinuities in the initial conditions, i.e., Riemann problems. Depending on the thickness of the thin film and the strength of the concentration gradients at either side of the initial discontinuity, a wide range of behaviour is possible, with shocks in both the film thickness and the concentration gradient relatively common among the problems that we considered. We also demonstrated that, in the same asymptotic regime, but for an insoluble surfactant, our model recovers the similarity solution found by Jensen and Grotberg [39] describing the spreading of an initially localised disturbance of insoluble surfactant along a free surface. Furthermore, when the solute is a "perfectly soluble" anti-surfactant, we derived two new similarity solutions. The former resembles a classical dam-break problem, like those we considered in the first part of Chapter 6. The latter resembles either the moving contact line of a contracting drop of anti-surfactant solution or the contact line region of a growing hole in a thin film of anti-surfactant solution when anti-surfactant is being added to the system at a constant rate.

Chapter 7

Conclusions and Future Work

7.1 Conclusions

In this thesis we have formulated a fluid dynamical model describing the flow of a solution consisting of a fluid solvent and a dissolved solute that is either a surfactant or an anti-surfactant. We have analysed the stability properties of an initially quiescent, two-dimensional layer of surfactant or anti-surfactant solution, and investigated some of the dynamical behaviour that can occur in such solutions.

In Chapter 2, the model used throughout the thesis was formulated for a layer of surfactant or anti-surfactant solution with a single free surface, sitting on top of a horizontal, impermeable substrate. In the model, the hydrodynamics is coupled to the transport of the surface and bulk concentrations of the dissolved solute through the balance of normal and tangential stresses at the free surface, i.e., through capillarity and the Marangoni effect. By considering the surface excess of the dissolved solute, and by prescribing a specific bulk–surface flux, we derived from the Gibbs isotherm an equation of state relating the surface tension of the fluid to the concentrations of the dissolved solute. This equation of state can describe not only classical surfactants, but also anti-surfactants.

In Chapter 3, we performed a linear stability analysis of the dimensionless system of equations describing the flow of a two-dimensional, initially quiescent layer of surfactant or anti-surfactant solution. In the special cases of a pure sol-

vent, and a "perfectly soluble" anti-surfactant solution, or when the solute is a surfactant, the system is unconditionally stable; this agrees with previous studies. However, in the special case of an infinitely deep layer of anti-surfactant solution the layer can be linearly unstable to perturbations of certain wavenumbers. Assuming that the principle of exchange of stabilities holds, a marginal stability analysis was performed, and instability conditions on the dimensionless parameters in the system were derived. The effects of finite depth were considered when the principle of exchange of stabilities is assumed to hold and it was found that the region of instability in parameter space is largest in the infinite-depth limit. When the principle of exchange of stabilities is not assumed to hold it was found numerically that the growth rate of perturbations to a layer of finite-depth can be complex, but that the associated oscillatory behaviour is an intrinsically long-wave phenomenon.

In Chapter 4, we investigated the behaviour of a thin film of surfactant or anti-surfactant solution by assuming that the aspect ratio of the layer is small, i.e., by making a classical lubrication approximation. Closure of the leading order problem for the evolution of the bulk concentration required going to higher order in the small aspect ratio limit. We also performed a linear stability analysis similar to that performed in Chapter 3, and found that a thin film of anti-surfactant solution is unstable to perturbations ofcertain wavenumbers. Stability diagrams for each of the dimensionless parameters were produced, showing the regions of instability, and also showing the regions in which oscillatory behaviour occurs. Furthermore, in the limit of fast bulk–surface flux, there is a separation of timescales with a short timescale over which the surface and bulk concentrations come into surface–bulk equilibrium, and a long timescale over which capillarity, diffusion, and the Marangoni effect are dominant.

In Chapter 5 we numerically integrated the thin-film equations derived in Chapter 4. In particular, we confirmed the results of the linear stability analysis performed in Chapter 4, and demonstrated that the linear theory performs well even for perturbations that are $O(1)$. We also considered the problem of adding a large amount of surfactant or anti-surfactant to a small region of either the

surface or the bulk of an otherwise clean solvent. Transient growth of either a peak or a depression in the free surface occurs, depending on whether the solute is a surfactant or an anti-surfactant, and on whether the solute is added to the surface or the bulk.

In Chapter 6 we found analytical solutions to the thin-film equations derived in Chapter 4 in the asymptotic regime in which the Marangoni effect is dominant over capillarity and diffusion, and the solute is a "perfectly soluble" anti-surfactant. By employing the method of characteristics, we found solutions to problems with discontinuities in the initial conditions, i.e., Riemann problems. Depending on the thickness of the thin film and the strength of the concentration gradients at either side of the initial discontinuity, a wide range of behaviour is possible, with shocks in both the film thickness and the concentration gradient common among the problems that we considered. We also demonstrated that, in the same asymptotic regime, but for an insoluble surfactant, our model recovers the similarity solution found by Jensen and Grotberg [39] describing the spreading of an initially localised disturbance of insoluble surfactant along a free surface. Furthermore, when the solute is a "perfectly soluble" anti-surfactant, we derived two new similarity solutions. One of these resembles a classical "dam-break" problem, like those we considered in the first part of Chapter 6, and the other may be interpreted as either the moving contact line of a contracting drop of anti-surfactant solution or the contact line region of a growing hole in a thin film of anti-surfactant solution when anti-surfactant is being added to the system at a constant rate.

7.2 Future Work

The work presented in this thesis can be extended and built upon in many ways.

The assumption of a simple linear bulk–surface flux in Chapter 2 led to a simple linear equation of state which contains an artificial parameter θ. While we fixed a value of θ from Chapter 4 onwards, it would certainly be worthwhile to analyse in more detail what effects different values of θ would have on the results

of more complicated calculations than the linear stability calculations performed in Chapter 3, such as those performed in Chapters 5 and 6. Also, by taking into account the saturation of the bulk and, in particular, the surface concentrations, a more complicated non-linear bulk–surface flux, and consequently a more complicated equation of state, could be obtained. An analysis of different equations of state and bulk–surface fluxes, and the stability of a layer governed by the resulting models, would be of interest to test the sensitivity of our results to these particular choices of constitutive relations. Similarly, when the solute is a salt consisting of ions, the model presented here could be extended to capture the complicated electrodynamics that occurs in these systems. The model could also be extended by assuming that the viscosity and density of the solutions, along with the diffusivity of the solute, vary with concentration — effects that have been neglected in this thesis..

It would be of great interest to include in the model the effects of evaporation of anti-surfactant solutions, both in the context of salt solutions and of binary mixtures of water and alcohol. While the particles of the anti-surfactant tend to be expelled from the free surface, if the solvent was evaporating, then this would lead to some degree of accumulation of particles at the free surface [50], and these competing effects could lead to interesting behaviour. Furthermore, in the context of water/alcohol binary mixtures, both the solvent (the alcohol) and the solute (the water) are volatile [64], which adds another level of complexity to the problem.

Binary mixtures of water and long-chain alcohols such as hexanol have the anomalous property that the surface tension of the mixture depends non-monotonically on the temperature of the fluid, with a well-defined minimum in surface tension at a critical temperature. As mentioned in Chapter 1, these fluids are named self-rewetting fluids and were our original motivation to consider the effects of surface tension increasing with respect to some field, namely temperature in the case of self-rewetting fluids, and concentration in the case of the anti-surfactant solutions considered in this thesis. While there is not, in general, a direct correspondence between the thermal and solutal problems [15], there is

such a correspondence when the solute in the latter is a "perfectly soluble" anti-surfactant [39]. The work presented in this thesis may therefore be regarded as a step towards understanding the behaviour of these self-rewetting fluids at temperatures above the critical temperature.

The coupling of thermal and solutal Marangoni effects has been considered previously [22], where the Soret and Dufour effects are important [61,76,77], but have been considered only in the context of surfactant solutions; similar analyses could be readily performed for anti-surfactant solutions.

The two-dimensional stability problems solved in Chapters 3 and 4 could also be readily extended to three dimensions. Surfactant solutions are stable to longitudinal perturbations, but are unstable to transverse perturbations, which leads to the well-known fingering phenomenon [15]. Perhaps a similar phenomenon will occur in anti-surfactant solutions. The present model may also be readily extended to include gravity and the effect of an inclined substrate. A similar model to the one used in this thesis may also be developed for multi-layer systems, or for the flow of a rivulet of surfactant or anti-surfactant solution. Another extension, which may have significant industrial importance, would be to include the effect of an anti-surfactant at a water-oil interface on the recovery of oil from oil reservoirs [37]. This latter problem would require the formulation of the appropriate two-layer model, and the possible addition of, for example, a porous matrix through which the fluids flow.

Finally, in Chapter 6, we noted that the equations governing the Marangoni-dominated flow of anti-surfactant solutions could be written in characteristic form, and used this to solve a family of Riemann problems. Similar methodology could be used to solve, or at least give insight into, several other types of problems, such as the local disturbance problems considered in Chapter 5. Also in Chapter 6 we performed a fairly general similarity transformation on the equations governing the flow of a thin film of surfactant or anti-surfactant solution. While we considered only three particular cases, there are many more cases that could be considered in which different physical mechanism are dominant over different timescales, such as problems in which diffusion and the Marangoni effect

dominate over capillarity. The equations obtained in Chapter 6 to describe self-similar flows are very rich, and an extensive survey of all possibilities would be a substantial, but potentially very rewarding, task.

Appendix A

Oscillatory Behaviour in a Layer of Finite Depth

In this Appendix, we describe the occurrence of oscillatory behaviour in the general finite-depth linear stability problem discussed in Chapter 3. The stability analysis in section 3.5 shows that oscillatory behaviour cannot occur in the infinite-depth limit. The stability analysis described in Chapter 4 shows that both stable and unstable oscillatory behaviour can occur in the thin-film limit, and the region of parameter space in which it occurs is relatively straightforward to locate. This Appendix shows that while oscillatory behaviour can occur in the general finite-depth problem for physically realisable parameter values, it occurs only for wavenumbers k and layer depths d such that the aspect ratio $kd \ll 1$, and it is therefore an inherently long-wave phenomenon.

A.1 Growth Rates

Oscillatory behaviour of the physical system corresponds to complex values of the growth rate ω. We therefore wish to investigate exactly where in parameter space ω is complex. In particular, we wish to know the extent of the region in parameter space in which ω is complex.

Figure A.1 shows an illustrative plot of the real part of the growth rate of perturbations $\Re(\omega)$ as a function of the wavenumber k. In fact, Figure A.1 is

simply a replot of the solid curve in Figure 3.15, but including the sub-dominant modes that were omitted from Figure 3.15. The sub-dominant modes are an infinite series of bulk-diffusive modes, as evidenced by the fact that they disappear in the limit of infinite depth $d \to \infty$ (see case 3 in section 3.5.5 for a brief discussion of this). The least negative of these sub-dominant modes can also be unstable, while all of the other sub-dominant modes remain stable (also shown in section 3.5.5).

Figure A.2 is a zoomed in version of Figure A.1 showing only the dominant mode and the two least negative sub-dominant modes, and in which the dashed curve corresponds to $\Re(\omega)$ when $\Im(\omega) \neq 0$. The main feature of note in this figure is that there is a pair of complex conjugate solutions for ω connecting the two branches of the sub-dominant modes. This "complex bridge" corresponds to stable oscillatory behaviour. In fact, every sub-dominant mode has a similar "complex bridge" between its branches, and so all sub-dominant modes will have oscillatory behaviour for a range of values of k.

Figure A.3 is a zoomed version in of Figure A.2 showing only the dominant mode and the least negative sub-dominant mode, and in which the dashed curve again corresponds to $\Re(\omega)$ when $\Im(\omega) \neq 0$. Figure A.3 shows that, for a narrow range of wavenumbers k, the *dominant* behaviour is oscillatory, as shown by the "complex bridge" connecting the two branches of the dominant mode. Crucially, a portion of the dashed curve has $\Re(\omega) > 0$, so that oscillatory *instability* is possible in addition to the oscillatory *stability* previously shown in figure A.2.

Figure A.4 shows a plot of the imaginary part of the growth rate $\Im(\omega)$ for the "complex bridge" region that is seen in figure A.3. The values $k = k_{\min}$ and $k = k_{\max}$ correspond to the minimum and maximum values of k, respectively, for which $\Im(\omega) \neq 0$.

The overall implication of Figures A.1–A.4 is that oscillatory behaviour that can occur in the general finite-depth problem is an inherently long-wave phenomenon (i.e., it always occurs for $kd \ll 1$), i.e., all of the oscillatory behaviour is captured by the thin-film stability analysis performed in Chapter 4.

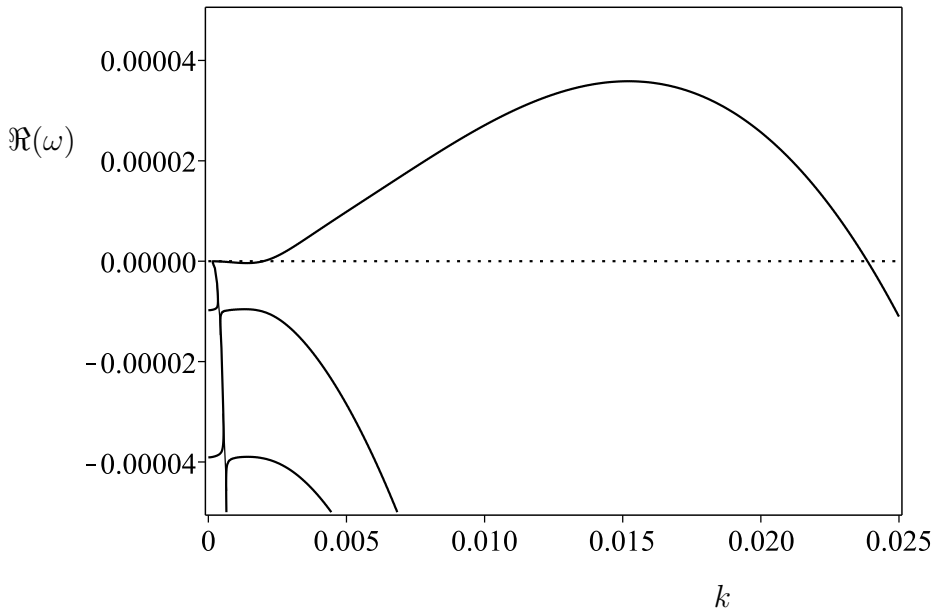

Figure A.1: The real part of the growth rate of perturbations $\Re(\omega)$ as a function of the wavenumber k in the general finite-depth regime with $\mathrm{Ma} = 1$, $\mathrm{P_s} = 1$, $\mathrm{P_b} = 1$, $\mathrm{Da_a} = 0.05$, $\mathrm{Da_d} = 0.5$, $K = 0.5$, $\theta = 1/(1-K) = 2$, $d = 1000$.

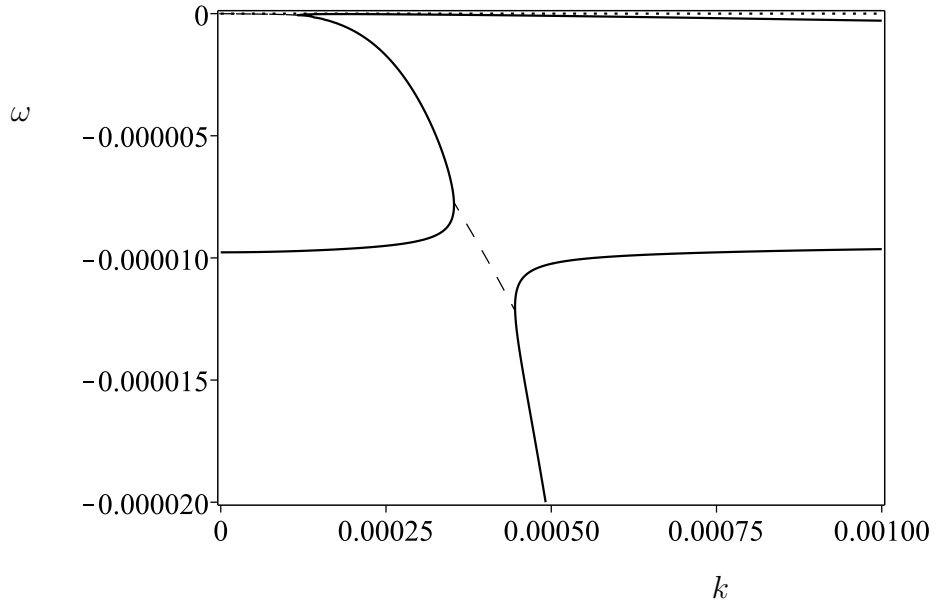

Figure A.2: As figure A.1, but zoomed in to show only the dominant mode and the two least negative sub-dominant modes. The dashed curve corresponds to $\Re(\omega)$ when $\Im(\omega) \neq 0$.

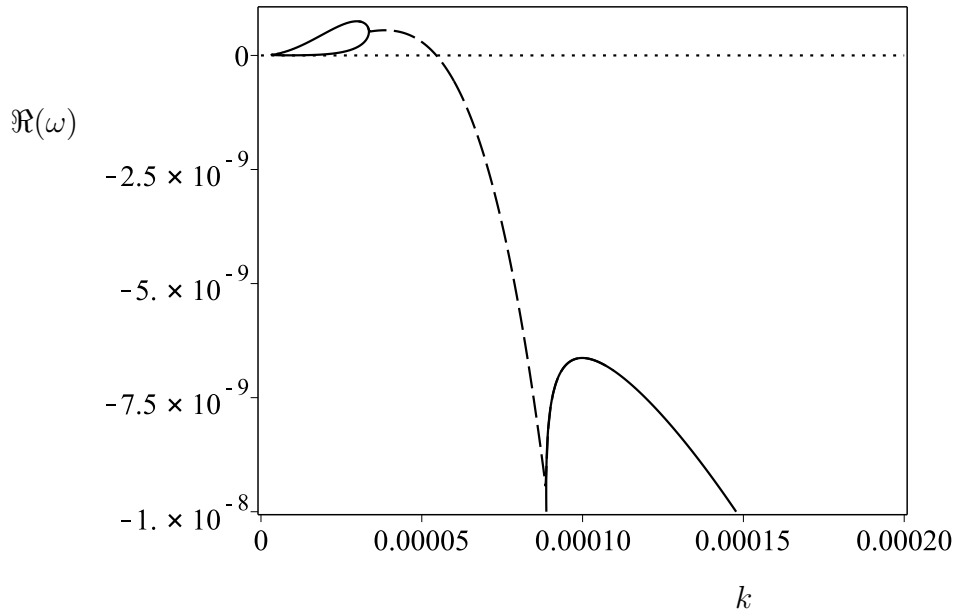

Figure A.3: As figure A.2, but zoomed in to show only the dominant mode and the least negative sub-dominant mode. The dashed curve corresponds to $\Re(\omega)$ when $\Im(\omega) \neq 0$.

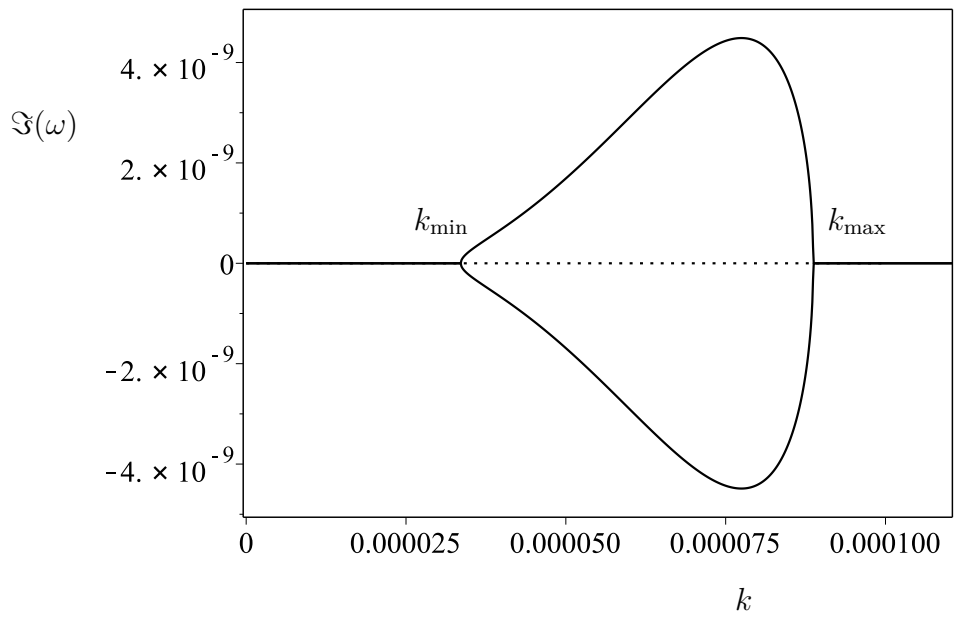

Figure A.4: The imaginary part of the growth rate $\Im(\omega)$ as a function of the wavenumber k for the dominant mode, for the same parameter values as Figures A.1–A.3.

A.2 Effects of Varying the Parameters

Figures A.5–A.9 show how Figure A.4, which shows $\Im(\omega)$, changes as each of the parameters in the problem is varied in turn, with all the others fixed.

Figure A.5 shows how $\Im(\omega)$ changes as Ma is varied. For $\mathrm{Ma} = 0$, ω is purely real, i.e., $k_{\min} = k_{\max} = 0$, but for $0 < \mathrm{Ma} \lesssim 1.606$ there is a range of values of k for which $\Im(\omega) \neq 0$, i.e., $0 < k_{\min} < k_{\max}$. As Ma is increased $k_{\max}$ behaves non-monotonically, first increasing up to its maximum value of $k_{\max} \approx 0.0000902$, which it attains at $\mathrm{Ma} \approx 0.803$, then decreasing until $k_{\max} = k_{\min} \approx 0.0000707$, which occurs for $\mathrm{Ma} \approx 1.606$, at which value ω becomes purely real once again. The value of $k_{\min}$ simply increases monotonically until $k_{\max} = k_{\min} \approx 0.0000707$. Above $\mathrm{Ma} \approx 1.606$ no oscillatory behaviour occurs.

Figures A.6 and A.7 show how $\Im(\omega)$ changes as K is varied, with $K \leq 0.5$ (Figure A.6) and $K \geq 0.5$ (Figure A.7). For $K = 0$, ω is purely real, but for any $0 < K < 1$, there is a range of k for which $\Im(\omega) \neq 0$. As K is increased $k_{\max}$ behaves non-monotonically, first increasing up to its maximum value of $k_{\max} \approx 0.0000902$, which it attains at $K \approx 0.85$, then decreasing until $k_{\max} = k_{\min} \approx 0.000055$, which occurs at $K = 1$ at which value ω become purely real. The value of $k_{\min}$ also behaves non-monotonically, first increasing up to $k_{\min} \approx 0.00003$, which it attains at $K = 0.5$, then decreasing to $k_{\min} \approx 0.000009$, which it attains at $K \approx 0.95$, then increasing until $k_{\max} = k_{\min} \approx 0.000055$. Above $K = 1$ no oscillatory behaviour occurs, demonstrating that the levelling of a layer of surfactant-laden fluid is always monotonic.

Figure A.8 shows how $\Im(\omega)$ changes as the ratio $\delta = \mathrm{Da_d}/\mathrm{Da_a}$ is varied. For $\delta = 0$, ω is purely real, but for any $0 < \delta \lesssim 16.1$, there is a range of k for which $\Im(\omega) \neq 0$. As δ is increased both $k_{\max}$ and $k_{\min}$ behave in a qualitatively similar way to how they behave when Ma was varied. The value of $k_{\max}$ increases up to its maximum of $k_{\max} \approx 0.0000915$, which it attains at $\delta \simeq 12.05$, then decreases until $k_{\max} = k_{\min} \approx 0.0000774$, which occurs for $\delta \approx 16.1$, at which value ω becomes purely real. The value of $k_{\min}$ simply increases monotonically until $k_{\max} = k_{\min} \approx 0.0000774$. For $\delta \gtrsim 16.1$ no oscillatory behaviour occurs.

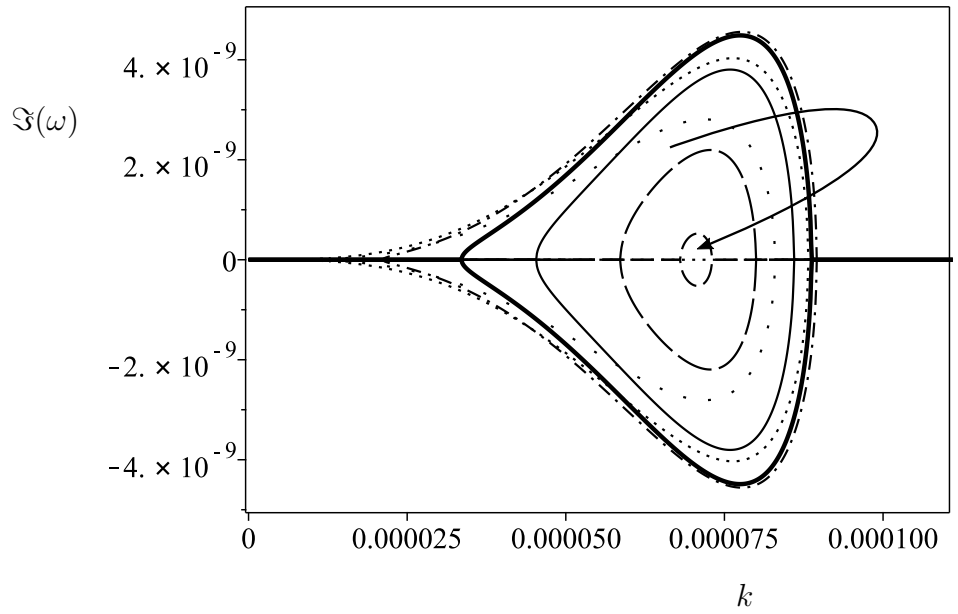

Figure A.5: As in Figure A.4, except that Ma = 0.25 (space-dot), 0.5 (dot), 0.75 (dash-dot), 1 (thick solid), 1.25 (thin solid), 1.5 (long-dash), 1.6 (dash). The arrow denotes increasing values of Ma.

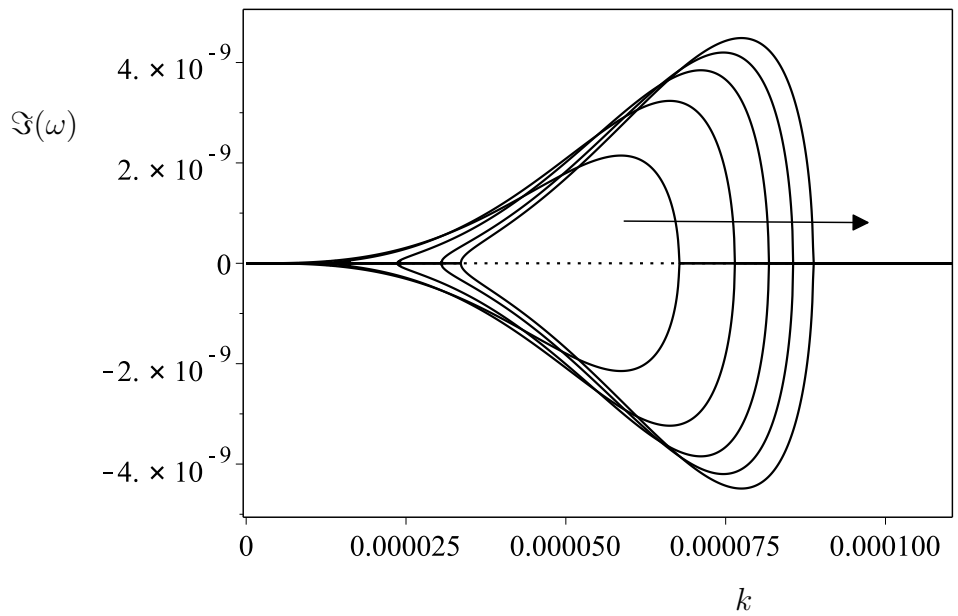

Figure A.6: As in Figure A.4, except that K = 0.1, 0.2, 0.3, 0.4, 0.5. The arrow denotes increasing values of K.

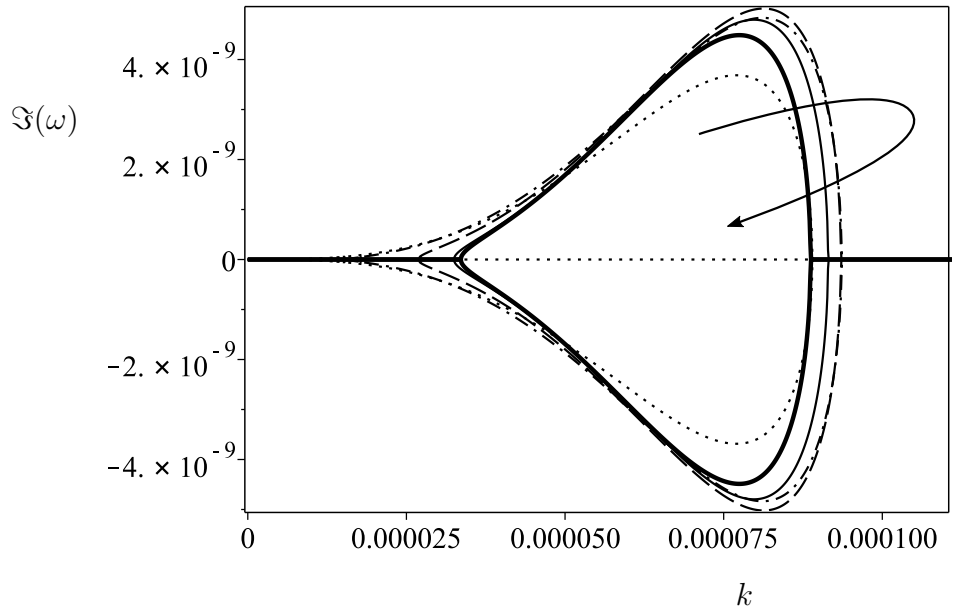

Figure A.7: As in Figure A.4, except that $K = 0.5$ (thick solid), 0.6 (thin solid), 0.7 (dash), 0.8 (dash-dot), 0.9 (dot). The arrow denotes increasing values of K.

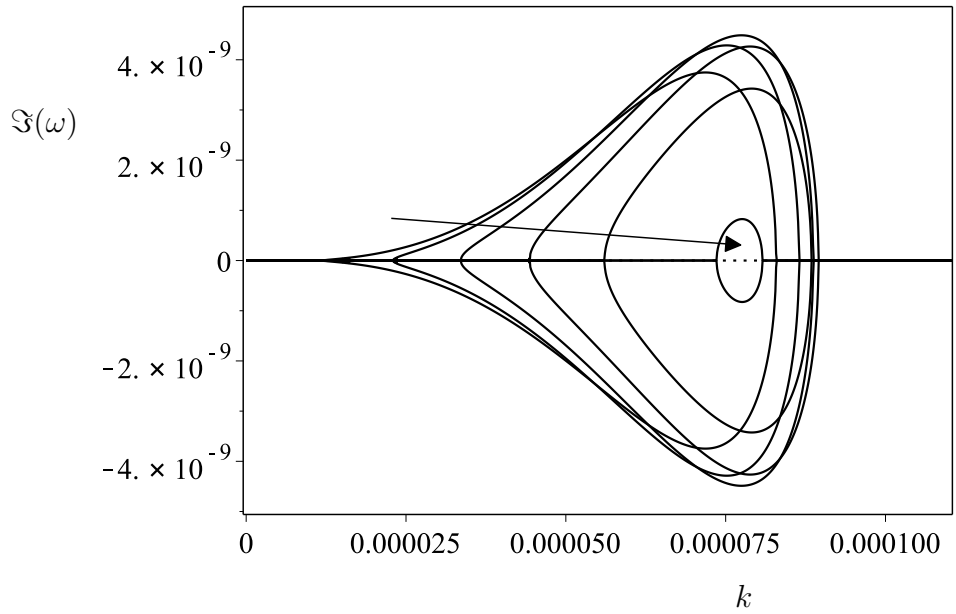

Figure A.8: As in Figure A.4, except that the ratio $\delta = \mathrm{Da_d}/\mathrm{Da_a}$ takes the values $\delta = 6$, 8, 10, 12, 14, 16. The arrow denotes increasing values of δ.

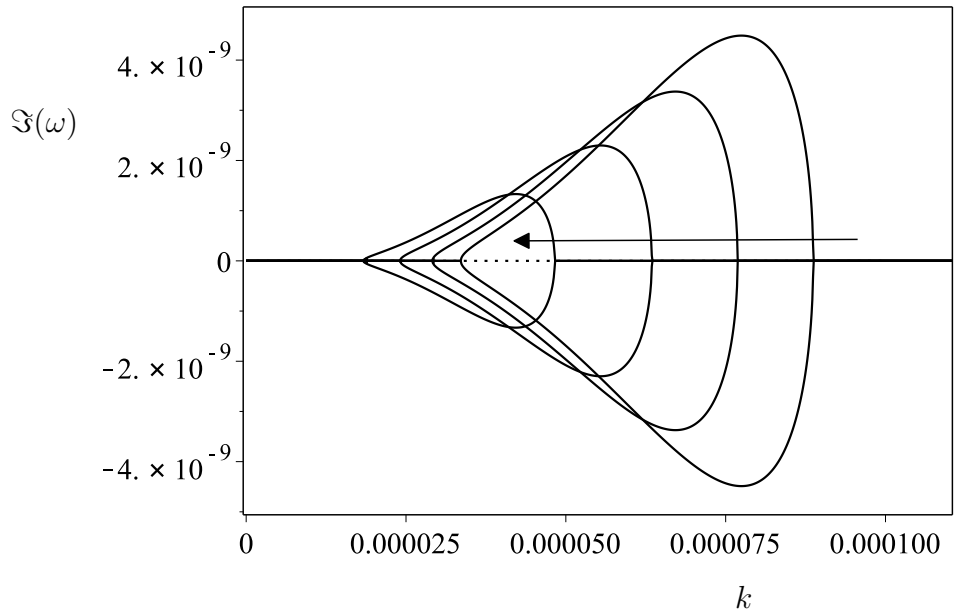

Figure A.9: As in Figure A.4, except that $d = 1000$, 1100, 1250, 1500. The arrow denotes increasing values of d.

Figure A.9 shows how $\Im(\omega)$ changes as d is varied. As d is increased from $d = 1000$ both $k_{\max}$ and $k_{\min}$ decrease. In the limit $d \to \infty$ (with k and ω kept $O(1)$, i.e., the infinite-depth limit), $\Im(\omega) \to 0$ for all k. Thus, there is no oscillatory behaviour present in the infinite-depth limit, as we know from section 3.5. As d is decreased from $d = 1000$, both $k_{\max}$ and $k_{\min}$ increase. In the limit $d \to 0$, $k_{\max} \to +\infty$ and $k_{\min} \to +\infty$, and so only sufficiently short waves lead to oscillatory behaviour, provided that the wavenumber still satisfies $kd \ll 1$. In fact, in order for oscillatory behaviour to occur for $O(1)$ dimensionless wavenumbers, an unphysically small dimensional layer depth smaller than η^*, the thickness of the free surface itself, is required.

The overall conclusion of this Appendix is that the parameter regime in which complex growth rates occur is small, i.e., increasing or decreasing any of the parameters (except d) too far from the values given in Table 3.2 or 3.3 leads to purely real growth rates. The wavenumbers that lead to oscillatory behaviour depend strongly on the depth of the layer; specifically, only a range of wavenumbers satisfying $kd \ll 1$ do so. Oscillatory behaviour is therefore an inherently long-wave phenomenon. Another important conclusion is that oscillatory behaviour can oc-

cur only for anti-surfactant solutions ($K < 1$), but never for surfactant solutions ($K > 1$).

Appendix B

Derivation of the Rankine–Hugoniot Shock Conditions

B.1 Introduction

In this Appendix we derive the Rankine–Hugoniot shock conditions that are used in Chapter 6. We follow the standard derivation of these shock conditions as given in, for example, the book by Whitham [117] by writing down the conservation laws in integral form for the film thickness h, the surface concentration s, and the bulk concentration across the layer hc (note that it is the quantity hc that is conserved, and not simply c). From these conservation laws we recover the PDEs that are analysed in Chapters 4–6 under the assumption that each of h, s, and hc is continuous, and the shock conditions used in Chapter 6 under the assumption that each of h, s, and hc is discontinuous at some time-dependent point, $x_{\mathrm{s}}(t)$.

B.2 Conservation Laws in Integral Form

Consider the conservation of some quantity g in one spatial dimension, x, where g may be discontinuous at some time-dependent point $x_{\mathrm{s}}(t)$. The rate of change of the total amount of g in some arbitrary interval $[x_1, x_2]$ containing the point

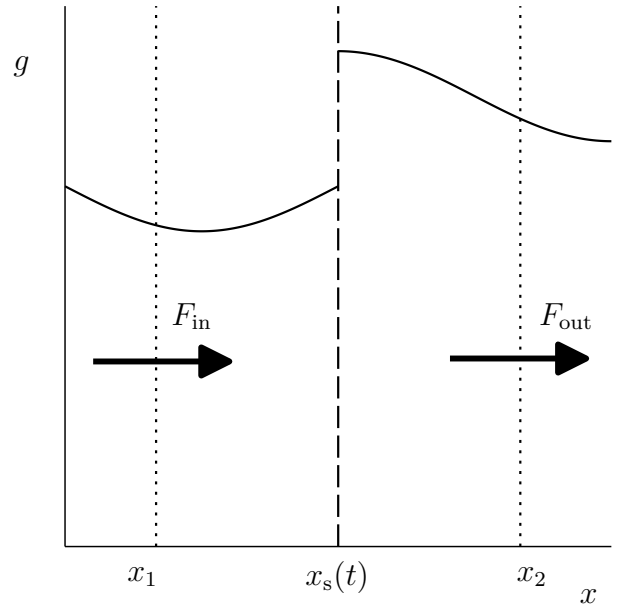

Figure B.1: The conservation of the (in general, discontinuous) quantity g.

$x_{\text{s}}(t)$ must balance the total amount of g that is being added to or removed from this interval due to some flux F, as shown pictorially in Figure B.1. Thus we write

$$\frac{\mathrm{d}}{\mathrm{d}t}\int_{x_1}^{x_2} g\,\mathrm{d}x = F_{\text{in}} - F_{\text{out}}, \tag{B.2.1}$$

where F_{in} and F_{out} are the fluxes of g across the point $x = x_1$ and $x = x_2$, respectively. For the particular equations we consider in Chapters 4–6, Table B.1 shows the flux F for each g, where Q is the horizontal mass flux given by (4.4.34), and u is the fluid velocity given by (4.4.33). Note that we neglect the bulk-surface flux in the expressions for F in Table B.1, since in Chapter 6 we consider only the special cases of an insoluble surfactant and a "perfectly soluble" anti-surfactant, for both of which the bulk–surface flux term J is identically zero. We also neglect diffusion since, again, the problems that we solve in Chapter 6 do not involve diffusion of either surface or bulk solute. Both of these physical effects could be readily incorporated into the following analysis, if necessary.

Conserved quantity, g	**Conservative flux,** F
h	Q
s	us
hc	Qc

Table B.1: The flux F for each g, for the particular equations we consider in Chapters 4–6.

B.3 The PDEs (4.7.1)–(4.7.3)

Under the assumption that g is continuous, equation (B.2.1) can be written

$$\int_{x_1}^{x_2} \frac{\partial g}{\partial t}\,\mathrm{d}x = \int_{x_1}^{x_2} -\frac{\partial F}{\partial x}\,\mathrm{d}x, \tag{B.3.1}$$

which holds for arbitrary x_1 and x_2. Thus, the integrands must be equal, and we recover the PDEs that are used in Chapters 4–6, i.e., for $g = h$, s, hc, and the appropriate choices of flux as in Table B.1, equation (B.3.1) yields

$$h_t + Q_x = 0, \tag{B.3.2}$$

$$s_t + (us)_x = 0, \tag{B.3.3}$$

$$(hc)_t + (Qc)_x = 0, \tag{B.3.4}$$

which are equations (4.7.1)–(4.7.3) written in flux-conservative form, with $\mathrm{Da_a} = \mathrm{Da_d} = 0$, since we neglect the bulk-surface flux, and with $\mathrm{P_s} \to \infty$ and $\mathrm{P_b} \to \infty$, since we neglect diffusion.

B.4 Shock Conditions

When g is discontinuous at some time-dependent point $x_\mathrm{s}(t)$ we cannot write equation (B.2.1) in the form (B.3.1). Instead, we must split the integral on the left-hand side of equation (B.2.1) and apply the Leibniz rule for differentiating under the integral sign, since the end points of the split integral are time-dependent. Thus, we write

$$\frac{\mathrm{d}}{\mathrm{d}t}\int_{x_1}^{x_\mathrm{s}(t)} g\,\mathrm{d}x + \frac{\mathrm{d}}{\mathrm{d}t}\int_{x_\mathrm{s}(t)}^{x_2} g\,\mathrm{d}x = F_\mathrm{in} - F_\mathrm{out}, \tag{B.4.1}$$

which upon application of the Leibniz rule yields

$$\int_{x_1}^{x_s(t)} \frac{\partial g}{\partial t}\,\mathrm{d}x + x_s'(t)g(x_s(t)^-) + \int_{x_s(t)}^{x_2} \frac{\partial g}{\partial t}\,\mathrm{d}x - x_s'(t)g(x_s(t)^+) = -\left[F\right]_{x_1}^{x_2}, \quad \text{(B.4.2)}$$

where the dash denotes (total) differentiation with respect to time, and the superscripts $-$ and $+$ denote evaluation of the function just to the left, and just to the right, of the point $x_s(t)$, respectively. Taking the limits $x_1 \to x_s(t)^-$ and $x_2 \to x_s(t)^+$ yields

$$x_s'(t)g(x_s(t)^-) - x_s'(t)g(x_s(t)^+) = -\left[F\right]_{x_s(t)^-}^{x_s(t)^+}, \quad \text{(B.4.3)}$$

which may be written in the form

$$\dot{x}_\mathrm{s}\left[\!\left[g\right]\!\right] = \left[\!\left[F\right]\!\right], \quad \text{(B.4.4)}$$

where we define the notation

$$\left[\!\left[\,\cdot\,\right]\!\right] = -\left[\,\cdot\,\right]_{x_s(t)^-}^{x_s(t)^+}, \quad \text{(B.4.5)}$$

and $\dot{x}_\mathrm{s} = x_s'(t)$ is the speed of the discontinuity, i.e., the shock speed. Using Table B.1, equation (B.4.4) becomes

$$\dot{x}_\mathrm{s}\left[\!\left[h\right]\!\right] = \left[\!\left[Q\right]\!\right], \quad \text{(B.4.6)}$$

$$\dot{x}_\mathrm{s}\left[\!\left[s\right]\!\right] = \left[\!\left[us\right]\!\right], \quad \text{(B.4.7)}$$

$$\dot{x}_\mathrm{s}\left[\!\left[hc\right]\!\right] = \left[\!\left[Qc\right]\!\right], \quad \text{(B.4.8)}$$

which are precisely the Rankine–Hugoniot shock conditions that are used in Chapter 6.

Appendix C

Parametric Solution to Equations (6.2.3) and (6.2.4)

C.1 Introduction

In this Appendix we derive explicit solutions to equations (6.2.3) and (6.2.4). These equations were first solved by Howison *et al.* [35], who obtained implicit solutions (for different initial conditions), and were also solved in section 6.2 of this thesis for a family of Riemann problems in which the initial condition was piecewise constant with a single discontinuity. We show here that it is possible to obtain explicit parametric solutions for any sufficiently well-behaved initial condition.

C.2 Transformation to a Decoupled System

Equations (6.2.3) and (6.2.4), restated, are

$$h_t + \frac{1}{2}\left[h^2 b\right]_x = 0, \tag{C.2.1}$$

$$b_t + \frac{1}{2}\left[b^2 h\right]_x = 0, \tag{C.2.2}$$

and are subject to the initial conditions

$$h = h_0(x), \quad b = b_0(x) \quad \text{at} \quad t = 0. \tag{C.2.3}$$

By defining $\phi = hb$ and $\psi = h/b$, we may rewrite these equations as a decoupled system, namely

$$\phi_t + \frac{3}{2}\phi\phi_x = 0, \tag{C.2.4}$$

$$\psi_t + \frac{1}{2}\phi\psi_x = 0, \tag{C.2.5}$$

which are an inviscid Burgers' equation for ϕ, and an equation for ψ that is slave to it. These transformed equations are subject to the transformed initial conditions

$$\phi = \phi_0(x), \quad \psi = \psi_0(x) \quad \text{at} \quad t = 0, \tag{C.2.6}$$

where

$$\phi_0(x) = h_0(x)b_0(x), \quad \psi_0(x) = \frac{h_0(x)}{b_0(x)}. \tag{C.2.7}$$

C.3 Parametric Solutions

Equation (C.2.4), subject to the initial condition (C.2.6), has the implicit solution

$$\phi = \phi_0\left(x - \frac{3}{2}\phi t\right), \tag{C.3.1}$$

which can be written in terms of a parameter q as

$$x = \frac{3}{2}t\phi_0(q) + q, \qquad \phi = \phi_0(q), \tag{C.3.2}$$

where q can, in general, take any real value.

Next, we write (C.2.5) in characteristic form, namely

$$\frac{\mathrm{d}\psi}{\mathrm{d}t} = 0 \quad \text{on the characteristic curves given by} \quad \frac{\mathrm{d}x}{\mathrm{d}t} = \frac{1}{2}\phi. \tag{C.3.3}$$

Substituting the expression for x and ϕ given by (C.3.2) into the second of equation (C.3.3) yields

$$\left(\frac{3}{2}t\phi_0'(q) + 1\right)\frac{\mathrm{d}q}{\mathrm{d}t} = -\phi_0(q). \tag{C.3.4}$$

Multiplying by the integrating factor $|\phi_0(q)|^{1/2}$, we may write this equation in exact form, namely

$$\left(\frac{3}{2}t\,|\phi_0(q)|^{1/2}\,\phi_0'(q) + |\phi_0(q)|^{1/2}\right)\mathrm{d}q + |\phi_0(q)|^{1/2}\,\phi_0(q)\,\mathrm{d}t = 0, \tag{C.3.5}$$

which has the solution

$$t\phi_0(q)\,|\phi_0(q)|^{1/2} + I(q) = \text{constant}, \tag{C.3.6}$$

where we have written

$$I(q) = \int |\phi_0(q)|^{1/2}\,\mathrm{d}q, \tag{C.3.7}$$

which is a known function. Thus, the general solution for ψ of (C.3.3) is

$$\psi = G\left(t\phi_0(q)\,|\phi_0(q)|^{1/2} + I(q)\right), \tag{C.3.8}$$

where G is an arbitrary function that may, in principle, be determined using the initial condition (C.2.6), i.e., G is determined from

$$\psi_0(q) = G\Big(I(q)\Big). \tag{C.3.9}$$

Determining G is a non-trivial task in general, but can always be done when the function I is invertible by defining $r = I(q)$ and inverting to obtain $q = I^{-1}(r)$. Then, equation (C.3.9) gives $G(r) = \psi_0(I^{-1}(r))$. When the function I is not invertible, this process is not applicable, and other methods must be used to determine G.

To summarise, we have solved equations (C.2.4) and (C.2.5) to obtain a parametric solution for any sufficiently well-behaved initial condition. Specifically, the solution for ϕ is given by (C.3.2), and the solution for ψ is given by (C.3.8). From these we may obtain the solution for the film thickness h and the bulk concentration c. The solution for the film thickness is simply

$$h = (\phi\psi)^{1/2}, \tag{C.3.10}$$

where we take the positive root, since h must be positive for all x. The solution for the concentration gradient is

$$b = \pm\left(\frac{\phi}{\psi}\right)^{1/2}. \tag{C.3.11}$$

Finally, the solution for the bulk concentration is given by

$$\begin{aligned} c &= \int b \, \mathrm{d}x \\ &= \int \operatorname{sgn}(b) \left(\frac{\phi}{\psi}\right)^{1/2} \frac{\mathrm{d}x}{\mathrm{d}q} \, \mathrm{d}q \\ &= \operatorname{sgn}(b) \int \left(\frac{\phi_0(q)}{G\Big(t\phi_0(q) \left|\phi_0(q)\right|^{1/2} + I(q)\Big)^{1/2}} \right) \left(\frac{3}{2} t\phi_0'(q) + 1\right) \mathrm{d}q, \end{aligned} \tag{C.3.12}$$

where $\operatorname{sgn}(b) = 1$ or $\operatorname{sgn}(b) = -1$ if b is positive, or negative, respectively. With the substitution

$$p = t\phi_0(q) \left|\phi_0(q)\right|^{1/2} + I(q) \tag{C.3.13}$$

equation (C.3.12) leads to

$$c = \operatorname{sgn}(b) \int \frac{\mathrm{d}p}{\left|G(p)\right|^{1/2}}. \tag{C.3.14}$$

C.4 An Example of an Explicit Solution

Given an arbitrary set of initial conditions, it is a non-trivial (or impossible) task to determine the function G analytically, because of the possible complexity of the function $I(q)$ defined in (C.3.7). However, for sufficiently well-behaved initial conditions (in particular, as long as $I(q)$ is invertible), it is possible to determine G; we provide an illustrative example here.

With the initial conditions

$$h_0(x) = 1, \qquad b_0(x) = \operatorname{sech}^2(x), \tag{C.4.1}$$

we have

$$\phi_0(q) = \operatorname{sech}^2(q), \qquad \psi_0(q) = \cosh^2(q), \tag{C.4.2}$$

and consequently, from (C.3.7),

$$I(q) = \int \operatorname{sech}(q) \, \mathrm{d}q = 2 \arctan(\mathrm{e}^q). \tag{C.4.3}$$

Thus (C.3.8) becomes

$$\cosh^2(q) = G\left(2 \arctan(\mathrm{e}^q)\right). \tag{C.4.4}$$

To determine G, we define r to be

$$r = 2\arctan(\mathrm{e}^q), \tag{C.4.5}$$

from which we have

$$q = \log\left(\tan\left(\frac{r}{2}\right)\right), \tag{C.4.6}$$

and it is then clear from (C.4.4) that

$$G(r) = \cosh^2\left(\log\left(\tan\left(\frac{r}{2}\right)\right)\right), \tag{C.4.7}$$

which may be simplified to

$$G(r) = \frac{1}{\sin^2(r)}. \tag{C.4.8}$$

Thus, the parametric solution for ϕ and ψ, from (C.3.2) and (C.3.8), respectively, is

$$x = q + \frac{3}{2}t\,\mathrm{sech}^2(q), \tag{C.4.9}$$

$$\phi = \mathrm{sech}^2(q), \tag{C.4.10}$$

$$\psi = \frac{1}{\sin^2\left(t\,\mathrm{sech}^3(q) + 2\arctan\left(\mathrm{e}^q\right)\right)}, \tag{C.4.11}$$

and the corresponding solutions for h and b, from (C.3.10) and (C.3.11), respectively, are

$$x = q + \frac{3}{2}t\,\mathrm{sech}^2(q), \tag{C.4.12}$$

$$h = \frac{1}{\cosh(q)\sin\left(t\,\mathrm{sech}^3(q) + 2\arctan\left(\mathrm{e}^q\right)\right)}, \tag{C.4.13}$$

$$b = \frac{\sin\left(t\,\mathrm{sech}^3(q) + 2\arctan\left(\mathrm{e}^q\right)\right)}{\cosh(q)}. \tag{C.4.14}$$

Finally, the solution for c, from (C.3.14) (with (C.3.13)), is

$$c = \int \frac{\mathrm{d}r}{G(r)^{1/2}} = -\cos\left(t\,\mathrm{sech}^3(q) + 2\arctan\left(\mathrm{e}^q\right)\right) + C \tag{C.4.15}$$

Figure C.1 shows a plot of this example solution for (a) the film thickness h, (b) the bulk concentration c, and (c) the concentration gradient b, given by equations (C.4.13)–(C.4.15), respectively. The initially flat free surface is pulled rightwards

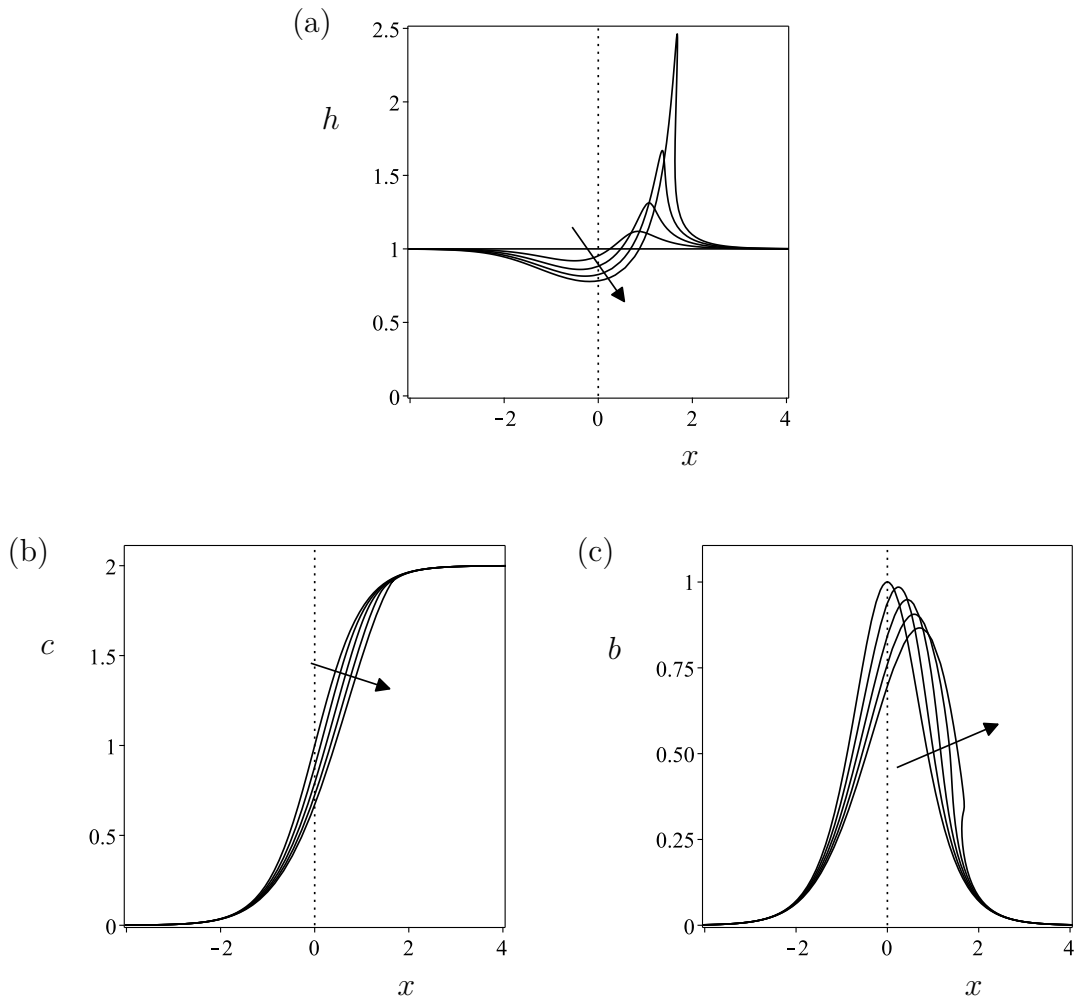

Figure C.1: Example solution for (a) the film thickness h, (b) the bulk concentration c, and (c) the concentration gradient b, given by equations (C.4.13)–(C.4.15), respectively, for $C = 1$. The arrow denotes the direction of increasing time.

because of the positive concentration gradient. The fluid exactly at the maximum of the concentration gradient is pulled right faster than the surrounding fluid and, as shown at the latest snapshot in time, becomes multi-valued at some finite time. This signifies that a shock forms, and finite-time blow-up of the derivatives of all of h, b, and c occurs. Calculating, say, $\mathrm{d}h/\mathrm{d}x$, we find that the first time that this shock occurs is

$$t = \min\left(\frac{\cosh^3(q)}{3\sinh(q)} : q \in \mathbb{R}\right) = \frac{\sqrt{3}}{2}. \tag{C.4.16}$$

Bibliography

[1] Y. Abe. Self-rewetting fluids. *Annals of New York Academy of Sciences*, 1077:650–667, 2006.

[2] D. J. Acheson. *Elementary Fluid Dynamics*. Oxford University Press, 1990.

[3] A. B. Afsar-Siddiqui, P. F. Luckam, and O. K. Matar. The spreading of surfactant solutions on thin liquid films. *Advances in Colloid and Interface Science*, 106:183–236, 2003.

[4] M. L. Agrawal and R. D. Neuman. Surface diffusion in monomolecular films. *Journal of Colloid and Interface Science*, 121:367–380, 1986.

[5] G. Barenblatt. *Scaling*. Cambridge University Press, 2003.

[6] D. R. Beacham and O. K. Matar. Surfactant-enhanced rapid spreading of drops on solid surfaces. *Langmuir*, 25:14174–14181, 2009.

[7] H. Bénard. Tourbillons cellulaires dans une nappe liquide. *Revue Générale des Sciences pures et appliquées*, 11:1261–1271, 1900.

[8] M. S. Borgas and J. B. Grotberg. Monolayer flow on a thin film. *Journal of Fluid Mechanics*, 193:151–170, 1988.

[9] C. J. W. Breward, C. Darton, P. D. Howell, and J. R. Ockendon. The effects of surfactants on expanding free surfaces. *Chemical Engineering Science*, 56:2867–2878, 2001.

[10] C. Caleman and D. van der Spoel. Evaporation from water clusters containing singly charged ions. *Physical Chemistry Chemical Physics*, 9:5105–5111, 2007.

[11] C.-H. Chang and E. I. Franses. Adsorption dynamics of surfactants at the air/water interface: a critical review of mathematical models, data, and mechanisms. *Colloids and Surfaces A*, 100:1–45, 1995.

[12] A. Cloot and G. Lebon. A nonlinear stability analysis of the Bénard–Marangoni problem. *Journal of Fluid Mechanics*, 145:447–469, 1984.

[13] COMSOL Ltd. Comsol multiphysics. `www.comsol.com`.

[14] J. J. A. Conn, B. R. Duffy, D. Pritchard, S. K. Wilson, P. J. Halling, and K. Sefiane. Fluid-dynamical model for antisurfactants. *Physical Review E*, 93:043121, 2016.

[15] R. V. Craster and O. K. Matar. Dynamics and stability of thin liquid films. *Reviews of Modern Physics*, 81:1131–1198, 2009.

[16] R. A. Curtis and L. Lue. Depletion forces due to image charges near dielectric discontinuities. *Current Opinion in Colloid and Interface Science*, 20:19–23, 2015.

[17] C. D. Daub, D. Bratko, and A. Luzar. Electric control of wetting by salty nanodrops: Molecular dynamics simulations. *Journal of Physical Chemistry C*, 115:22393–22399, 2011.

[18] S. H. Davis. Thermocapillary instabilities. *Annual Review of Fluid Mechanics*, 19:403–435, 1987.

[19] M. E. Derrick. Agnes Pockels, 1862–1935. *Journal of Chemical Education*, 59:1030–1031, 1982.

[20] A. P. dos Santos, A. Diehl, and Y. Levin. Surface tensions, surface potentials, and the Hofmeister series of electrolyte solutions. *Langmuir*, 26:10778–10783, 2010.

[21] J. Eastoe and J. S. Dalton. Dynamic surface tension and adsorption mechanisms of surfactants at the air-water interface. *Advances in Colloid and Interface Science*, 85:103–144, 2000.

[22] B. D. Edmonstone and O. K. Matar. Simultaneous thermal and surfactant-induced Marangoni effects in thin liquid films. *Journal of Colloid and Interface Science*, 274:183–199, 2004.

[23] F. F. Espinosa, A. H. Shapiro, J. J. Fredberg, and R. D. Kamm. Spreading of exogenous surfactant in an airway. *Journal of Applied Physiology*, 75:2028–2039, 1993.

[24] D. P. Gaver III and J. B. Grotberg. The dynamics of a localized surfactant on a thin film. *Journal of Fluid Mechanics*, 213:127–148, 1990.

[25] D. P. Gaver III and J. B. Grotberg. Droplet spreading on a thin viscous film. *Journal of Fluid Mechanics*, 235:399–414, 1992.

[26] P. A. Good and R. S. Schecter. Surface diffusion in monolayers. *Journal of Colloid and Interface Science*, 40:99–106, 1971.

[27] M. Hanak, A. A. Darhuber, and M. Ren. Surfactant-induced delay of levelling of inkjet-printed patterns. *Journal of Applied Physics*, 109:074905, 2011.

[28] M. Hanak, D. K. N. Sanz, and A. A. Darhuber. Soluble surfactant spreading on spatially confined thin liquid films. *Soft Matter*, 8:7660, 2012.

[29] M. Hanak, D. K. N. Sinz, and A. A. Darhuber. Insoluble surfactant spreading along thin liquid films confined by chemical surface patterns. *Physical Chemistry Chemical Physics*, 12:9768–9777, 2012.

[30] I. Hashim and S. K. Wilson. The onset of Bénard-Marangoni convection in a horizontal layer of fluid. *International Journal of Engineering Science*, 37:643–662, 1999.

[31] I. Hashim and S. K. Wilson. The onset of oscillatory Marangoni convection in a semi-infinitely deep layer of fluid. *Zeitschrift für angewandte Mathematik und Physik*, 50:546–558, 1999.

[32] W. M. Haynes (ed.). *CRC Handbook of Chemistry and Physics*. Langmuir, 2009.

[33] J. F. Hernandez-Sanchez, A. Eddi, and J. H. Snoeijer. Marangoni spreading due to a localized alcohol supply on a thin water film. *Physics of Fluids*, 27:032003, 2015.

[34] P. D. Howell and C. J. W. Breward. Mathematical modelling of the overflowing cylinder experiment. *Journal of Fluid Mechanics*, 474:275–298, 2003.

[35] S. D. Howison, J. A. Moriarty, J. R. Ockendon, E. L. Terrill, and S. K. Wilson. A mathematical model for drying paint layers. *Journal of Engineering Mathematics*, 32:377–394, 1997.

[36] C. Huh and L. E. Scriven. Hydrodynamic model of steady movement of a solid/liquid/fluid contact line. *Journal of Colloid and Interface Science*, 35:85–101, 1970.

[37] S. Iglauer, Y. Wu, P. Shuler, Y. Tang, and W. A. Goddard III. New surfactant classes for enhanced oil recovery and their tertiary oil recovery potential. *Journal of Petroleum Science and Engineering*, 71:23–29, 2010.

[38] O. E. Jensen. Self-similar, surfactant-driven flows. *Physics of Fluids*, 6:1084–1094, 1994.

[39] O. E. Jensen and J. B. Grotberg. Insoluble surfactant spreading on a thin viscous film: shock evolution and film rupture. *Journal of Fluid Mechanics*, 240:259–288, 1992.

[40] O. E. Jensen and J. B. Grotberg. The spreading of heat or soluble surfactant along a thin liquid film. *Physics of Fluids A*, 5:58–68, 1993.

[41] O. E. Jensen, D. Halpern, and J. B. Grotberg. Transport of a passive solute by surfactant-driven flows. *Chemical Engineering Science*, 49:1107–1117, 1994.

[42] G. Jones and W. Ray. The surface tension of solutions of electrolytes as a function of the concentration, I: A differential bubble method for measuring relative surface tension. *Journal of the American Chemical Society*, 59:187–198, 1937.

[43] G. Jones and W. Ray. The surface tension of solutions of electrolytes as a function of the concentration II*. *Journal of the American Chemical Society*, 63:288–294, 1941.

[44] S. Kalliadasis, C. Ruyer-Quil, B. Scheid, and M. G. Velarde. *Falling Liquid Films*. Springer, 2011.

[45] G. Karapetsas, R. V. Craster, and O. K. Matar. On surfactant-enhanced spreading and superspreading of liquid drops on solid surfaces. *Journal of Fluid Mechanics*, 670:5–37, 2011.

[46] G. Karapetsas, K. C. Sahu, K. Sefiane, and O. Matar. Thermocapillary-driven motion of a sessile drop: effect of non-monotonic dependence of surface tension on temperature. *Langmuir*, 30:4310–4321, 2014.

[47] D. Langevin. Rheology of adsorbed surfactant monolayers at fluid surfaces. *Annual Review of Fluid Mechanics*, 46:47–65, 2014.

[48] P. Leroy, A. Lassin, M. Azaroual, and L. André. Predicting the surface tension of aqueous 1:1 electrolyte solutions at high salinity. *Geochemica et Cosmochimica Acta*, 74:5427–5442, 2010.

[49] W. Li and S. Kumar. Thin-film coating of surfactant-laden liquids on rotating cylinders. *Physics of Fluids*, 27:072106, 2015.

[50] Y. Li, Q. Yang, M. Li, and Y. Song. Rate-dependent interface capture beyond the coffee-ring effect. *Scientific Reports*, 6:24628, 2016.

[51] C.-Y. Liu, E. Vandre, M. S. Carvalho, and S. Kumar. Dynamic wetting failure in surfactant solutions. *Journal of Fluid Mechanics*, 789:285–309, 2016.

[52] F. A. Long and G. C. Nutting. The relative surface tension of potassium chloride solutions by a differential bubble pressure method. *Journal of the American Chemical Society*, 64:234–243, 1942.

[53] C. Marangoni. Difesa della teoria dell'elasticità superficiale dei liquidi. *Il Nuovo Cimento*, 3:97–115, 1878.

[54] A. Marin, R. Liepelt, M. Rossi, and C. J. Kähler. Surfactant-driven flow transitions in evaporating droplets. *Soft Matter*, 12:1593–1600, 2016.

[55] T. Markovich, D. Andelman, and R. Podgornik. Surface tension of electrolyte solutions: A self-consistent theory. *Europhysics Letters*, 106:16002–16009, 2014.

[56] O. K. Matar and R. V. Craster. Dynamics of surfactant-assisted spreading. *Soft Matter*, 5:3801–3809, 2009.

[57] O. K. Matar and S. M. Troian. The development of transient fingering patterns during the spreading of surfactant coated films. *Physics of Fluids*, 11:3232–3246, 1999.

[58] A. D. McNaught and A. Wilkinson (compilers). *IUPAC. Compendium of Chemical Terminology, 2nd ed. (the "Gold Book").* Blackwell Scientific Publications, 1997.

[59] A. C. Mitropoulos. What is a surface excess? *Journal of Engineering Science and Technology Review*, 1:1–3, 2008.

[60] C. E. Morgan, C. J. W. Breward, I. M. Griffiths, P. D. Howell, J. Penfold, R. K. Thomas, I. Tucker, J. T. Petkov, and J. R. P. Webster. Kinetics of surfactant desorption at an air-solution interface. *Langmuir*, 28:17339–17348, 2012.

[61] M. Morozov, A. Oron, and A. A. Nepomnyashchy. Long-wave Marangoni convection in a layer of surfactant solution: Bifurcation analysis. *Physics of Fluids*, 27:082107, 2015.

[62] D. A. Nield. Surface tension and buoyancy effects in cellular convection. *Journal of Fluid Mechanics*, 19:341–352, 1964.

[63] B. A. Noskov. Fast adsorption at the liquid–gas interface. *Advances in Colloid and Interface Science*, 69:63–129, 1996.

[64] K. D. O'Hare and P. L. Spalding. Evaporation of a binary liquid mixture. *The Chemical Engineering Journal*, 48:1–9, 1992.

[65] L. Onsager and N. N. T. Samaras. The surface tension of Debye-Hückel electrolytes. *The Journal of Chemical Physics*, 2:528–536, 1934.

[66] S. E. Orchard. On surface levelling in viscous liquids and gels. *Applied Scientific Research, Section A*, 11:451–464, 1963.

[67] A. Oron, S. H. Davis, and S. G. Bankoff. Long-scale evolution of thin liquid films. *Review of Modern Physics*, 69:931–980, 1997.

[68] W. S. Overdiep. The levelling of paints. *Progress in Organic Coatings*, 14:159–175, 1986.

[69] O. Ozdemir, S. I. Karakashev, A. V. Nguyen, and J. D. Miller. Adsorption and surface tension analysis of concentrated alkali halide brine solutions. *Minerals Engineering*, 22:263–271, 2009.

[70] J. R. A. Pearson. On convection cells induced by surface tension. *Journal of Fluid Mechanics*, 4:489–500, 1958.

[71] A. Pellew and R. S. Southwell. On maintained convective motion in a fluid heated from below. *Proceedings of the Royal Society of London, Series A*, 176:312–343, 1940.

[72] A. Pereira and S. Kalliadasis. On the transport equation for an interfacial quantity. *European Physical Journal Applied Physics*, 44:211–214, 2008.

[73] P. B. Petersen and R. J. Saykally. Adsorption of ions to the surface of dilute electrolyte solutions: the Jones–Ray effect revisited. *Journal of the American Chemical Society*, 127:15446–15452, 2005.

[74] P. B. Petersen and R. J. Saykally. On the nature of ions at the liquid water interface. *Annual Review of Physical Chemistry*, 57:333–364, 2006.

[75] A. Pockels. Surface tension. *Nature*, 43:437–439, 1891.

[76] A. Podolny, A. Oron, and A. A. Nepomnyashchy. Long-wave Marangoni instability in a binary-liquid layer with deformable interface in the presence of Soret effect: Linear theory. *Physics of Fluids*, 17:104104, 2005.

[77] A. Podolny, A. Oron, and A. A. Nepomnyashchy. Linear and nonlinear theory of long-wave Marangoni instability with the Soret effect at finite Biot numbers. *Physics of Fluids*, 18:054104, 2006.

[78] R. F. Probstein. *Physicochemical Hydrodynamics: An Introduction*. Wiley, 1994.

[79] Lord Rayleigh. On convection currents in a horizontal layer of fluid, when the higher temperature is on the under side. *Philosophical Magazine Series 6*, 21:529–546, 1916.

[80] F. M. Richter. Experiments on the stability of convection rolls in fluids whose viscosity depends on temperature. *Journal of Fluid Mechanics*, 89:553–560, 2005.

[81] M. J. Rosen and J. T. Kunjappu. *Surfactants and Interfacial Phenomena*. Wiley, 1978.

[82] P. G. Saffman and G. I. Taylor. The penetration of a fluid into a medium or Hele–Shaw cell containing a more viscous liquid. *Proceedings of the Royal Society of London, Series A*, 245:312–329, 1958.

[83] R. Savino, A. Cecere, and R. Di Paola. Surface-tension-driven flow in wickless heat pipes with self-rewetting fluids. *International Journal of Heat and Fluid Flow*, 30:380–388, 2009.

[84] R. Savino, N. di Fracescantonio, R. Fortezza, and Y. Abe. Heat pipes with binary mixtures and inverse Marangoni effects for microgravity applicaitons. *Acta Astronautica*, 61:16–26, 2007.

[85] R. Savino and D. Paterna. Marangoni effect and heat pipes dryout. *Physics of Fluids*, 18:118103, 2006.

[86] L. Schwartz, R. A. Cairncross, and D. E. Weidner. Anomalous behaviour during leveling of thin coating layers with surfactant. *Physics of Fluids*, 8:1693–1695, 1996.

[87] L. W. Schwartz, D. E. Weidner, and R. R. Eley. An analysis of the effect of surfactant on the leveling behavior of a thin liquid coating layer. *Langmuir*, 11:3690–3693, 1995.

[88] L. E. Scriven and C. V. Sternling. On cellular convection driven by surface-tension gradients: effects of mean surface tension and surface viscosity. *Journal of Fluid Mechanics*, 19:321–340, 1964.

[89] D. J. Shaw. *Introduction to Colloid and Surface Chemistry*. Butterworths, 1970.

[90] A. Sheludko. Thin liquid films. *Advances in Colloid and Interface Science*, 4:391–464, 1967.

[91] R. I. Slavchov and J. K. Novev. Surface tension of concentrated electrolyte solutions. *Journal of Colloid and Interface Science*, 387:234–243, 2012.

[92] K. A. Smith. On convective instability induced by surface-tension gradients. *Journal of Fluid Mechanics*, 24:401–414, 1966.

[93] V. Starov, V. Zhdanov, and N. M. Kovalchuk. Kinetic models for micelle formation. *Colloids and Surfaces A*, 354:268–278, 2009.

[94] V. Starov, V. Zhdanov, and N. M. Kovalchuk. Kinetic models of micelles formation. *Colloids and Surfaces A: Physicochemical and Engineering Aspects*, 354:268–278, 2010.

[95] J. J. Stoker. *Water Waves*. Interscience Publishers, Inc., New York, 1957.

[96] H. A. Stone. A simple derivation of the time-dependent convective diffusion equation for surfactant transport along a deforming interface. *Physics of Fluids A*, 2:111–112, 1990.

[97] S. L. Strickland, M. Hin, M. R. Sayanagi, C. Gaebler, K. Daniels, and R. Levy. Self-healing dynamics of surfactant coatings on thin viscous films. *Physics of Fluids*, 26:042109, 2014.

[98] E. R. Swanson, S. L. Strickland, M. Shearer, and K. E. Daniels. Surfactant spreading on a thin liquid film: reconciling models and experiments. *Journal of Engineering Mathematics*, 94:63–79, 2014.

[99] M. Takashima. Nature of the neutral state in convective instability induced by surface tension and buoyancy. *Journal of the Physical Society of Japan*, 28:810–810, 1970.

[100] M. Takashima. Thermal instability of fluid layer bounded below by a solid layer of finite conductivity. *Journal of the Physical Society of Japan*, 31:283–292, 1971.

[101] M. Takashima. Surface tension driven instability in a horizontal liquid layer with a deformable free surface I. Stationary convection. *Journal of the Physical Society of Japan*, 50:2745–2750, 1980.

[102] M. Takashima. Surface tension driven instability in a horizontal liquid layer with a deformable free surface II. Overstability. *Journal of the Physical Society of Japan*, 50:2751–2756, 1980.

[103] L. H. Tanner. The spreading of silicone oil drops on horizontal surfaces. *Journal of Physics D: Applied Physics*, 12:1473–1485, 1979.

[104] K. Tanzawa, N. Hirota, and M. Terazima. Molecular diffusion in a monolayer on water surface detected by the transient grating method. *Chemical Physics Letters*, 274:159–164, 1997.

[105] U. Thiele, A. J. Archer, and M. Plapp. Thermodynamically consistent description of the hydrodynamics of free surfaces covered by insoluble surfactants of high concentration. *Physics of Fluids*, 24:102107, 2012.

[106] J. Thomson. On certain curious motions observable at the surfaces of wines and other alcoholic liquors. *Philosophical Magazine Series 4*, 10:330–333, 1885.

[107] B. Tsai, M. S. Carvalho, and S. Kumar. Leveling of thin films of colloidal suspensions. *Journal of Colloid and Interface Science*, 343:306–313, 2010.

[108] G. Vázquez, E. Alvarez, and J. M. Navaza. Surface tension of alcohol + water from 20 to 50 degrees C. *Langmuir*, 28:1304–1308, 2011.

[109] A. Vidal and A. Acrivos. Nature of the neutral state in surface-tension driven convection. *Physics of Fluids*, 9:615, 1966.

[110] R. von Helmholtz. Untersuchungen über dämpfe und nebel, besonders über solche von lösungen. *Annalen der Physik*, 263:508–543, 1886.

[111] K. von Neergaard. Neue Auffassungen uber einen Grundbegriff der Atemmechanik. Die Retrakionskraft der Lunge, abhangig von der Oberflachenspannung in der Alveolen. *Zetischrift für die gesamte experimentelle Medizin*, 66:373–394, 1929.

[112] B. B. Wang, X. D. Wang, M. Chen, and J. L. Xu. Molecular dynamics simulations on evaporation droplets with dissolved salts. *Physical Chemistry Chemical Physics*, 9:5105–5111, 2007.

[113] Q. Wang, M. Siegel, and M. R. Booty. Numerical simulation of drop and bubble dynamics with soluble surfactant. *Physics of Fluids*, 26:052102, 2014.

[114] M. R. E. Warner, R. V. Craster, and O. K. Matar. Fingering phemonena associated with insoluble surfactant spreading on thin liquid films. *Journal of Fluid Mechanics*, 510:169–200, 2004.

[115] D. E. Weidner, L. W. Schwartz, and M. H. Eres. Suppresion and reversal of drop formation in a model paint film. *Chemical Product and Process Engineering*, 2, 2007.

[116] E. W. Weisstein. Polynomial discriminant. *MathWorld – A Wolfram Web Resource*. [Online, accessed 21st May 2015].

[117] G. B. Whitham. *Linear and Nonlinear Waves*. Wiley, 1974.

[118] S. K. Wilson. The levelling of paint films. *IMA Journal of Applied Mathematics*, 50:149–166, 1993.

[119] H. Wong, D. Rumschitzki, and C. Maldarelli. On the surfactant mass balance at a deforming free surface. *Physics of Fluids A*, 8:3203–3204, 1996.

[120] M. Yamada, S. Fukusako, T. Kawanami, I. Sawada, and A. Horibe. Surface tension of aqueous binary solutions. *International Journal of Thermophysics*, 18:1483–1493, 1997.

[121] R. W. Zeren and W. C. Reynolds. Thermal instabilities in two-fluid horizontal layers. *Journal of Fluid Mechanics*, 53:305–327, 1972.

[122] J. Zhang, M. K. Borg, K. Sefiane, and J. M. Reese. Wetting and evaporation of salt-water nanodroplets: A molecular dynamics investigation. *Physical Review E*, 92:052403, 2015.

[123] L. Zhibao and L. Benjamin. Surface tension of aqueous electrolyte solutions at high concentrations – representation and prediction. *Chemical Engineering Science*, 56:2879–2888, 2000.